POLITECNICO
MILANO 1863

SCUOLA DI INGEGNERIA INDUSTRIALE
E DELL'INFORMAZIONE

Experimental and modeling investigation of thermal properties degradation in lithium-ion battery with internal temperature measurements

Tesi di Laurea Magistrale in
Energy Engineering - Ingegneria Energetica

Author: **Pietro Bertocchi**

Student ID: 220271
Advisor: Prof. Claudio Rabissi
Co-advisor: Ing. Martino Fortunati
Academic Year: 2024-25

Abstract

Lithium-ion batteries proposed themselves as the reference technology for the support of decarbonization in the EU, especially in the transportation and energy generation sectors. Their market is expected to continuously grow in the upcoming years, creating the need for an innovative framework for their life cycle, with a view to circular economy and second life assessment. In this context, the characterization of the main degradation phenomena of these devices is crucial for the definition of new strategies to prolong their service life, minimizing their waste and environmental impact. One of the main stressors for degradation is represented by temperature, which influences greatly the aging effects during operation. Consequently, an experimental methodology was defined and implemented for the characterization of the thermal behavior of cylindrical lithium-ion batteries. This was accomplished through the estimation of the specific heat capacity and thermal conductivity parameters, by means of four analytical models for physical interpretation. In parallel, a new methodology was established for the insertion of FBG optical sensors inside cylindrical batteries, allowing for the dynamic measurement of internal temperature during operation. Finally, the obtained experimental results were interpreted through the derivation of a physics-based thermo-electrochemical model, with successful results.

Keywords: lithium-ion battery, thermal parameters, aging, physical model, sensors

Abstract in lingua italiana

Le batterie agli ioni di litio si sono proposte come la tecnologia di riferimento per il supporto della decarbonizzazione nell'UE, specialmente nei settori dei trasporti e della produzione di energia. Si prevede che il loro mercato continui a crescere nei prossimi anni, creando la necessità di un quadro innovativo per la gestione del loro ciclo di vita, in un'ottica di economia circolare e seconda vita. In questo contesto, la caratterizzazione dei principali fenomeni di degrado di questi dispositivi è cruciale per la definizione di nuove strategie per prolungare la loro vita utile, minimizzando il loro spreco e impatto ambientale. Uno dei principali fattori che influenzano il degrado è rappresentato dalla temperatura operativa, che influisce notevolmente sugli effetti di invecchiamento durante il funzionamento. Conseguentemente, è stata definita e implementata una metodologia sperimentale per la caratterizzazione del comportamento termico delle batterie cilindriche agli ioni di litio. Questo obiettivo è stato raggiunto attraverso la stima del calore specifico e della conduttività termica, utilizzando quattro modelli analitici per l'interpretazione fisica. In parallelo, è stata stabilita una nuova metodologia per l'inserimento di sensori FBG ottici all'interno di batterie cilindriche, consentendo la misura dinamica della temperatura interna durante il loro funzionamento. Infine, i risultati sperimentali ottenuti sono stati interpretati attraverso la derivazione di un modello termo-elettrochimico basato su equazioni fisiche, con risultati positivi.

Parole chiave: batteria agli ioni di litio, parametri termici, invecchiamento, modello fisico, sensori

Contents

Introduction

Energy has always been of fundamental importance to the social and economic development of nations, throughout the entire history of mankind [1]. For this reason, understanding the key dynamics of the energy sector is essential to comprehend the world we live in. The "Energy Trilemma" [2] - Energy security, equity and environmental sustainability - describes the defining dimensions of a country's energy framework, so that a healthy system has to find a balance between the three, guaranteeing secure, reliable and universal access to energy at an affordable price, but also avoiding potential negative impacts on the environment. If in the previous centuries, starting from the industrial revolution, the main driver for the development was secure and cheap access to energy supplies, nowadays the attention of policy makers and citizens has shifted more and more towards less harmful and more sustainable energy systems. It's in this dynamic and complex context that the European energy transition, one of the most demanding challenges of our time [3], takes place.

The heavy use of fossil fuels for energy generation and conversion has contributed strongly to climate change, causing the emission of massive amounts of greenhouse gases at the global level and leading many countries to introduce new policies to counteract this trend. Starting from the Kyoto Protocol (2005-2012) [4], the European Union has always maintained a leading position in the fight against climate change, creating the Emission Trading System [5] and pushing for "green technologies" and process efficiency [3]. After the Paris agreement [6] (2015), in December 2019, the EU adopted the European Green Deal [7], a strategic package of initiatives and propositions with the goal of reaching net zero emissions by 2050 and thus becoming the first continent to do so.

The chosen strategy envisions the construction of a resilient society with the aid of renewable, sustainable and ecologically friendly alternatives to traditional technologies: renewable energy sources are the ideal option to substitute fossil fuels in the near future, particularly in the power generation sector [8]. Moreover, electrification of key sectors, such as residential and transportation, has shifted the attention on new methods to produce energy in a clean way.

For these reasons, renewable energy sources (and in particular new technologies like solar PV and wind turbines) have obtained great interest from governments and companies as generation technologies characterized by a very low cost and a completely decarbonized production [9]. However, they are intermittent and non-programmable, generating energy only when the natural source is present and not when consumption is done, causing issues and imbalances into the electrical grid [9].

An interesting solution for this continuously changing scenario can be found in energy storage, which can accumulate excess renewable energy (by converting it from/to electricity to a different kind), decoupling in this way production and consumption and employing useful energy that would be otherwise lost. In this regard, multiple technologies are present on the market, characterized by different conversion processes, efficiency and lifetime [10].

Another field which is transforming very rapidly, traditionally very difficult to decarbonize [11], is the transportation sector, with the growing introduction of electric vehicles (EV) on the market. Adoption of light-duty EV has increased swiftly for more than ten years [11] and is expected to keep going in the following decades [12], driven by the continuous reduction of the prices of battery packs employed in this technology [13].

At the present time, the predominant technology for this ever changing context is represented by electro-chemical battery storage, and in particular lithium-ion batteries, characterized by high energy and power density, low self-discharge, high cell voltage and an excellent round-trip efficiency [14, 15]. Moreover, lithium-ion batteries are very versatile, with the ability of extremely fast responses and easy coupling with renewable energy sources generators and other systems. However, they are characterized by a short lifetime compared to other storage technologies and often employ critical raw materials for the EU [16] that, coupled with their growing demand, call for the necessity of a new management paradigm for these resources. In this regard, a new circular economy for lithium-ion batteries must be developed, providing an adequate framework for their reuse and recycling after they reach the end of life, minimizing waste and environmental impacts.

The definition of this new approach must necessarily pass through the understanding of the degradation phenomena that occur during operation and their effects on the overall performance of batteries. In this regard, it was demonstrated that the operating temperature is one of the main stressors for degradation, leading to the necessity of a thorough study of the thermal behavior of batteries.

During this thesis, the thermal characterization of cylindrical lithium-ion batteries was carried, through the definition of innovative experimental methodologies for the estimation of the most important thermal parameters and a physics-based thermo-electrochemical

model. Batteries at both beginning and end of life were analyzed, allowing for the comparison between different aging conditions.

The thesis is structured in the following way:

Chapter 1: it presents the current state of the art of the lithium-ion battery technology, including operating principles, main components, thermal behavior and degradation mechanisms. Afterwards, the main goals of the thesis are presented.

Chapter 2: it describes the battery samples and the experimental stations employed during the work of the thesis. Additionally, the main instrumentation and diagnostic techniques used for the experimental campaigns are presented.

Chapter 3: in this chapter, the thermal characterization experimental campaign is described. In this regard, the methods, models and consequent results are presented and explained, focusing on the most important methodological and logical steps. In particular, a new methodology for the insertion of temperature sensors inside lithium-ion batteries is defined.

Chapter 4: in the first part, it describes the experimental campaign for the characterization of the internal temperature, for which a thorough description is provided focusing on the most important aspects of batteries operation; subsequently, it presents the experimental campaign for the entropic coefficient estimation.

Chapter 5: in this chapter, the conceptualization and definition of a physics-based thermo-electrochemical model is presented, useful for the physical interpretation of the obtained experimental data.

Chapter 6: in the final chapter, the conclusive remarks of this work are presented, emphasizing the key results of the experimental campaign and the models and suggesting possible future developments.

1 State of the art

1.1. Introduction to Lithium-ion batteries

A Lithium-ion battery (LIB) is a rechargeable electrochemical device capable of storing energy in chemical form and converting, by accumulating or releasing it, to electrical energy, through the exploitation of reduction-oxidation (redox) reactions involving lithium ions. It is also a closed system, so that reactants, products and other components are completely confined within the device: for this reason, energy and power capabilities of lithium-ion batteries are strictly correlated with each others and are influenced by the size of the battery itself.

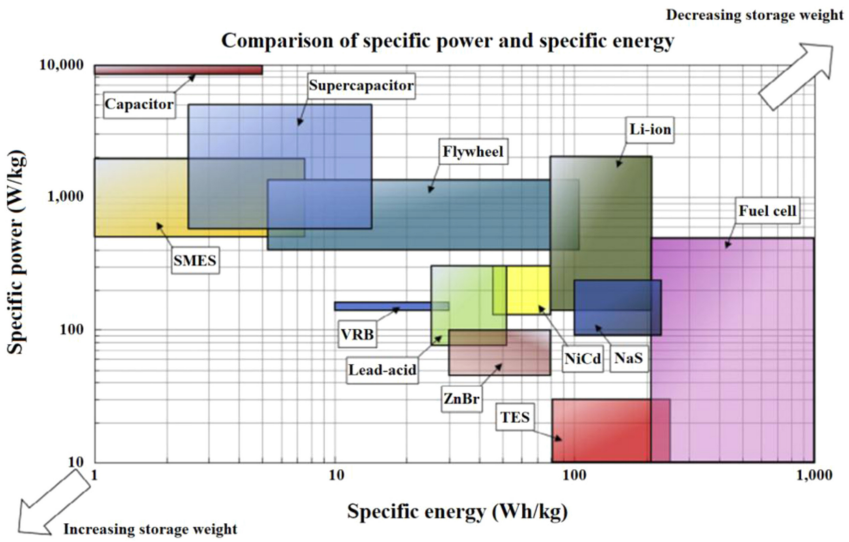

Figure 1.1: Ragone plot of the main electrochemical technologies [17]

Most of the advantages of lithium-ion batteries come from the favorable features of Lithium and its compounds. Lithium (Li) was discovered by Berzelius and Arfwedson in 1817 and later isolated by Brande and Davy in 1821 from the electrolysis of a lithium oxide [18]. It is characterized by excellent physical and electrochemical properties, such as the lowest mass density among metals (534 kg/m^3), low atomic number (3), very low standard electrode potential, corresponding to -3.04 $[V]$ vs Standard Hydrogen Electrode

(SHE), and high specific capacity (3860 $[mAh\ g^{-1}]$). These attributes allowed lithium based batteries to be more compact and lighter than other similar electrochemical devices to parity of costs, reaching higher specific energy and power densities (figure 1.1).
For these reasons, in the past they established themselves as the main technology in different applications, including portable electronic devices, aerospace and medical systems [17]. Nowadays, the market of lithium-ion batteries is expected to grow considerably, particularly as power generation systems of EVs in the automotive sector and for stationary applications, such as services to the electrical grid, behind the meter operations or coupled with non-programmable renewable energy sources [19, 20].

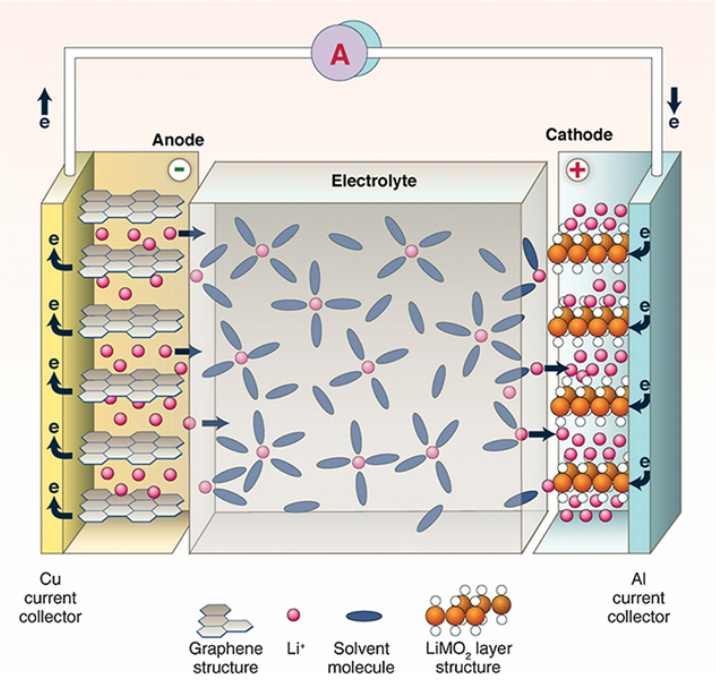

Figure 1.2: Schematic model of a lithium-ion battery [21]

Moreover, another important advantage of batteries (and electrochemical devices in general) lies in the strong modularity (and thus scalability) of the system, so that an elementary unit can be electrically connected in parallel or in series to obtain tailored power and energy ratings. In general, the cell is composed by [17] (figure 1.2):

- **Two electrodes**, characterized by different electric potentials, so that the electrode with the higher potential is defined as the positive electrode while the one with lower potential is the negative electrode. They are the components where the electrochemical reactions take place.
- **A separator**, situated between the two electrodes; it is a thin membrane with a porous structure which allows ion transport but hinders electron transport, to avoid

short circuits between the positive and negative electrodes.

- **An electrolyte**, generally fluid, which wets the internal surfaces of the cell, allowing for lithium ions transport between the electrodes
- **Two current collectors**, one for each electrode, which are made of electrically conductive materials and serve as preferred path for electrons transport between the electrodes.

1.1.1. Main Parameters

The fundamental parameters regarding the operation of the electrochemical cell are the voltage V (measured in volts, $[V]$) and the current I (measured in amperes, $[A]$). The voltage, defined as the potential difference between the positive and the negative electrodes, depends in general on many parameters, such as the materials of the electrodes, thermodynamic conditions (temperature, pressure, concentrations of chemical species), degradation, so that it is rarely constant during operation. The current, defined as the flow of charged particles (electrons in this case) over time (equation 1.1), can be either positive or negative depending on the operation, meaning that the cell can store or release energy, respectively: in particular, if the cell is releasing energy to an electrical load (so it is discharging), the electrons travel through the current collectors from the negative electrode to the positive one and by convention the current is defined as negative, while if the cell is storing energy (charging), the opposite situation occurs and the current is defined as positive.

$$I = \frac{dQ}{dt} \qquad [\mathrm{A}] \qquad (1.1)$$

In general, to avoid issues regarding safety or damage to the cell, battery manufacturers define upper and lower voltage limits, mainly depending on the electrodes' materials, as well as a maximum current limit during charge and discharge.

Another very important quantity for the operation of the cell is the exchanged capacity Q (measured in coulomb, C, in the international System, but more commonly expressed as milliampere-hour, mAh), which can be obtained by reverting equation 1.1, through the integration of the operating current over the time of operation.

$$Q = \int_{t_1}^{t_2} I(\tau) d\tau \qquad [\mathrm{mAh}] \qquad (1.2)$$

If the current I is assumed to be constant during operation the exchanged capacity can be computed as:

$$Q = I\Delta t \qquad [\text{mAh}] \qquad (1.3)$$

Generally, a nominal capacity Q_{nom} is made available by the battery manufacturers, but in reality the available capacity really depends on the operating and thermodynamic conditions at which the cell is working. The given value is commonly determined through a 10 hours long (close to quasi-static conditions) discharge from maximum to minimum voltage, occurring at a temperature of around 20 $[°C]$.
It is not immediate to assess the exchanged capacity of a given electrochemical battery cell so it is often related to the nominal capacity Q_{nom}, through the definition of the dimensionless Depth of Discharge (DoD) parameter, defined as the ratio between the exchanged capacity Q, as defined in equation 1.2, and Q_{nom}:

$$DoD = \frac{Q}{Q_{nom}} \qquad [-] \qquad (1.4)$$

A DoD of 1 represents to a full discharge of the battery, from maximum to minimum voltage limits. Equally, the parameter describing the residual available capacity of a battery is the State of Charge (SoC), defined as:

$$SoC = \frac{Q_{nom} - Q}{Q_{nom}} \qquad [-] \qquad (1.5)$$

Due to their definition, these two parameters range from 0 to 1 and are complementary, as it can be seen in equation 1.5. Moreover, given that they are dimensionless, they can be used to compare batteries with different capacities.
Additionally, the C-rate ("Current Rate") can be defined as for equation 1.6. This is an important parameter which relates the operating current of a cell with its nominal capacity, producing a relative indication of the current which can be compared also with cells of different capacity. Practically, it corresponds to the inverse of the number of hours needed to fully charge or discharge the nominal capacity of a cell at a certain operating current [22].

$$C - rate = \frac{I}{Q_{nom}} \qquad [\text{h}^{-1}] \qquad (1.6)$$

Furthermore, also the exchanged energy J (measured in joule, J) can be defined on the basis of the exchanged charge Q, by introducing the voltage V:

$$J = \int_{t_1}^{t_2} VId\tau \qquad [\text{J}] \qquad (1.7)$$

The electrical power W (measured in watts, W), can be thus defined as the instantaneous energy exchanged by the system, so its derivative over time:

$$W = \frac{dJ}{dt} = VI \qquad [\text{W}] \qquad (1.8)$$

1.1.2. Operating principles

A lithium-ion battery converts the chemical energy stored within its components to electrical energy, through reversible reduction-oxidation reactions. A reduction is a chemical reaction during which electrons are consumed, decreasing the oxidation state of a chemical species; an oxidation, instead, is a reaction during which electrons are produced, increasing the oxidation state of a chemical species. The amount of energy associated with these reactions strictly depends on the materials of the electrodes of the cell, but in general two main half-reactions (one reduction and one oxidation) take place, one for each electrode. The electrode where the oxidation occurs is defined as the anode, while the electrode where the reduction occurs is called the cathode but, given that the reactions are reversible, a certain electrode (positive or negative) can behave either like a cathode or an anode, depending on the reaction occurring. In literature, negative and positive electrodes are sometimes referred to as anode and cathode, respectively, using the discharge process designation. Keeping in mind their definition, these terms will be used in an equivalent way for simplicity. The typical half-reactions for lithium-ion batteries are:

$$\textbf{Negative}: \qquad Li_xC_6 \rightleftharpoons xLi^+ + C_6 + xe^- \qquad (1.9)$$

$$\textbf{Positive}: \qquad xLi^+ + Li_{1-x}MO + xe^- \rightleftharpoons LiMO \qquad (1.10)$$

The most common material for the negative electrode is graphite (C_6), while the positive electrode is generally made by a transition metal oxide (MO), but many possible combinations and configurations are available on the market, depending on the application. The most widely used chemistries are:

- **LCO**: Lithium-Cobalt Oxide;

- **LMO**: Lithium-Manganese Oxide;
- **NCA**: Lithium-Nickel-Cobalt-Aluminum;
- **NMC**: Lithium-Nickel-Manganese-Cobalt;
- **LFP**: Lithium-Iron Phosphate.

If the cell is completely charged, a condition represented by $SoC = 1$, the bulk of the lithium present in the cell is stored in the negative electrode, hosted in the layers of graphite. During a discharge, the reaction in equations 1.9 and 1.10 develop from left to right: an oxidation reaction occurs in the negative electrode, with the production of electrons (e^-) and lithium ions (Li^+), while a reduction takes place at the positive electrode. These reactions are spontaneous, meaning that they occur without an external generator. In this way, the negative electrode gets gradually delithiated throughout the process, while the positive electrode acquires lithium ions. The transport of ions occurs through the electrolyte and across the separator, while electrons travel through the current collectors and the external circuit connected to the battery, recombining afterwards in the positive electrode. The opposite process occurs during a charge process, during which the positive electrode gets progressively delithiated while the negative electrode gets lithiated. This process, however, is not spontaneous and a charging device is needed to reverse the reaction.
Both electrodes are characterized by a certain electric potential, higher for the positive one, which depends on their materials. Given its very low standard potential, a variation of the lithium content in the electrodes' structure induces a change in their potential, increasing or decreasing the overall voltage of the cell. The equilibrium potential (also called Open Circuit Potential, OCP) of each electrode can be expressed through Nernst's Law, which derives directly from the law of conservation of energy of the system. For the reaction in equations 1.9 and 1.10, the OCP can be computed as:

$$\textbf{Negative}: \qquad E_{ocp,n} = E^0_{ocp,n} + \frac{RT}{F} ln\left(\frac{a_C a_{Li^+}}{a_{LiC}}\right) \qquad [\text{V}] \qquad (1.11)$$

$$\textbf{Positive}: \qquad E_{ocp,p} = E^0_{ocp,p} + \frac{RT}{F} ln\left(\frac{a_{MO} a_{Li^+}}{a_{LiMO}}\right) \qquad [\text{V}] \qquad (1.12)$$

Where:

- $E_{ocp,n}$ and $E_{ocp,p}$ are the equilibrium potentials of the negative and positive electrodes, respectively;
- $E^0_{ocp,n}$ and $E^0_{ocp,p}$ are the standard reduction potentials of negative and positive

electrodes, respectively;

- R is the universal gas constant, corresponding to 8.314 $[J\ mol^{-1}K^{-1}]$;
- F is the Faraday constant, corresponding to 96485 $[C\ mol^{-1}]$;
- T is the temperature, $[K]$;
- a_i is the chemical activity of the species i $[-]$.

A reference condition is always necessary to define the electrodes' electric potentials: in general, the adopted convention is to express them in V vs. Li/Li^+, thus using the lithium standard electrode potential (corresponding to -3.04 $[V]$ vs. SHE) as a reference. The overall equilibrium voltage (also called Open Circuit Voltage, OCV) is defined as the difference between the positive and the negative electrodes open circuit potentials, respectively (equation 1.13) and represents the global thermodynamic behavior of the cell when no current is flowing, so when the battery is not attached to any load.

$$E_{OCV} = E_{ocp,p} - E_{ocp,n} \quad [\text{V}] \qquad (1.13)$$

This condition corresponds to the electrochemical equilibrium state for the system, but only represents an ideal description of the behavior of the cell because, in general, any operating current applied to the battery is met with a certain irreversible loss. In a practical manner, the OCV is typically determined by measuring the voltage of the cell during a very slow discharge (usually done with C-rates equal to or lower than 0.1 h^{-1}), to minimize the magnitude of such losses and represent as closely as possible the thermodynamic equilibrium condition.
As it can be seen in figure 1.3, the OCV and the SoC are strictly correlated with each other, meaning that each value of OCV is associated with a value of SoC: indeed, the SoC is an indirect representation of the lithium concentration in the electrodes and thus of the chemical activity of the species involved in the reduction-oxidation reactions, which are present in equations 1.11 and 1.12. During a discharge process, the negative electrode progressively loses lithium ions, increasing its electric potential, while the positive electrode gets lithiated, decreasing its potential: as a result, the equilibrium potential (OCV) decreases as well.
It can be also noted that the operating ranges of the full cell and of the two electrodes don't correspond: theoretically, it could be possible to operate at SoC higher than 100%, but this is not done to respect the maximum and minimum cut-off voltage limits, and thus avoid safety or damage issues and preserve the lifetime and performance of the cell.

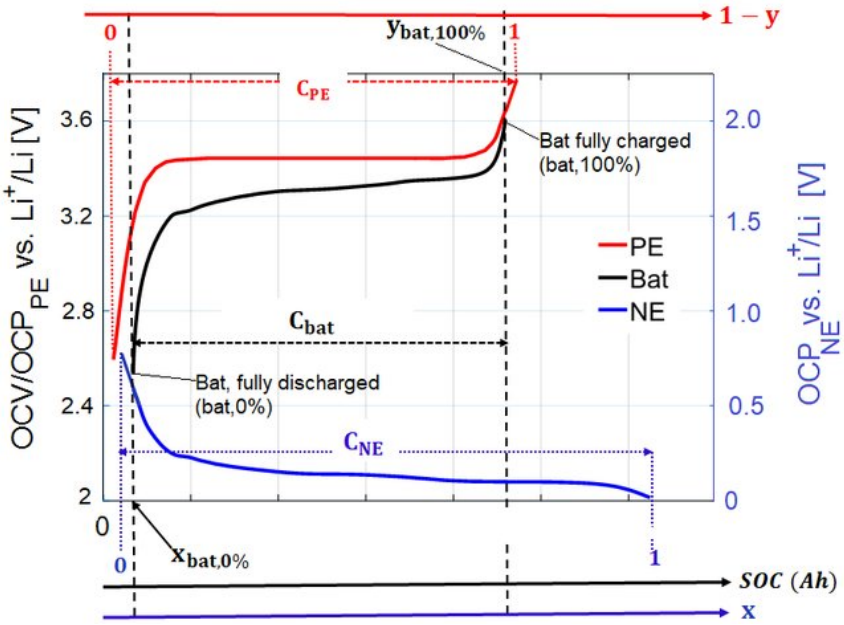

Figure 1.3: Open Circuit Voltage curve for a graphite anode and LFP cathode lithium-ion battery [23]

1.1.3. Non-ideal behaviour

The thermodynamic equilibrium condition described in the previous section doesn't represent the real operation of a lithium-ion battery. The approximated OCV curve in figure 1.3 was obtained during a very slow, quasi-static discharge, performed at a low current rate, but at the higher operating currents demanded by real applications, the battery voltage doesn't correspond to the OCV, due to the fact that irreversible voltage losses appear. These are called overpotentials and are defined as for equation 1.14

$$\eta = \Delta V - E_{OCV} \qquad [\mathrm{V}] \qquad (1.14)$$

The overpotentials arise due to the fact that, to have a change of state in the battery, and thus a flux (charge or mass transport it is), a disequilibrium needs to be introduced in the system, so that the reduction-oxidation reactions are unbalanced towards one direction and can take place: this disequilibrium leads to irreversibilities in the system, which inevitably downgrade its performance. The comprehension of this aspect, which is fundamentally rooted in the second law of thermodynamics, is key to understand the different nature of the voltage losses, which are described below [24]:

- **Ohmic losses** are related to the ohmic resistance of the cell, which refers to ionic resistance in the electrolyte and electronic resistance in the electrodes, as well as in

other components of the cell (Contact losses). The ohmic overpotential produces a fully resistive effect, which translates in an almost instantaneous voltage drop (gain) at the very beginning of a discharge (charge) process. Moreover, because they respect ohm's law, ohmic losses are linearly proportional to current.

- **Charge Transfer losses** are associated with the charge transfer process happening between different phases inside the cell: when chemical reaction occurs, a certain energy barrier, called activation energy, needs to be overcome to allow the transfer of charges from one phase to another. In general, the activation energy depends on many factors, including the type of reaction, temperature and reaction rate (and thus on the operating current, meaning that a higher C-rate will translate in a higher voltage loss).
- **Diffusion losses** arise from the diffusion phenomena of lithium ions in the components of the cell. Both in the solid active material particles in the electrodes and in the liquid electrolyte, a concentration gradient of lithium ions is established: only the lithium concentration at the particles surface is available for the reactions, limiting the transport and thus decreasing the overall voltage. Given that diffusion phenomena are generally slower than the others described above, the diffusion overpotential is usually low at the beginning of a process, but grows considerably towards the end, when the gradient is fully formed; moreover, also in this case, a higher current will result in a higher voltage drop.

The overpotentials are always present during discharge/charge processes and represent the energy dissipated as heat following transport phenomena. Their effect on the equilibrium voltage of the battery is equivalent to a vertical shift in the OCV curve in figure 1.3. In particular, during a discharge process, overpotentials lead to a decrease in the overall voltage, so that less potential energy is available; during charge, instead, losses lead to an increase of the voltage, meaning that a higher amount of energy is needed to increase the energy state of the battery. For a fast representation of the losses in the system, efficiency indicators can be specified. In particular, for lithium-ion batteries the following indexes can be defined:

- **Coulombic Efficiency**: represents the capability of a battery to release its capacity during a discharge-charge cycle. It is defined as the ratio between the discharged capacity after a full charge and the charge capacity necessary for that discharge.

$$\eta_c = \frac{\int_{dis} dQ}{\int_{ch} dQ} \qquad [-] \qquad (1.15)$$

Where Q is the exchanged battery capacity. The value of the coulombic efficiency depends on the conditions at which the cycle is performed, but in general lies between 99.5% and 99%, so that the capacity discharged is always lower that the charged one. The loss is caused by side reactions of lithium with other chemical species present in the cell and by internal resistance of the battery.

- **Energy Efficiency**: it is analogous to the coulombic efficiency and represents the amount of useful energy that the battery is able to provide with respect to the one needed to fully charge it. It is defined as the ratio between the energy released during a discharge process and the energy needed to charge the battery during the same cycle, with a coulombic efficiency equal to 1.

$$\eta_{en} = \frac{\int_{dis} \Delta V dQ}{\int_{ch} \Delta V dQ} \qquad [-] \qquad (1.16)$$

The energy efficiency typically ranges between 60% and 90%, but really depends on the C-rate of the cycle, due to the fact that higher currents translate to higher overpotentials and thus lower efficiencies.

1.2. Components

The components of a system are at the core of its performance, so materials and structures are carefully selected and engineered to obtain the best properties for a given application. As briefly described before (section 1.1), the elementary unit of a battery, is composed by two electrodes, two current collectors, a separator and an electrolyte. In this section, the essential components and their most utilized materials will be detailed thoroughly.

1.2.1. Electrodes

The positive and negative electrodes are the components where the reduction and oxidation reactions occur during operation. To increase the operating voltage of the cell, the difference between the electric potentials of the electrodes should be maximized, so a high potential for the positive electrode and a low potential for the negative one are wanted characteristics. The main properties required for an electrode are, in general:

- **High gravimetric and volumetric capacity**, measured in $[mAh\ g^{-1}]$ and $[mAh\ cm^{-3}]$, respectively, to increase the maximum charge storable in the particles, per unit of mass and volume, respectively;

- **High electronic conductivity**, to decrease the electronic resistance and so the associated ohmic losses;
- **High lithium solid diffusion coefficient**, to increase the lithium transport by solid state diffusion inside the electrodes' particles, thus lowering the diffusion overpotential;
- **High mechanical, thermal and chemical stability**, to minimize excessive decay by pressure and volume changes, thermal degradation and side reactions with other chemical species, respectively.
- **Highly reversible behavior**, meaning that the electrode material must be able to store and release lithium ions easily, ie. the energy barrier for the reaction must be low.

Moreover, a suitable electrode material should be non-toxic, non-flammable and environmentally friendly, as well as cheap and abundant in nature.
Their structure is porous, consisting of an active material, which stores the lithium and defines the chemistry of the redox reactions, a conductive agent, to improve the electronic conductivity and a binder, which is needed to strengthen the porous structure and merge the active material with its current collector.

Negative electrode

In the early stages of the lithium-ion batteries development, lithium metal and its alloys were used as negative electrodes, thanks to its favorable properties. However, lithium was soon abandoned due to safety concerns regarding dendrites formation, which formed during repeated cycles and caused the short-circuiting of the battery, leading to thermal runaway. From the 1970s-80s the attention shifted towards more stable carbon based materials, such as graphite, which can easily store and release lithium through the intercalation reaction [18, 25]. In fact, graphite is characterized by low electric potential, high gravimetric capacity, a regular and stable layered structure and high reversibility of reaction [26–29].

The intercalation process in graphite consists in the subsequent insertion of lithium ions in the structure, following the so-called "staging mechanism" (figure 1.4): during lithiation and delithiation, graphite undergoes several phase transitions between Li-C solid state phases, which are called "stages" due to the ordering of lithium ions inside the graphene layers. The graphite structure allows the intercalation mechanism due to its layered shape, characterized by one atom thin carbon sheets, which are linked together by weak Van der

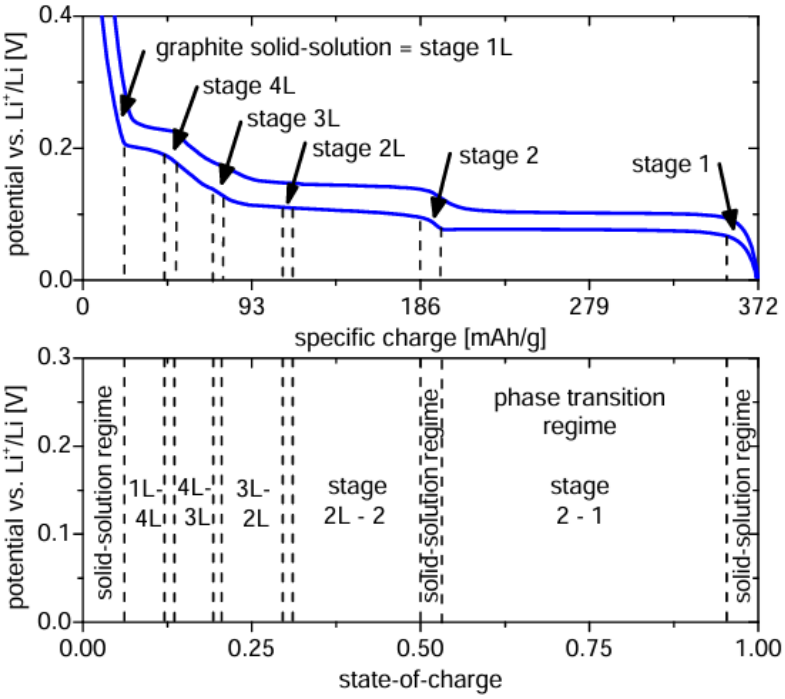

Figure 1.4: OCP curve of graphite anodes highlighting phase transitions [30]

Waals atomic bonds: thanks to this configuration, the lithium ions can be stored in the inter-layer spaces between sheets without the need to break strong atomic bonds [26]. Starting from graphite solid solution (1L), where the letter "L" indicates a disordered, liquid-like distribution, the structure begins to host lithium ions during a charge process. A phase transition occurs between stages 1L and 4L, in which lithium ions are intercalated in every fourth slab. As the lithium content in the layer increases, the structure undergoes several other transitions, decreasing the distance between occupied inter-layers (4L-3L-2L), up until the stage 2 is reached, which presents a more ordered and stable structure due to its symmetry. After that, a longer phase transition between stages 2 and 1 begins, ultimately reaching the stage 1 configuration, in which the layered structure is completely filled [30] (figure 1.5).

Thermodynamically, the staging mechanism is related to the balance between the energy required by the intercalants to expand the inter-layer space and the repulsive interaction between layers [26]. The succession of phase changes of graphite can be clearly seen in figure 1.4, in the OCP curve of the electrode: during a phase change, two phases are simultaneously present and coexist in the structure and a plateau can be identified on the potential curve; on the other hand, when only one phase is present, the potential decreases monotonously.

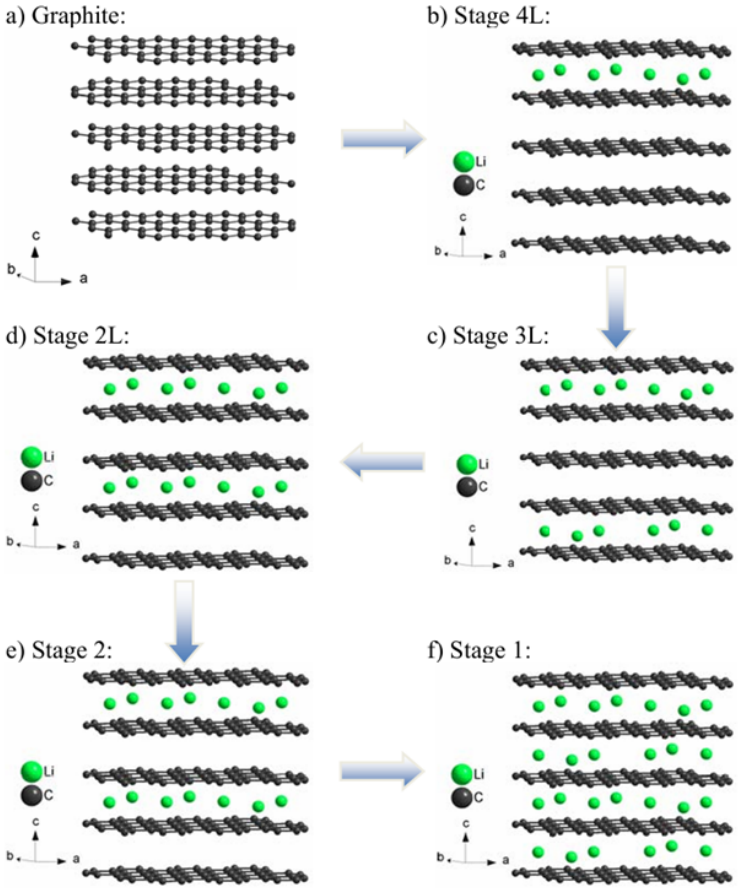

Figure 1.5: Staging of graphite during lithium intercalation [30]

Even though graphite is characterized by many advantages, it presents some drawbacks, which have to be taken into account [26]:

- **Volume variation during cycling**: is in the order of 10% [26] during cycling and causes an increase in the operating pressure and mechanical stresses, which leads to structural damage and integrity issues;
- **Limited rate capability**: more important during charge (lithiation process), a too high reaction rate could lead to a risk of lithium metal plating on the electrode surface, with consequent shot-circuit of the cell;
- **Aging**: due to its layered structure characterized by low energy atomic bonds, graphite tends to continuously exfoliate; this process is not stable at the low potentials of the negative electrode, so that an intermediate layer, the Solid Electrolyte Interphase (SEI) is formed. The SEI is a passivation film that forms at the anode-electrolyte interface because of the high reactivity between them; it is one of the most important degradation mechanisms of lithium-ion batteries, as it will be ex-

plained in section 1.5.1.

Despite many research efforts on substitutes, graphite is still the dominant material for negative electrodes in modern LIBs. Alternative configurations of carbon-based materials are present on the market [31], such as graphite-silicon mixtures, characterized by a higher gravimetric capacity (but also higher volume variations), amorphous carbon, with a disordered structure which allows for higher specific capacity.
Research focuses nowadays on the improvement of carbon-based materials and the development of new materials, including [28]:

- **Transition Metal Oxides**: they have a high gravimetric capacity (up to 1000 $[mAh\ g^{-1}]$) and good cycling performance. Moreover, they completely avoid the formation of the SEI and lithium dendrites; on the other hand, they are characterized by poor conductivity and cause the decomposition of the electrolyte. The main representative of this category is the lithium-titanate oxide (LTO), characterized by excellent thermal stability, negligible volume variations and very good reaction reversibility; however, this material has a high electric potential (1-2 $[V]$), which limits the specific capacity to 175 $[mAh\ g^{-1}]$.
- **Alloy based materials**: including Si, Ge, Sn, these materials are characterized by excellent gravimetric capacity, but also high volumetric changes, that cause structural damages [27].

Positive electrode

The development of positive electrode materials progressed in parallel with anode materials, leading to the commercialization of the first LIB as it is known today, the rocking chair battery [25]. Unlike graphite for the negative electrode, numerous cathode chemistries established themselves on the market over the years, focusing on transition metal oxides and polyanions compounds, due to their very high operating voltage (3-5 $[V]$) and specific capacity (100-200 $[mAh\ g^{-1}]$) [32]. The main positive electrode materials available are [13, 27, 29, 32]:

- **Lithium-Cobalt Oxide (LCO)**: $LiCoO_2$
  it was the first commercially successful cathode material, characterized by a two-dimensional layered structure, high energy density and specific and volumetric capacity (274 $[mAh\ g^{-1}]$ and 1363 $[mAh\ cm^{-3}]$, respectively). Moreover, it is characterized by stable electrochemical performance, cycle efficiency and steady charge and discharge voltage. Its major weaknesses lie in the poor thermal stability, fast capacity fade, high pollution, toxicity and cost, which limits the use of this chemistry

to applications where energy density is of paramount importance, such as consumer electronics. Additionally, the use of Cobalt must come to terms with the ethical problems related to the raw material and its extraction.

- **Lithium-Manganese Oxide (LMO)**: $LiMnO_2$
  these cells rely on manganese oxides, with the same two-dimensional structure of LCO. Moreover, due to the high discharge voltage ($\tilde{4}.1$ $[V]$), intrinsic safety and eco-friendliness, low toxicity and low cost (manganese is five times less expensive than cobalt [13]), this chemistry is one of the main alternatives to replace LCO. Unfortunately, the layered structure tends to change into the spinel structure $LiMn_2O_4$, which is more stable but characterized by lower specific capacity (148 $[mAh\ g^{-1}]$) and suffers from important capacity losses (low cycling efficiency and stability). For these reasons LMO cells have lower energy performance and lower lifetime compared to other cells.

- **Lithium-Nickel-Cobalt-Aluminum (NCA)**: $LiNi_{0.8}Co_{0.15}Al_{0.05}O_2$
  this chemistry was proposed as an evolution of early LCO structures, substituting Co with Ni for higher energy density and lower costs. Adding Al in small quantities is useful to improve electrochemical and thermal stability, with negligible downgrades in the available capacity [33]. As a result, the NCA cells reach high theoretical specific (279 $[mAh\ g^{-1}]$) and usable discharge capacity (200 $[mAh\ g^{-1}]$) and long storage calendar life compared to conventional LCO. However, NCA batteries suffer from high capacity fade at elevated temperatures (40-70 $[°C]$) and micro-crack growth at grain boundaries during operation.

- **Lithium-Nickel-Manganese-Cobalt (NMC)**: $LiNi_xCo_yMn_xO_2$
  the acronym NMC indicates a family of materials, characterized by different relative dosage of Ni, Mn and Co inside the layered structure. These cells are characterized by improved structural stability compared to LCO, but comparable or higher achievable specific capacity and average voltage, while having lower costs and toxicity and higher safety (due to the lower amount of Co). The main representative of this class and the most widely used on the market is $LiNi_{0.33}Co_{0.33}Mn_{0.33}O_2$ (also known as NMC111), which showed a reversible specific capacity of 234 $[mAh\ g^{-1}]$ and good cycle stability even at high operating temperatures. Another example is the NMC811 ($LiNi_{0.8}Co_{0.1}Mn_{0.1}O_2$), characterized by a lower amount of cobalt and thus more ethically sustainable. Novel NMC cathode materials employ a double layer particle structure (with average formula $LiNi_{0.68}Co_{0.18}Mn_{0.18}O_2$), formed by a bulk of nickel-rich layered oxide ($LiNi_{0.8}Co_{0.1}Mn_{0.1}O_2$) and an outer layer of a Mn and Co substituted structure ($LiNi_{0.46}Co_{0.23}Mn_{0.31}O_2$), for a good combination

of high energy/power density and improved cycle life and safety.

- **Lithium-Iron Phosphate (LFP)**: $LiFePO_4$
  this cathode chemistry is part of the polyanions compound family, a new class of materials based on $(XO_4)^{3-}$ (X = S, P, Si, As, Mo, W) ions, which increase the equilibrium potential and stabilize the structure. The LFP is the only commercialized cathode with olivine structure, favorable due to its excellent thermal and electrochemical stability and high power capability. Moreover, it presents a very high cycle life, very useful in long lifetime applications, low cost and low toxicity. The main drawbacks consist of its lower average potential compared to layered structure materials, which results into lower energy density and specific capacity (170 $[mAh\ g^{-1}]$), other than the low electrical and ionic conductivity. In last few years, extensive research on this chemistry lead to considerable improvements in its performance: the main breakthrough came with reduction of the particles size, in combination with carbon coating, that allowed to increase the rate performance and prevented the metal dissolution in the electrolyte [29, 32].

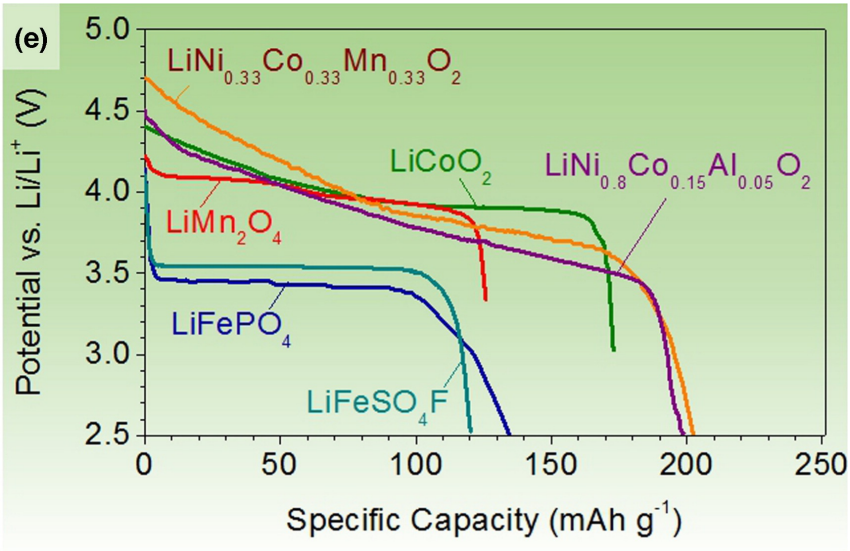

Figure 1.6: OCP Curves for the most important cathode materials

1.2.2. Electrolyte

The electrolyte is the component that allows the lithium ions transport between electrodes and thus is crucial for the correct functioning of the cell. In early iterations of the first LIBs, a solid polymer-based electrolyte (PEO:Li) was developed [18]: solid-state batteries have the advantage of using metallic lithium as negative electrode, so a higher energy density can be achieved; however, they exhibit a poorer ionic conductivity compared to

liquid electrolytes and the risks associated with Li metal hindered their commercial development [25]. The electrolyte must be a good ionic conductor but also electric insulator, should be stable, non-toxic and sustainable. Modern lithium-ion batteries employ a non-aqueous organic solution [34], composed by a solvent, which accounts for about 80% of the mass, a lithium salt and a series of additives, to improve or enhance the properties of the electrolyte.

Solvents

The main properties that a solvent should have are, in general: high dielectric constant, to dissolve lithium salts, low viscosity, high stability and compatibility with electrodes and other components, low melting point, high evaporation point, high safety, low toxicity and cost. The principal solvents employed in batteries are cyclic (EC, PC) and chain carbonate compounds (DMC, DEC, EMC), which are generally mixed in a 1:1 ratio to obtain multiple advantageous properties.

Salts

The choice of lithium salts must respect the following conditions: high solubility, stability and conductivity in organic solvents, easy dissociation of Li ions, environmentally friendly and easy to produce. LIBs mostly employ $LiPF_6$, a salt characterized by high ionic conductivity and solubility, but poor thermal stability.

Additives

Additives can greatly improve battery performance, in an economic and efficient way. In general they can be classified into [34, 35]:

- film-forming (SEI) additives: when added in traces, they promote the formation of a stable protective layer at the electrodes interfaces, which can improve the cycle performance and reduce the irreversible capacity loss;
- electrolyte salt stabilizers: they can greatly improve the salt performance (up to 20%), providing higher stability, efficiency and capacity retention;
- high ion conductivity additives;
- safety protection additives: can be further divided into flame retardant additives, which increase the boiling point of the solvents and make them less flammable, and overcharge protection additives, which are able to protect the electrodes from overcharge issues at too high voltage.

1.2.3. Separator

The separator functions as a physical barrier between the electrodes, separating the two sides of the electrochemical cell, but also serves as an electrolyte reservoir, enabling lithium ions transport across its structure [36]. It must be chemically, thermally and mechanically stable, very thin but able to withstand the pressure variations inside the cell [37]. Moreover, the separator should be able to act as a blocking interface when an internal short-circuit occurs. The most common separators materials [18, 37] are porous poly-olefin (polypropylene - PP, polyethylene - PE) based structures, characterized by a relatively low melting point (135 $[°C]$ for PE and 165 $[°C]$ for PP, respectively), which make them able to shut the battery down when overheating occurs, and good mechanical properties.

1.2.4. Current Collectors

Current collectors [38, 39] serve a fundamental role inside the battery cell, as conductive materials for electrons transport to the external electrical circuit, but also in supporting active materials structures (electrodes) and binders. The main property that CCs must have is high electrical conductivity, but it should also be resistant to corrosion (which is enhanced in the high voltage environments of LIBs), electrochemically stable and characterized by high mechanical strength, adhesive to electrodes, thin, light and cost effective. To this day, the most common materials employed as current collectors are copper on the negative electrode and aluminum on the positive one:

- copper (Cu) is characterized by a standard redox potential of 3.38 $[V]$ (vs Li/Li^+), higher than the average electric potentials of the graphite anodes (0-2 $[V]$) and thus electrochemically stable. it is one of the highest conductivity materials available, at a competitive price;
- aluminum (Al), although characterized by a lower redox potential (1.37 $[V]$ vs Li/Li^+), is used as cathode CC due to the passivation Al_2O_3 layer that it forms when in contact with the organic solvents of the electrolyte; the resistance to corrosion can be enhanced by introducing specific electrolyte additives, which protect the passivation layer.

Current collectors are generally fabricated in the form of 10-20 $[\mu m]$ thick foils (most common, easier to produce but at the price of lower performance), meshes and foams, which increase the surface area and the mass loading. Moreover, treatments such as chemical etching and carbon coatings are often employed to improve the adhesion with electrodes, reduce contact resistances and enhance electrochemical stability and charge-

transfer properties.

1.3. Cell Geometries

The components described in the previous section are always present in the structure of the elementary electrochemical cell and can be stacked and arranged following the specific needs of a real application. In fact, as stated before, one of the main advantages of battery systems is their modularity and scalability, allowing for the design of batteries with tailored size or capacity. However, no standardization of cell geometries exist as of today, due to the presence of a large number of manufacturers on the market, each one with proprietary designs. As a result, many different geometries and shapes are commercially available, with distinct properties (figure 1.7), that can be classified as follows.

1.3.1. Coin (or Button) cells

Coin cells are typically characterized by small size and are thus generally employed in small portable devices or applications which require little space footprints. Moreover, small coin cells are mainly used for testing purposes in universities' laboratories, because they don't necessitate high amounts of materials to build and expensive or sophisticated infrastructure [40]. They are usually characterized by a single stack of components, so that the majority of the cell weight contribution is given by the non active materials layers, such as the outer case (figure 1.7) The most common designation is given by a four digit number indicating the cell diameter and thickness, respectively (for instance, a 2032 coin cell has a 20 $[mm]$ diameter and is 3.2 $[mm]$ thick).

1.3.2. Pouch cells

Also known as flat-cells [41, 42], they are characterized by a soft and flexible heat-sealed pouch. The components are stacked on top of each others and inserted inside the pouch during manufacturing. No universal format exists for this type of cell, so its size and thickness can be tailored to the specific application. The absence of a metal enclosure and the flexible structure allow for a strong weight decrease and packaging efficiency, as well as cost-effectiveness, due to its simpler manufacturing process. However, this solution is characterized by a very low resistance to impacts and requires additional support. Furthermore, pouch cells suffer from swelling, caused by excessive gas formation during overcharge operation.

1.3.3. Prismatic cells

Prismatic cells employ a hard and stiff aluminum housing, in which the cell's components are enclosed. To increase the energy density and optimize the available space, several layers of the main components assembly are wrapped on each others, creating a flattened spiral-shaped roll, called "jelly-roll", or simply stacked like in pouch cells. The jelly-roll is connected with the external circuit by the means of aluminum and copper foils, for positive and negative electrodes, respectively. Prismatic cells are characterized by higher structural stability compared to pouch and thanks to their regular shape the capacity of the single cell can be increased considerably, up to 30-40 $[Ah]$. Like pouch cells (but not as much), they tend to swell during operation, slightly increasing their volume. This kind of cell is often employed in portable electronic devices, such as mobile phones, but it is gaining increasing interest and importance in the automotive sector.

1.3.4. Cylindrical cells

As the name suggests, cylindrical cells are characterized by a cylinder build aluminum casing, that houses the internal components. Due to its shape, this geometry is well suited for jelly-roll packing of the assembly, which is wound on a hollow smaller cylinder, the mandrel, and inserted in the aluminum canister. Moreover, thanks to the higher mechanical stability given by their symmetric shape, these cells employ thinner casings compared to other geometries. Cylindrical cells have built-in safety features, which mitigate catastrophic failure and inherent risks. The main ones are [43–45]:

- Current Interrupt device (CID), which is designed to disconnect the battery's internal current flow in case of excessive internal pressure, by breaking the weak welded connection between the top and bottom disks situated at the positive pole, thus preventing thermal runaway;
- Positive temperature coefficient (PTC) thermistor, which protects the battery from external short circuits and electrical abuse conditions by limiting current flow when the cell reaches a particular temperature;
- Safety vents, whose function is to release internal pressure caused by gas formation: when the cell pressure reaches a certain limit a notch opens, allowing for the gases to escape

Because of these reasons, cylindrical cells are considered as inherently safer than other geometries. Similarly to coin cells, some common, more or less unified size designation exists in the cylindrical cells market: five digits numbers are used, indicating the diameter

and length in the axial direction; for instance, a 18650 designation indicates a cylindrical cell with a diameter of 18 $[mm]$ and a length of 65 $[mm]$, but many configurations exist, from 10440 (also known as "AAA" batteries) to the much bigger 46950, employed in Tesla's EVs' powertrain.

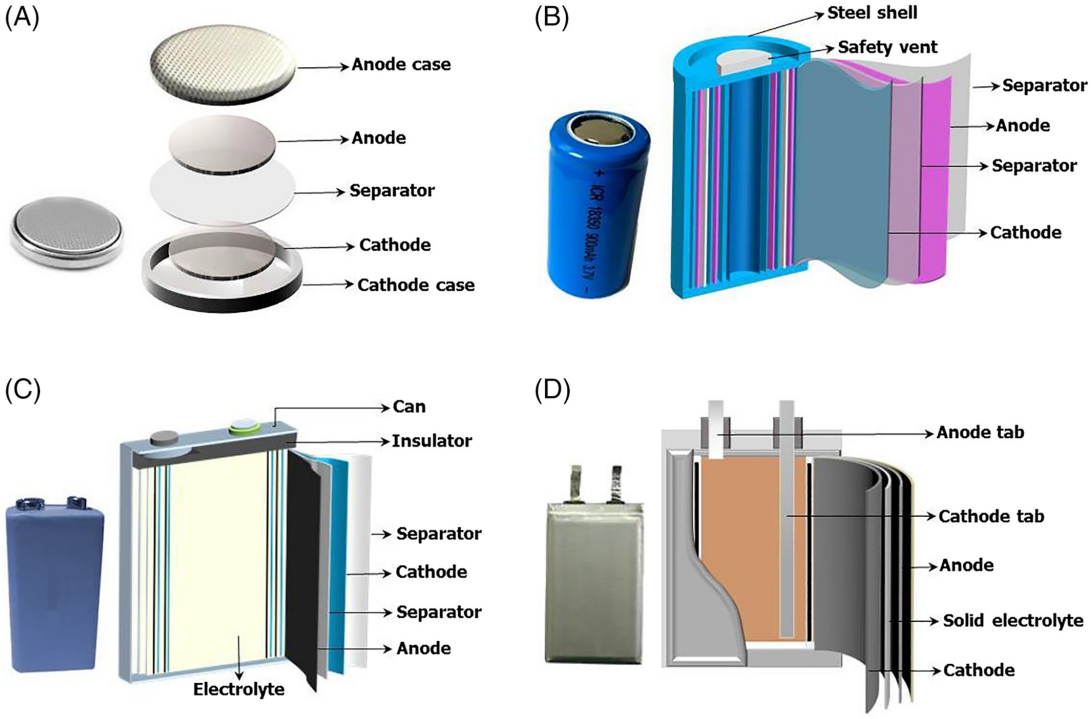

Figure 1.7: Most diffused cell geometries for lithium-ion batteries

1.4. Thermal behavior of lithium-ion batteries

As described in the previous sections, lithium-ion batteries are characterized by a very complex structure, where components are fine-tuned to obtain specific properties and features; at the same time, they are required to function in a rather aggressive environment, marked by high electric potential which can promote unwanted reactions. As a result, the normal operation of the cells is very sensitive to working conditions, which greatly influence their performance and degradation phenomena.

In general, the thermal behavior of LIBs mainly depends on the combination of extrinsic stress factors such as temperature, state of charge (SoC) and current load: extreme temperatures, weather conditions and other stressors have strong negative effects on batteries' activity and can lead to failure in some cases, so the control system must be able to maintain the cells within a suitable intermediate range at all times. Furthermore, during operation, a battery inevitably generates heat, increasing its operating temperature as a

result and thus requiring an appropriate cooling system and thermal management strategy. This aspect is generally handled through a Battery Thermal Management System.

1.4.1. Thermal stability

From literature, it was assessed that the optimal range for lithium-ion battery operation should be between 15-25 [$°C$] and 40 [$°C$] [46]. Outside of the optimal operating temperature range, at either low or high temperatures, lithium-ion batteries suffer from high performance and capacity losses, which reduce their cycle life (through degradation phenomena) and have an impact on safety concerns, such as thermal runaway. In general, this aspect is exacerbated by the cell (and module) design, its shape and the components stability (especially of the electrolyte) [47].
At sub-zero temperatures the chemical viability of LIBs can be significantly altered: an important efficiency drop is experienced due to the increase of the overpotentials of the cell which leads to a reduction of its power and energy potential.
The main phenomena occurring at the particles level are linked with the temperature dependency of the components parameters; in general they are: the reduction of lithium ions diffusivity in the electrodes particles and the decrease of the electrical conductivity of the electrolyte and the SEI at the negative electrode. Moreover, the reaction rate is inversely proportional to the temperature, so at lower operating temperatures electrochemical reactions are strongly hindered, resulting in increased charge transfer resistance at the electrodes-electrolyte interfaces.
Sub-zero temperature operation is crucial for automotive applications, where range and cycle life are key parameters: on top of the increased losses associated with cold environments, a significant portion of the available capacity of the battery pack must be employed to provide heating to itself and to the cabin, further reducing the usable charge. Other important issues are related to the limited battery propulsion and regenerative power and high battery internal resistance [46].
In contrast, operation in hot climates doesn't necessarily coincide with performance losses [47], but it strongly affects the maximum discharge capacity and degradation of batteries, as it will be described in the following sections.
However, the greatest threat to the battery integrity is related to operation at too high temperatures, which can be easily achieved if working under abusive conditions, at high current rates and with sub-optimal thermal management and safety systems [48]. After a critical threshold temperature is reached, the thermal degradation of some components lead to a series of exothermic chain-reactions involving the available chemical species, which are able to sustain themselves until complete failure of the entire system [49]. This

mechanism is known as thermal runaway, that can be defined as a process initiated by production of more internal heat than what a battery can dissipate, often leading to a destructive result. In general, thermal runaway can happen as a consequence of a battery's mechanical, electrical (internal short-circuit), electrochemical (overcharge abuse), or thermal failure and thus can be triggered in different ways (figure 1.8) [47, 48].

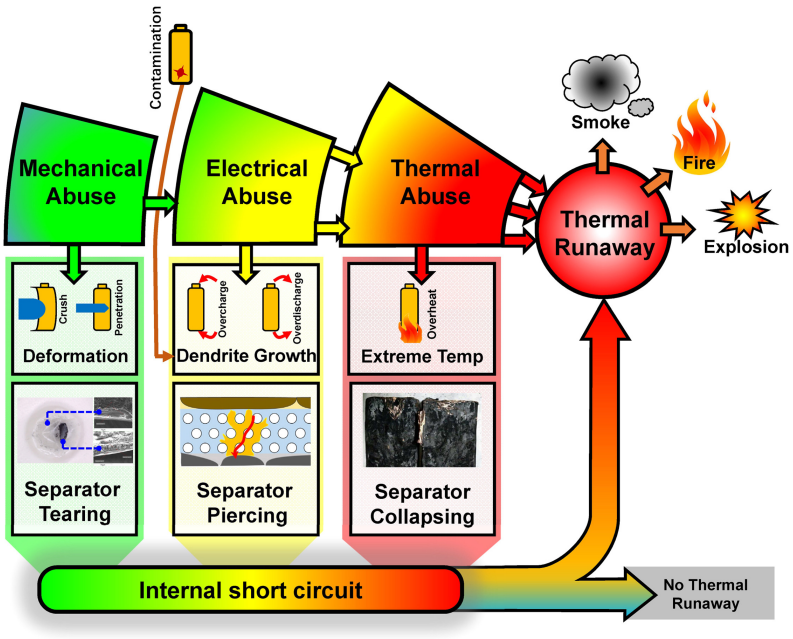

Figure 1.8: Main abuse conditions which could trigger thermal runaway [49]

At around 80 - 100 [$°C$] the SEI dissolution in the electrolyte starts to occur, leaving the negative electrode graphite particles without a protective layer and so free to react with the electrolyte; this reaction is highly exothermic [49], increasing the temperature even more; moreover at this stage, some of the solvents of the electrolyte reach their boiling point, producing gases which increase the pressure as well [48]. After 120 [$°C$] the separator melts, short-circuiting the cell and liberating the energy stored within, until the decomposition of the cathode materials and of the electrolyte (figure 1.9). As described in the previous sections, different battery chemistries are characterized by different thermal stability and thus have different responses to failure [46]. The chain reaction ends with the combustion of the internal components (caused by the release of oxygen from the cathode) and the emission of a high amount of heat and gases [49].
For this reason, the failure of a single cell can trigger a thermal runaway of adjacent cells, causing the disruption of the entire battery pack [50].

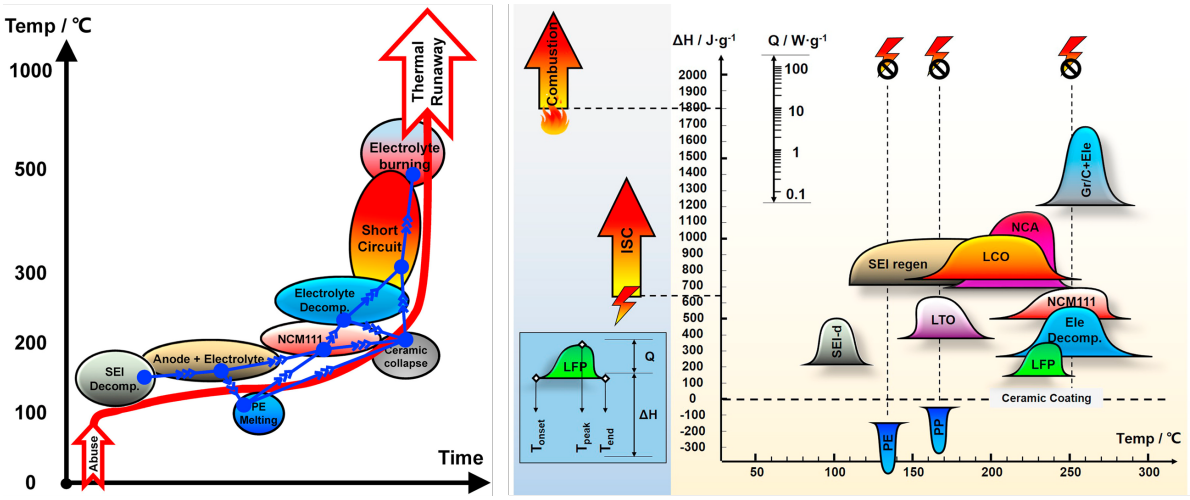

Figure 1.9: Interpretation of thermal runaway chain reactions and their energy release

In order to improve lithium-ion battery safety, various mitigation strategies can be employed, both at the cell and at the system level [48]:

- better protection against any kind of mechanical,electrical or thermal abuse;
- more thermally stable components, SEI and safer electrolyte, achieved through the use of additives, such as stabilizers and flame retardants;
- a stronger separator, generally attained with ceramic coatings;
- thermal insulation and thermal barriers with high heat capacity and working temperature, other than heat transfer pathways at the system level, to absorb high amounts of heat and control the speed of thermal runaway propagation; in this regard the battery shape was found to be influential [51].

Of course the design of the safety strategy of battery storage system is crucial in reducing or ruling out abusive conditions and should primarily take into account the mechanisms of thermal runaway and its spreading.

1.4.2. Battery thermal management system

One of the fundamental components of a lithium-ion battery storage system is the battery thermal management system (BTMS) [46, 47, 51, 52], required to keep the operating temperature of the cells in an optimal range at all times, other than a uniform temperature distribution within the single cells. This can be achieved by definition of a sophisticated control strategy and the employment of materials with suitable properties, such as external thermal insulation to avoid sudden temperature changes. In general, BTMS must

meet many requirements: it should be compact and light and have low upfront and operational costs, high reliability and easy maintenance characteristics [53]. BTMS have been extensively characterized in the literature and can be classified by different metrics, such as cooling medium [46], power consumption (active or passive) and thermal cycle [52]; the main configurations for high energy density battery packs are:

- Air-based, generally with active cooling; the air can be taken either from the air-conditioned vehicle cabin or treated in a dedicated secondary loop cooling system;
- Liquid-based, exploiting the higher heat transfer properties of liquid coolants or refrigerants; this layout generally achieves better performance in terms of temperature uniformity [46];
- PCM-based, a passive solution which exploits the large latent heat of specific materials to maintain the temperature almost constant.

Other configurations being investigated in literature are heat pipe cooling and thermoelectric element cooling. In general, hybrid solutions might provide the best performance, thanks to the combination of advantages of the individual configuration and mitigation of their drawbacks.

1.4.3. Heat generation

Through the course of charge and discharge processes, several sources generate heat within the jelly-roll of the battery at the elementary cell level, mainly corresponding to the overpotential of the cell [50]:

- Joule heating, or ohmic heating, is associated with the electrons transport inside the battery, because of which a part of their energy is lost as heat;
- Reaction heating, is linked to the charge transfer occurring between electrodes and electrolyte following the reduction-oxidation reactions at their interface;
- Entropic heating, is related to the re-arrangement of atoms within the electrodes crystalline structures as a consequence of lithium ions intercalation and de-intercalation mechanisms; as opposed to the first two, this is the only reversible contribution to heat generation.

Bernardi et al. [54] proposed a comprehensive battery thermodynamic energy balance which accounted for reactions, polarization, entropic heat, mixing effects and phase changes. From the assumptions of: (1) average heat capacity, (2) only two relevant reactions, (3) negligible enthalpy of mixing and (4) phase change contributions, a simple yet effective

expression was derived for the computation of heat generation within the cell:

$$\dot{Q} = I(\Delta V - E_{OCV}) + IT\frac{dE_{OCV}}{dT} + mc_p\frac{dT}{dt} = \\ = I\eta + IT\frac{dE_{OCV}}{dT} + mc_p\frac{dT}{dt} \quad [\text{W}] \quad (1.17)$$

Where:

- $\dot{Q}$ is the generated heat;
- I is the current $[A]$;
- ΔV is the voltage $[V]$;
- E_{OCV} is the equilibrium potential $[V]$;
- T is the temperature $[K]$;
- m is the mass of the battery $[kg]$;
- c_p is the specific heat capacity $[J\ kg^{-1}K^{-1}]$;

The first term is defined as polarization heat and represents the heat generation associated with joule heating and the electrodes overpotentials; the second term is the (reversible) entropic heat while the third one is the accumulation term. Heat generation is affected by several stressors, such as [50]: C-rates, ambient temperature and SoC, particularly at the limits. Moreover, also the electrodes microstructure and porosity have an impact on the distribution of generated heat and temperature.
Heat production must be accounted for accordingly by the thermal management system, reducing the uneven temperature distribution both in the cell and at the battery pack level. In fact, uneven cooling of the cells in battery modules can lead to a high level of degradation heterogeneity within the same pack [55].

1.4.4. Heat transfer

Heat transfer can be defined as the transport of thermal energy originated by a temperature difference between a system and its surroundings [56, 57]. When a temperature gradient exists between two points, thermal energy will always flow irreversibly from the point with the highest temperature to the colder one. Three different modes of heat transfer can be identified and defined:

- **Heat conduction**
  It is the transfer of energy between adjacent molecules of a body due to a temper-

ature gradient [57]. Given that the temperature difference is the cause of the heat flux, a proportionality law exists between them, the Fourier's law:

$$\dot{q}(x,t) = -k\frac{dT}{dx} \tag{1.18}$$

Where:

- $\dot{q}$ is the heat flux $[W\ m^{-2}]$;
- $\frac{dT}{dx}$ is the temperature gradient along the direction x of the flux;
- k is the thermal conductivity of the body $[W\ m^{-1}K^{-1}]$.

The Fourier's law states that, in heat conduction, thermal energy always flows in the opposite direction of the thermal gradient, and it is related to it through the proportionality parameter k. Thermal conductivity is a material property and strongly depends on the molecular/atomic structure of the medium. If k is the same in every direction, the medium is said to be "isotropic", while if not the material is called "anisotropic". If the Fourier's law is introduced in the conservation of energy equation, the general heat conduction equation can be obtained:

$$\rho c(T)\frac{\partial T}{\partial t} = \frac{\partial}{\partial x}\left(k\frac{\partial T}{\partial x}\right) + q(T,x,t) \tag{1.19}$$

Where:

- ρ is the material mass density $[kg\ m^{-3}]$;
- q is the volumetric heat generation term in the domain $[W\ m^{-3}]$;

In three dimensional heat flow, the heat equation becomes [57]:

$$\rho c_p(T)\frac{\partial T}{\partial t} = \nabla \cdot [k(T,\boldsymbol{x})\nabla T] + q(T,\boldsymbol{x},t) \tag{1.20}$$

Where ∇ is the Nabla operator, corresponding to the vector of the derivatives in the three directions of the Cartesian space:

$$\nabla = \left[\frac{\partial}{\partial x}, \frac{\partial}{\partial y}, \frac{\partial}{\partial z}\right] \tag{1.21}$$

Many assumptions can be applied to the equation to obtain simpler forms; for example, if k doesn't depend on temperature or direction (which is, in general,

a reasonable assumption for many materials in many applications) and no heat generation occurs within the body, the equation can be simplified as:

$$\rho c_p \frac{\partial T}{\partial t} = k \left(\frac{\partial^2 T}{\partial x^2} + \frac{\partial^2 T}{\partial y^2} + \frac{\partial^2 T}{\partial z^2} \right) \tag{1.22}$$

Or in contracted form:

$$\rho c_p \frac{\partial T}{\partial t} = k \nabla^2 T \tag{1.23}$$

$$\frac{\partial T}{\partial t} = \alpha \nabla^2 T \tag{1.24}$$

Where ∇^2 is the Laplace operator and α is the thermal diffusivity, defined as:

$$\alpha = \frac{k}{\rho c_p} \qquad [\mathrm{m^2 s^{-1}}] \tag{1.25}$$

Thermal diffusivity is a parameter which involves both the thermal conductivity and the volumetric heat capacity (ρc_p) and thus is a measure of how quickly a material or a medium can transport heat from a hot source to its surroundings.

- **Heat convection**
  Heat convection represents the superposition of energy transfer by heat conduction (at the microscopic level) and from a flowing fluid (at the macroscopic level). At the interface between a solid and a fluid, the total heat flux depends both on temperature and velocity field in the fluid [57]. To simplify things, convective heat transfer is often described by the relation:

$$\dot{q}_{conv} = h(T - T_\infty) \tag{1.26}$$

  Where T_∞ is the temperature far enough from the solid surface and h $[W\ m^{-2}K^{-1}]$ is the heat transfer coefficient. In general h is determined by the temperature field in the fluid at the surface, but strongly depends on the geometry of the solid, velocity fields and fluid properties; for its computation several empirical (and some analytical) correlations exist.

- **Thermal radiation**
  Thermal radiation indicates the heat transfer through electromagnetic radiation, caused by a temperature difference between two bodies. In fact, all bodies continu-

ally emit energy across their surfaces and, in general, the intensity of the flux (the "emissive power", e $[W\ m^{-2}]$) depends on temperature and surfaces' properties [56], through the Stefan-Boltzmann law:

$$e(T) = \epsilon \sigma T^4 \tag{1.27}$$

Where:

- ϵ $[-]$ is the body emissivity, a property representing the amount of emitted radiation with respect to the perfect emitter, the black body;
- σ is the Stefan-Boltzmann constant $[W\ m^{-2}K^{-4}]$.

Because of the issues described above and the high amount of generated heat within cells, thermal characterization is becoming more and more important for lithium-ion batteries. Temperature is one of the main stressors during operation and thus a correct modeling is required for the BTMS to efficiently control it.
The main heat transfer mode inside the cell is conduction [58], even if the electrolyte is fluid: due to its high viscosity the velocity field is often negligible with respect to diffusion phenomena. The thermal characterization of lithium batteries is typically carried through the determination of thermal conductivity and specific heat capacity of cells, which depend in general on the temperature, internal structure, materials and SoC.

Thermal conductivity

The thermal conductivity of lithium-ion batteries greatly influences the temperature gradient within the internal components and may cause severe differences in how quickly the heat is dispersed. Due to their multilayer rolled structure, cells are characterized by a highly anisotropic behavior, which is reflected into two main values of thermal conductivity, namely the in-plane and the through-plane (or cross-plane) thermal conductivities.

The through-plane value refers to the thermal conductivity in the direction perpendicular to the layers of the cell, while the in-plane one describe its behavior in the direction parallel to the layers [58] (figure 1.10). In general, the thermal conductivity depends on several factors, such as the geometry of the cell, internal components (cathode chemistry, electrolyte, etc.), temperature and pressure, but at least one order of magnitude can be expected between the two values, so that the in-plane conductivity is significantly larger than the through-plane one. However, the estimations in the literature are very diversified, even for the same geometry or chemistry [58]. Tendera et al. [60], Murashko et al. [61]

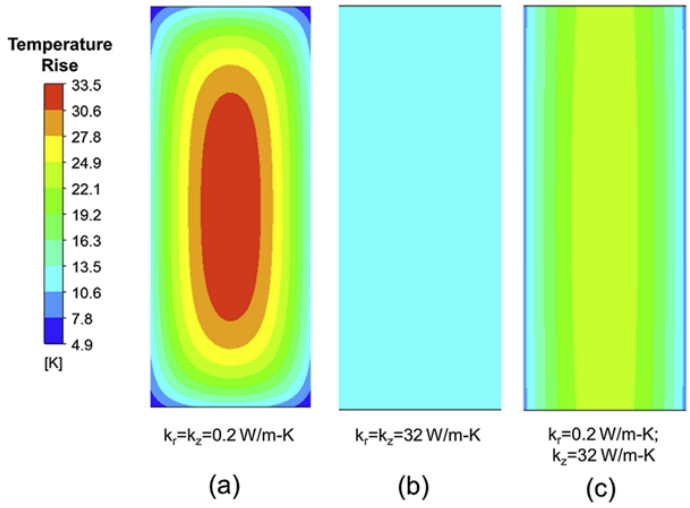

Figure 1.10: Effect of the nature of thermal conductivity on expected temperature profile. [The anisotropic case (c) is more representative of LIBs [59]]

and Caillez et al. [62] reported a linear trend with negative slope between the through-plane thermal conductivity and temperature. Moreover, both Tendera and Kovachev [63] reported a parabolic dependency between the through-plane component and the SoC. On the other hand, Tendera et al. [64] reported no clear correlation between the in-plane thermal conductivity component and SoC or temperature. Various methodologies are available in literature for the estimation of this parameter, generally employing the solution of the heat equation in Cartesian or cylindrical coordinates for different boundary conditions [59, 61, 62, 65].

Specific heat capacity

The specific heat capacity is defined as the amount of energy required to increase the temperature of a body or system by one unit. It is a crucial parameter in the thermal characterization of lithium batteries because it dictates their tendency to raise their temperature. Like the thermal conductivity, its value depends on many other parameters, mainly temperature but also SoC and cathode chemistry, even if the value range is less extensive than thermal conductivity. Several methodologies are present in the literature, generally employing a calorimeter, but due to its high cost numerous innovative approaches are being presented [66–68], also coupled with thermal conductivity estimation [59, 61, 62, 69]. Several papers report a clear positive linear trend between specific heat capacity and temperature [61, 67, 69].

1.5. Degradation of lithium-ion batteries

In the early applications of lithium-ion batteries, the main focus was on compactness and lightness, other than high energy density. Nowadays, with the advent of the EV market, much emphasis is given to the range and cycle life of battery systems and the research is focused on enhancing and improving their lifetime and operation. Moreover, degradation and aging favor dangerous phenomena such as internal short-circuits and overheating issues and thus pose a non negligible threat related to safety issues. For these reasons, a thorough understanding of the main mechanisms that cause aging and their underlying phenomena and stressors is key for modeling and predicting the behavior and performance of LIBs.

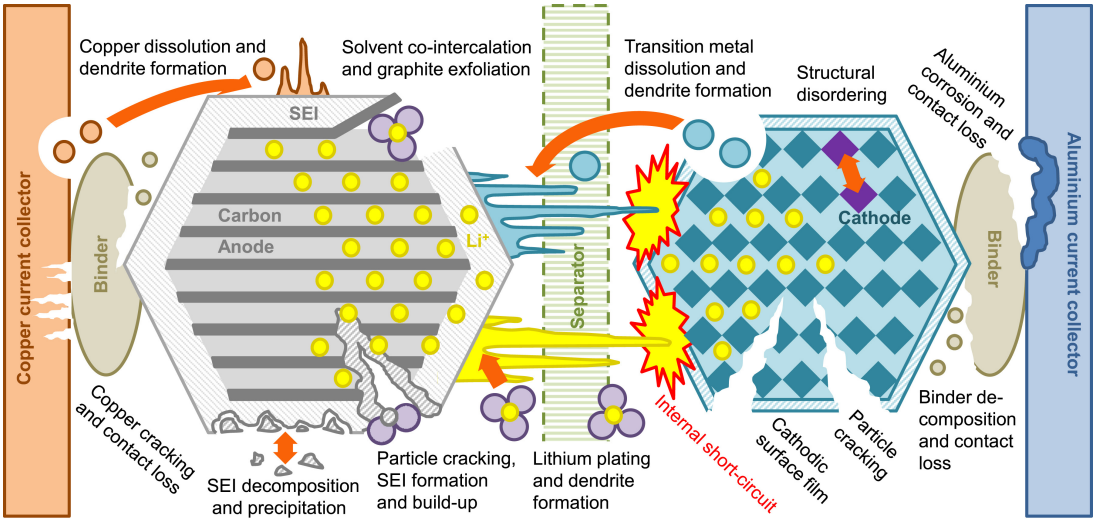

Figure 1.11: Main degradation phenomena in lithium-ion batteries [70]

In this regard, the comprehension of degradation modes can be also indirectly useful for recycling purposes and second life assessments of high performance EV's lithium batteries, which generally employ critical raw materials for the European Union. Depending on the level of degradation withstood by a cell, an appropriate second life can be defined in less demanding applications (such as stationary), decreasing costs and waste of rare materials.

1.5.1. Degradation mechanisms and diagnosis

Because of the complex structure of cells, several degradation mechanisms can arise during both operation and storage (idle) periods, that can lead to the same performance reduction. The origin of aging mechanisms can be either chemical or mechanical [71] and they can be grouped as capacity fade and power fade, referring to the effects they have

on overall operation.

Capacity fade represents the loss of available capacity in the cell, which corresponds to a decrease in the lithium ions that can cycle between the electrodes (often denoted as Loss of Lithium Inventory, LLI) or to the depletion of active materials and their structure in the electrodes (called Loss of Active Materials, LAM).

Power fade corresponds to the drop in power capabilities of batteries, often related to resistive layers formation on the electrodes surfaces and resistance increase, due to lower available surfaces for reactions.

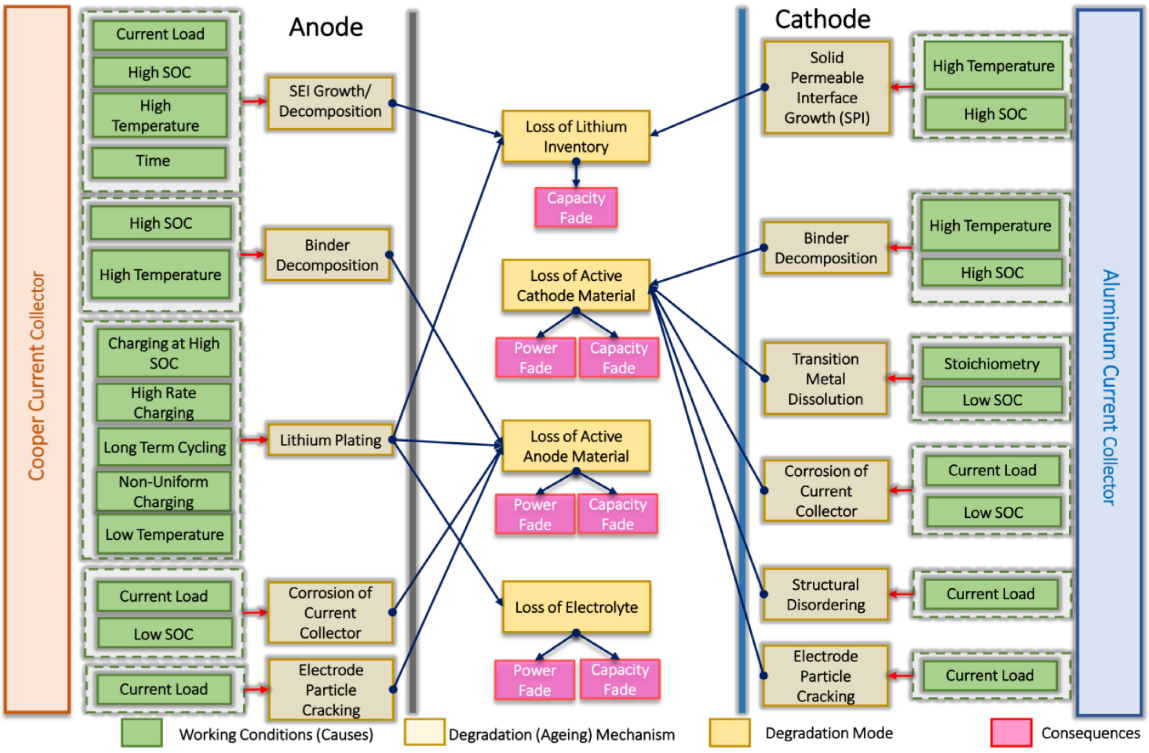

Figure 1.12: Degradation mechanisms in LIBs associated with their stressors [72]

More specifically, LLI can be influenced by several aging mechanisms:

- **SEI growth and decomposition**
  As briefly mentioned in section 1.2.1, the Solid Electrolyte Interphase (SEI) is an intermediate layer that generates on the carbon based negative electrodes surface as a result of the instability of graphite at low potentials [73, 74]. In general, the electrolyte reacts with the carbon atoms and lithium ions to form a protective layer at the electrode-electrolyte interface, which hinders further reactions and thus self-limits its growth: the exact composition depends on various factors (such as the

electrolyte formulation and the thermodynamic conditions at which is formed) and typically includes Li, C and electrolyte solvent/salt/additives specific components (P, F, Br) [73], such as lithium carbonates, Li_2CO_3, and inorganic products [75]. Even if the SEI is the result of an undesired reaction, great importance is given to its generation during the first formation cycles, because some advantageous features can be achieved: the structure can be optimized to be able to completely separate the anode and the electrolyte, protecting the charged electrode from corrosion, and to deliver uniformly the lithium ions to the negative electrode's layers, other than decrease the unavoidable self discharge [71, 75, 76]. For these reasons the electrolyte composition and its additives must be carefully selected to induce a stable and durable thin film [77, 78].

The SEI is permeable to lithium ions, but it introduces an additional layer which has to be overcome, increasing the internal resistance of the cell. Moreover, the SEI continuously grows during the whole lifetime of a battery, promoted by high temperatures, high C-rates and low potentials (in charged state) [71, 77, 79]. As described in section 1.4.1, this layer is not thermally stable after a temperature threshold is reached, which leads to the dissolution of its components in the electrolyte and its subsequent regeneration, further increasing the irreversible loss of available lithium [77, 80]. Additionally, due to its often unknown exact composition, no indication on the thermal parameters of the SEI is available in literature.

- **CEI growth**

  CEI (Cathode Electrolyte Interphase) is analogous to SEI, but develops on at the positive electrode-electrolyte interface. Its composition includes organic polycarbonates and Li, P, F based products, which are more or less common to all cathode chemistries. The formation and expansion of CEI is favored at high voltage and temperature, outside of the electrolyte chemical stability window. This surface film doesn't represent a limit to performance as much as the SEI on the anode [75, 81], but is has nonetheless detrimental effects on the availability of lithium and cell impedance. For this reason, similarly to the SEI layer, the formation of a stable CEI is key to hinder further electrolyte decomposition [82].

- **Electrolyte decomposition**

  The electrolyte is only thermodynamically stable in a range of operating voltage [76], outside of which it starts to degrade and participate in unwanted side reactions, such as the formation of SEI and CEI, as explained before; in particular, at high potential, the oxidation of electrolyte with the positive electrodes materials can occur, leading to an increase in temperature (the reaction is exothermic). These

interactions with other components drive a modification of its composition and properties, often leading to a decrease in ionic conductivity and stability.
As described in section 1.4.1, at too high temperatures the electrolyte decompose and promotes gas formation within the cell [79]: these gases are highly flammable and could assist the risk of thermal runaway. Moreover, they cause an increase in pressure and produce mechanical stress on the other components.

- **Lithium deposition**
  As described in section 1.2.1, during charging processes Li ions are de-intercalated from the positive electrode and migrate towards the anode through the electrolyte. At the electrode-electrolyte interface, solvated Li ions are stripped of the solvent and travel to the graphite layers [83, 84]. However, intercalation into the graphite layers is not the only reaction allowed, as also Li deposition could occur [85]. In general, if the transport rate of Li ions from electrolyte exceeds the Li-intercalation rate, Li^+ are accumulated on the electrode surface, driving the potential below 0 V vs Li/Li^+ [83]. In this conditions, a metallic lithium film is deposited on the anode surface, leading to an irreversible LLI. This degradation phenomenon is favored by charging processes at low temperature or high C-rates or SoC, all circumstances which decrease the electrode potential through polarization losses (overpotentials) or slow down the Li-intercalation kinetics [72, 84]. Lithium deposition often leads to capacity and power fade, other than a lower Columbic efficiency. The reaction is highly exothermic, locally leading to increased temperature. Moreover, if the metallic lithium plating is sustained, it develops in dendritic form, needle-shaped protuberances which can pierce through the separator and cause internal short-circuits and the failure of the cell through thermal runaway [84].

The mechanisms producing LAM are, instead:

- **Electrodes particle cracking**
  Phase transitions and structural changes in the lattices of electrodes can cause severe shape and volume variations, which generate mechanical stresses or defects and thus might result in cracking of particles [86]. Particle cracking is common to both electrodes and can lead to fracture or delamination, resulting in non homogeneous intercalation/de-intercalation reactions [77]. Moreover, fragmentation can lead to exposure of electrodes particles to the electrolyte, increasing their degradation due to formation of new SEI [82].

- **Graphite exfoliation**
  If the SEI layer is not fully formed, solvents (an in particular Propylene Carbonate,

PC) might co-intercalate in graphite layers and generate mechanical stresses due to the expansion of the inter-layer space, finally leading to the exfoliation of graphene layers [82]. In general, graphite exfoliation is favored by particles with low specific surface, which increase the surface defects, and high current rates during the formation cycles, which can lead to poor SEI performance [75]. Graphite exfoliation doesn't completely destroy the bulk electrode, but gives rise to significant changes in surface structure [87]. Similarly to particle cracking, graphite exfoliation can drive the disruption of the anode morphology, exposing the particles to the electrolyte and further causing loss of lithium inventory, other than LAM [77]. Moreover,the co-intercalated solvents can cause propylene gas formation, aggravating the situation even more [75].

- **Transition metal dissolution, migration and deposition**
  As described in section 1.2.1, transition metal (TM) oxides are the main materials for positive electrodes. During electrochemical reactions, small amounts of TM can dissolve in the electrolyte because of too high or too low potential; this process is also favored at elevated temperature [88] and for Mn based electrodes. The dissolution of TM results in the loss of active material at the cathode, directly leading to capacity and power fade. Moreover, the dissolved transition metal ions can relocate on the anode surface, following the dissolution, migration, deposition process (DMD), impacting the electrolyte properties and the composition of both CEI and SEI [82], driving further the loss of performance. The application of special cathode coatings or the addition of metal-capturing additives in the electrolyte can mitigate this phenomenon.

- **Irreversible phase transitions and Structural disordering**
  Transition metal migration might induce an irreversible phase change in LMO cathodes, shifting to a spinel structure with lower oxygen stoichiometry [82]. This deleterious effect is enhanced during charging at high C-rates and temperature and could promote other degradation phenomena in the cell.
  Moreover, also graphitic layers can suffer structural disordering after many cycles, particularly from over-discharge at high currents.

- **Current Collectors corrosion**
  Current collectors' main aging mechanism is corrosion. Given that the cell operates at very high or low potential depending on the region, copper and aluminum based CC could be subjected loss of material and surface disruption. In general, this type of degradation is strongly dependent on the materials, electrochemical potential, other than electrolyte composition and current collectors' microstructure [89]. Cu

corrosion is favored at high potentials and expected at values higher than 3.5 $[V]$ vs. Li/Li^+, but the presence of impurities, such as water traces, can greatly decrease the threshold. On the other hand, aluminum has a much lower standard equilibrium potential than copper, but it exhibits a more stable behavior due to the formation of an alumina based passivation film on its surface. Current collector corrosion causes an increase of the cell impedance and inhomogeneous distribution of current within their surface [77]. Moreover, ions dissolved in the electrolyte can redeposit on other components, particularly on the SEI, degrading the protective layer and impeding lithium mobility [89].

- **Binder decomposition**
  Mechanical stresses caused by volumetric variations and high temperature can promote polymeric binder decomposition. This can cause the detachment from the active materials and fracturing, leading to loss of electric contact and electrodes instability. This aspect is particularly detrimental for anode materials characterized by high volumetric expansion, such as carbon-silicon based electrodes [90].

Even if these degradation mechanisms might be different from each others, they often lead to similar macroscopic performance losses and aging of LIBs. A further classification can be established, depending on the operational state of cells:

- **Calendar aging** refers to all aging phenomena which are not related to the utilization of batteries but only to their storage conditions [71]. Due to the fact that calendar aging doesn't depend on the usage of cells, it always occurs, even during cycling processes. The main degradation phenomena associated with calendar aging are related to the growth of SEI and CEI, thus the capacity fade in these conditions is primarily caused by variations in the electrode balancing instead of degradation of active materials, so this type of aging is mostly linked to LLI [91, 92]. The most important parameters enhancing calendar aging are high temperature and SoC, because they favor phases development at the electrodes-electrolyte interfaces [93].

- **Cycle aging**, instead, indicates all mechanisms associated with charge and discharge processes during operation. The principal factors involved in cycle aging are current rates and DoD, other than the already cited temperature and SoC [71]. In fact, high DoD and C-rates lead to increased capacity losses due to extreme voltage and current conditions, causing undesired side reactions and mechanical stresses [94]. However, also in this case, operating temperature has the strongest effect on lifetime [93].

Degradation diagnosis

The identification and characterization of degradation mechanisms and their extent is crucial for the prediction of batteries' behavior. However, their differentiation is generally intricate because they are often caused by the same stressors and lead to the same macroscopic effects. The most widely used way to determine the condition of cells is by the State of Health parameter, which can be defined as:

$$SoH = \frac{Q_{res}}{Q_{nom}} \qquad [-] \qquad (1.28)$$

This value directly relates the available residual capacity to the nominal one, but doesn't carry any information on the type of degradation nor on the state of the internal components. For this reason, more sophisticated methods were defined:

- OCV curve manipulation can be employed, primarily to enhance some of its features, such as accentuating the slope variations; these aspects can help to identify changes related to electrodes degradation.
- Electrochemical Impedance Spectroscopy (EIS) is a powerful non destructive technique, that can be even used during operation. By applying a small sinusoidal current signal, it is possible to compute the impedance of the cell in a spectrum of frequencies through the measurement of the voltage response. The identification of degradation mechanisms can then be done by comparing the spectra of cells in different aging conditions.
- Post-mortem analysis is a destructive method, because it makes use of the disassembling of batteries. However, it is the most important approach to completely characterize the internal components of the cell and their degradation state. Physicochemical analysis can be then performed, such as Scanning Electron Microscopy (SEM) or Energy Dispersive X-ray Spectroscopy (EDX), which are useful to describe surfaces morphology and composition.

1.5.2. Effects of degradation on thermal parameters

As described in section 1.4, the understanding of thermal behavior of lithium-ion batteries is crucial during operation, because temperatures outside the optimal range can lead to enhanced degradation or safety issues. Generally, BTMS's models employ thermal parameters which are estimated at the beginning of life and thus neglect every possible effects of degradation on heat transfer. This approach is certainly simpler but can lead to

errors in the estimation of the internal temperature and thus of the modeling of the real operation of the cell. For this reason, a thermal characterization which also takes into account aging phenomena and their effect on parameters should be performed.
Kovachev et al. [63] reported a reduction of thermal conductivity of NMC pouch cells with respect to the level of compression force during calendar aging. The cause was believed to be linked to the consumption of electrolyte, which greatly affects the thermal conductivity value [69].

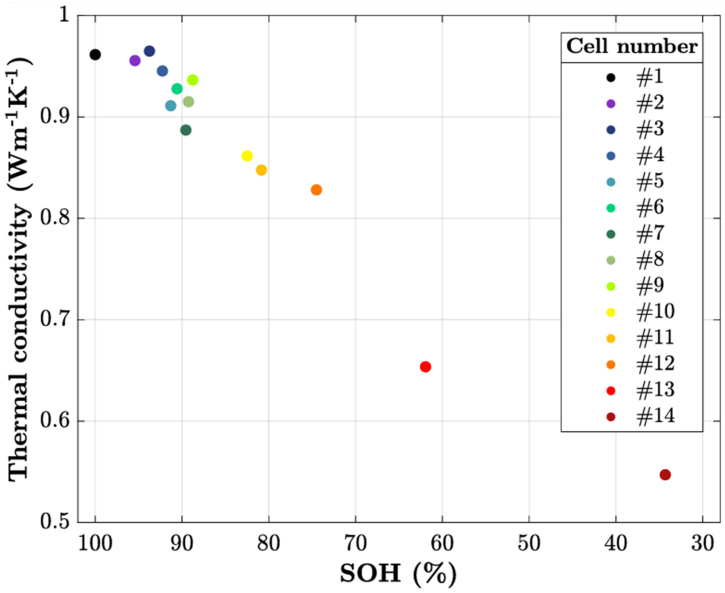

Figure 1.13: Effect of the SOH on the mean thermal conductivity [95]

Tendera et al. [95] performed a thorough experimental campaign, analyzing pouch cells at different SoH and cycling conditions. Also in this case, a clear negative linear correlation was found between thermal conductivity and state of health (figure 1.13). Moreover, they analyzed degradation mechanisms singularly, by artificially isolating them with tailored procedures. It was found that excessive electrolyte consumption and gas formation have the greatest negative effects on thermal conductivity, because they can generate a thermally insulating layer between components.

1.6. Aim of the thesis

This thesis work was carried out at the MRT Fuel Cell & Battery Lab of Politecnico di Milano as the continuation of the research started from a previous thesis [55], aimed at the definition of innovative and easy-to-implement approaches for the characterization of LIBs.
The main aim of this work lies in the definition of innovative methodologies for the thermal characterization of lithium-ion batteries and in the physical comprehension of the effects of degradation on their thermal behavior. In fact, as demonstrated by the literature review on the current state of the art of lithium-ion batteries, very limited investigation was done on the effects of aging on their thermal behavior.

For these purposes, the following steps are performed:

- Development and implementation of novel methodologies and modeling approaches for accurately estimating the thermal parameters of the analyzed batteries. This includes determining key properties such as specific heat capacity and thermal conductivity, which are crucial for understanding heat generation, dissipation, and overall thermal behavior.
- Carrying of a calendar aging campaign conducted at 60 $[°C]$ on four batteries at various storage conditions, with the aim of characterizing their thermal behavior at different aging states.
- Validation and application of the defined methodologies and models on real lithium-ion batteries, both at the beginning of life and under aged conditions, through targeted experimental campaigns. This process aims to assess how thermal properties, such as specific heat capacity and thermal conductivity, evolve with aging and how these variations influence the overall thermal behavior of the battery. By analyzing these changes, the study would provide insights into the impact of aging on heat generation, dissipation, and thermal management, contributing to the development of more accurate models and improved battery lifespan predictions.
- Conceptualization, derivation, and validation of a physics-based thermo-electrochemical model for the interpretation of the experimental results obtained from the previous campaigns. The aim of this model would be to provide a detailed and physically grounded representation of the battery's thermal behavior, incorporating key mechanisms such as heat generation, transport, and dissipation. By integrating electrochemical and thermal processes, it would enable a deeper understanding of how operating conditions and aging affect the thermal response of the battery, ensuring a

more accurate and predictive framework for thermal management and performance evaluation.

2 | Experimental methodology

In this chapter, the experimental setup for the thesis is presented, with the description of the battery samples, the experimental station, the measurement systems and the methodology.

2.1. Battery samples

The experimental campaign focused on the electrochemical and thermal characterization of singular cells. Two similar cylindrical LFP batteries from the same manufacturers were employed, namely the A123's "ANR26650 M1A" [96] and its subsequent version "ANR26650 M1B" [97] (figure 2.1); these cells were employed in real-life automotive battery pack modules, from which they were attained; in the following sections they will be referred to as "M1A" and M1B" for brevity. The main characteristics of these samples are reported in table 2.1

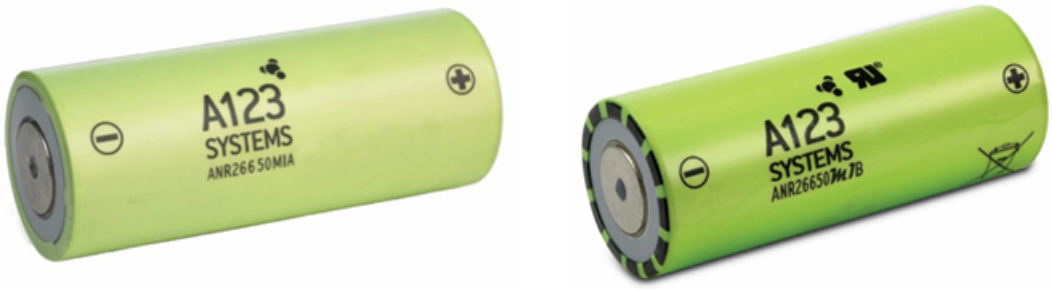

(a) ANR26650M1A (b) ANR26650M1B

Figure 2.1: Images of the two samples

As it can be seen, the two samples share many specifications, such as the geometry and voltage thresholds. The main difference lies in the higher capacity of the M1B cell, where it was possible to insert a greater amount of active materials. This aspect is particularly important, because the higher amount of active material is reflected into a higher mass, and thus a higher density at parity of volume (the dimensions are the same). Moreover,

Battery cell characteristics		
Manufacturer	A123	
Model	ANR26650 M1A	ANR26650 M1B
Design	Cylindrical	
Anode Chemistry	Graphite	
Cathode Chemistry	LFP	
Cell dimensions $[mm]$	$\varnothing 26 \times 65$	
Weight $[g]$	72	76
Capacity (nom/min) $[Ah]$	2.3 / 2.2	2.5 / 2.4
Voltage (nom/min/max) $[V]$	3.3 / 2.0 / 3.6	
Internal impedance $[m\Omega]$	8	6
Maximum continuous discharge $[A]$	70	50
Maximum pulse discharge $(10s)$ $[A]$	120	
Operating temperature [min;max] $[°C]$	$[-30; +55]$	
Storage temperature [min;max] $[°C]$	$[-40; +60]$	

Table 2.1: Main characteristics of battery samples

a greater power density ($[W\ kg^{-1}]$) is achieved in the M1B sample.
As described in Section 1.3, the cylindrical geometry is inherently safer than other shapes, due to the presence of built-in safety devices, such as the CID and the PTC; in the two samples, they were placed on the negative pole.

2.2. Experimental stations

During this work, all of the activities were performed at the MRT Fuel Cell & Battery Laboratory of the Politecnico di Milano. In particular, two stations were employed: a testing station, for the thermal and electrochemical characterization of batteries, and a glove-box, which was utilized for the drilling of cylindrical cells.

2.2.1. Testing Station

The testing station was developed during the work of previous theses at the same laboratory [98–100]. During the period of this thesis no modifications were performed. The main components of the testing station are: two climatic chambers, electronic loads, power supplies and acquisition boards (figure 2.2).

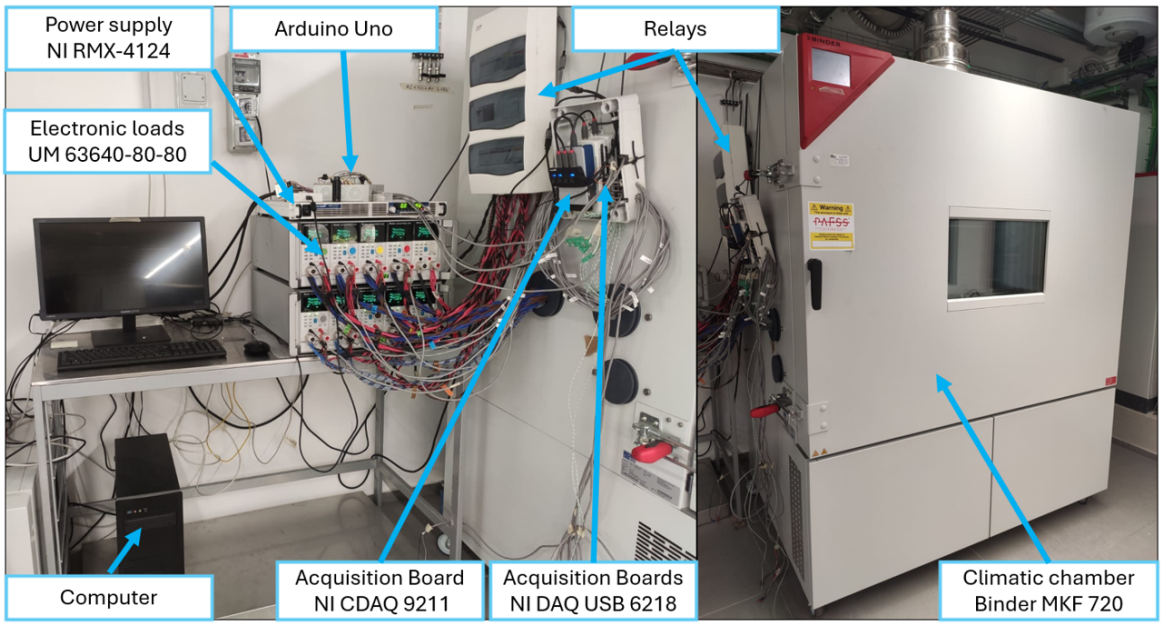

Figure 2.2: Instrumentation of the testing station

In this particular setup, up to eight individual cells can be tested independently. This is achieved by the means of a modular structure of the electronic loads: two separate parallel circuits are present, comprising each of four independent channels equipped with a Chroma UM 63640-80-80 electronic load [101]; a fifth load identical to the others is used to modulate the current in each circuit by changing its internal resistance. Thanks to this arrangement, only a single power supply connected to both parallels is adopted, namely the NI RMX-4124 [102], able to fulfill both charging and discharging processes requirements of the tested cells. Each battery is connected to two pairs of electrical wires, where one couple is employed for the supply of power while the second is connected to sensors and thus used for voltage measurement purposes. In this regard, the voltage of cells is determined through a NI DAQ USB 6218 [103] acquisition board. Moreover, also superficial temperature of cells can be measured through the exploitation of type K thermocouples, connected to two additional NI CDAQ 9211 [104] acquisition boards.
The battery holders (figure 2.3) are situated in the biggest of the two climatic chambers, a Binder MKF 720 Eucar 6 [105]: this environmental simulation chamber can control temperature and relative humidity in a very broad range, from -40 [$°C$] to +180 [$°C$] and from 10% to 98%, respectively. Moreover, this chamber employs a built-in safety system against fire hazards.

An electrical circuit scheme of the testing station is available in figure 2.4. As it can be seen, the power supply is connected in parallel with both independent circuits. The current in the two circuits is imposed through the "Load 9" and "Load 10" variable

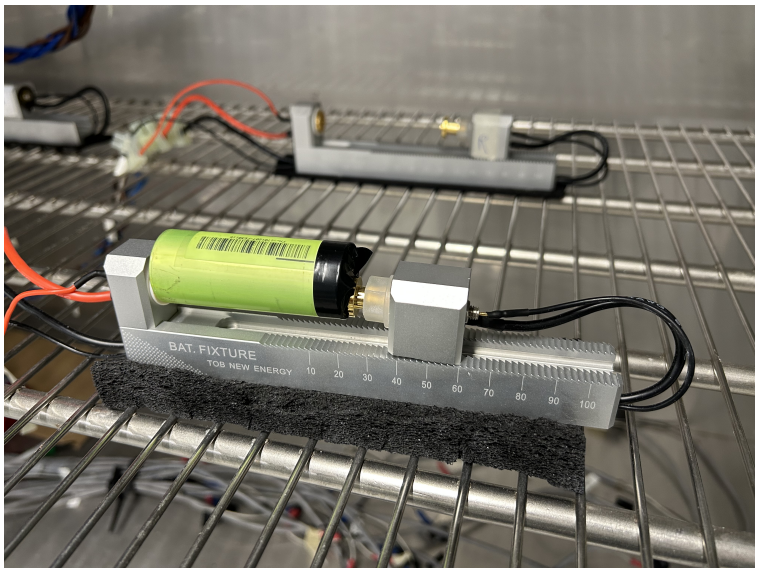

Figure 2.3: Cylindrical cells holder

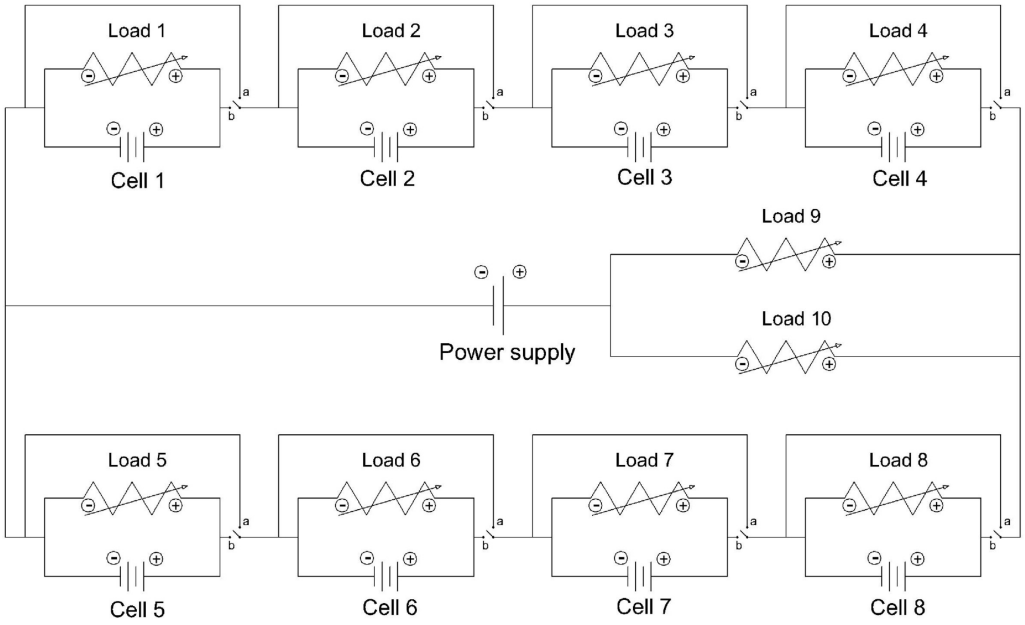

Figure 2.4: Scheme of the electric circuit of the testing station

resistances, while each one of the other eight Chroma loads is able to control voltage and current for the singular cell. Finally, a relay switch is connected to every electronic load, to possibly disconnect each cell from the main circuit. In particular, if the switch is closed, the channel is connected to the primary circuit and the tested cell can be charged by modulating the current and the voltage at its poles; on the other hand, if the switch is open, the cell is separated from the main circuit and it can be discharged through the electronic load.

The smaller climatic chamber, a Binder KT 53 [106], instead, was used for the thermal characterization of cells. This chamber is able to work in a narrower temperature range (4 $\div$ 100 $[°C]$) compared to the other and employs a fan with adjustable speed. Thermal tests also utilized an additional DC power supply, the Chroma 62006P-300-80 [107], mainly for heat generation through resistive heaters, as it will be described in the following sections. In table 2.2, the main characteristics and uncertainties of the instrumentation utilized in this work are reported.

Instrument	Equipment	Quantity	Uncertainty
NI RMX-4124	Power supply	Current Voltage	$\pm 0.5\% \pm 0.1\% rtg$ $0.025\% + 0.01\% F.S.$
Chroma UM 63640-80-80	Electronic load	Current Impedance	$0.1\% + 0.1\% F.S.$ variable
NI DAQ USB 6218	Acquisition board	Voltage	$\pm 0.0085\% \pm 0.002\% F.S.$
NI CDAQ 9211 w/K-TC	Acquisition board	Temperature	$\pm 3\,[K]$
Chroma 62006P-30-80	Power supply	Voltage Current	$0.01\% + 3\,[mV]$ $0.01\% + 10\,[mA]$
BINDER KT53	Climate chamber	Temperature	$\pm 0.3\,[K]$
BINDER MKF 720	Climate chamber	Temperature	$\pm 1\,[K]$

Table 2.2: Characteristics and uncertainty of the testing station equipment

All devices described above are digitally connected to a computer, which is able to manage them through tailored GUIs developed in the NI Labview® programming environment software [108]. These interfaces are able to collect measurement data - related to current, voltage and temperature - from the acquisition boards, and store them. Moreover, they allow for the control of the operating conditions during tests.
Additionally, an Arduino Uno micro-controller [109] is connected to both the loads and the computer; it behaves as a safety system, verifying that voltage limits and other parameters are respected during tests and disconnecting electronic loads if the conditions are not met.

2.2.2. Glove-box

A glove-box is defined as a closed transparent vessel in which dangerous substances can be touched safely using gloves attached to holes on one of its sides [110]. The one present in the laboratory is a JACOMEX Puresmart glove-box [111] (figure 2.5), which employs an hermetically sealed chamber, completely filled with inert argon gas. The internal atmosphere is constantly controlled through very sensitive pressure and concentration sensors and filters, which guarantee a minimal amount of contaminants, corresponding

to 0.1 $[ppm]$ of O_2 and 0.8 $[ppm]$ of H_2O. External objects can be inserted inside the glove-box through two smaller intermediate chambers, which are mounted on one side of the main structure and connected to both internal and external environments with a double access point. Both chambers are connected to a PFEIFFER Pascal vacuum pump [112], which is used to completely remove air, and to an Ar tank, to flush the system and obtain similar conditions to the ones of the main chamber. Thanks to the inert environment, it is possible to safely and directly analyze the internal structure of batteries, by opening the cells and/or extracting the components. In fact, in the presence of oxygen and water, the hydrocarbon-based electrolyte would react dangerously, leading to gas formation, temperature increase and possibly the failure of the cell.

Figure 2.5: JACOMEX Glove-box

2.3. Diagnostic methods

As briefly described in section 1.5.1, several diagnostic methodologies exist for lithium-ion batteries, not only for degradation assessment but also for the electrochemical characterization of cells. The main tools employed during this thesis consisted of charge and discharge tests, Differential Voltage (DV) and Incremental Capacity (IC) curves and EIS analyses.

2.3.1. Capacity test

Capacity tests are used to obtain the voltage-capacity curve of a battery and consequently the residual charge capacity of a battery. In general, to perform a capacity test, the cell is either charged or discharged at a certain C-rate (which is defined as the ratio between the operating current and the nominal capacity of the cell, as described in section 1.1.1) while its voltage is recorded, until the voltage limits are reached: the curve can be then constructed through the combined information of current and time. In this regard, the selection of the C-rate really depends on the kind of test to perform and its desired features: if the objective is to obtain a behavior as close as possible to equilibrium, a very low C-rate should be chosen (typically lower than 0.1C, as described in section 1.1.1); to obtain the residual capacity in nominal conditions a certain C-rate between 0.5C and 2C is defined by battery manufacturers (figure 2.6). As shown in section 2.1, a maximum operating current is defined for each battery, depending on their power capabilities, so an upper limit of C-rate always exists. Capacity tests at high or extreme C-rates are often performed for cycling purposes or internal heat generation, as they seldom represent real life operation, especially in EV applications.

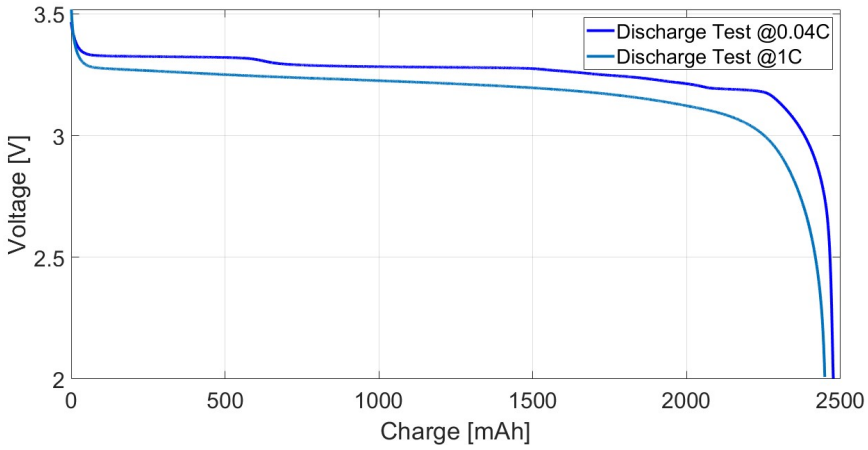

Figure 2.6: Discharge processes at different C-rates

The procedure to perform a capacity test can be schematized as follows (figure 2.7), assuming that the battery has a SoC lower than 1:

1. A Constant Current (CC) is applied during a charge process, until the upper voltage limit is reached. As described in section 1.5.1, the charging process is a delicate step for lithium-ion batteries and should be performed at low C-rates to avoid unwanted mechanical stresses and lithium plating; for this reason the charging protocol and its current rate is often defined by the manufacturer.

2. A Constant Voltage (CV) phase follows, during which the battery's voltage is kept constant and equal to the upper limit, while the current progressively decreases until a lower current boundary is met: this is called the termination current and is generally defined as the one corresponding to a quasi-static process; during the work of this thesis, this value was set as the current corresponding to a C-rate equal to 0.02 $[h^{-1}]$.

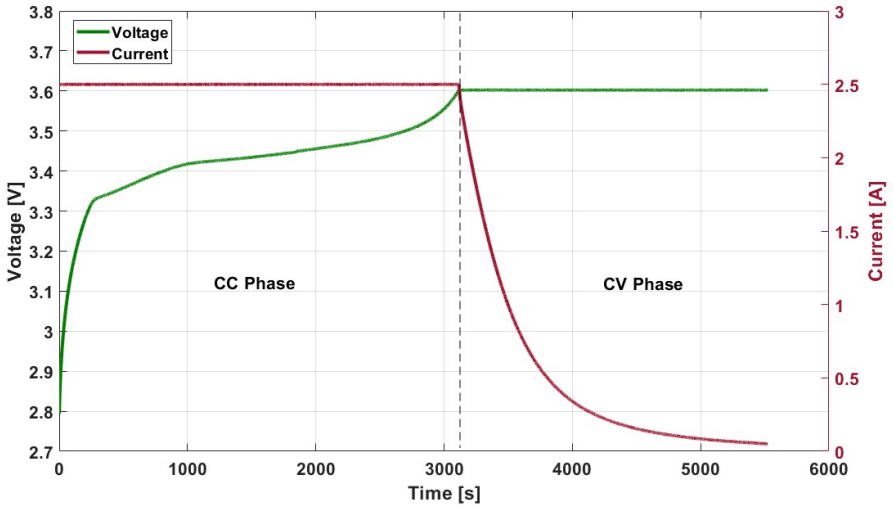

Figure 2.7: Charge process at C-rate = 1 $[h^{-1}]$, separating CC and CV phases

3. At the end of the charging process, the condition of $SoC = 100\%$ is reached. However, a lithium ions concentration disequilibrium exists inside electrodes' particles, mainly introduced by the CC phase. Because of this, a relaxation period is observed, during which the concentration gradients are slowly smoothed out by diffusion phenomena inside particles [113].

4. Once the cell is completely relaxed, a discharge process can be performed, at a constant current until the lower voltage limit is reached.

Other than from current, the voltage-capacity curve is strongly affected by the temperature at which the test is conducted: as described in the first chapter (section 1.4.1), this parameter has an impact on physical and electrochemical phenomena occurring inside a cell and could shift its available residual capacity due to a change of voltage. For this reason, the same parameters and protocol should always be applied to compare different batteries.

2.3.2. Incremental Capacity (IC) and Differential voltage (DV)

Capacity tests performed in quasi-static conditions, ie. with adequately low current rates, allow for a further manipulation of the voltage curve, as briefly mentioned in section 1.5.1. Two additional curves can be produced by computing the derivatives of voltage with respect to charge and vice-versa; these are called Differential voltage (DV) and Incremental Capacity (IC) and are defined as follows:

$$DV = -\frac{\partial V}{\partial Q} \qquad IC = \frac{\partial Q}{\partial V} \tag{2.1}$$

By definition, these two curves highlight the slope variations of the voltage-capacity curve, allowing to characterize features and aspects related to electrodes behavior (figure 2.8).

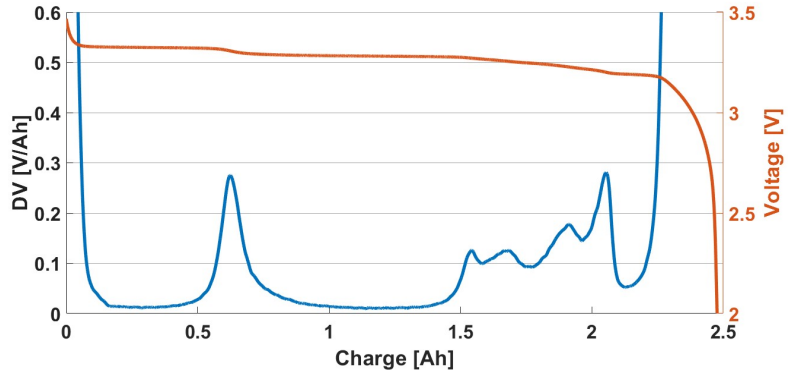

(a) DV Curve

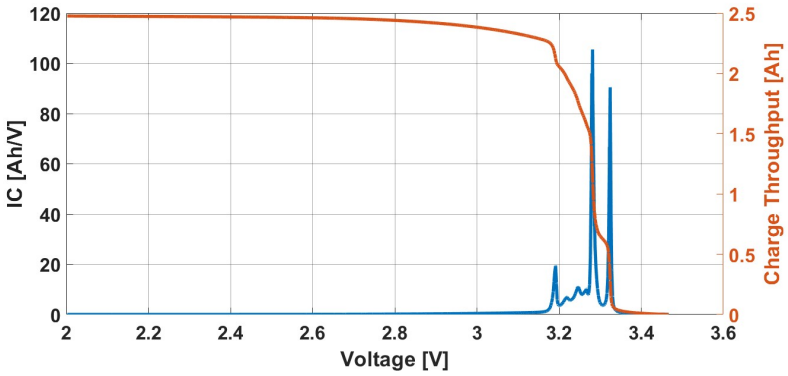

(b) IC Curve

Figure 2.8: DV and IC curves for a 0.02C Discharge process on a M1B sample, compared to the afferent discharge curve

A plateau in the OCV curve coincides with a phase transition occurring within either electrodes and is represented by a notch and a peak in the DV and IC, respectively. Vice-versa, if the OCV is characterized by a certain slope the electrodes behave like solid

solutions and a maximum is present in the DV and a valley in the IC. Moreover, as demonstrated during previous thesis works [22], the shift in position and height of peaks and valleys is an indicator of degradation phenomena occurring inside the cell, namely LLI and LAM. In particular, the first peak visible in the DV curve is very significant for the assessment of aging for the samples, as it corresponds to a phase change present in the equilibrium curve of graphite.

2.3.3. Electrochemical Impedance Spectroscopy (EIS)

As described in section 1.5.1, EIS is a very powerful and widely used diagnostic tool for electrochemical devices [114]. It is non-destructive, in-situ and in-operando technique, meaning that it can be used during the normal operation of cells [115]. In general, every phenomenon shows a specific characteristic time, depending on the speed at which it occurs and its underlying mechanisms. By applying a known sinusoidal current signal of little amplitude and subsequently recording the voltage response, it is possible to compute the impedance for the cell, as the ratio between the two values:

$$Z(\omega) = \frac{V(\omega)}{I(\omega)} = \frac{V_0 e^{i\varphi_1(\omega)}}{I_0 e^{i\varphi_2(\omega)}} = Z_0 e^{i[\varphi_1(\omega)-\varphi_2(\omega)]} = Z_0\{cos\left[\varphi(\omega)\right] + isin\left[\varphi(\omega)\right]\} \tag{2.2}$$

Where:

- $Z(\omega)$ is the impedance, $[\Omega]$;
- ω is the signal angular frequency, $[Hz]$;
- Z_0 is the module of the impedance;
- φ is the phase shift between voltage and current;

The signal's frequency range must be chosen reasonably, to detect all the timescales of the phenomena occurring inside the battery: in this way an impedance spectrum is obtained, which can be used to characterize the electrochemical behavior of cells. The EIS method is based on three underlying assumptions that have to be respected to obtain reliable values [114]:

1. Stability: the obtained value of impedance must be consistent if current perturbation is the same, meaning that for a repeated input, the same output must be obtained;
2. Causality: the voltage response mus be only caused by the input current perturbation and thus no external influence should be present;

3. Linearity: in a linear system, the superposition principle holds true, meaning that for every linear combination of inputs, the system responds in turn with a linear combination of the responses to the single perturbation inputs. Lithium-ion batteries are, in general, not linear, but if the output voltage response has a small amplitude the system can be approximated as such.

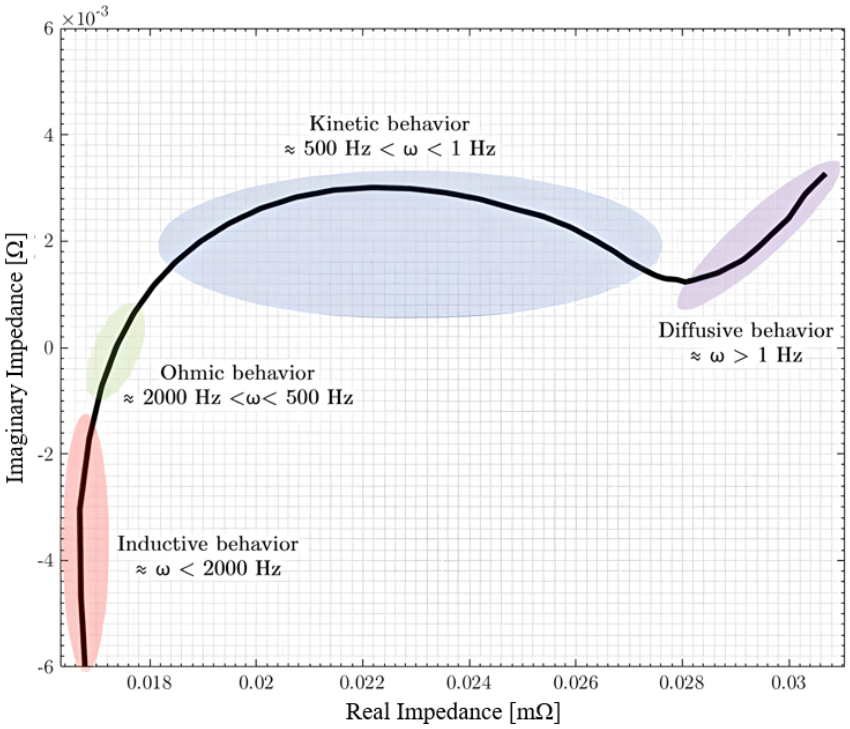

Figure 2.9: Example of a Nyquist plot for the EIS of a battery

The features of the obtained spectrum, which are highlighted in figure 2.9, can be classified depending on the characteristic frequency of phenomena:

- $\omega > 2000Hz$, Inductive Behavior [116]: at the extremely high frequency the imaginary part of the impedance is positive, suggesting an inductive behavior. This aspect is related to the battery wire inductance.
- $\omega \in [500; 2000]\, Hz$, Ohmic behavior [116, 117]: in this frequency range the imaginary part of the impedance becomes negative, thus showing a capacitive behavior. The ohmic region contains all of the very fast phenomena occurring in the cell, including the contributions of electronic and ionic conductivity, ohmic losses and contact losses. At the point for which the imaginary part switches sign, it is possible to define the high frequency resistance (HFR), which represents the purely ohmic behavior of the cell, without considering diffusion or mass transport phenomena.

- $\omega \in [0.5; 500]\, Hz$, Kinetic behavior [117]: in this region, up to three dome shaped features can be seen on the impedance spectrum, which are generally attributed to the charge transfer resistance of the cell and other phenomena related to the reactions kinetics.
- $\omega < 1 Hz$, Diffusive behavior [118]: at such low frequencies, the dominant occurring phenomena are related to diffusion of lithium ions in the electrodes particles and the electrolyte. On the spectrum, this region shows a monotonous increase of the impedance.

The results of EIS measurements are affected by the operating parameters of the cell: temperature, in fact, has an impact on the shape of the impedance spectrum, shifting the frequency at which some phenomena start to appear and lowering the absolute value of the impedance [115, 119]. The SoC has an impact as well, but only circumscribed to its extreme values, thus when the electrodes are completely lithiated/delithiated [115].

2.4. Measurement systems

Together with the experimental station described above, other measurement systems were used. In particular, temperature and volume measurement set-ups were defined, primarily for the thermal characterization of cell.

2.4.1. Temperature measurements

Two types of temperature sensors were used during the work of this thesis, namely thermocouples and Fiber Bragg Gratings (FBG).

Thermocouples

Thermocouples are one of the most widely used temperature sensors in literature. They are based on the thermo-electric effect (or Seebeck effect), which states that a measurable electromotive force (emf) is generated in a conductive circuit if a temperature gradient is present in the materials. Thermocouples consist in general of two different metallic conductors welded together at one side, constituting two junctions (called hot and cold junctions); when a temperature difference is present at the cold junction, an electric potential difference is generated between the two conductors, which can then be measured with an acquisition board through a known function. The response of a thermocouple material to a temperature gradient is referred to as Seebeck coefficient ($[\mu V\ K^{-1}]$) and depends on the material itself, its microstructure and its stability. In this regard, any defect

in the structure of a material can cause measurement errors, so very homogeneous and stable metallic conductor materials are needed for this application. Thermocouples designation depends on the combination of the employed materials and usually corresponds to a capital letter: type K thermocouples, for instance, are based on Chromel (90% Ni, 10% Cr) and Alumel (95% Ni, 2% Al, 2% Mn, 1% Si) and are the most commonly used nowadays [120].

Fiber Bragg Gratings (FBG)

Fiber Bragg gratings are optical-based passive sensors capable of measuring strain, temperature and relative humidity. In general, an optical fiber consists of a circular dielectric waveguide which allows the propagation of light with very low loss of signal. The structure of an optical fiber is constituted by a cylindrical core surrounded by a cladding, with a slightly lower refractive index. Both core and cladding are fabricated with fused silica-based materials and are covered by a protective layer that surrounds the cladding, called coating. The variation in the refractive index of the silica core is obtained through doping of the microstructure with Ge or P based-compounds [121].
More in particular, Fiber Bragg Gratings are multi-point sensors which are fabricated through etching by a precise laser beam: a pulsed infrared laser at high intensity is directed towards the fiber core to produce a controlled series of defects onto the surface, characterized by a certain period. This periodic pattern is called grating and it produces locally a permanent increase of the refractive index of the core. In this way, when light is transmitted through the fiber, a portion of it is reflected by the grating at a specific wavelength, called "Bragg wavelength", while other wavelengths are transmitted and lost. The Bragg wavelength satisfies the Bragg law, which describes constructive interference condition of the interacting radiation with a periodic structure:

$$\lambda_B = 2n_i\Lambda \qquad [\text{nm}] \qquad (2.3)$$

Where:

- n_i is the refractive index, $[-]$;
- Λ is the grating period $[nm]$;

The index of refraction n is not just a material property, but depends also on the design of the waveguide and on the propagating modes considered. Moreover, since λ_B is dependent on Λ, multiple sensors with unique grating periods can be etched on the same fiber, thus obtaining a series of reflected wavelength as output. The FBG is extremely sensitive to

temperature gradients and external deformations: the thermal response arises due to the inherent thermal expansion of the fiber and the temperature dependence of the refractive index, known as thermo-optic effect; the strain response, instead, arises due to both the physical elongation of the FBG and n variations due to the photo-elastic effect. The relations between the Bragg wavelength λ_B and temperature and strain ϵ can be written as follows:

$$\left.\frac{\Delta\lambda_B}{\lambda_B}\right|_T = \Delta T\left[\frac{1}{\Lambda}\frac{\partial\Lambda}{\partial T}+\frac{1}{n}\frac{\partial n}{\partial T}\right] = \Delta T(\beta+\gamma) \tag{2.4}$$

And

$$\left.\frac{\Delta\lambda_B}{\lambda_B}\right|_\epsilon = \epsilon\left[1+\frac{1}{n}\frac{\partial n}{\partial \epsilon}\right] = \epsilon(1+p_\epsilon) \tag{2.5}$$

Where:

- β is the relative thermal expansion coefficient, $[^\circ C^{-1}]$; this contribution generally accounts for less than 5 % of the total variation and is sometimes neglected;
- γ is the relative thermal index refraction dependency coefficient $[^\circ C^{-1}]$;
- p_ϵ is the strain-optic coefficient, given by axial deformation, $[-]$

FBGs are characterized by many advantages related to their structure and material choice: primarily, small scale, light weight and long term reliability. Moreover, unlike thermocouples, optical fiber have very high electro-magnetic interference tolerance and chemical stability and inertness, particularly helpful in harsh chemical environment [121, 122]. In this regard, their implementation as temperature sensors for lithium-ion batteries has been extensively analyzed in literature [123–127].
During the work of this thesis several fibers were available, characterized by the use of draw tower gratings sensors (DTG®s), written on low bend loss fibers, allowing a minimum radius bend of 6 $[mm]$; this was done in order to keep the surface strain level below 1%. All the fibers were coated by a 70 $[\mu m]$ layer of a material called ORMOCER-T®, guaranteeing operational thermal stability in the range of $[-20; 200]\,[^\circ C]$. The temperature and strain sensitivities were, respectively:

$$\frac{\Delta\lambda}{\lambda\cdot\Delta T} = 6.5\cdot 10^{-6}\left[^\circ C^{-1}\right]; \tag{2.6}$$

$$\frac{\Delta\lambda}{\lambda\cdot\epsilon} = 7.8\cdot 10^{-7}\left[\mu\epsilon^{-1}\right] \tag{2.7}$$

Where $\mu\epsilon$ is a unit of microstrain, representing a relative elongation of 10^{-6} $[\mu m\ m^{-1}]$. All the used fibers employed up to 5 DTGs of 8 $[mm]$, nominal wavelength in the range of $[1535; 1555]$ $[nm]$ and an accuracy of ± 0.03 $[nm]$.

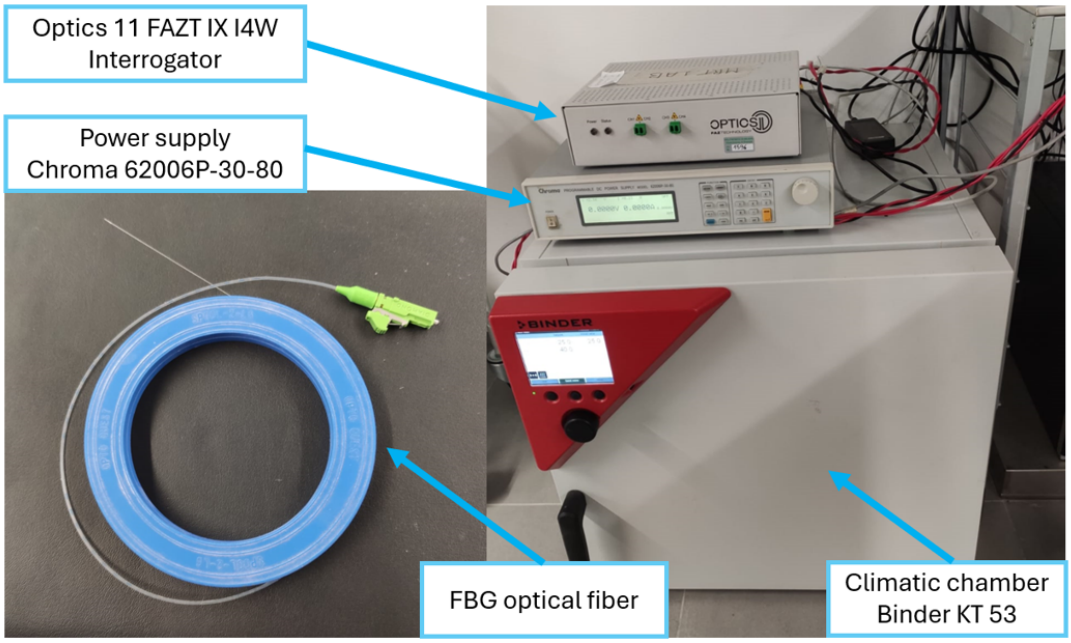

Figure 2.10: Instrumentation for thermal experimental tests

To acquire and store data related to temperature and strain measurements, an interrogator must be used. During this work a Optics 11 FAZT IX I4W interrogation device was used, employing four measurement channels, a sweep range on 35 $[nm]$ (between 1529 $[nm]$ and 1564 $[nm]$) and a channel scan frequency of 1 $[kHz]$. The absolute wavelength accuracy of this device is of ± 3 $[pm]$.
The interrogator and fibers were controlled on the testing station computer through the software Femtosense®, allowing to extract and store data in combination with NI Labview®.

In a previous thesis work [55] it was demonstrated that FBG lead to more dynamically accurate measurements compared to thermocouples. In fact, due to some delay in data acquisition and a much higher thermal inertia, thermocouples could be regarded as unreliable sensors for transient measurements (figure 2.11). This was highlighted also in [124]. For these reasons, only FBGs were used for dynamic temperature measurements.

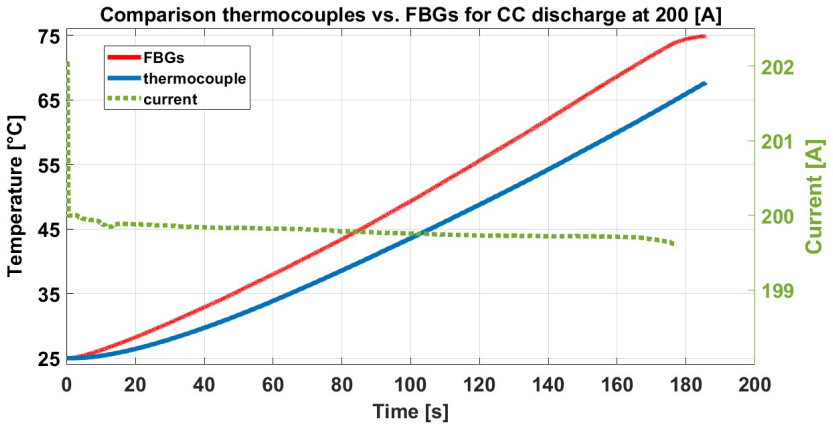

Figure 2.11: Comparison between FBG and thermocouple temperature measurement on the lateral surface of the same cell during a discharge of its module at 200 [A][55]

2.4.2. Volume measurements

The determination of the volume of batteries is very useful to compute their density, which is an important property for the thermal characterization of cells. The dimensions and mass of the samples are already available from their datasheet; Moreover, the analyzed cells have both the same cylindrical geometry, which facilitates the volume computation through the equation:

$$V_{cyl} = \pi R^2 L \qquad [\mathrm{m}^3] \qquad (2.8)$$

Where: R and L are the radius and the length of the cylinder, respectively.
However, their shape is not a perfect cylinder and the measured dimensions are characterized by some uncertainty. For this reason, the Archimedean principle was used to compute the volume of cells and to confirm the assumption of perfect cylinder. The Archimedean principle relates the buoyant force of an object to its volume, stating that a body immersed in a fluid receives a buoyant force equal to the weight of the fluid displaced by the object. In this regard it represents a direct measurement method for the volume [128].
In practice, to measure the volume of a body, this is left to hang from a hook with a cord of negligible volume; it is then immersed in a container full of fluid, following the scheme in figure 2.12.

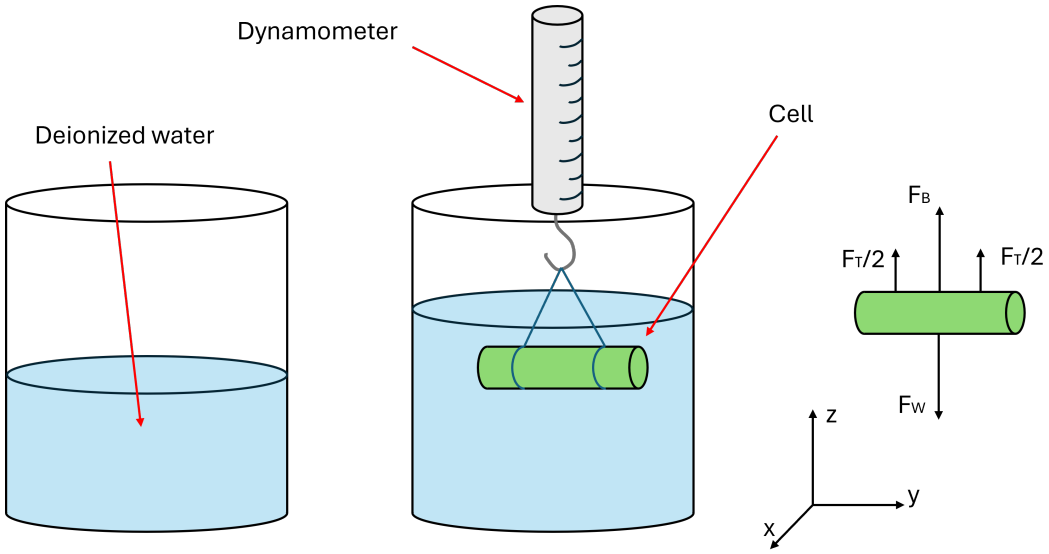

Figure 2.12: Scheme of the Archimedean principle for the cell

The balance of forces acting on the body are the following:

$$\sum \boldsymbol{F} = \boldsymbol{F_w} + \boldsymbol{F_b} + \boldsymbol{F_T} \tag{2.9}$$

Where $\boldsymbol{F_w}$ is the weight force, $\boldsymbol{F_b}$ is the buoyancy force and $\boldsymbol{F_T}$ is the tension applied by the hook $[N]$. These forces all act in the vertical direction and the balance can be translated into:

$$F_w = F_b + F_T \tag{2.10}$$

and then, following the definition of the weight force and the Archimedean principle stated above:

$$m_b g = \rho_f g V_b + F_T \tag{2.11}$$

Where ρ_f is the density of the fluid (which has to be known), m_b and V_b are the mass and volume of the immersed body. Solving for the volume, the following expression is obtained:

$$V_b = \frac{m_b g - F_T}{\rho_f g} \tag{2.12}$$

Where the only two unknowns are V_b and F_T. The tension force can be easily measured

through a dynamometer attached to the hook. The density can be then be computed through its definition.
The Archimedean principle is a very easy and cheap method to directly measure the volume of an object of whatever shape, but some considerations must be observed when working with batteries and electrochemical devices in general. In particular, the fluid must be a strong insulator, to avoid any short-circuit of the cell: in literature, deionized water and silicon mechanical pump oil were reported, for their insulating properties and excellent thermal stability [128–131].
In this thesis work, deionized water with a minimum electrical resistance of 0.2 $[M\Omega\ cm^{-1}]$ was used [132], due to availability.

2.4.3. Uncertainty analysis

Every measurement system is characterized by a certain error on the measured value, which has to be taken into account when the results are presented.

Uncertainty on experimental discharge

The uncertainty analysis on the measured voltage was carried out in a previous thesis at the same laboratory [99]. Given that many parameters affect the measured voltage, all possible sources of errors must be taken into account. In this regard, the voltage uncertainty can be computed through the expression:

$$u_V = \sqrt{(\sigma_V V)^2 + \left(\frac{\Delta V}{\Delta Q} u_Q\right)^2 + \left(\frac{\Delta V}{\Delta T} u_T\right)^2 + u_{OCV}^2} \tag{2.13}$$

Where the four terms represent uncertainties on the power supply, the exchanged charge, the temperature and the OCV value, respectively. The global average uncertainty u_V was estimated to be around 6.5 $[mV]$ for a typical discharge process.

Uncertainty on impedance measurement

The uncertainty on EIS measurements is given by the contributions of the electronic load and the power supply, described in section 2.2.1. in [99], a type A uncertainty was computed for the measurement system, performed through a series of ten repeated EIS measurements performed on the same sample. The uncertainty was determined for three frequency ranges and real and imaginary part and the results are reported in table

Hz	High Frequency $[100; 4000]$	Mid Frequency $[1; 100]$	Low Frequency $[0.02; 1]$
$u_{Z_{Re}}\,[m\Omega]$	1.3775	3.7430	0.7166
$u_{Z_{Im}}\,[m\Omega]$	1.6820	6.5779	0.7126

Table 2.3: Results of the uncertainty analysis on the battery impedance

Uncertainty on temperature measurements

As described in section 2.4.1, the most reliable temperature sensors were found to be the FBGs. These are characterized by an accuracy equal to $u_{FBG}(\lambda) = 30\,[pm]$ for the fibers and to $u_{int}(\lambda) = 3\,[pm]$ for the interrogator. In a previous thesis [55], the uncertainty of the FBG measurement system on the temperature was found to be $\pm 0.055\,[K]$.

Uncertainty on volume measurements and density

The uncertainty of the volume measurements only depends on the uncertainty on the dynamometer. For this instrument no datasheet was available, so a type A uncertainty was calculated. Ten repeated measurements were done using the set-up described in section 2.4.2, using a cylindrical aluminum body with known dimensions and mass. The uncertainty was estimated to be equal to $u_{Vol} = \pm 0.161\,[cm^3]$ on the volume and $u_\rho = \pm 13.83\,[kg\ m^{-3}]$ on the density.

2.5. Experimental campaign description

In this section, the experimental campaign will be briefly described, following the main logical and methodological steps. The thorough description of the methods, models and results will be provided in the following chapters.

As stated before, the primary goal of this thesis stands in the thermal characterization of the samples described in section 2.1. For this reason, a thorough literature analysis was carried to define a robust and innovative experimental methodology for the determination of the specific heat capacity and the thermal conductivity.

Following a similar approach as Cailliez et al. [62] and Drake et al. [59], an analytical model was defined for the cylindrical cells, considering several external heat generation cases as boundary conditions. Moreover, a comparison was carried between the model and the results of a COMSOL Multiphysics® simulation constructed with the same assumptions. After the methodology for the estimation of parameters was defined, it was validated by the means of a simulacrum, which is a body of the same shape of the samples and known thermal properties. In this regard, an aluminum alloy cylinder was used for

this validation step. Following the validation of the methodology, the latter was applied to the battery samples described in section 2.1, allowing for the estimation of thermal parameters in beginning of life (BoL) and aged cells, also at different temperatures. Taking into account only external measurements it was possible to assess the thermal conductivity only in the axial direction.

For this reason, during the experimental campaign, a methodology for the drilling of cylindrical cells was defined: this novel technique was aimed at obtaining temperature measurements internal to the batteries, allowing for the thermal characterization also in the radial direction. This was achieved through the use of the optical fibers described in section 2.4.1, which were inserted inside the mandrel of the cylindrical cells. An electrochemical diagnosis characterization was done before and after this operation on the drilled cells, to verify their integrity before subsequent tests.

The second part of the thesis was dedicated to the assessment of the impact of thermal parameters on the internal thermal behavior of batteries. Thanks to the methodology defined for the drilling and insertion of temperature sensors inside the cells, it was possible to obtain precise and reliable internal temperature measurements.

An interpretation of these results was made through the construction of a physics-based model, known as Single Particle Model (SPM), able to describe the internal state of the samples. The model was calibrated through previously available data obtained at the same laboratory and additional measurements done during the work of this thesis.

3 | Thermal Characterization

In this chapter, a thorough description of the thermal parameters experimental campaign will be carried. In particular, the methodologies, models and results obtained during the work of this thesis will be presented and explained.

3.1. Methodology for thermal characterization

As explained in section 1.4.4, lithium-ion batteries are characterized by a strong anisotropic behavior, because of the geometric features of the jelly-roll. In fact, this component greatly affects the thermal behavior of cells, due to its wound structure and the heat generation within it. Moreover, due to the slow mobility of the electrolyte, the main heat transfer mode inside cells is conduction, while other modes are typically neglected. In this regard, a methodology for thermal characterization should be conceived following these ideas as starting points.
As described in sections 1.4.4, several scientific papers addressed in recent years the need for innovative methodologies for the estimation of thermal parameters in LIBs:

- Sheng et al. [66] defined a new calorimetric method for the estimation of specific heat capacity. In this approach, cells are wrapped in a thermal insulation material and left in a thermostatic environment until thermal equilibrium is achieved. The cell is then heated through a surface heater to obtain a temperature ramp until an arbitrary maximum value is reached. Once the heater is turned off, the temperature of the cell slowly decreases with time. By calibrating the heat losses during both periods, the specific heat capacity is obtained through the conservation of energy equation for the system. As demonstrated by the authors, this method is characterized by a great accuracy and reliability of measurement in a short time, other than being easy to implement. On the other hand, only the specific heat capacity is obtained through this experimental test and a very long time is needed for the calibration of losses. Similar techniques were used by [67] and [68].
- Cailliez et al [62], instead, defined a methodology to simultaneously estimate ther-

mal conductivity and specific heat capacity for prismatic cells. In this method, a three-dimensional analytical model is applied to obtain the thermal parameters of batteries, by fitting the measured temperature during a heating period trough the use of T-type thermocouples. Drake et al [59] applied a similar approach to cylindrical cells in adiabatic conditions, predicting the in-plane and through-plane thermal conductivity as well as the specific heat capacity with ad-hoc experimental campaigns.

All of the mentioned scientific papers presented novel and effective methodologies for the thermal characterization of cells of various geometries, relying on cost-effective materials. However, they all make use of thermocouples for temperature measurements which, as explained in section 2.4.1, are characterized by a certain thermal inertia and could produce a distortion in the estimation of parameters during dynamic testings. This aspect becomes more important in smaller samples, such as cylindrical cells, where these secondary effects could become non-negligible.
For these reasons, a fast and reliable methodology was developed during the work of this thesis for the estimation of thermal parameters of the samples of section 2.1. This method follows a similar approach as the mentioned [59] and [62], employing the analytical solution of the heat equation for both adiabatic and convective boundary conditions of an homogeneous cylindrical body, but introducing optical fiber sensors as reliable temperature measurement devices in dynamic thermal tests. In this regard, the Fiber Bragg Gratings (FBGs) described in section 2.4.1 were employed for this methodology. The sensors are placed on several points of the external surface of the tested samples and fixed using 10 $[mm]$ wide kapton tape.

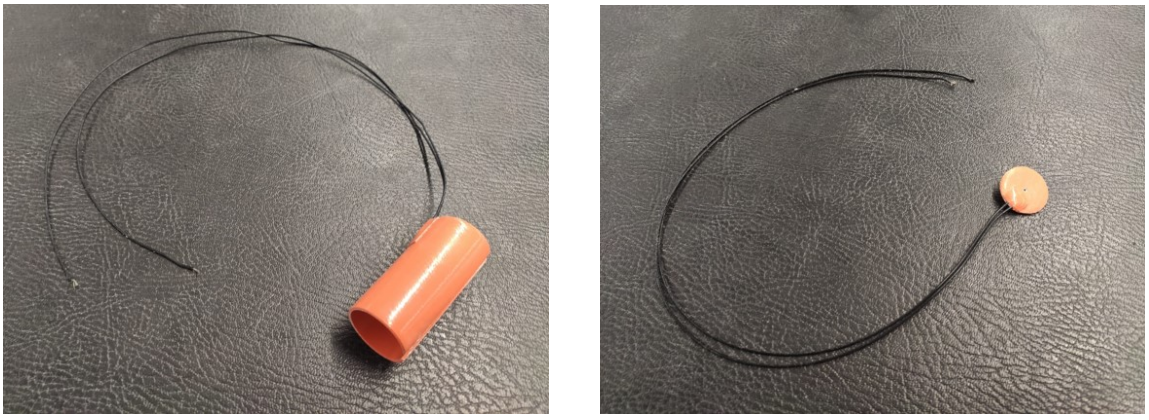

(a) Radial heater (b) Axial heater

Figure 3.1: Images of the silicon electrical heater employed in the experimental campaign

A silicon electrical surface heater is subsequently installed on the cells to provide thermal

power either in the axial or radial direction. In this thesis, two different types of custom tailor-made heater were used: in particular, the first one was a hollow cylindrical heater with the same height of the samples (both 26650 and 18650), which encapsulates the battery and heats the bulk radially; the second one used was a circular heater with the same diameter of the cells' tab, which was sticked together with one of the axial surfaces of the cell (figure 3.1). In the following paragraphs the two devices will be called radial heater and tab heater, respectively.
The specimens are then covered by a 1 $[cm]$ thick insulation material layer (silica aerogel) on all surfaces and left in the Binder KT 53 climatic chamber (described in section 2.2.1) at a certain temperature, until thermal equilibrium is reached.
The cells are then heated through the surface heater by providing a certain electrical power through the Chroma 62012P-100-50 DC power supply (section 2.2.1) and the evolution of temperature is measured through the FBGs. The heater is stopped once the temperature difference reaches a certain level, which for this experimental campaign was set to 2.5 $[°C]$; then the samples are left to relax.
The aerogel insulation material is characterized by a very low thermal conductivity and thus provides a very high thermal resistance towards the external environment; however, a certain thermal power, proportional to the supplied one, is always lost to convection during the experiment due to temperature differences, leading to non-adiabatic boundary conditions. On the other hand, a lower power necessarily leads to longer tests to obtain the same temperature difference. Moreover, as described in section 1.4.4, another aspect that must be taken into account is the temperature dependency of thermal parameters: in this regard a little temperature difference should be attained at the end of the test. For these reasons, a trade-off must be found between the provided electrical power, the length of the tests and the final temperature difference, so to neglect the heat loss along the whole duration of the experiment (and thus verify the assumption of adiabatic conditions) and to correctly estimate values of said parameters at the given temperature.
After the definition of the experimental tests, a method for parameters estimation must be established. As a general idea, the thermal parameters of a system can be determined through the solution of the heat equation: after the direct solution is found, ie. the temperature distribution inside the body given its properties and specific boundary and initial conditions, it can be reversed by coupling temperature profiles and experimental data in certain geometrical positions and fitting said parameters to minimize the error between them. The goodness of the fitting depends strongly on the goodness of the experimental methodology, but also the complexity of the system itself and the fitting algorithm influence greatly the outcome. For this reason a robust and reliable experimental setup and the correct algorithm are required to obtain acceptable results.

After the determination of the solving equations, the models were realized in MATLAB®, considering a discretization through time and space. The data fitting was done through a least square optimization by using the function *lsqcurvefit*: after noting the position of the sensors, their temperature profiles are fitted through time with the modeled profiles in the same points. In this way the thermal parameters can be determined. In general, the error can be decreased by increasing the number of sensors and positions within the domain.
In conclusion, this methodology is able to provide a reliable estimation of thermal parameters in a very short time, thanks to its core aspects of utilizing FBGs as temperature sensors and employing an analytical model to predict the thermal behavior of cells.

3.2. Thermal models for external heat generation

A model is an approximation of a system that can be applied to reproduce some of its aspects in specific and circumscribed applications. A good model is of fundamental importance to describe the behavior of said system and characterize its evolution in time and space. This can be achieved by finding a compromise between accuracy and complexity, through the definition of the main assumptions.
During this thesis, four analytical thermal models with external heat generation were derived, whose main goal is to correctly describe the thermal behavior of cells through the determination of the most important thermal parameters, in particular the thermal conductivity and the specific heat capacity.
External heat production models are characterized by a lower complexity compared to internal generation ones, due to the fact that, in this context, the cylindrical cells can be assumed as homogeneous bodies. For this reason it was possible to solve the heat equation in closed form, computing the analytical solution for the problem. An analytical model involves no solving error, but errors only come from the made assumptions [62]. In this regard, this model works very well with simple homogeneous bodies (which of course lithium-ion batteries are not), but it can also give a very good estimation for the parameters of more complex and elaborate systems. Following this idea, the main goal of these models is not necessarily to describe the exact thermal behavior of LIBs, but to estimate the global thermal parameters of cells which represent the closest description with respect to the real performance.

3.2.1. Problem description and assumptions

The samples were modeled as homogeneous solid cylinders with anisotropic thermal conductivity, representing the in-plane and through plane contributions, as described in section 1.4.4. As a result of this assumption the only considered heat transfer mode was conduction, neglecting convection and radiation inside the cylinder. Moreover, no internal generation was considered in the model.
Given that the heat generation is external, the internal layers were neglected and a unique thermal conductivity value was considered for radial and axial directions. In this way, every differentiation given by the internal components is not taken into account, greatly reducing the complexity of the model.
Furthermore, the temperature is assumed to not depend on the angular coordinate, but only on the radial and axial ones, assuming also in this case the radial symmetry. Finally, constant specific heat capacity and thermal conductivities were assumed, as well as density. These assumptions are justified by the very low temperature differences obtained from the experimental methodology. From the hypothesis described above, the heat equation to be solved, considering cylindrical coordinates, is the following:

$$\rho c \frac{\partial T}{\partial t} = k_r \left(\frac{1}{r} \frac{\partial T}{\partial r} + \frac{\partial^2 T}{\partial r^2} \right) + k_z \frac{\partial^2 T}{\partial z^2} \tag{3.1}$$

Where:

- $T = T(r, z, t)$ is the temperature $[^\circ C]$;
- t, r, z are the time, radial and axial coordinates, respectively;
- ρ is the density $[kg\ m^{-3}]$;
- c_p is the specific heat capacity $[J\ kg^{-1}K^{-1})]$;
- k_r and k_z are the radial and axial thermal conductivities, respectively $[W\ m^{-1}K^{-1}]$.

Boundary and initial conditions

As described in section 3.1, the experimental setup was covered by a layer of thermal insulating materials, to minimize the thermal losses, thus maximizing the efficiency of the heater. The external heat generation was translated as a constant thermal flux boundary condition on the outer surfaces of the cylinder, in the radial direction for the radial heater and on one of the axial facets for the tab heater. The other surfaces of the cylinder were modeled both with adiabatic and convective boundary conditions and compared, to also

take into account inevitable thermal losses (even if potentially negligible). In the case of convective boundary conditions the heat transfer coefficient is fictitious and only useful to model real convective and radiation heat losses outside of the insulating material.
As a convention for heat exchange with the external environment, the thermal flux was taken as positive when exiting the system.

Radial heater - Adiabatic boundary condition For the ideal case of adiabatic condition on the surfaces of the cylinder, the boundary and initial conditions for the heat equation were defined as:

$$\begin{cases} -k_r \left.\dfrac{\partial T}{\partial r}\right|_{r=R} = -\dot{q}_r & \text{(3.2a)} \\ \left.\dfrac{\partial T}{\partial r}\right|_{r=0} = 0 & \text{(3.2b)} \\ \left.\dfrac{\partial T}{\partial z}\right|_{z=-L/2} = \left.\dfrac{\partial T}{\partial z}\right|_{z=L/2} = 0 & \text{(3.2c)} \\ & \text{(3.2d)} \end{cases}$$

Where:

- R is the radius of the cylinder;
- L is the length of the cylinder in the axial direction; given that this problem is symmetric both in the radial and axial directions, the origin of the domain is placed at the core of the body, at half length.
- $\dot{q}_r$ is the heat flux through the lateral surface of the cylinder

Due to the adiabatic condition, the temperature doesn't depend on the axial coordinate, but only on the radial one and the problem is analogous to the flow of heat in radial direction in an infinitely long cylinder [133]. As a result, only conditions 3.2a and 3.2b remain relevant.

Radial heater - Convective boundary condition For convective conditions, a thermal flux directed towards the environment is introduced. The boundary conditions are thus:

$$\begin{cases} -k_r \left.\dfrac{\partial T}{\partial r}\right|_{r=R} = -\dot{q}_r & \text{(3.3a)} \\ \left.\dfrac{\partial T}{\partial r}\right|_{r=0} = 0 & \text{(3.3b)} \\ k_z \left.\dfrac{\partial T}{\partial z}\right|_{z=-L/2} = h(T - T_0) & \text{(3.3c)} \\ -k_z \left.\dfrac{\partial T}{\partial z}\right|_{z=L/2} = h(T - T_0) & \text{(3.3d)} \end{cases}$$

Where h is the heat transfer coefficient.

Tab heater - Adiabatic boundary condition Similarly to the radial heater, the boundary conditions for the tab heater in the adiabatic case can be defined. In this instance, heat is supplied through one of the cylinder lateral facets, perpendicularly to the symmetry axis, so the conditions can be written as:

$$\begin{cases} k_z \left.\dfrac{\partial T}{\partial z}\right|_{z=0} = -\dot{q}_z & \text{(3.4a)} \\ \left.\dfrac{\partial T}{\partial z}\right|_{z=L} = 0 & \text{(3.4b)} \\ \left.\dfrac{\partial T}{\partial r}\right|_{r=R} = \left.\dfrac{\partial T}{\partial r}\right|_{r=0} = 0 & \text{(3.4c)} \end{cases}$$

Where:

- L is the length of the cylinder (in this case the problem is not symmetric anymore along the axial direction, so the origin is placed at one end of the cylinder);
- $\dot{q}_z$ is the heat flux through the heated side.

Also in this instance only conditions 3.4a and 3.4b can be taken into account and the problem is analogous to heat exchange in a slab of length L and infinite surface.

Tab heater - Convective boundary condition In this case, the body exchanges heat with the environment through both the radial surface and the side not warmed by

the heater.

$$\begin{cases} k_z \left.\dfrac{\partial T}{\partial z}\right|_{z=0} = -\dot{q}_z & (3.5a) \\ -k_z \left.\dfrac{\partial T}{\partial z}\right|_{z=L} = h(T - T_0) & (3.5b) \\ -k_r \left.\dfrac{\partial T}{\partial r}\right|_{r=R} = h(T - T_0) & (3.5c) \\ \left.\dfrac{\partial T}{\partial r}\right|_{r=0} = 0 & (3.5d) \end{cases}$$

Note that, in general, the heat transfer coefficient could be different in the axial and radial directions due to geometry.

The initial condition was the same for all four problems and was defined as:

$$T(r, z, 0) = T_0 \tag{3.6}$$

Analytical solutions of the heat equation

The analytical solutions of these Cauchy problems can be obtained through some manipulation and re-formulation of the equations, which greatly decrease their complexity without losing information or accuracy.

1. In general, the solution of a problem with certain boundary and initial conditions can be seen as superposition of solutions with complementary conditions, as described in [133]. In this regard, the boundary and initial conditions described for the above problems can be decoupled into two complementary problems each, for which the first one only "inherits" the initial condition and has null boundary conditions and vice-versa for the second one. For instance, for the case of radial heater with adiabatic condition the two complementary problems become:

$$\begin{cases} \left.\dfrac{\partial T}{\partial r}\right|_{r=R} = \left.\dfrac{\partial T}{\partial r}\right|_{r=0} = 0 & (3.7a) \\ T(r, z, 0) = T_r(r, 0) = T_0 & (3.7b) \end{cases}$$

   and

$$\begin{cases} -k_r \left.\dfrac{\partial T}{\partial r}\right|_{r=R} = -\dot{q}_r & \text{(3.8a)} \\ \left.\dfrac{\partial T}{\partial r}\right|_{r=0} = 0 & \text{(3.8b)} \\ T(r,z,0) = T_r(r,0) = 0 & \text{(3.8c)} \end{cases}$$

Naturally, the solution of the first problem is trivial and coincides with the initial condition itself, while the second one has to be solved. If the problem is well posed, this concept is valid for any initial condition $T(t=0) = T_0$ and boundary conditions, so it will also be used for other analogous instances.

2. The solution of the heat equation for special multi-dimensional domains (such as prismatic solids or finite cylinders) and some types of boundary and initial conditions, can be found by intersection - ie product - between the solutions of mono-dimensional problems, each one with adequate boundary and initial conditions, as described in [133], §1.15.
   For example, following the same idea, the radial heater problem with convective boundary conditions (equation 3.3) can be split into an infinitely long cylinder problem with constant radial heat flux and one of a solid slab of finite thickness bounded by two parallel planes with convective heat transfer; the solution of the initial problem is then found by multiplying both solutions. In particular, after the application of step 1., the new boundary and initial conditions for the investigated problem would be:

$$\begin{cases} -k_r \left.\dfrac{\partial T}{\partial r}\right|_{r=R} = -\dot{q}_r & \text{(3.9a)} \\ \left.\dfrac{\partial T}{\partial r}\right|_{r=0} = 0 & \text{(3.9b)} \\ \left.\dfrac{\partial T}{\partial z}\right|_{z=-L/2} = \left.\dfrac{\partial T}{\partial z}\right|_{z=L/2} = 0 & \text{(3.9c)} \\ T(r,z,0) = T_r(r,0) = 0 & \text{(3.9d)} \end{cases}$$

and

$$\begin{cases} k_z \left.\dfrac{\partial T}{\partial z}\right|_{z=-L/2} = hT & \text{(3.10a)} \\ -k_z \left.\dfrac{\partial T}{\partial z}\right|_{z=L/2} = hT & \text{(3.10b)} \\ \left.\dfrac{\partial T}{\partial r}\right|_{r=0} = \left.\dfrac{\partial T}{\partial r}\right|_{r=R} = 0 & \text{(3.10c)} \\ T(r,z,0) = T_z(z,0) = 1 & \text{(3.10d)} \end{cases}$$

Where $T_i(i,t)$ is the solution of the heat equation in the i coordinate, with $i = r, z$ The initial condition of the complete problem is given by the product of the initial conditions of the separate problems, so in this case: $T(r,z,0) = T_r(r,0) \cdot T_z(z,0) = 0$

Note that the first problem now only depends on the radial coordinate (and coincides with the adiabatic case for the radial heater with null initial condition), while the second set of conditions depends only on the axial one. Finally, the complete solution is given by:

$$T(r,z,t) = T_r(r,t) \cdot T_z(z,t) \tag{3.11}$$

Thanks to this procedure, all four problems can be reduced to much simpler and manageable mono-dimensional problems with null or unitary initial conditions.

Radial heater - Adiabatic boundary condition Summarizing the previous steps, the complete problem can be stated as:

$$\rho c \frac{\partial T}{\partial t} = k_r \left(\frac{1}{r} \frac{\partial T}{\partial r} + \frac{\partial^2 T}{\partial r^2} \right) \tag{3.12}$$

with boundary and initial conditions as for equations 3.2 and 3.6. The solution of the problem with null initial condition is then ([133], §7.8):

$$T_r(r,t) = \frac{2\dot{q}_r \alpha_r}{k_r R} t + \frac{\dot{q}_r R}{k_r} \left\{ \frac{r^2}{2R^2} - \frac{1}{4} - 2 \sum_{n=1}^{\infty} \frac{J_0(r\lambda_n/R)}{{\lambda_n}^2 J_0(\lambda_n)} \exp\left(-\frac{\alpha_r {\lambda_n}^2 t}{R^2} \right) \right\} \tag{3.13}$$

where λ_n, $n = 1, 2, ..$ are the positive roots of $J_1(\lambda) = 0$ and α_r is the thermal diffusivity in the radial direction, as defined in section 1.4.4.
$J_n(\xi)$ represents the Bessel function of the first kind of order n, which is defined as:

$$J_n(\xi) = \sum_{m=0}^{\infty} \frac{(-1)^m}{m!(m+n)!} \left(\frac{\xi}{2}\right)^{2m+n}$$

It can be noted that the temperature evolution inside the body is given by three general terms [59]: a steady-state contribution that depends on the model parameters, a linear asymptotic trend, which corresponds to the average temperature of the sample, and an exponentially decaying term, which cancels out after a certain amount of time.
This time transient contribution strongly depends on the thermal diffusivity (and thus thermal conductivity) of the body and is responsible for its internal temperature gradient between different positions.

Finally, the solution of the global problem is given by:

$$T(r,t) = T_0 + T_r(r,t) \tag{3.14}$$

Radial heater - Convective boundary condition In this case, the problem to be solved is given by equation 3.1, with boundary and initial conditions as for equations 3.3 and 3.6.
As explained in the previous section, this Cauchy problem can be seen as the superposition of the problems with boundary conditions in equations 3.9 and 3.10. The solution of the first problem is, of course, equation 3.13, while the second one is given by ([133], §3.11):

$$T_z(z,t) = \sum_{n=1}^{\infty} \frac{2H \cdot \cos(2\lambda_n z/L) \cdot \sec(\lambda_n)}{H(H+1) + \lambda_n^2} \exp\left(-\frac{4\alpha_z \lambda_n^2 t}{L^2}\right) \tag{3.15}$$

Where λ_n, n=1,2,... are the roots of $\lambda \cdot \tan(\lambda) = H$ and $H = Lh/2k_z$. The complete solution is obtained as:

$$T(r,z,t) = T_0 + T_r(r,t) \cdot T_z(z,t) \tag{3.16}$$

Tab heater - Adiabatic boundary condition Similarly to the adiabatic problem for the radial heater, also in this case heat transfer in the body develops only along the axial direction. For this reason, the domain can be expressed as solid of infinite surface and bounded by two parallel planes, referred as a slab. By applying the two simplifying steps described in the previous paragraphs, the problem becomes:

$$\rho c \frac{\partial T}{\partial t} = k_z \frac{\partial^2 T}{\partial z^2} \tag{3.17}$$

with boundary and initial conditions:

$$\begin{cases} k_z \left.\dfrac{\partial T}{\partial z}\right|_{z=0} = -\dot{q}_z & \text{(3.18a)} \\ \left.\dfrac{\partial T}{\partial z}\right|_{z=L} = 0 & \text{(3.18b)} \\ \left.\dfrac{\partial T}{\partial r}\right|_{r=R} = \left.\dfrac{\partial T}{\partial r}\right|_{r=0} = 0 & \text{(3.18c)} \\ T(r,z,0) = T_z(z,0) = 0 & \text{(3.18d)} \end{cases}$$

As it can be guessed, the solution of this problem has the same structure as the adiabatic radial heater case, with the three contributions of steady-state, linear asymptotic behavior with time and a sum of terms which disappear after a certain transient.

$$T(z,t) = \frac{\dot{q}_z}{\rho c_p L} t + \frac{\dot{q}_z L}{k_z} \left\{ \frac{3z^2 - L^2}{6L^2} - \frac{2}{\pi^2} \sum_{n=1}^{\infty} \frac{(-1)^n}{n^2} \cos\left(\frac{n\pi z}{L}\right) \exp\left(-\frac{\alpha_z n^2 \pi^2 t}{L^2}\right) \right\} \tag{3.19}$$

with $n = 1, 2, 3, ...$

The global solution is then given by:

$$T(r,z,t) = T_0 + T_z(z,t) \tag{3.20}$$

Tab heater - Convective boundary condition Finally, in this case, the same approach can be applied. Starting from the problem described by equation 3.1 and boundary and initial conditions 3.5 and 3.6, the following problems can be obtained:

$$\begin{cases} k_z \left.\dfrac{\partial T}{\partial z}\right|_{z=0} = -\dot{q}_z & \text{(3.21a)} \\ -k_z \left.\dfrac{\partial T}{\partial z}\right|_{z=L} = hT & \text{(3.21b)} \\ \left.\dfrac{\partial T}{\partial r}\right|_{r=0} = \left.\dfrac{\partial T}{\partial r}\right|_{r=R} = 0 & \text{(3.21c)} \\ T(r,z,0) = 0 & \text{(3.21d)} \end{cases}$$

in the axial direction and

$$\begin{cases} \left.\dfrac{\partial T}{\partial z}\right|_{z=0} = \left.\dfrac{\partial T}{\partial z}\right|_{z=L} = 0 & \text{(3.22a)} \\ \left.\dfrac{\partial T}{\partial r}\right|_{r=0} = 0 & \text{(3.22b)} \\ -k_r \left.\dfrac{\partial T}{\partial r}\right|_{r=R} = h(T - T_0) & \text{(3.22c)} \\ T(r, z, 0) = 1 & \text{(3.22d)} \end{cases}$$

in the radial one.
The solution of the problem in the axial direction is ([133], §3.11):

$$T_z(z,t) = \frac{\dot{q}_z}{h}\left\{1 + H\left(1 - \frac{z}{L}\right) - \sum_{n=1}^{\infty} \frac{2H\left[H^2 + {\lambda_n}^2\right]\cos(\lambda_n z/L)}{{\lambda_n}^2\left[H + H^2 + {\lambda_n}^2\right]} \exp\left(-\frac{\alpha_z {\lambda_n}^2 t}{L^2}\right)\right\} \tag{3.23}$$

where λ_n, $n = 1, 2, ..$ are the positive roots of $\lambda \tan(\lambda) = H$ and $H = hL/k_z$.
The solution in the radial direction is, instead ([133], §8.4):

$$T_r(r,t) = \frac{2h}{k_r R} \sum_{n=1}^{\infty} \frac{J_0(r\lambda_n)}{\left[(h/k_r)^2 + {\lambda_n}^2\right] J_0(\lambda_n R)} \exp\left(-\alpha_r {\lambda_n}^2 t\right) \tag{3.24}$$

where λ_n, $n = 1, 2, ..$ are the positive roots of $\lambda k_z J_1(\lambda R) = h J_0(\lambda R)$.
The global solution can then be computed in the same way of equation 3.16.

Given that the analytical solutions consist on a superposition of an infinite number of terms, they must be necessarily approximated by finite sums to be implemented in a digital model. For this reason, the equations were truncated at 25 eigenvalues, as a trade-off between accuracy and computational speed. Moreover, a discretization on the temporal and dimensional coordinates was applied, considering 100 points along the radial and axial domains and 600 points in time.

3.2.2. COMSOL Multiphysics simulation and comparison

A transient finite-element simulation was carried in COMSOL Multiphysics®, version 6.2 as comparison with the described models.
COMSOL Multiphysics® is a powerful simulation software environment capable of cou-

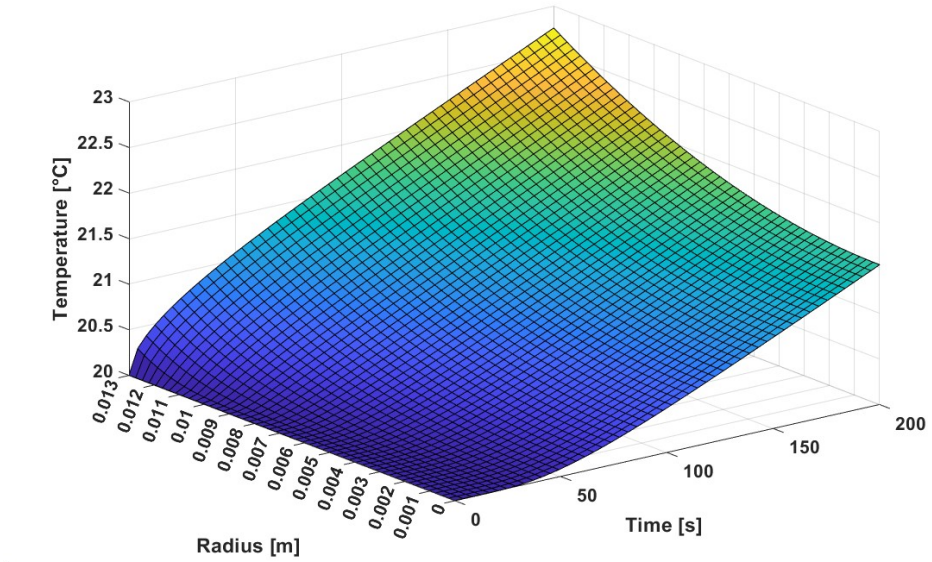

(a) Radial model

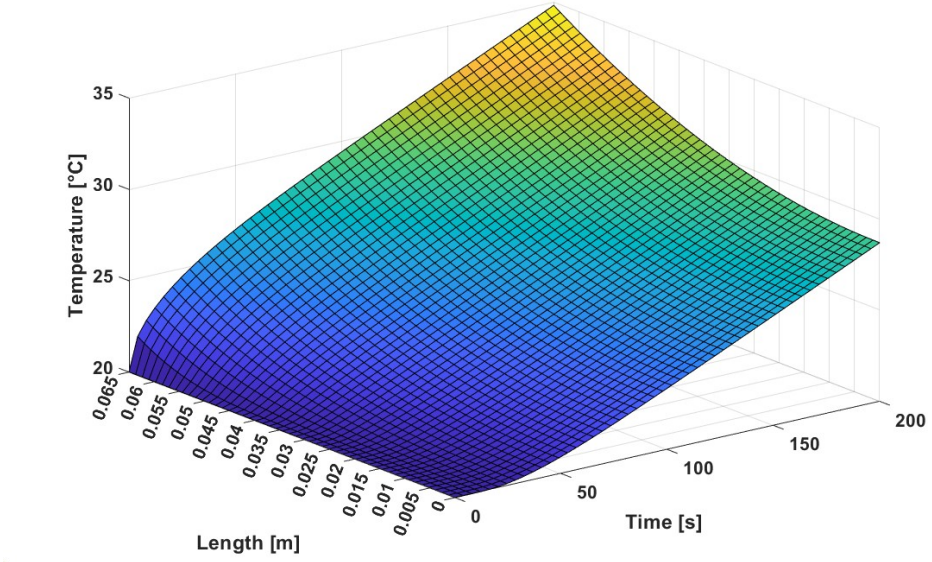

(b) Axial model

Figure 3.2: Surface representation of the evolution of temperature in the cylindrical volume from the analytical model, as a function of space and time

pling together numerous phenomena characterized by different underlying physical laws. This aspect enables the possibility to combine different physics in any three-dimensional geometry, avoiding simplifying assumptions which could lead to a loss of information or decrease the accuracy of the model.

For the comparison, the simulation was built only considering time-dependent heat trans-

fer phenomena and the same assumptions of the analytical models were imposed. In the same way, two geometries were defined, accounting for the radial and tab heaters, which were applied on the appropriate surfaces.

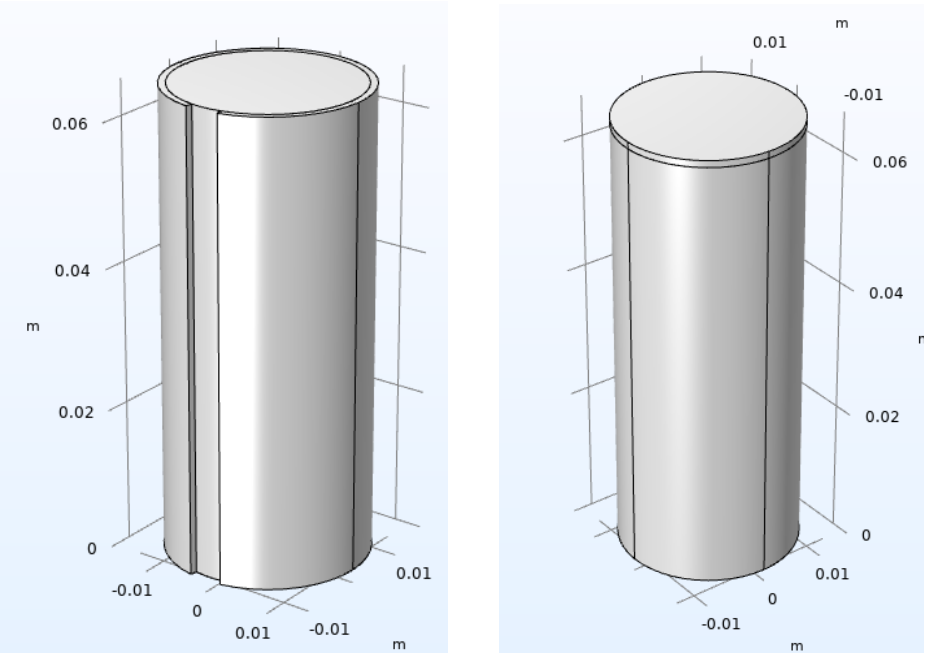

(a) Radial model (b) Axial model

Figure 3.3: 3D Geometries of the COMSOL Multiphysics simulation for the radial (a) and axial (b) heaters

An homogeneous heat generation rate per unit of volume was applied to the bulk of the heaters, while either adiabatic or convective boundary conditions were considered for the remaining surfaces. The materials and their properties for the simulation are listed in table 3.1.

Following the definition of the necessary parameters, a fine mesh of the geometry was created, after which the time-transient simulation was performed. As it can be seen from the final results (figure 3.4), a gradient is present in the temperature distribution along the longitudinal and radial coordinates for the tab and radial heaters respectively. This differentiation directly depends on the thermal conductivity of the body, as described in section 3.2.1, and decreases as the thermal conductivity increases.

Finally, a comparison between the results of the COMSOL simulation and the analytical models was carried and is available in figure 3.5. As it can be seen, the temperature curves are almost completely overlapping and there is excellent agreement between the models, both in the radial and axial heater cases. In fact, the maximum error between the curves

Material	Property	Radial heater	Axial heater
Aerogel (SiO2 based)	k_{iso} $[W\ m^{-1}K^{-1}]$	0.019	
	c_p $[J\ kg^{-1}K^{-1}]$	1100	
	ρ $[kg\ m^{-3}]$	100	
Silicon [solid;bulk]	k_{iso} $[W\ m^{-1}K^{-1}]$	"k_solid_bulk_1(T)"	
	c_p $[J\ kg^{-1}K^{-1}]$	"C_solid_1(T)"	
	ρ $[kg\ m^{-3}]$	"rho_solid_1(T)"	
Custom material	k_{iso} $[W\ m^{-1}K^{-1}]$	5	172
	c_p $[J\ kg^{-1}K^{-1}]$	897	
	ρ $[kg\ m^{-3}]$	2710	

Table 3.1: Materials' parameters definition for the COMSOL Multiphysics simulations. [k_{iso} represents the isotropic thermal conductivity; c_p represents the specific heat capacity; ρ represents the volumetric density]

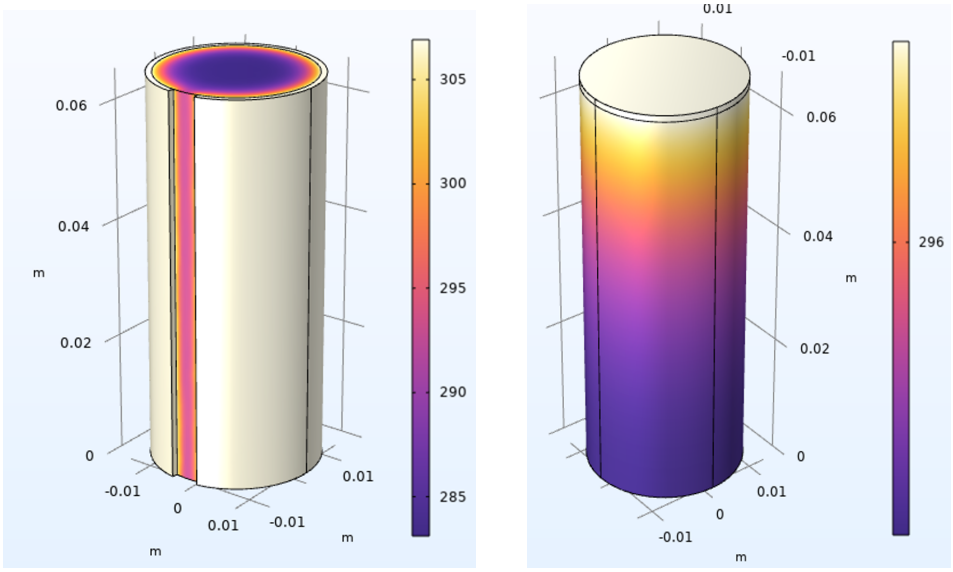

(a) Radial model (b) Axial model

Figure 3.4: Temperature results of the COMSOL Multiphysics simulations for the radial (a) and axial (b) heaters

was computed as 0.17% and 0.24%, for the radial and axial models, respectively.

However, the analytical models results were obtained in a much smaller time compared to the finite-element numerical simulation, due to the greater amount of domains to be solved. Moreover, the analytical models are much more useful for providing a fundamental understanding of the involved physical phenomena, directly correlating the thermal parameters to the temperature evolution inside the sample's volume; this is not possible for the numerical simulation [59].

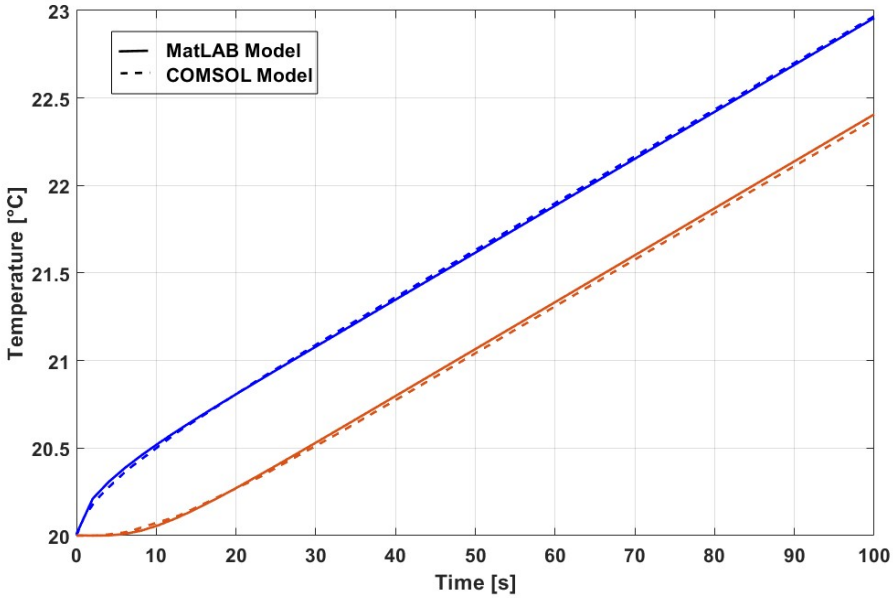

(a) Radial model at positions $r = 0, R$

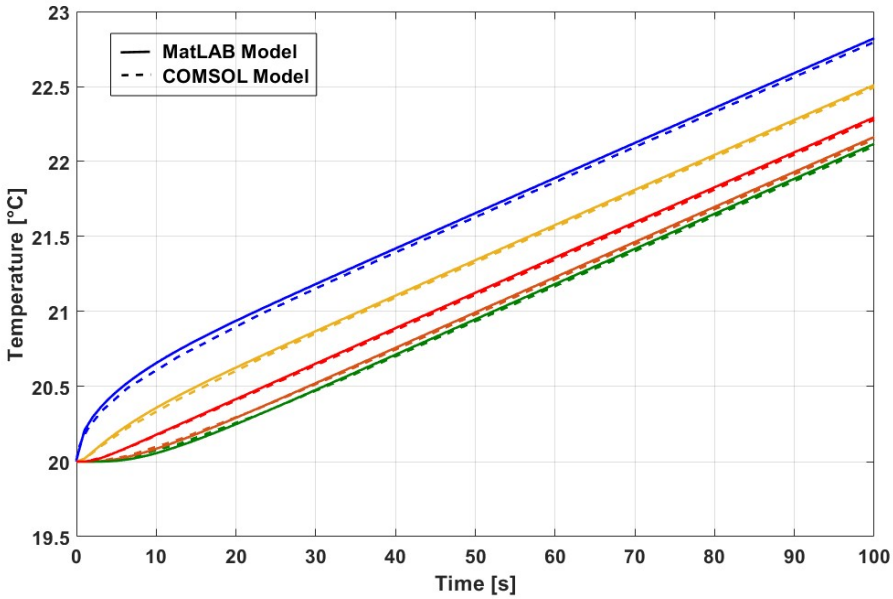

(b) Axial model at equi-spaced positions along the sample

Figure 3.5: Comparison between COMSOL Multiphysics simulations and analytical models for the radial (a) and axial (b) heaters. Different colored curves correspond to different positions

3.2.3. Simulacrum validation

The experimental methodology was validated on a real case through the utilization of a "simulacrum". In this context, this is an object of the same size and shape of the

samples and known properties, used to assess the method's feasibility and its limits. In the following sections, this denomination will be used. For this validation step, an aluminum alloy (Al 6082 T6) cylinder with the same dimensions of a 26650 cylindrical cell was employed, due to the fact that Al is one of the main components of LIBs, as described in section 1.2.
The properties of this alloy useful for the thermal tests are stated in table 3.2.

Property	Symbol	Value
Density $[kg\ m^{-3}]$	ρ	2710
Specific heat capacity $[J\ kg^{-1}K^{-1}]$	c_p	897
Thermal conductivity (isotropic) $[W\ m^{-1}K^{-1}]$	k	172

Table 3.2: Thermal properties of the simulacrum

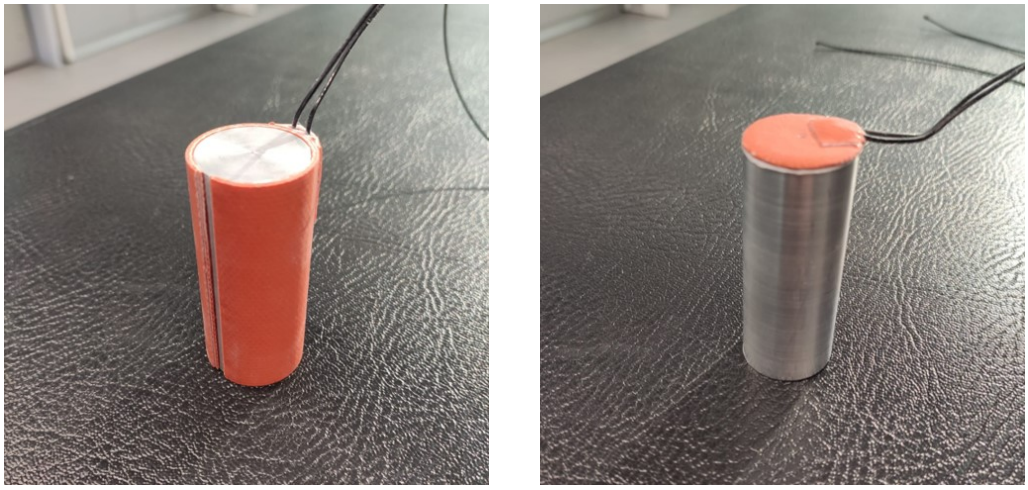

(a) Radial heater (b) Axial heater

Figure 3.6: Images of the cylindrical simulacrum with applied heaters for the radial (a) and axial (b) cases

As described in section 3.1 a trade-off must be found between the length of tests and the amount of provided thermal power. For this reason, several tests at different power levels were performed, measuring the duration of tests and the temperature reached at the end of the experiment. A power of 0.5 $[W]$ was chosen for the tests.
After obtaining the experimental data regarding temperature measurement and provided electrical power, these were used an inputs for the model, as well as the density of the simulacrum (which was not a fitting parameter and was estimated using the Archimedean principle model described in section 2.4.2) and the initial conditions of the test.

An example of the temperature measurements acquired during a test with axial heater is presented in figure 3.7. It is important to note some of the main features of this data:

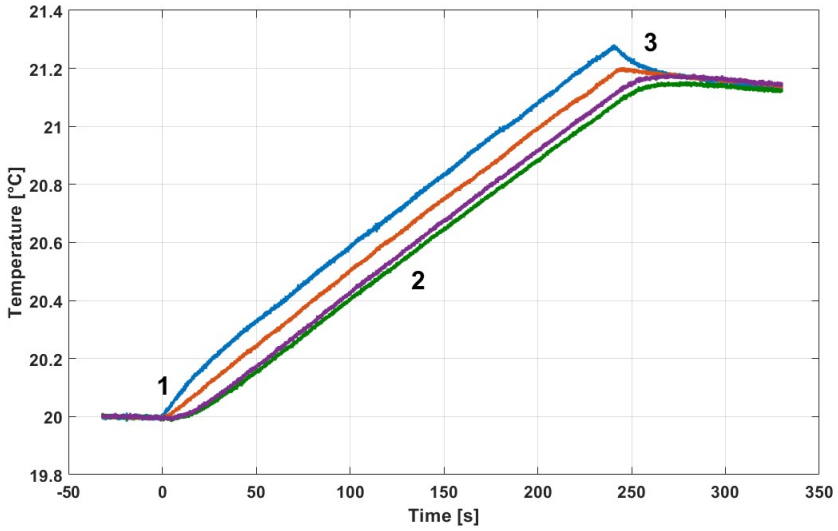

Figure 3.7: Example of axial thermal test FBGs temperature measurements on the simulacrum. Provided power: 0.5 [W]

- Beginning of test, point 1: after complete thermal equilibrium is reached, the heater is turned on and the time $t = 0$ is set; in this first period, the temperature curves associated with different sensors diverge from each others, reaching a differentiation after a certain time transient; the extent of the transient and the final difference directly depend on the value of thermal conductivity of the body.
- Asymptotic behavior, point 2: After the first time transient has ended, the temperature inside the body reaches an asymptotic trend, whose slope is directly dependent on the heat capacity of the material; in this period the temperature difference between sensors is kept constant and all trends are somewhat linear; if the temperature becomes too high, heat transfer towards the external environment becomes more important and a descending trend appears.
- End of test, point 3: after a pre-set time duration, the heater is set off and the temperature curves tend to get closer with time, finally reaching a complete homogenization; at this point the test is stopped. Also in this case, the duration of this time transient depends on the thermal properties of the body, but it is not considered in the fitting range.

Following the fitting process, the model curves are superimposed onto the experimental data and compared with the latter (figure 3.8). In the first seconds of the heating period, the temperature ramp is subjected to a certain delay with respect to the beginning of the model curves: this is related to the thermal inertia of the heater itself, leading to an

imperfect fitting for the initial data.
Other than this fact, it can be observed that the fitted curves are in very good agreement with the experimental data during the differentiation period and in the first part of the asymptotic section. If the duration of the test is extended too much, a divergence between the two sets of curves appears, related to heat losses towards the external environment; if losses are too high, the convective models can be considered, but an estimation of the heat transfer coefficient must be done.

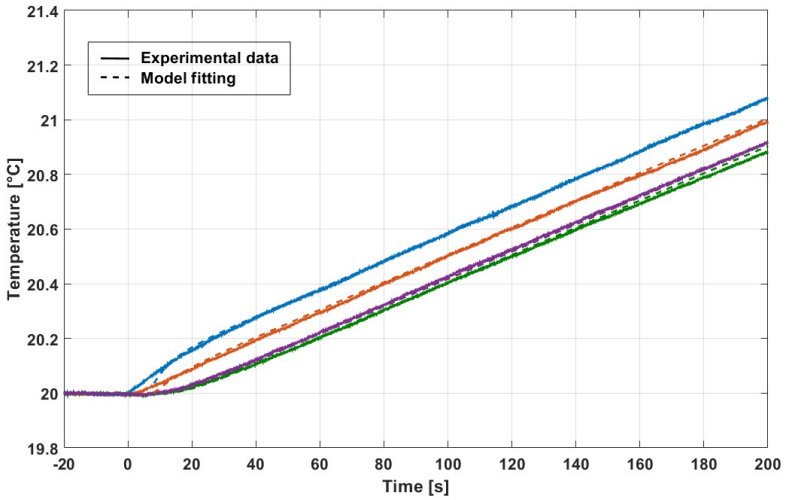

Figure 3.8: Data fitting between experimental and model curves on the simulacrum

The estimated parameters of figure 3.8 are stated in table 3.3.

Property	Fitted value	Real value	Error [%]
c_p $[J\ kg^{-1}K^{-1}]$	915.24	897	2.03
k_{iso} $[W\ m^{-1}K^{-1}]$	159.00	172	7.56

Table 3.3: Fitting results for the simulacrum experimental data

The fitted values are very close to the known thermal parameters of the aluminum alloy, particularly for the specific heat capacity, for which a 2.03% error is attained. On the other hand, an error of 7.56% is reached for the thermal conductivity. This could be considered too high for a robust parameters estimation method; however, it must be taken into account that the value of k_{iso} for the 6082 T6 is very high, leading to small temperature differences between sensors during the test and thus to a measured value more affected by uncertainty. To confirm this aspect, the curves corresponding to the real thermal parameters of the simulacrum were obtained from the model and overlaid to the same experimental data (figure 3.9).

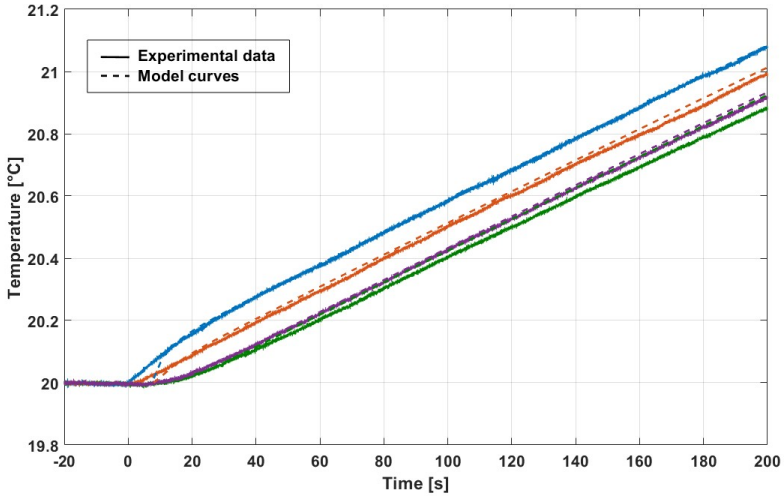

Figure 3.9: Analytical model curves using the correct thermal parameters of the simulacrum in table 3.2, compared to the previous experimental data

As it can be seen, the difference between curves is very small also in this case. In this regard, it can be stated that the analytical models are very sensitive to the thermal conductivity (as opposed to the specific heat capacity), leading to big variations from small temperature divergences.
However, as it can be understood from section 1.4.4, the actual values of thermal conductivity for real lithium-ion batteries are much lower than the one of the aluminum alloy of the simulacrum. For this reason, a higher accuracy of the models can be expected at such low values.

Afterwards, the characterization of the radial tests was done, employing the same aluminum simulacrum. A validation for this kind of tests was necessary for the subsequent experimental investigation on radial thermal parameters, described in section 3.3.4. Several experiments were done at the same power level of the axial tests, one of which is presented in figure 3.10.

The fitted estimation of the specific heat capacity obtained from this test was equal to 1055 $[J\ kg^{-1}K^{-1}]$, much higher than the actual value for the analyzed aluminum alloy. Consequently, the error was found to be equal to 17.6 [%]. A similar error was attained at all power inputs, but considered to be extremely high, especially compared to the one obtained from the axial test, where a value around 2 [%] was estimated. Consequently, it was regarded as a systematic error for the radial test methodology. As such, a calibration could be done.

The temperature curves visible in figure 3.11 were obtained from a radial and an axial

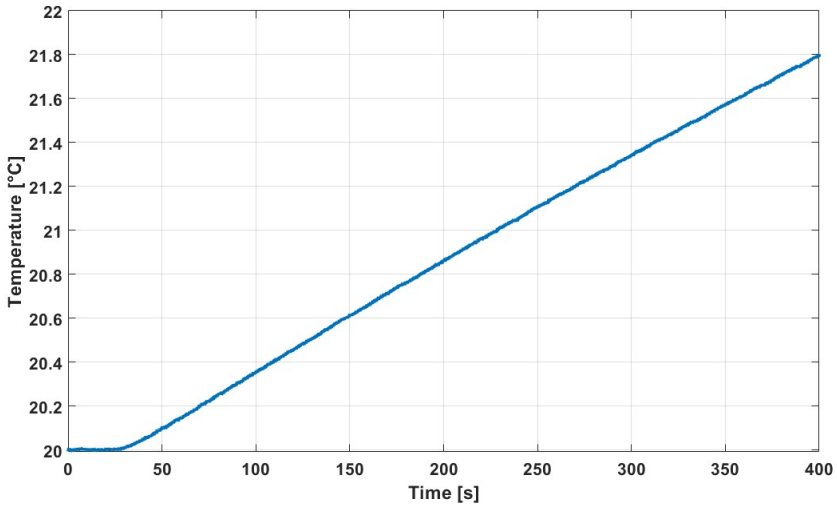

Figure 3.10: Example of radial thermal test FBGs temperature measurements on the simulacrum

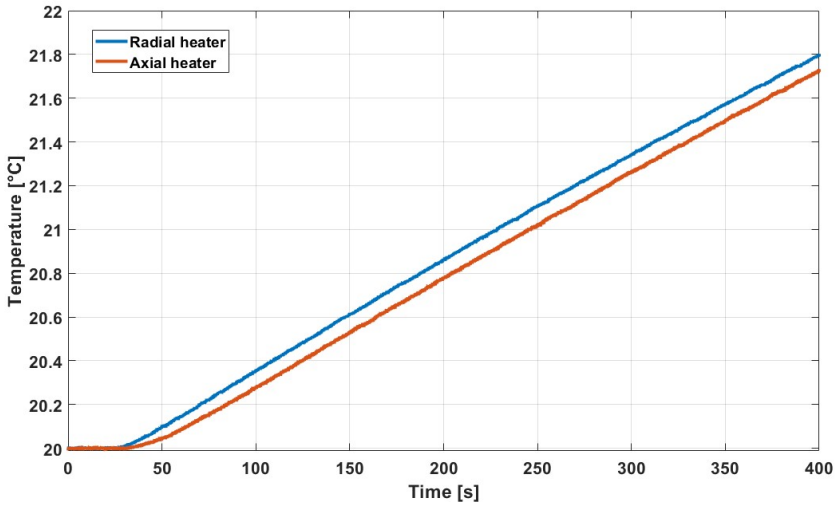

Figure 3.11: Comparison between radial and axial tests on the simulacrum, at different power levels

test at different average electrical power inputs (respectively of 0.4885 and 0.445 $[W]$, as measured by the power supply). It must be stressed that very similar slopes can be observed in the curves within the asymptotic behavior range: as explained previously, this region of the graph is strongly dependent on the specific heat capacity of the tested body, which in turn is directly proportional to the input thermal power. Given that the utilized simulacrum is the same for both tests, it is impossible to find the same temperature slopes for different power inputs, as the specific heat capacity must be consistent between

the two models. Moreover, the only differences between the two tests are related to the heater properties, due to the fact that this is the only component that changes. For these reasons, it could be hypothesized that the actual thermal flux entering within the bulk of the simulacrum is not the same as the electrical power given to the radial heater, generating a certain loss. In general, these inefficiencies could depend on several factors, such as the shape, mass or thermal properties of the silicon rubber heater, other than the different contact resistance between it and the tested body.
Consequently, a sensibility analysis was done on the analytical models, the aim of which was the assessment of the power input error of the radial heater. In this regard, it was chosen to allocate the entire error obtained from the radial test to the inefficiencies of the corresponding heater, by the introduction of a correction factor, defined as the ratio between the power inputs of the axial and radial tests, respectively (equation 3.25).

$$\xi = \frac{W_{ax}}{W_{rad}} \tag{3.25}$$

This value was found to be equal to about 0.911, which was used also for the subsequent estimation of the thermal parameters of lithium batteries.

3.3. Characterization of LIB samples

The experimental methodology and analytical models defined and validated in the previous sections were used for the thermal characterization of the cylindrical LFP lithium-ion batteries samples described in section 2.1.
In this section, only the "M1B" battery types will be considered and described thoroughly, due to the fact that only for this specific sample, cells at different aging states were available. The electrochemical and thermal description of two "M1A" cells is presented in appendix A.
Several cells were used during the experimental campaign, mainly differentiated by the available capacity and aging degree, through the SoH parameter defined in section 1.5.1. Most of the samples were taken at beginning of life (BOL) conditions and were considered as equivalent throughout the experimental campaign. The other cells, characterized by different aging levels or degradation phenomena, were separated from the first class and tested singularly. In this regard, four M1B cells were subjected to a calendar aging campaign.

In the following sections, the description of the experimental campaign and the main results will be presented: an electrochemical characterization of the battery samples

was carried prior to the thermal parameters experimental campaign. Moreover, a new methodology for the drilling of cylindrical cells and the insertion of internal sensors will be presented, aimed at the description of the radial thermal behavior of batteries.

3.3.1. Electrochemical characterization

Before the thermal characterization, an electrochemical diagnostic campaign was performed, primarily for the assessment of the integrity of cells and their residual capacity. In this regard, the methodologies described in section 2.3 were employed; in particular, EIS analysis at $SoC = 0$ and $SoC = 100$ were executed, other than discharge tests at different current rates. In this regard, discharge processes were done at the nominal C-rate $= 1\,[h^{-1}]$ and, to better characterize the thermodynamic behavior of the samples, at quasi equilibrium conditions at C-rate $= 0.04\,[h^{-1}]$. All of the tests were performed maintaining the temperature at 25 $[°C]$, through the Binder MKF 720 climatic chamber, described in section 2.2.1.

Beginning of life samples

The beginning of life samples are characterized by the parameters described in section 2.1. Many cells were usable at the same conditions and were considered equal from the point of view of available charge and overall performance.
Figure 3.12 shows a discharge test in quasi-equilibrium conditions, with a C-rate $= 0.04\,[h^{-1}]$ and a duration of around $25\,[h]$, which was performed to precisely evaluate the residual capacity of the batteries.

As it can be seen, all of the discharge curves follow the same trend and are characterized by a final available capacity in the neighborhood of $2500\,[mAh]$.
Analogously, the same BOL cells were analyzed through a discharge test at C-rate $= 1\,[h^{-1}]$, using the nominal condition from the manufacturer.

It can be observed that, also in this case, the total available capacity is pretty much the same for each sample, confirming the assumption of equal behavior among beginning of life cells.
Moreover, as it can be noticed, the shape of the curve is slightly different from the previous one, due to the fact that in equilibrium conditions the open circuit voltage describes closely the phase changes and thermodynamic behavior of batteries (section 1.1.2), while for a higher current rate some of the features of the voltage curve are less visible. Additionally, the total charge throughput is somewhat lower than the one obtained from the discharge

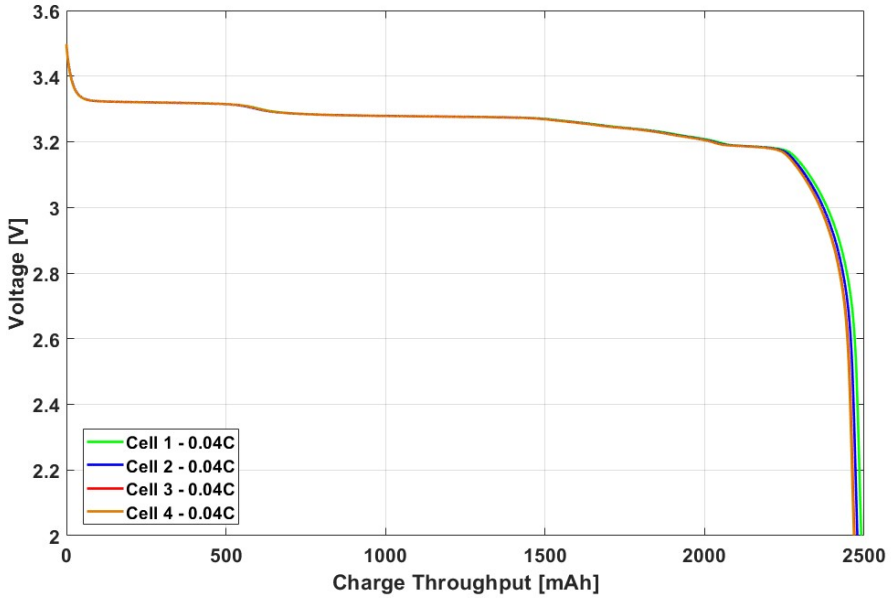

Figure 3.12: Discharge tests at 0.04C for M1B samples at BOL conditions

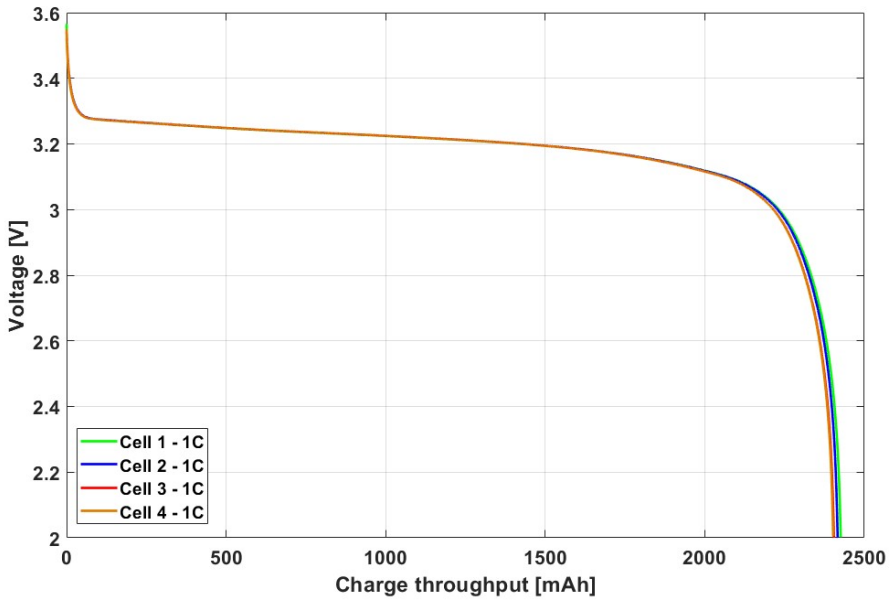

Figure 3.13: Discharge tests at 1C for M1B samples at BOL conditions

tests at 0.04C. This is because, due to overpotentials arising during operation, a reduced voltage is obtained for higher current rates and the lower voltage limit is reached earlier (figure 3.14).

Furthermore, from the manipulation of discharge curves at $0.04C$ it was possible to extrapolate DV and IC curves (figure 3.15 and figure 3.16, respectively)

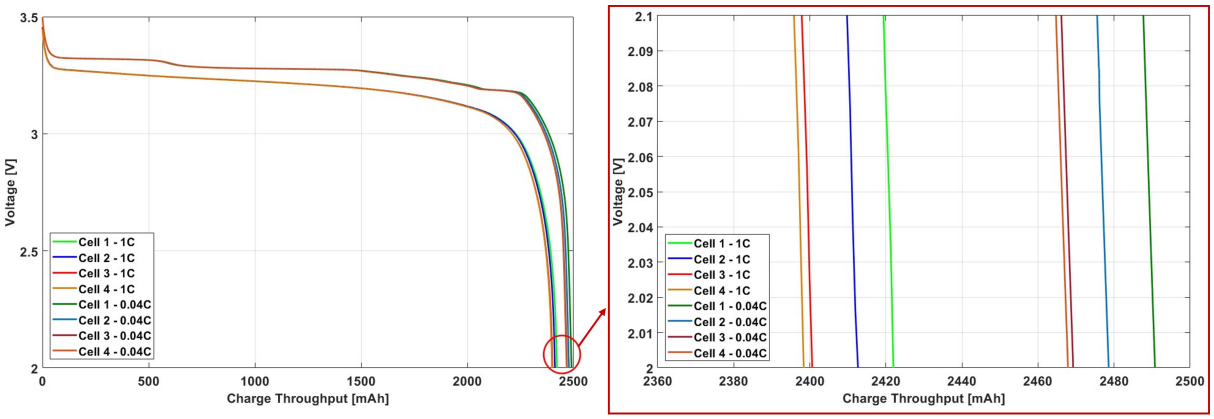

Figure 3.14: Comparison between discharge tests at 1C and 0.04C for M1B samples at BOL conditions

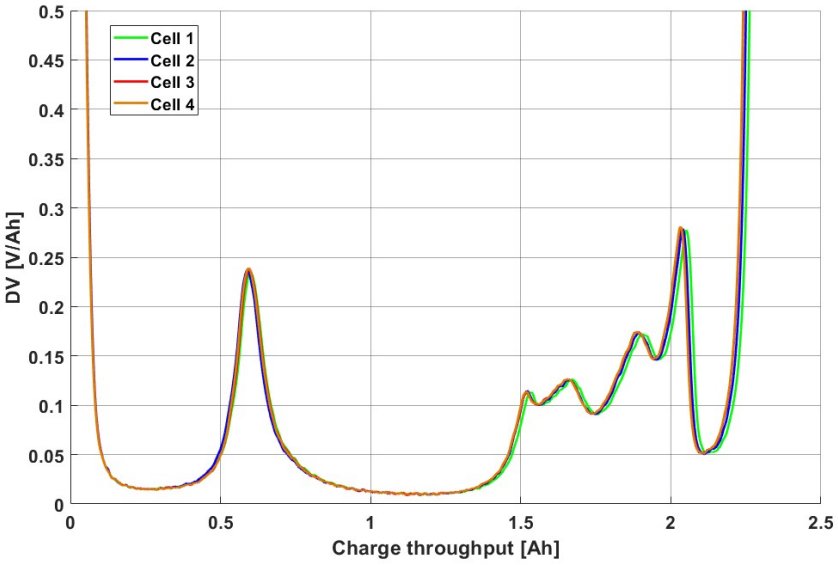

Figure 3.15: DV curves obtained from a discharge at 0.04C for M1B samples at BOL conditions

As described in section 2.3.2, by highlighting the slope variations of the open circuit voltage trend, these curves are very useful in the characterization of features directly related to electrodes behavior. In first instance, it can be further confirmed that the tested cells all present the same behavior, with minimal differences. Secondly, several peaks can be seen in both DV and IC curves, corresponding to the features described in section 2.3.2 for the samples.
In particular, the most representative feature of the graphite negative electrode is represented by the first peak in the DV curve, which corresponds to the first step change visible in figure 3.12, at around 500 $[mAh]$.

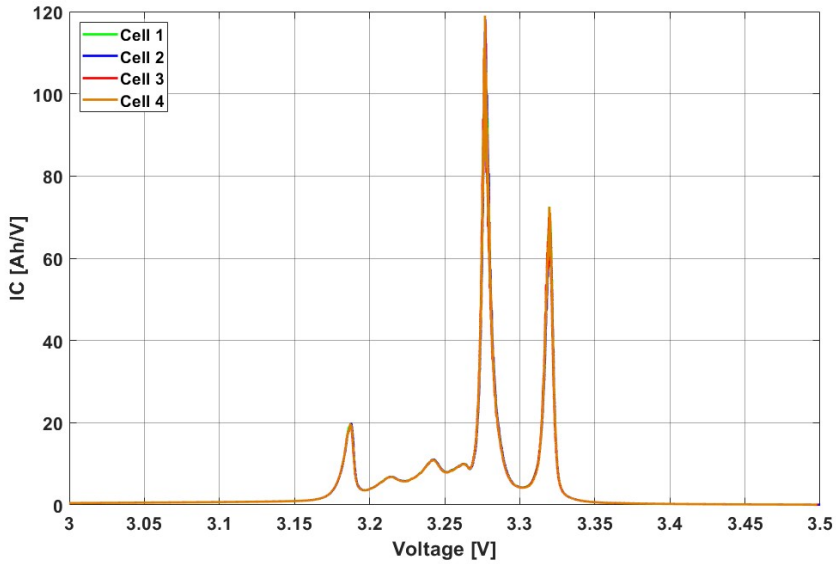

Figure 3.16: IC curves obtained from a discharge at 0.04C for M1B samples at BOL conditions

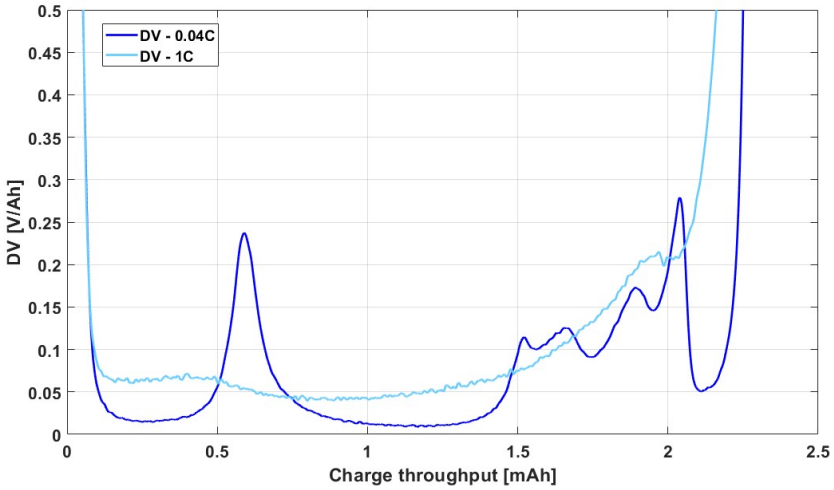

Figure 3.17: Comparison between DV curves obtained from discharge tests at 1C and 0.04C for M1B samples at BOL conditions

In figure 3.17, the comparison between DV curves obtained at 1C and 0.04C can be seen. It can be easily understood that tests done at higher C-rates, and thus that are not in quasi-equilibrium conditions, don't provide much information about the thermodynamics of the cell. In fact, it can be noticed that the DV curve obtained at 1C is characterized by an almost homogeneous trend on the graph, such that the peaks corresponding to specific thermodynamic features are spread over the whole curve. For this reason, only DV curves

obtained at equilibrium conditions were used during this thesis.

In addition, a charge test was performed at quasi-static conditions on a M1B sample at BOL conditions. In particular, a test at $C - rate = 0.04\ [h^{-1}]$ was done, recording the voltage (figure 3.18).

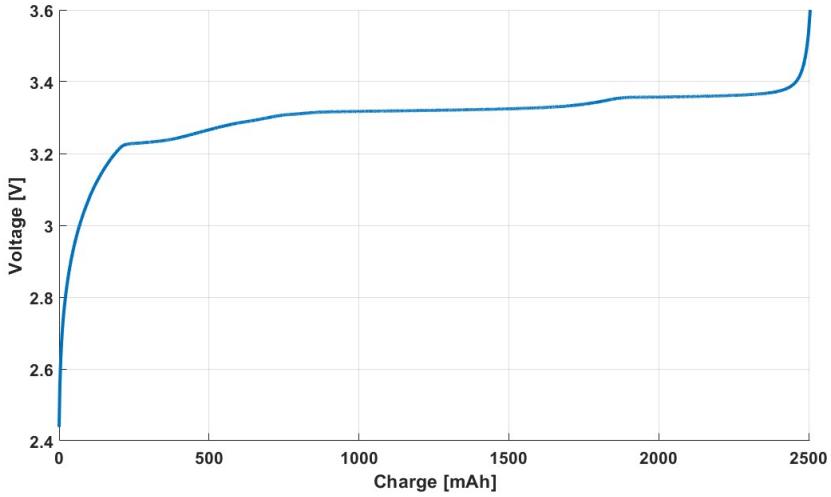

Figure 3.18: Charge test at 0.04C for M1B samples at BOL conditions

Consequently, the curve was flipped and compared to the analogous discharge test at 0.04C (figure 3.19).

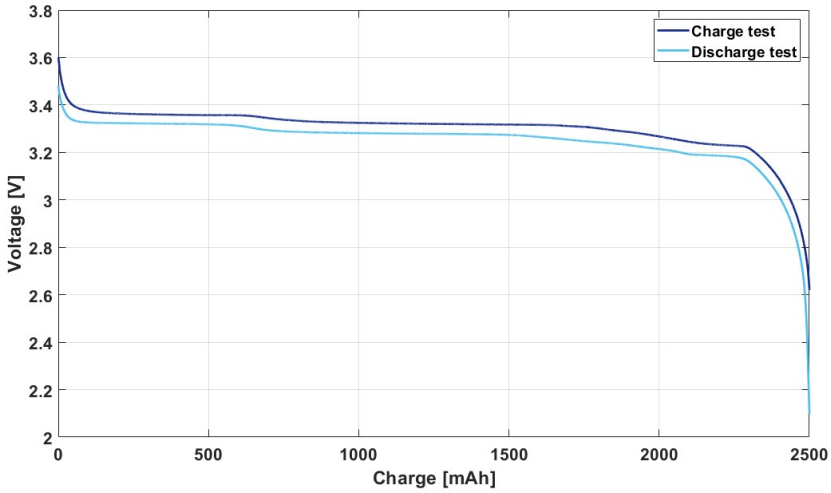

Figure 3.19: Comparison between charge and discharge tests at 0.04C obtained from M1B samples at BOL conditions

It can be seen that, even at such low C-rates, a certain hysteresis is experienced by the cell: in fact, the charge test voltage curve is always characterized by a higher voltage

compared to the discharge curve at the same charge throughput; this phenomenon is more important for LFP cathodes, due to their intrinsic structure [134]. In this regard, the real equilibrium voltage lies theoretically between these two curves, but it is practically very difficult to characterized, if not for long-lasting tests. For this reason, an approximation is accepted.

Additionally, EIS tests were performed as diagnostic analyses of the cells to assess the importance of different phenomena (and their associated impedance) at different frequencies. In particular, an EIS analysis both at $SoC = 0$ and $SoC = 1$ was executed for each cell, due to the fact that at extreme SoC different features can be observed. The operating parameters were equally set for all tests and are stated in table 3.4. The frequencies were selected using a logarithmic scale between the maximum and minimum frequency.

Parameter	Symbol	Value
N° of frequencies	N_f $[-]$	30
Maximum frequency	f_{max} $[Hz]$	10000
Minimum frequency	f_{min} $[Hz]$	0.1
Semi-amplitude	I_0 $[A]$	0.5
N° of cycles	N_c $[-]$	3

Table 3.4: Parameters for the EIS analyses

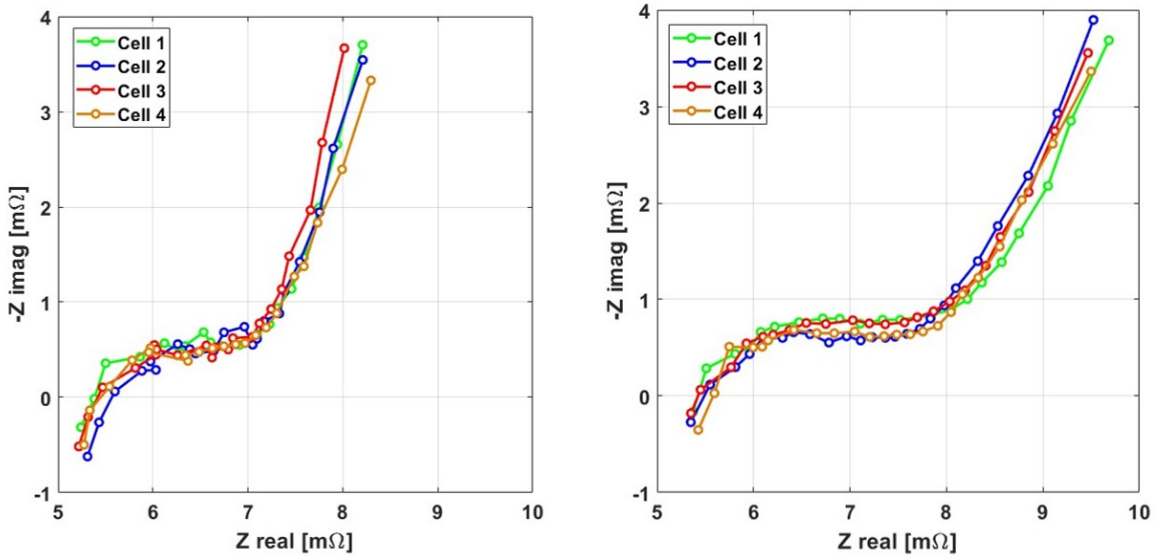

(a) EIS at SoC = 1 (b) EIS at SoC = 0

Figure 3.20: EIS spectra results for M1B samples at SoC = 1 (a) and SoC = 0 (b) at BOL conditions

In figure 3.20, the EIS of the same cells of the discharge tests were executed. It can

be noted that, also in this case, the trend is the same throughout all of the frequency spectrum.
All of the cells present an high frequency resistance (HFR) corresponding to around 5.5 $[m\Omega]$, which is equal at both states of charge. At $SoC = 1$ the spectrum is characterized by a small charge-transfer and kinetic resistance, as depicted from the corresponding semi-circle. Moreover, the diffusion resistance is and represented by a steep linear behavior.
At $SoC = 0$, instead, a bigger radius of the kinetic semi-circle is found, suggesting a greater impedance related to the phenomena at these frequencies. Additionally, the linear behavior related to the diffusion resistance is characterized by a less marked slope, leading to a higher impedance.
A comparison between the two sets of curves is available in figure 3.21, where spectra at the same state of charge are depicted with the same color.

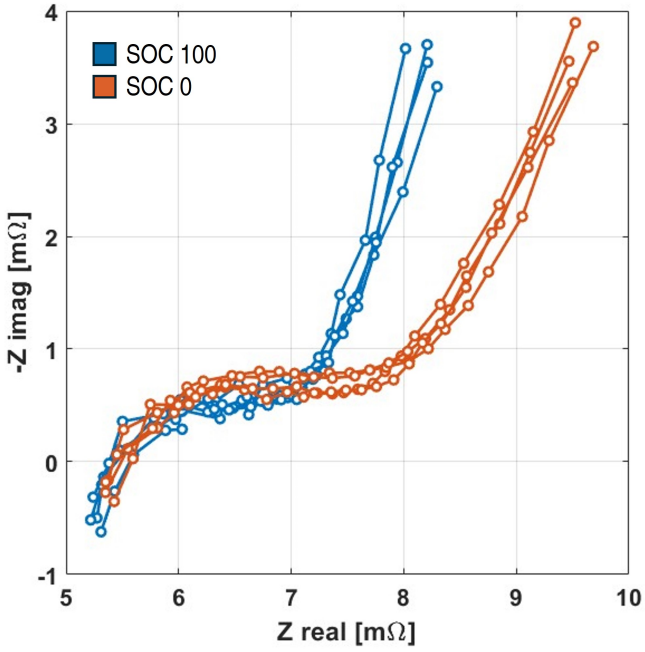

Figure 3.21: Comparison between EIS spectra results for M1B samples at SoC = 0 and SoC = 1 at BOL conditions

Aged sample

As described in section 1.6, one of the main goal of this thesis lies in the assessment of the effects of degradation on the thermal parameters of lithium-ion batteries. However, as mentioned in section 1.5.2, very little information exists in literature about these aspects.

Moreover, at the start of this work, no "M1B" samples were available at conditions different from BOL.
For these reasons, a calendar aging campaign was carried during the period of this work on four M1B cells at different SoC. The samples were left in a climatic chamber for five months, between September 2024 to January 2025, at 60 $[°C]$. The storage conditions are expressed in table 3.5.

Sample	**SoC** $[\%]$	**Temperature** $[°C]$
Cell 1	10	60
Cell 2	50	
Cell 3	80	
Cell 4	100	

Table 3.5: Calendar aging campaign storage conditions

As described in section 1.5.1, calendar aging of LIBs is strongly favored at high temperatures and SoCs, because at these conditions degradation side reactions, such as SEI and CEI formation, are benefited. Due to this aspect, the "Cell 4" sample in table 3.5 was expected to lose the highest capacity among the four cells in the experimental campaign. This was later confirmed from the capacity tests performed after the calendar aging period: as it can be seen in figures 3.22 and 3.23, all four samples lost an appreciable amount of capacity during the period at high temperature and the voltage curves were subjected to a shift towards the left of the graph; moreover, it can be noted that the discharge curves strictly follow the order of SoC conditions during the storage period.

A comparison between discharge tests operated at 0.04C for cells at different aging states is available in figure 3.24.

The residual capacities of the aged samples were computed from the discharge tests at C-rate $= 0.04\,[h^{-1}]$ and are stated in table 3.6 (approximated at the closest integer). Subsequently, the SoH was calculated using the expression defined in section 1.5.1.

Sample	$\mathbf{Q_{residual}}$ $[mAh]$	**SoH** $[\%]$
Cell 1	2353	94.12
Cell 2	2164	86.56
Cell 3	2139	85.56
Cell 4	2071	82.84

Table 3.6: Residual capacity and SoH of M1B samples after the calendar aging campaign

It can be noticed that, also in this case, the values of SoH for the samples follow the order of the different states of charge at which they were stored. Moreover, during this brief

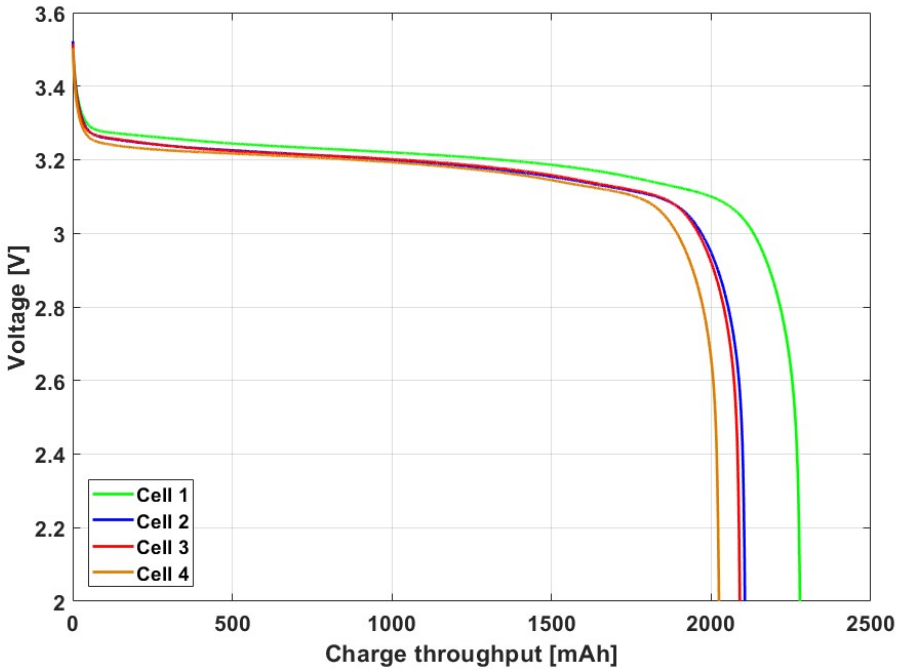

Figure 3.22: Discharge tests at 1C for M1B samples after calendar aging campaign

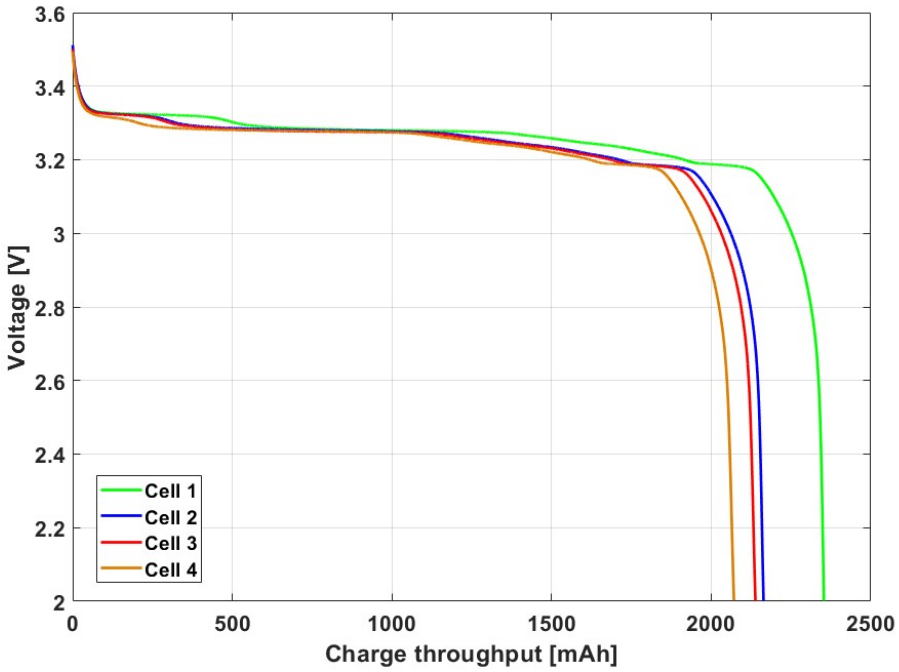

Figure 3.23: Discharge tests at 0.04C for M1B samples after calendar aging campaign

period, "Cell 4" reached an approximated capacity loss of almost 20%, demonstrating the great importance that temperature holds on the operation of batteries. In addition, this

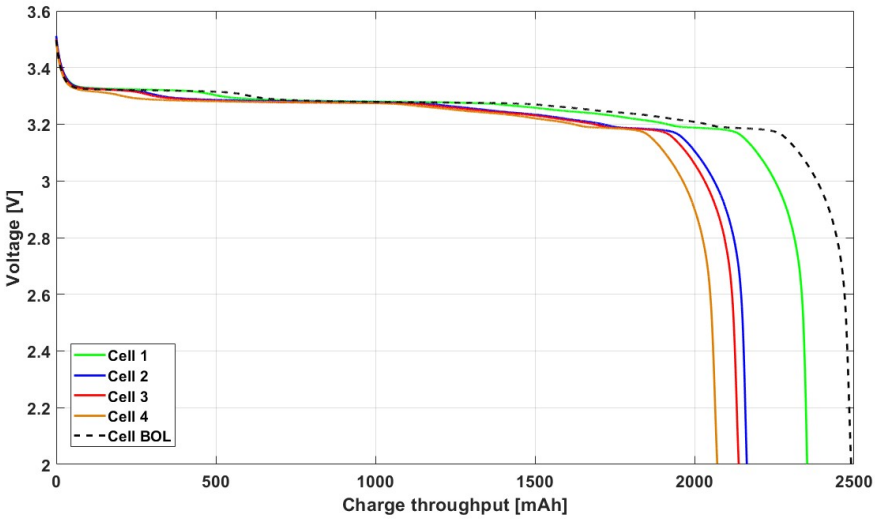

Figure 3.24: Comparison between discharge tests at 0.04C for M1B samples at BOL and aged conditions

level of degradation is crucial for automotive applications, as it indicates the substitution mark for batteries.
Furthermore, also in the case of aged cells, the DV and IC curves were obtained from the discharge curves (figure 3.25 and figure 3.27, respectively). A clear shift of the graphite peak towards lower exchanged charge values can be observed in the DV graph.

It is very interesting to note that the main difference between the two sets of samples lies in the first peak present in the DV curves: a relative shift of this feature with respect to the BOL conditions can be clearly seen in the graph.
As described in a previous thesis [22], this is one of the main features that represent aging and SEI formation at the graphite anode. The peak gradually shifts as the SoH decreases (so it is directly correlated with the amount of capacity loss), while the other peaks at lower SOC shift of the same amount. In fact, as already mentioned in section 1.5.1, calendar aging is mostly caused by the formation of passivation layers at the electrodes-electrolyte interfaces, namely SEI and CEI, which consume cyclable lithium and thus decreases the total available capacity.
In this regard, the peak shift symbolizes that the main degradation phenomena from calendar aging are more important at the negative electrode, as the graphite is highly reactive with the electrolyte compounds: during charge, the cell is not able anymore to reach a lithiation level at the anode as the beginning of life condition, due to the experienced LLI. This aspect then causes the discharge curve to shift to lower discharged capacity. The value related to this degradation mode was computed using the thermodynamic model

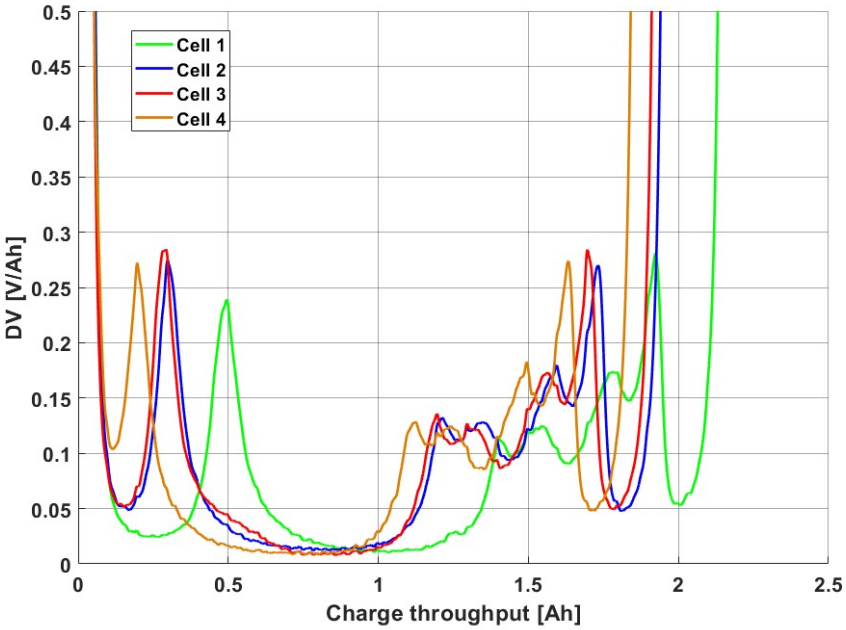

Figure 3.25: DV curves obtained from a discharge at 0.04C for M1B samples after calendar aging campaign

presented in a previous thesis work at the same laboratory [22], and estimated to be around 17.5 [%]. The results of the model estimation can be seen in figure 3.26.

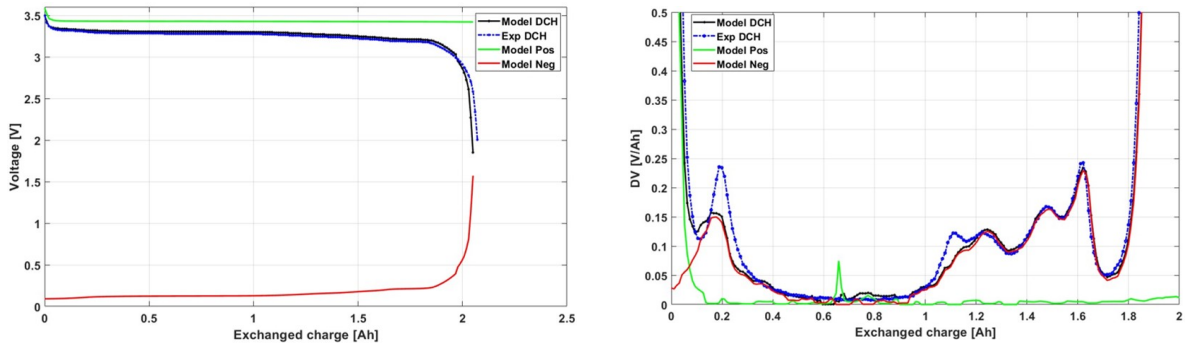

(a) Voltage curves (b) DV curves

Figure 3.26: Voltage and DV curves results of the estimation of LLI for the most degraded cell from the calendar aging campaign

This assessment is in accordance with the assumption that calendar aging is caused mainly by the formation of interphases, which consume lithium but not degrade the active material sites.

The same aspect can be highlighted in the IC curve, particularly at the peak between

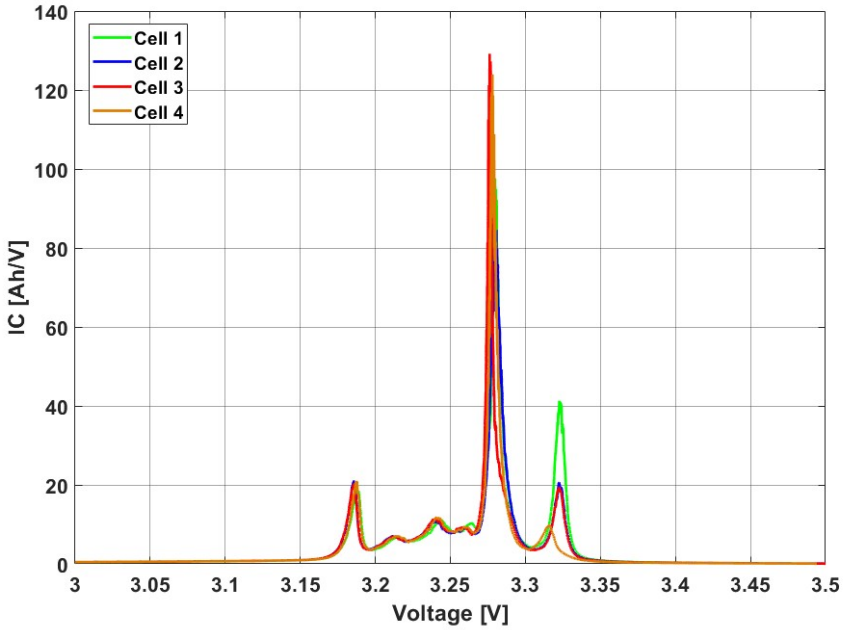

Figure 3.27: IC curves obtained from a discharge at 0.04C for M1B samples after calendar aging campaign

3.3 and 3.35 V: a lower peak means that the first plateau in the discharge curve shrinks gradually with the aging advancement.

Moreover, to better understand the extent of the shift of the first peak, the DV curves of the aged cells were compared with the ones of cells at BOL conditions (figure 3.28). Also in this case, the same argument holds true, as the shift of the graphite peak is even more visible.
If the same DV curves were artificially paired at the end of the discharge tests (figure 3.29), it can be plainly seen that the peaks in the curves, corresponding to different thermodynamics states in the equilibrium curves, remain practically unchanged. This condition corresponds to pairing the equilibrium states for which the graphite anode is the least lithiated. Then, the only difference that can be assessed is observed in the region at very low charge throughput, at the beginning of the discharge tests, meaning that only a portion of the initial capacity can be exploited in aged cells.

Finally EIS tests were carried at extreme SoC values and compared with BOL results (figure 3.30). The same features described for the cells at beginning of life can be observed in aged cells.
However, it can be noticed that a clear increase of the HFR appears at the aging increases.

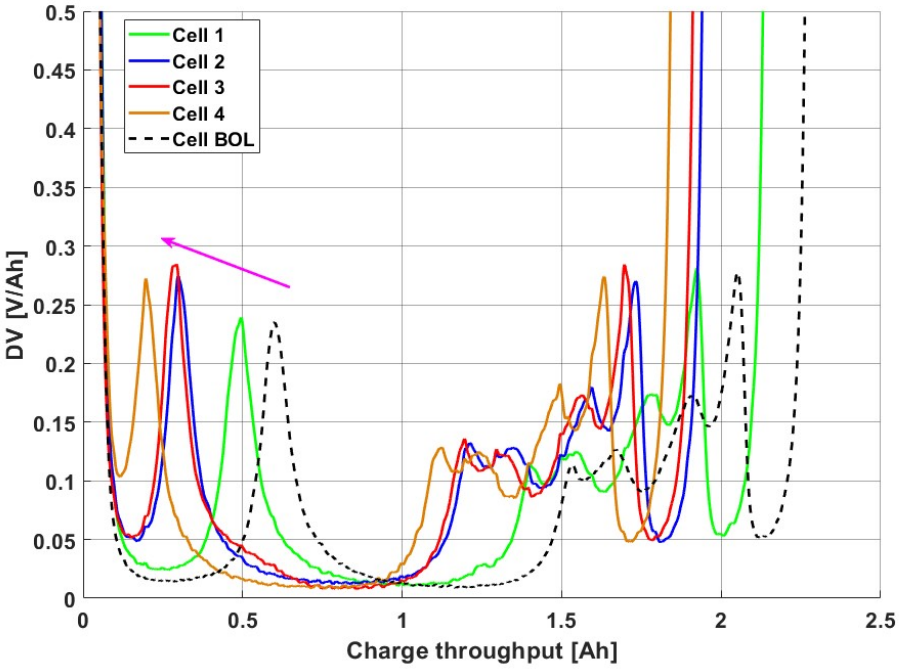

Figure 3.28: Comparison between DV curves of M1B samples at BOL and aged conditions, obtained from discharge tests at 0.04C

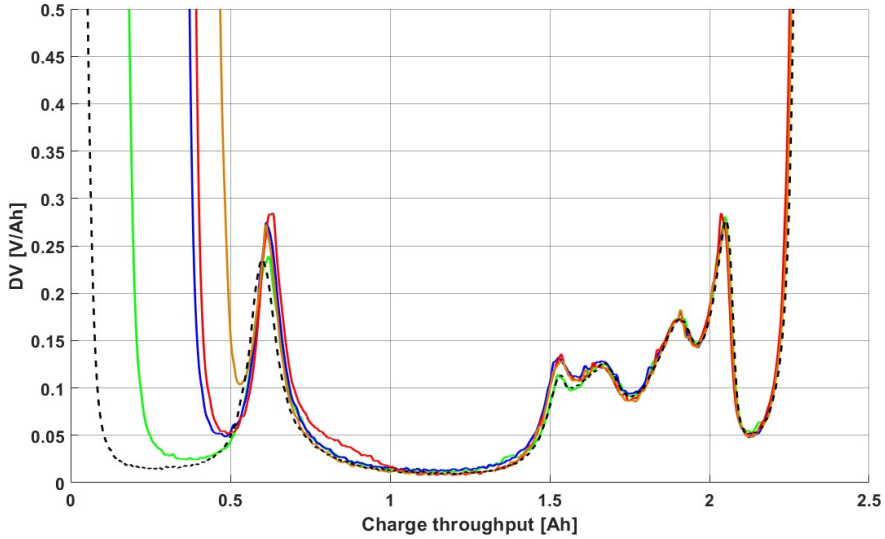

Figure 3.29: Comparison between DV curves of M1B samples at BOL and aged conditions, paired at the end of the test

This is strongly related to the formation of SEI, which consumes lithium ions and acts as an electrical barrier between electrodes, causing an increased ohmic resistance. The kinetic semi-circles visible in the spectra, instead can be regarded as very similar, as well

as the diffusive behavior observed at the lowest frequencies. Of course, the HFR remains constant also for the EIS spectra at $SoC = 0$, while the charge transfer resistance increases considerably, as described also for the BOL case.

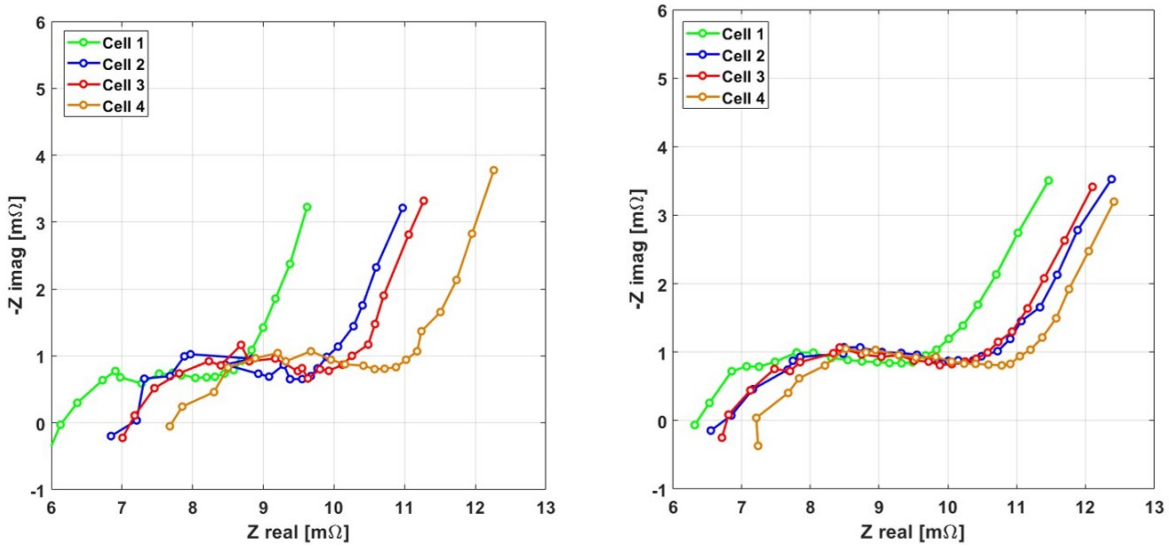

(a) EIS at SoC = 1 (b) EIS at SoC = 0

Figure 3.30: EIS spectra results for M1B samples at SoC = 1 (a) and SoC = 0 (b) after calendar aging campaign

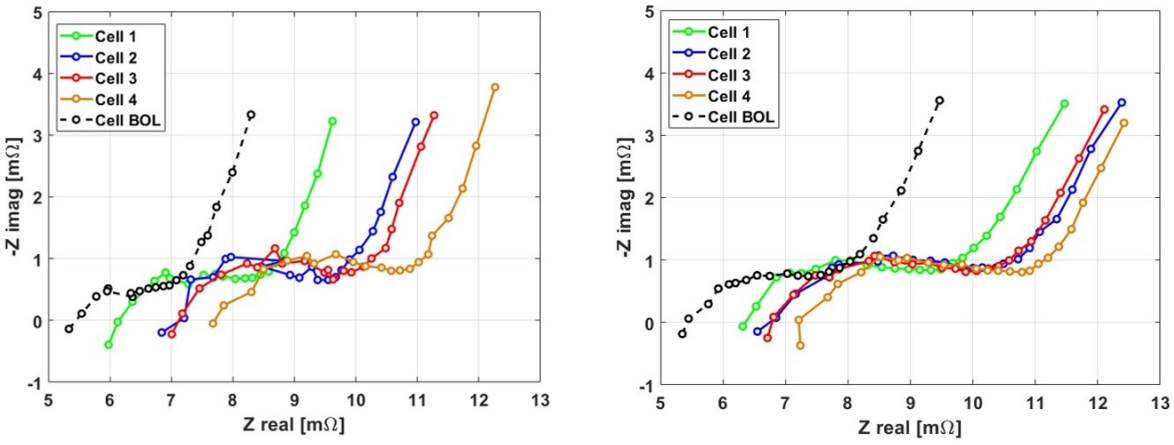

(a) EIS at SoC = 1 (b) EIS at SoC = 0

Figure 3.31: Comparison between EIS spectra results for M1B samples at BOL and calendar conditions, at SoC = 1 (a) and SoC = 0 (b)

When comparing the aged cells with the ones at beginning of life conditions (figure 3.31), it can be seen that the high frequency resistance is directly correlated with the amount of lost capacity, which in turn depends on the thickness of the formed SEI layer. Additionally,

a slight increase in the radius of the kinetic domain can be observed, suggesting also in this case a dependency of the charge transfer resistance with the SEI.

3.3.2. Axial thermal tests

Subsequently to the assessment of the electrochemical properties of the samples through the characterization described in the above sections, the cells were prepared for the first thermal tests. Batteries at beginning of life conditions were discharged at different states of charge separated by 10%, ranging between $SoC = 0$ and $SoC = 1$.
Following the methodology described in section 3.1 for the axial tests, a tab heater was applied at the negative pole of the sample, fixed through a two-sided adhesive tape. Consequently, the FBG temperature sensors were attached on the cell surfaces at multiple positions and the whole assembly was covered with the aerogel insulation material and placed in the climatic chamber. After achieving complete thermal equilibrium, a certain electrical power was applied to the heater and the temperatures in different positions were measured.

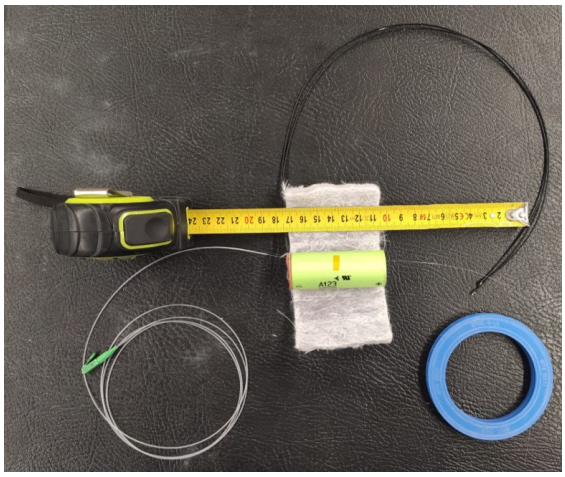

(a) Fiber positioning

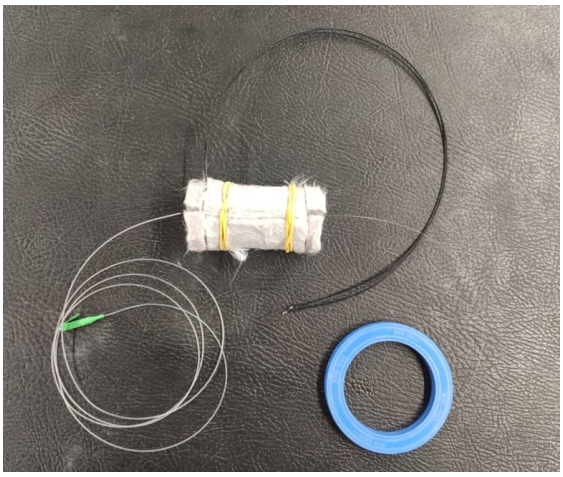

(b) Closed envelope

Figure 3.32: Images of the axial test assembly before being inserted in the climatic chamber

For the thermal tests, an input power of 0.5 $[W]$ was employed, following the compromise between heat introduction and heat transfer losses described in section 3.1.
An example of an axial thermal test is available in figure 3.33. As it can be seen, the temperature measurement between sensors differs during the test, as a consequence of thermal parameters. A first differentiation appears in the beginning stages of the tests

until a certain point in time, where temperature curves reach a seemingly linear asymptotic behavior, confirming the trends described previously for the simulacrum (section 3.2.3). After a temperature difference of 2.5 $[°C]$ with respect to the beginning of the test is reached, the heater is shut off and temperature differences tend to cancel out during a final time transient. Afterwards, the test is stopped.

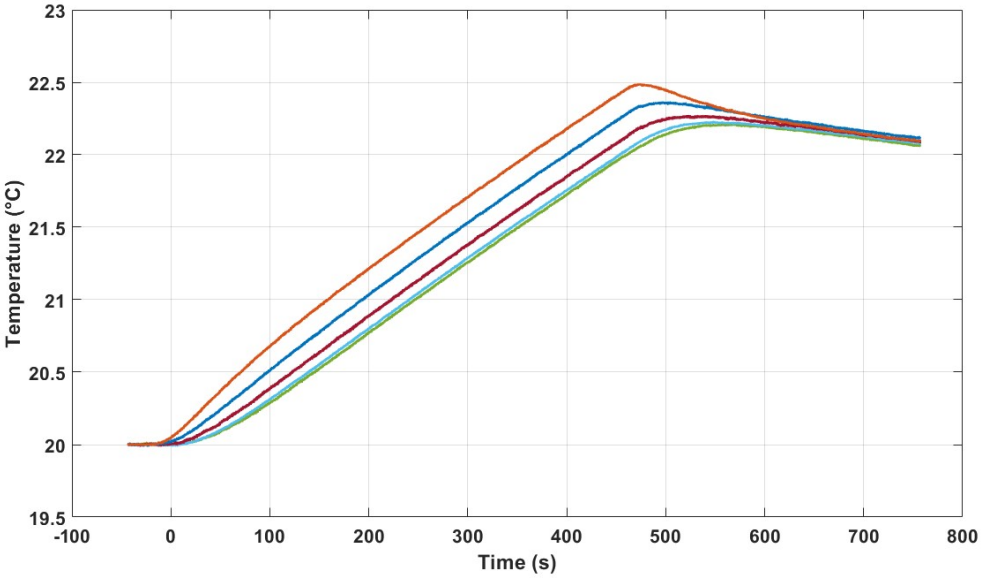

Figure 3.33: Example of axial thermal test FBGs temperature measurements

After the experimental test has finished, data regarding temperature measurements and input electrical power are saved in digital files and imported in the MATLAB® environment. Furthermore, useful parameters of the test, such as density (estimated experimentally through the Archimedean test, as described in section 2.4.2), initial condition and sensors positions are inserted in the model. Finally, temperature curves are fitted with the model through the function "*lsqcurvefit*" in the stated positions. The two sets of curves are then overlaid together for comparison and analyzed (figure 3.34). The comparison is needed to assess similarities between experimental data and model and guarantee the correctness of the fitted parameters. In first instance, it can be noticed that in this case, the delay related to the heater thermal inertia in the first seconds of the test is very limited, due to the higher heat capacity of the cells, compared to the simulacrum. However, it can be observed that the curve fitting in the first period is not perfectly aligned with the experimental data: this could be attributed to the fact that lithium-ion battery cells are not ideal homogeneous cylinders and, due to internal components differences, could experience an unusual initial transient. The asymptotic region, instead, is clearly visible and the differentiation is respected throughout this period, similarly to the simulacrum

(section 3.2.3).

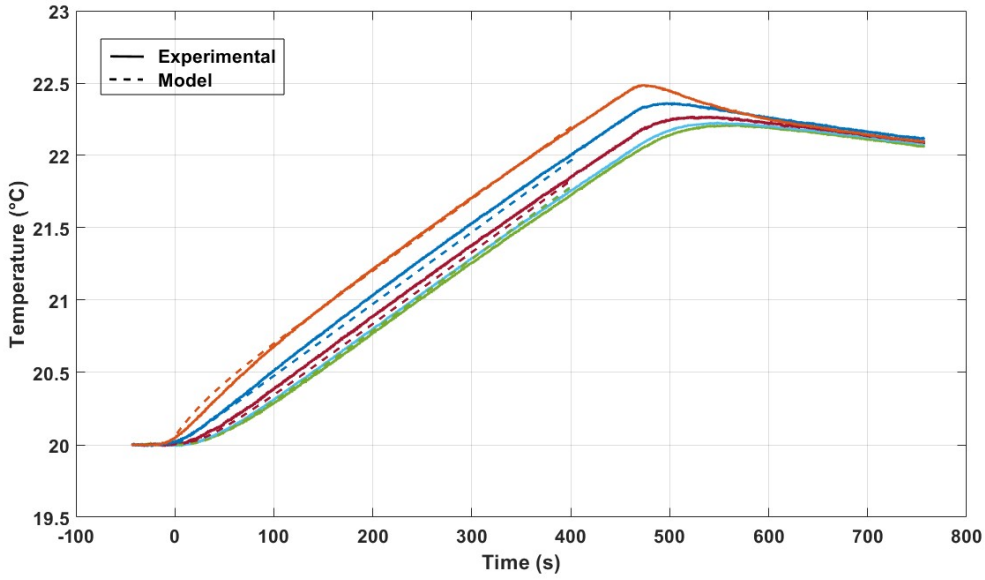

Figure 3.34: Example of axial thermal test data fitting between experimental and model curves

Due to these considerations, during the parameters estimation process the same experimental temperature curves are fitted two times, in the ranges described below:

- $[t_1 \div t_{end}]$, where t_1 is generally equal to 30 $[s]$ and t_{end} is set between 300 and 400 $[s]$, depending on the material. By using this range, the first part of the experimental data, greatly influenced by the thermal inertia of the heater, is neglected. Nevertheless, the major part of the first time transient is maintained (and thus considered in the fitting), leading to an acceptable estimation of the thermal parameters.
- $[t_1 < t_2 \div t_{end}]$, where t_2 lies between 100 and 200 $[s]$. The aim of this range is to neglect the first temperature differentiation and only consider the asymptotic behavior of the body, where a more correct estimation of the specific heat capacity can be attained. In fact, given that LIBs don't exactly behave as an ideal homogeneous body, if too much importance is given to the first period of the test, the model could return a bad fitting or values not representative of the second part of it, which in turn is strongly related to the specific heat capacity.

Following this procedure, the real value of the fitted parameters for the test is expected to lie within the obtained range, which is generally very low anyway. In the experimental campaign for the thermal characterization of cells, The same time parameters were used

for each test, to guarantee a correct comparison between estimated values; these were $t_1 = 30$ $[s]$, $t_2 = 100$ $[s]$, $t_{end} = 300$ $[s]$.
For each SoC, several tests were performed, to prove repeatability of the experimental methodology and obtain a more reliable and robust evaluation of parameters. The results of the thermal tests employing the axial heater for the BOL M1B samples are available in figures 3.35 and 3.36.

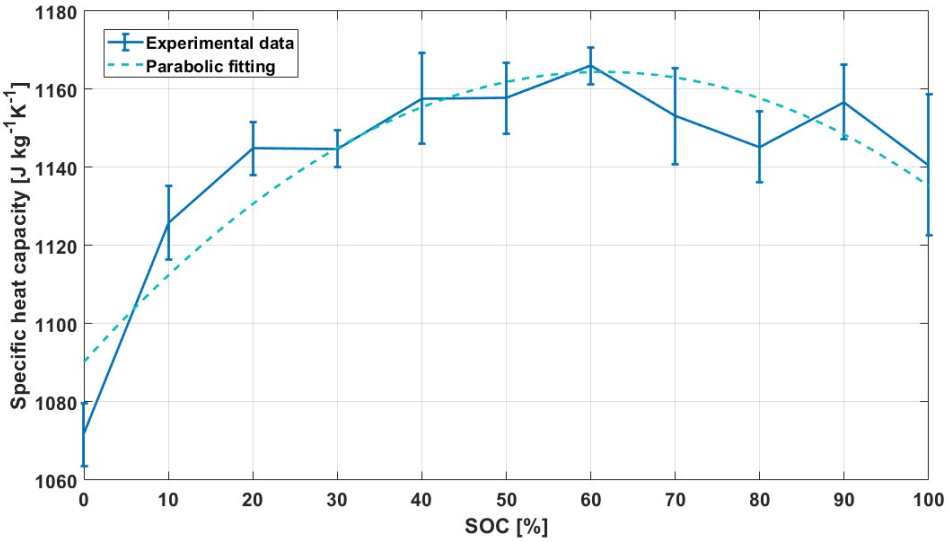

Figure 3.35: Specific heat capacity estimated values from axial thermal tests as a function of SOC

In the first graph (figure 3.35), the specific heat capacity is represented as a function of the SoC. It can be seen that the value is subjected to an increase in the first part of the curve, leading to a maximum value around the central $SoCs$; finally, the value decreases at the higher states of charge. The uncertainty of the measurement can be regarded as very low and a somewhat clear trend can be observed: a parabolic fitting is proposed, due to the shape of the trend of the experimental results.
In the second graph (figure 3.36), the fitting results of the axial thermal conductivity are displayed. In this case, the trend is not particularly clear and a great variation exists between values of this parameter at different $SoCs$: a higher thermal conductivity was found at lower values of state of charge, which then decreases in the middle part of the curve.
Additionally, the trend of the axial thermal diffusivity as a function of the SoC was computed from its definition and presented in figure 3.37. As it can be observed, the values follow closely the ones of the thermal conductivity, as this parameter is subjected to a higher variance than the specific heat capacity.

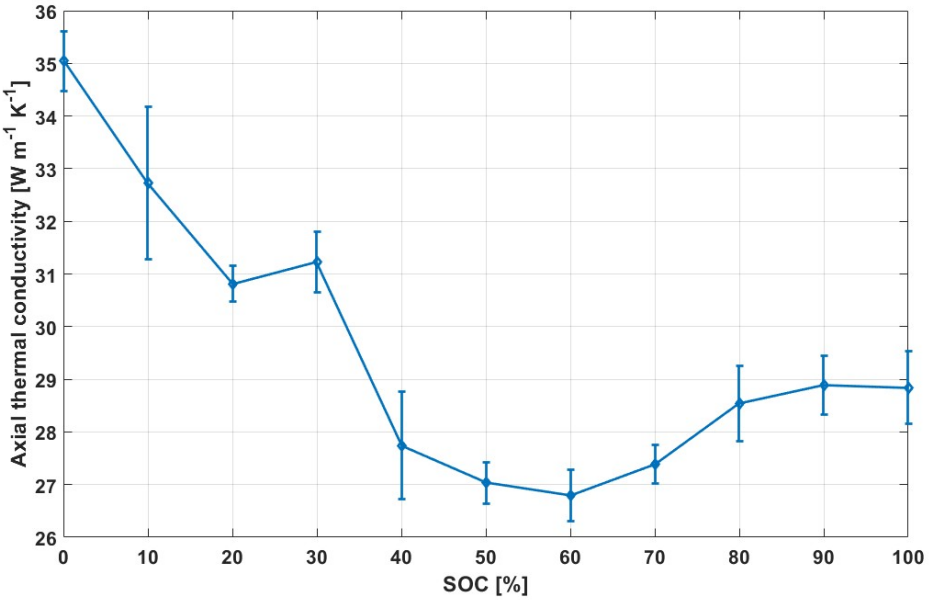

Figure 3.36: Axial thermal conductivity estimated values from axial thermal tests as a function of SOC

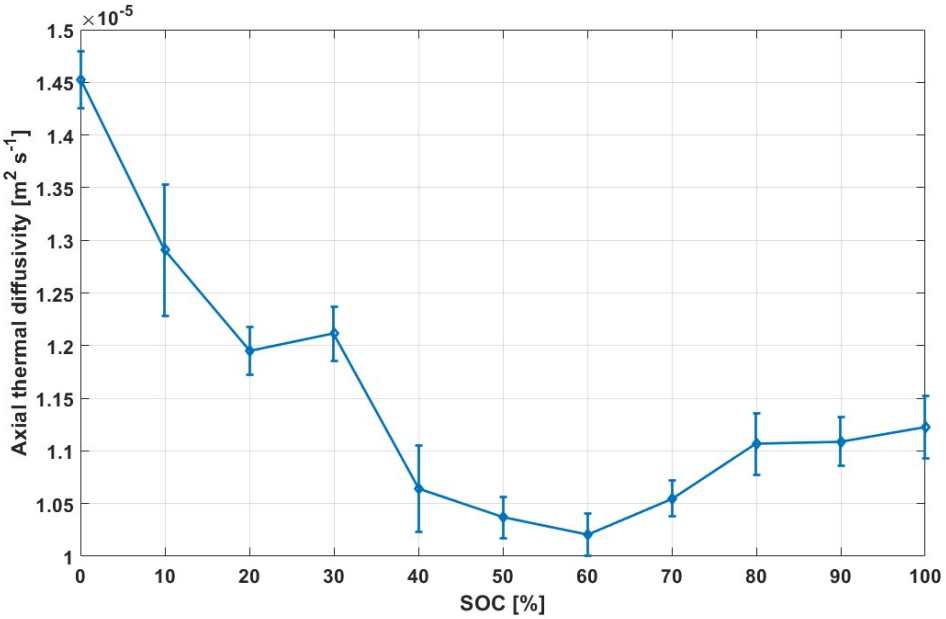

Figure 3.37: Axial thermal diffusivity estimated values from axial thermal tests as a function of SOC

The experimental methodology applied to the axial thermal tests presented in this section allowed for an estimation of the parameters described above.
One of the main limits of this kind of test is represented by the fact that only the axial

thermal conductivity could be fitted and no estimation was possible for the radial counterpart, given that the two values differ by around two orders of magnitude, as explained in section 1.4.4.
Theoretically, the radial thermal conductivity could be estimated by considering the temperature differences along the cells' radius on one or both of the electrical poles. However, the length of the gratings on the optical fibers is around 8 $[mm]$, as described in section 2.4.1, hindering the possibility of a precise measurement on such small bodies. Moreover, given that the two tabs are made of the same material (aluminum, which is characterized by a very high isotropic conductivity and constitutes the entirety of the external case), it is practically impossible to obtain a good estimation of said parameter. Furthermore, a radial description of this kind wouldn't even take into account the internal components of the cell, leading to a bad estimation of the thermal parameters values. Indeed, this "case effect" must be expected every time in which both the heat generation and temperature measurements are external to the tested volume.

3.3.3. Methodology for cylindrical cells drilling

Because of the issues related to the case effects of lithium-ion batteries and the impossibility to estimate a value for the radial thermal diffusivity, a new methodology was defined for the insertion of temperature sensors inside the core of the sampled cylindrical cells. The process of insertion is non-destructive, as it will be explained later in this section, allowing for a complete characterization of the thermal and electrochemical properties of the samples.
Still, this method only applies to the cylindrical geometry, due to its specific features. In fact, only in this case, a mandrel is present at the core of the cell and is generally only filled with surplus electrolyte. Moreover, in the samples described in section 2.1, the safety systems are all located at the negative pole, while at the positive one only the tab is present.
In literature, few scientific papers presented methodologies for the insertion of sensors inside lithium-ion batteries [135]:

- Novais et al. [123] presented a novel method for the integration of FBGs sensors in a LFP lithium-ion battery pouch cell. The chemical stability of silica fibers was tested by immersing them in conventional LIB electrolytes, such as the EC:DMC (50:50 weight%), described in section 1.2; little to none degradation was observed. The pouch cells were assembled in-situ and the internal FBGs sensors were placed within the internal structure of the assembly.

- Fleming et al. [126] introduced a methodology for the insertion of temperature sensors inside cylindrical cells, using modified FBGs for the in-situ and in-operando monitoring of internal behavior. In this study, a negligible effect of the procedure on the electrochemical behavior of cells was assessed through an EIS analysis. Moreover, the complete list of materials used for the instrumentation production was available.
- Matuck et al. [135] provided a similar method for the introduction of optical fibers sensors inside the mandrel of 18650 cylindrical cells. In this instance, an FBG optical fiber was modified by the installation of an additional Fabry-Perot interferometer (FPI), for the measurement of pressure variations, and an hybrid sensor composed of both types at the tip of the fiber. This approach allowed for the simultaneous measurement of temperature and pressure variations inside the cell's core. Furthermore, given that the sensors were positioned in an open cavity, this procedure was regarded as less invasive than others employing infra-electrodes positioning.

As implicitly determined by the presented papers, the top choice for internal temperature sensing in lithium batteries are optics-based sensors. In fact, thanks to their advantages described in section 2.4.1, they are very easy to implement in such devices, as opposed to thermocouples for example. Moreover, they provide very accurate measurements for the dynamic variations typical of lithium-ion batteries, due to their low thermal inertia, other than chemical inertness.

A computer tomography (CT) scan of a cell's internal components was available (figure 3.38) and was thoroughly analyzed to assess the feasibility of the drilling process. In this image, brighter colors correspond to higher density materials.

As it can be seen, the jelly roll occupies the majority of the volume, ranging from the mandrel to the external case. At the negative tab, several safety devices (PTC, CID, safety vents) are present: these, of course, must be maintained intact, to not compromise their functioning. In addition, under the positive pole, the aluminum current collector stripes can be noticed. Moreover, a triangular shadow can be spotted between the external tab and the mandrel, suggesting the presence of a body characterized by a low density.
A slight reduction of the mandrel's diameter is present at the positive pole, used to join this piece with the low density component. The mandrel is filled up to a certain level of the excess electrolyte, but no presence of other solid objects can be detected inside it.
Additionally, a M1B sample's tab was cut in the inert environment of the glove-box to provide a more precise description of this component and guarantee a better understanding of the internal structure of the cell (figure 3.39).

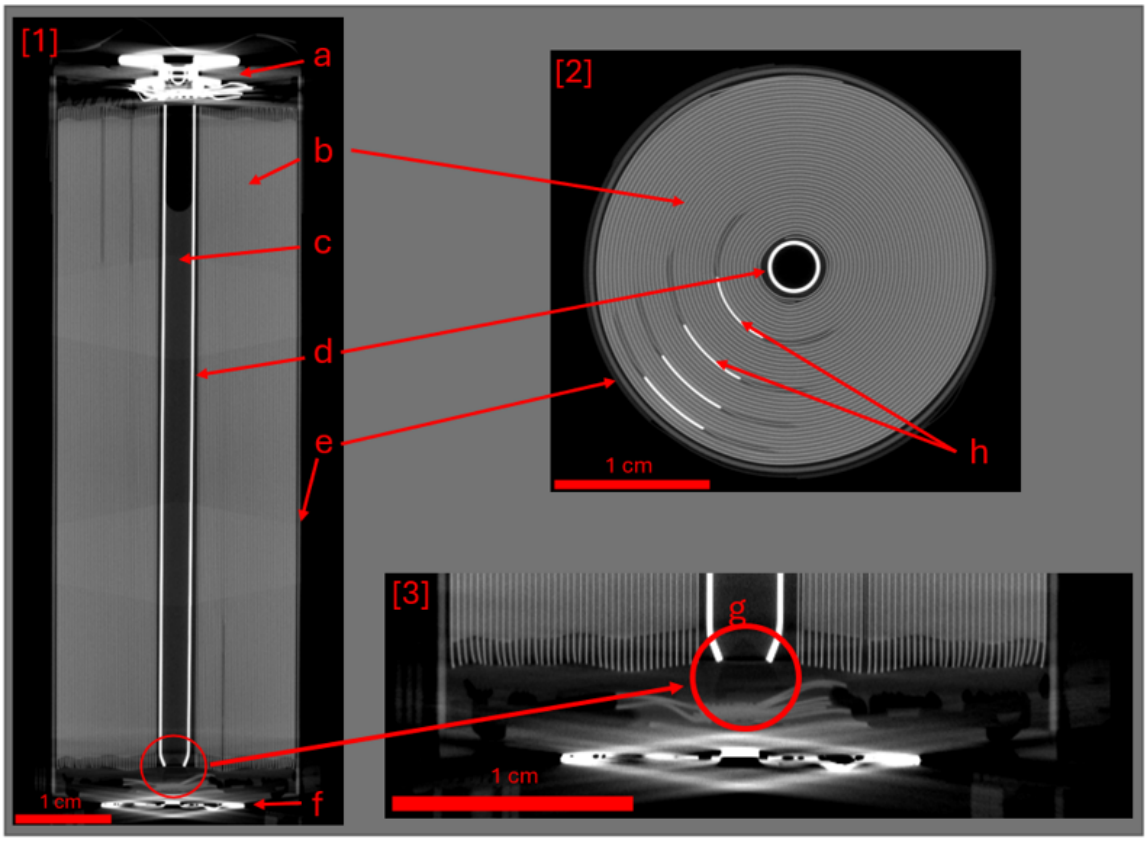

Figure 3.38: CT scans of an M1B sample.
[**[1]**: front view; **[2]**: top view; **[3]**: detail of front view. **a**: negative pole; **b**: jelly roll; **c**: excess electrolyte; **d**: mandrel; **e**: external case; **f**: positive pole; **g**: low density material; **h**: current collectors]

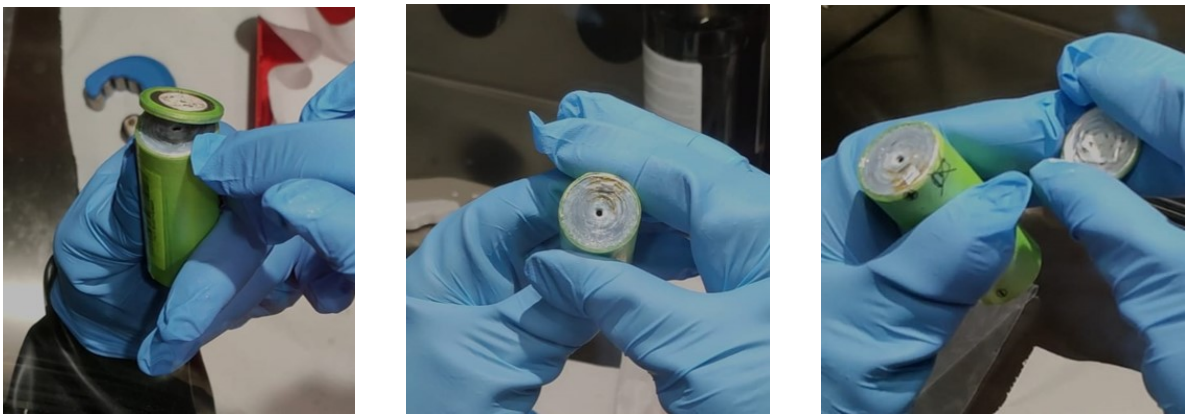

(a) Cutting of the external case (b) Top view of the cut cell (c) Cut cell with positive pole tab

Figure 3.39: Cutting process of an M1B sample cell

It was observed that, after the first layer of the aluminum tab, only a polymeric structure

was present between this component and the mandrel, corresponding to the low density material piece seen from the cell's tomography.
After these considerations, a viable strategy for the insertion of the optical fiber sensors could be defined:

1. by employing a small drill head, a hole can be performed at the center of the positive tab until reaching the mandrel; with this approach, only a small depth would need to be reached, due to the fact that only the aluminum tab, the positive electrode current collector and the plastic structure would be crossed. Moreover, the safety devices would be kept intact as they are positioned at the negative pole of the cells.
2. Subsequently, an optical fiber can be inserted, covering the whole length of the cell. In this step, no resistance should be encountered, due to the fact that the mandrel is hollow.
3. Finally, the fiber is fixed in place through the utilization of a self-hardening glue. This is needed also to completely seal the cell and make sure that no air or water enters into it during subsequent operations.

For this methodology, a 0.6 $\varnothing$ $[mm]$ drill head was employed; moreover, a two-components epoxy resin (ARALDITE® 2080-15 A) was applied to seal the cells. This was chosen for its high durability and fast setting, other than its thermal stability.
The whole procedure was carried out inside the glove-box described in section 2.2.2, to guarantee that the levels of oxygen and moisture were kept below 0.1 and 0.8 $[ppm]$, respectively.
A first tentative was performed on the positive tab of the previously cut cell, to assess the feasibility of drilling process.

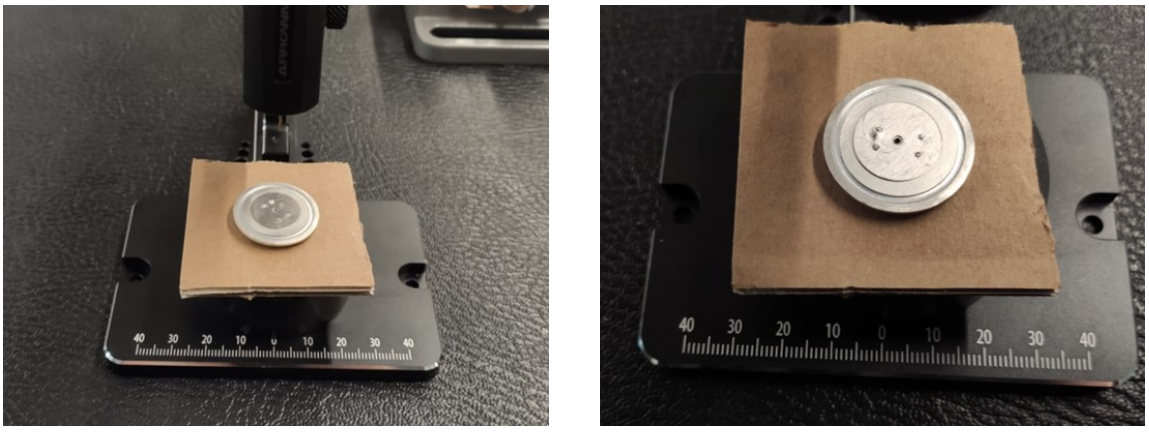

(a) Drilling setup (b) Detail of tab after drilling

Figure 3.40: Drilling process of the positive tab of an M1B sample cell

Consequently, the methodology was validated through several verification attempts, assessing the impacts of the procedure on the operation of the batteries. Finally, the methodology was applied to the samples, by inserting one or more FBG sensors inside the cells.

(a) Cell without silica fiber (b) Cell with silica fiber

Figure 3.41: Images of two M1B samples, with and without the insertion of an optical fiber sensor

Integrity assessment

To assess the integrity of the opened cells, several diagnostic tests were performed, in a similar manner as the first electrochemical characterization. In this regard, discharge tests at C-rate = 1 $[h^{-1}]$ were compared before and after the drilling and insertion of the temperature sensors. Moreover, EIS analyses at $SoC = 0$ and $SoC = 1$ were performed and put alongside with the spectra previously obtained for the same cells. In figure 3.42, the two discharge curves were represented.

As it can be seen, the discharge curves are practically the same and no appreciable differences can be observed. A small decrease in the operating voltage and final discharged capacity can be noticed, but it is included in the uncertainty range of the instrumentation

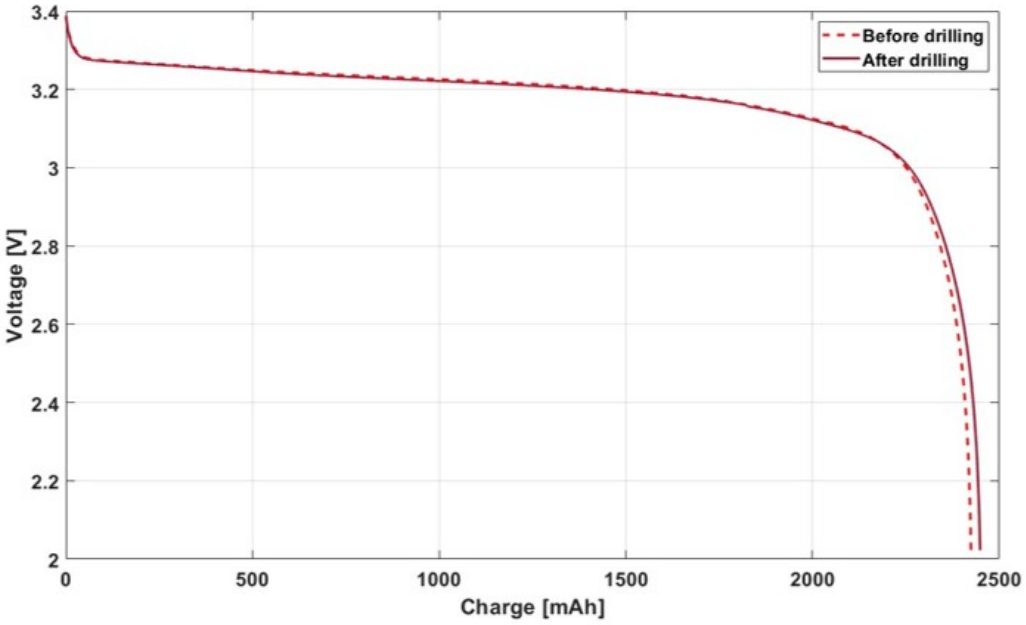

Figure 3.42: Comparison between discharge curves at 1C of the same M1B sample before and after the drilling process

and could be regarded as negligible.

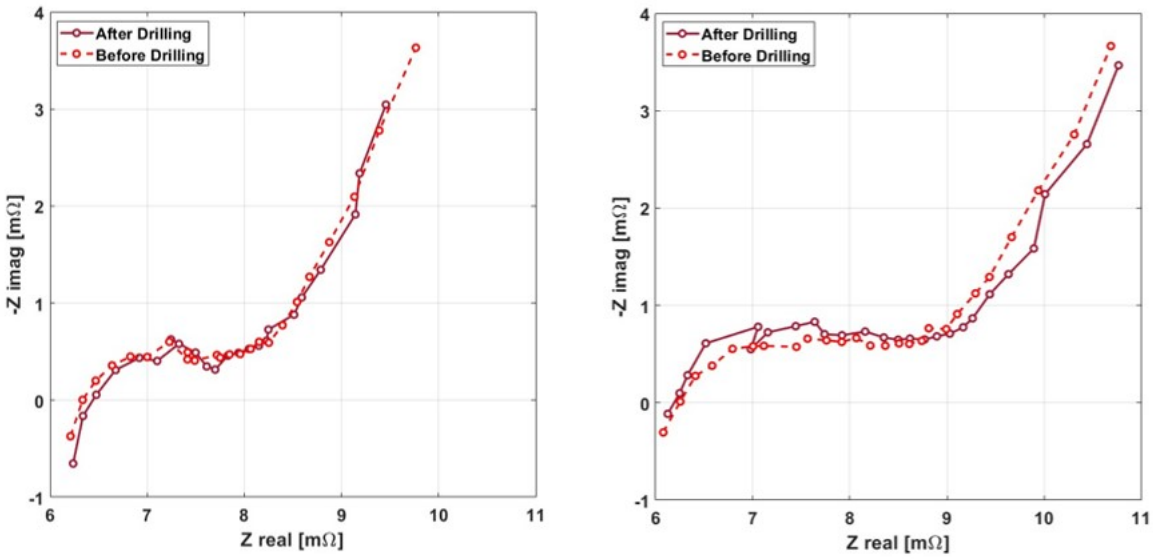

(a) EIS at SoC = 1 (b) EIS at SoC = 0

Figure 3.43: Comparison between EIS spectra results for the same M1B sample at SoC = 1 (a) and SoC = 0 (b), before and after the drilling process

Furthermore, the EIS spectra were compared at extreme state of charges. In figure 3.43 it can be seen that, also in this case, there was no apparent modification in the behavior of

the cell: the HFR remains the same, showing that no increase in the electrical resistance was caused by the drilling procedure; moreover, also the charge transfer, kinetic and diffusion related impedances weren't significantly modified by the process.

Additionally, a very slow discharge at C-rate = 0.1 $[h^{-1}]$ was performed on the BOL cell in a climatic chamber, with the simultaneous measurement of the internal temperature variations thanks to the inserted FBG sensors. This test was done to detect any strain or pressure associated variations of the internal measurement, which could cause a drift on the temperature value: in fact, given that FBGs are able to measure temperature and strain differences at the same time, it is not trivial to separate both contributions. In this case, a very slow discharge, close to the equilibrium conditions for the cell, is needed to disregard any heat generation caused by overpotential related losses.

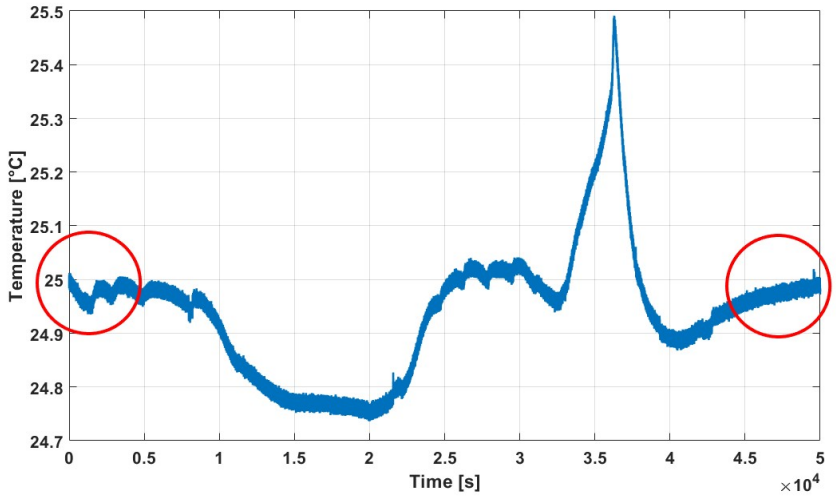

Figure 3.44: Internal temperature measurement on an M1B sample at BOL conditions, during a discharge test performed at 0.1C

In figure 3.44, the internal temperature of the tested cell can be observed: a distinguishable temperature variation can be noted in the graph. However, this deviation from the equilibrium value is very small, such that the maximum temperature difference during the whole experiment was around 0.5 $[°C]$, at the end of the test. In fact, a peak can be seen at around 3.6 x 10^4 $[s]$, that corresponds to the end of the discharge process. After that, a temperature transient was experienced by the cell, until returning to the initial state at 25 $[°C]$. Additionally, during the discharge test (and particularly when the temperature value was close to the set-point of the climatic chamber at 25 $[°C]$), several "jumps" can be noticed on the curve: these were assumed to be related with the internal control of the chamber.

As described in section 1.2, the graphite experiences a volumetric expansion of up to

10% between extreme states of charge, so that an increase of the internal pressure can be detected within the cell [135]. However, given that after a 10 hours long discharge, the temperature measured by the optical fiber sensor returns to its starting value, it can be assumed that no strain or pressure related effects were detected by the FBG. In fact, as described in section 2.4.1 Bragg gratings are several orders of magnitude more sensitive to strain than to temperature, such that a difference would be clearly visible if strain effects were present. Moreover, it is known that the inserted fiber was positioned in the mandrel of the cylindrical sample and not in the electrodes where the expansion takes place. If pressure-induced strain variations were detected by the fiber during the test, they would have been conserved also in the last period, because the final state of charge is the same. Furthermore, even if the irreversible heat production can be neglected, the reversible entropic heat generation must be taken into account, as defined from the Bernardi's model in section 1.4.3. In fact, this contribution becomes more and more important as the current rate decreases and was deemed to be the major contribution to the measured temperature difference.
If this term is considered, it becomes clear that no effect of strain and pressure can be perceived within the internal measurement.

In addition, an analogous charge test at C-rate = 0.1 $[h^{-1}]$ was performed to provide further proof of this point (figure 3.45).

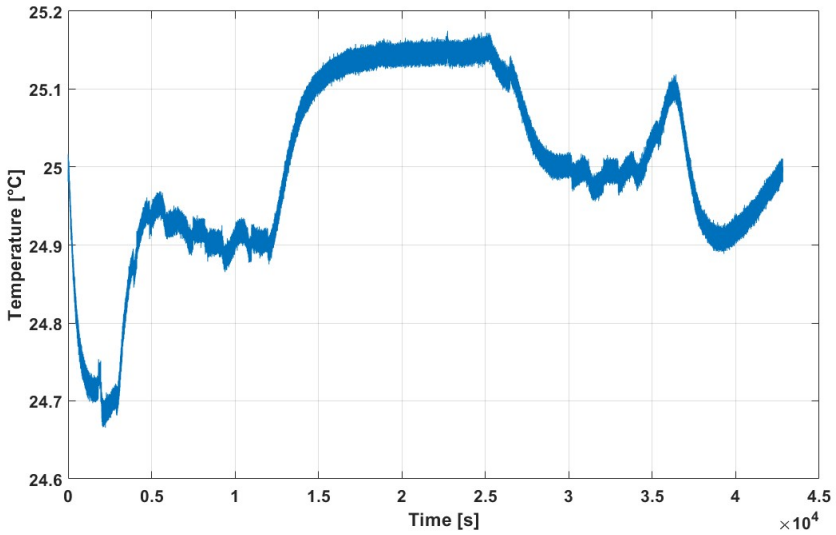

Figure 3.45: Internal temperature measurement on an M1B sample at BOL conditions, during a charge test performed at 0.1C

As it can be observed, the same considerations hold true, as the temperature goes back to

its initial point after the test. Moreover, it can be noticed that the trend of the curve is somehow opposite to the one obtained from the discharge test. In particular, this aspect is related to the reversible entropic heat generation within the cell, that will be described more in depth in section 4.2.

3.3.4. Radial thermal tests

After the insertion of the optical fibers inside the mandrel of the cells, it was possible to perform thermal tests with simultaneous measurements of the internal and external temperature. In this regard, the same methodology as for the axial thermal tests was employed, with the necessary differences of the analytical model, with radial thermal flux boundary conditions, and the radial silicon heater applied to the cells (described in section 3.1).
Because of these aspects, it was possible to characterize the radial thermal behavior of the samples, by the estimation of the radial thermal conductivity, which was previously unachievable. Moreover, the possibility to measure the internal temperature allowed to avoid the "case effect" described previously, which was an important limit for the axial thermal tests.
Apart from the internal sensors, an additional optical fiber was placed on the external surface of the tested cells, to obtain a temperature deviation between the two positions.

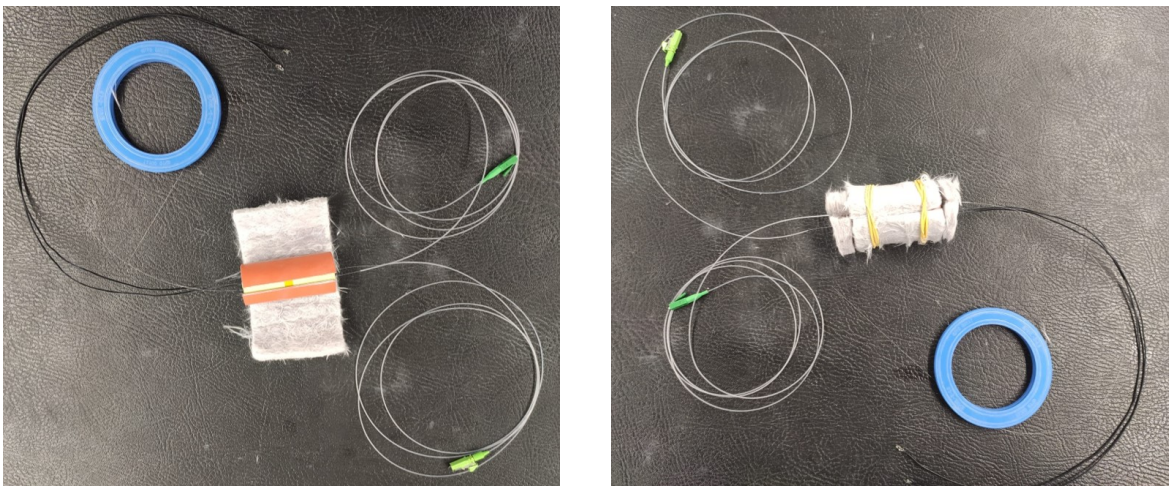

(a) Fiber positioning (b) Closed envelope

Figure 3.46: Images of the radial test assembly before being inserted in the climatic chamber

This was achieved due to the shape of the radial heater, which left a wide enough empty space on the outer surface to apply an FBG.

An example of a radial thermal test can be analyzed in figure 3.47.

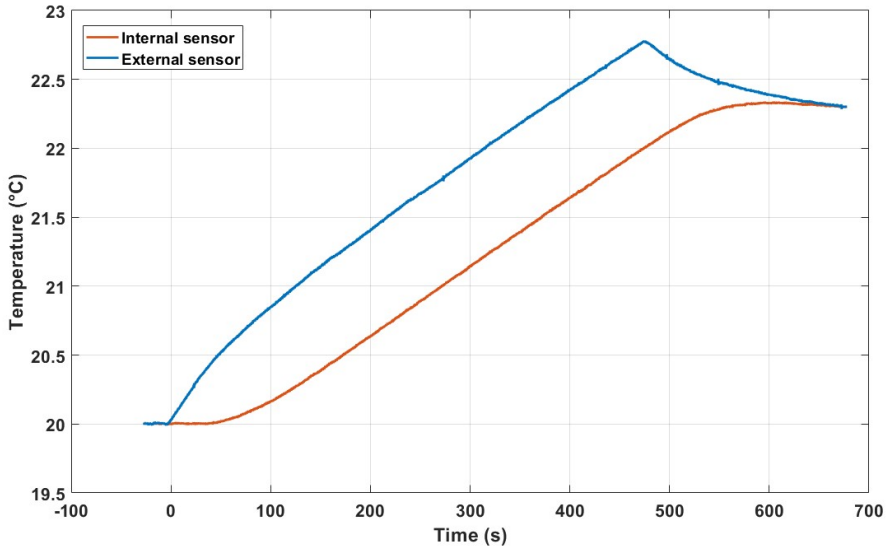

Figure 3.47: Example of radial thermal test FBGs temperature measurements

The same considerations as the axial tests can be made for the radial counterparts: after a first differentiation between sensors, caused by turning on the heater power, an asymptotic behavior is reached, which lasts until the heater is turned off; an homogenization period is then experienced by the cell, until the test is stopped.

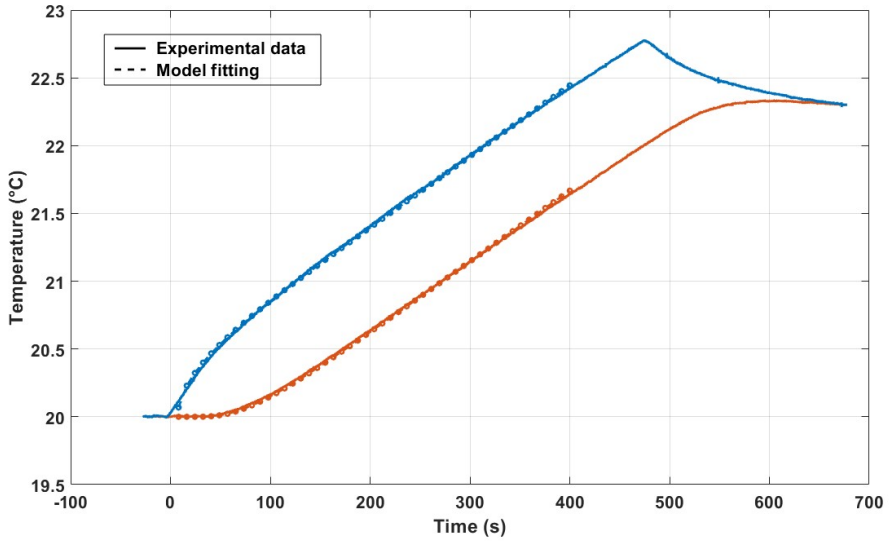

Figure 3.48: Example of radial thermal test data fitting between experimental data and model curves

The appropriate analytical models are then applied to the experimental data and series

of fitting curves are obtained for the same positions of the temperature sensors (figure 3.48).
As it can be clearly noted, the fitting curves from the model are completely overlaid on the experimental data, leading to a more faithful description of the radial thermal behavior. Given that for the adiabatic radial thermal model the axial position is meaningless (due to its specific boundary conditions, section 3.2.1), all of the sensors locations only included the radial coordinate. On the other hand, if the convective model would be used, the internal sensors would be assumed to be positioned at the half height of the cell. This assumption can be disregarded if the position of sensors is well known along the fiber length inserted inside the cell.

Beginning of life sample

The results for the radial thermal tests of the M1B sample at BOL conditions are presented in this section.
In the first graph (figure 3.49), the specific heat capacity is represented as a function of the state of charge.

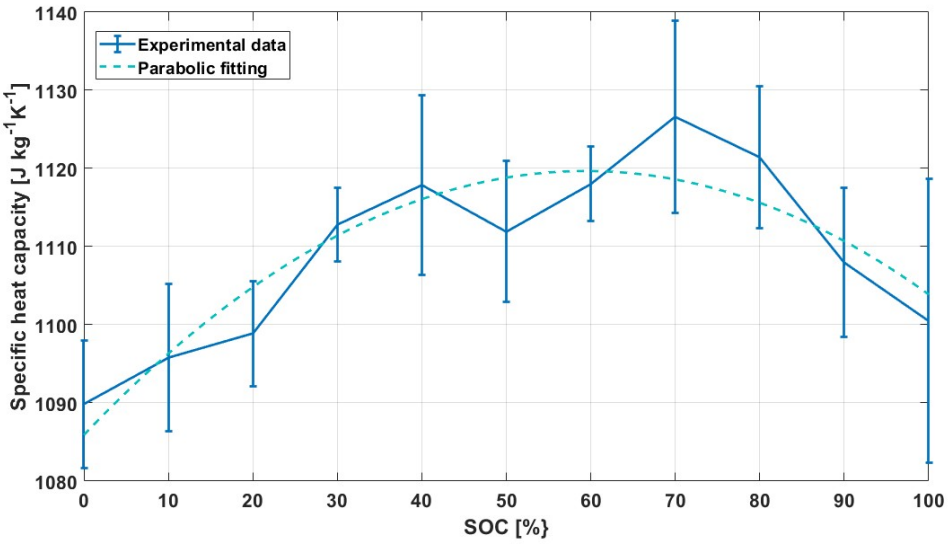

Figure 3.49: Specific heat capacity estimated values from radial thermal tests as a function of SOC

As it can be seen, the specific heat capacity graph follows a somewhat parabolic curve, as it was the case for the axial thermal tests. However, the actual values obtained from this second experimental campaign have a lower variance as a function of the SoC. In this regard, the values of specific heat capacity estimated for both types of tests are somewhat similar. Indeed, the two tests must be consistent with each others, given the assumption

that the analyzed cells are the same.

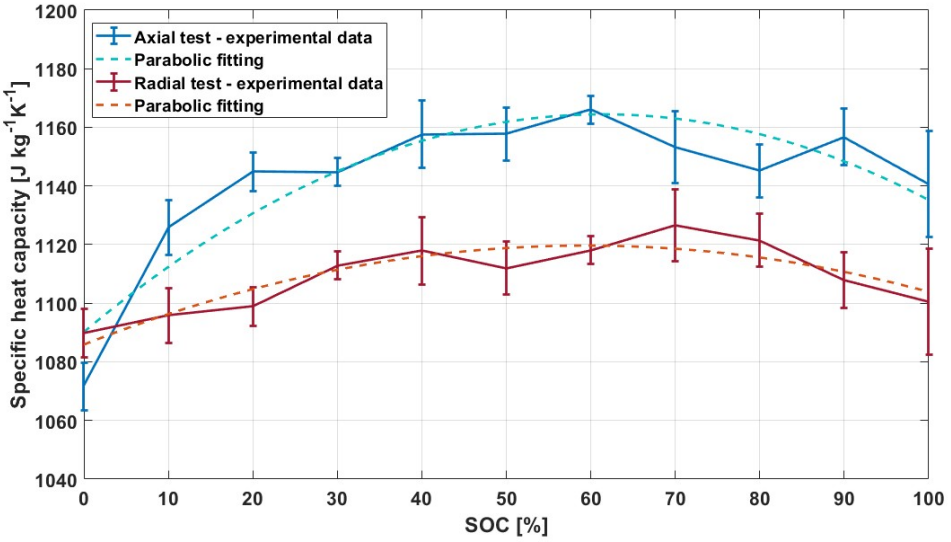

Figure 3.50: Comparison between specific heat capacity estimated values from radial and axial thermal tests, as a function of SOC

The radial thermal conductivity, instead, can be seen in figure 3.51.

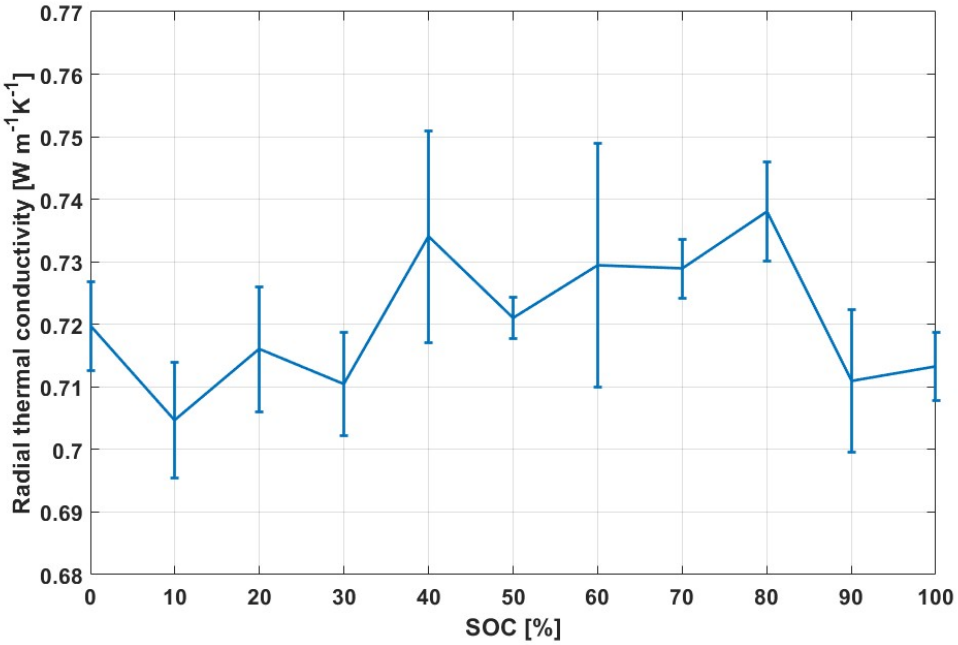

Figure 3.51: Estimated values of thermal conductivity from radial thermal tests for BOL samples, as a function of SOC

The average value lies around 0.72 $[W\ m^{-1}K^{-1}]$, as shown from the graph, with a some-

what lower value at the extreme states of charge. As it was expected from the literature analysis (section 1.4.4), more than one order on magnitude was estimated between the two values of thermal conductivity. In this case, however, much lower variation is found from the fitting process, that could lead to the assumption of a constant value with respect to the SoC. Moreover, a lower uncertainty on the estimated values was found, that could be attributed to the presence of only two positions along the radial coordinate.

Subsequently, the radial thermal diffusivity was computed and plotted from the measured thermal parameters (figure 3.52). Also in this case, similar observations as the corresponding thermal conductivity can be made.

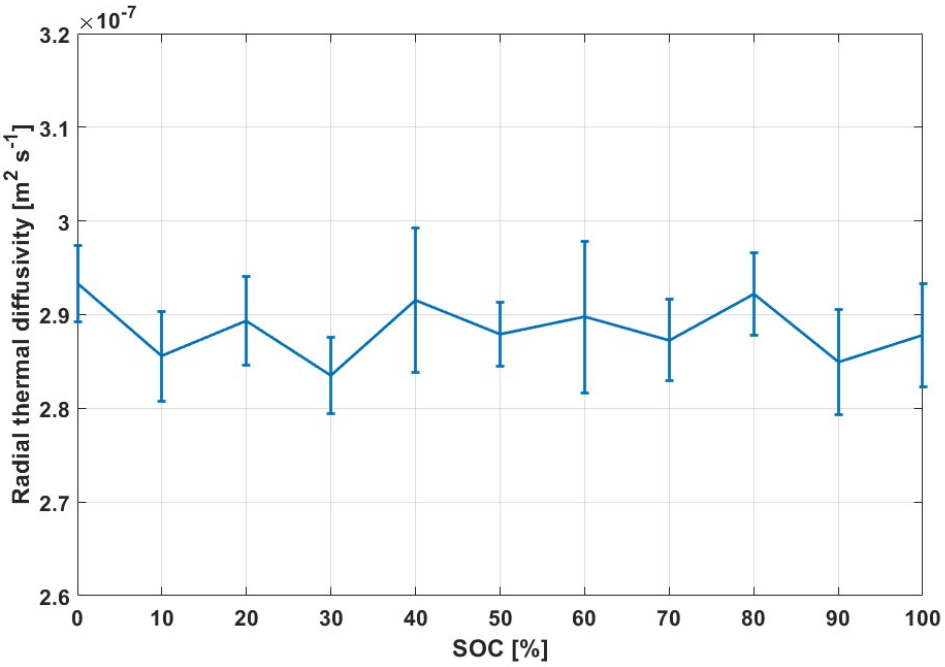

Figure 3.52: Estimated values of thermal diffusivity from radial thermal tests for samples in BOL conditions, as a function of SOC

Additionally, a brief experimental campaign to assess the dependency of the thermal parameters on the operating temperature was carried. In this regard, the same M1B sample used for the radial thermal characterization was tested at different temperatures, thanks to the climatic chamber control. As explained in section 1.4.4, a linear trend with temperature is expected from literature for the thermal parameters, particularly for the specific heat capacity, for which many references can be found [61, 62, 66, 67]. This was later verified by the results, which can be seen in figure 3.53.

In fact, an ascending trend can be observed for both the specific heat capacity and the

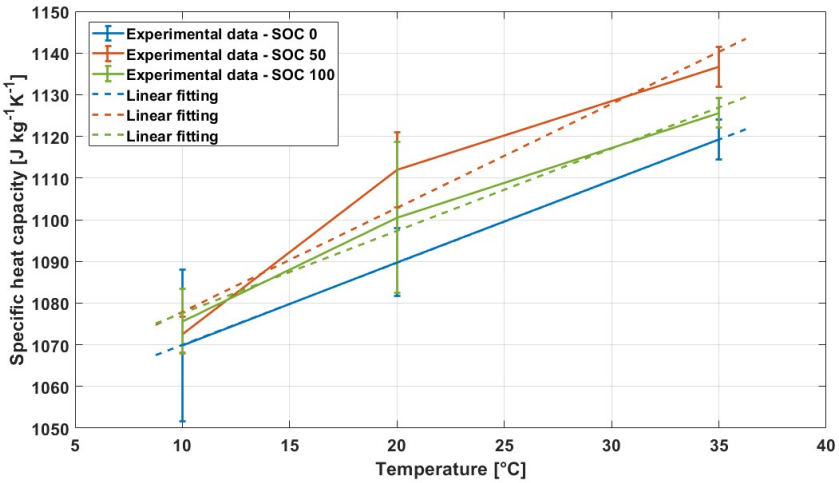

(a) Specific heat capacity

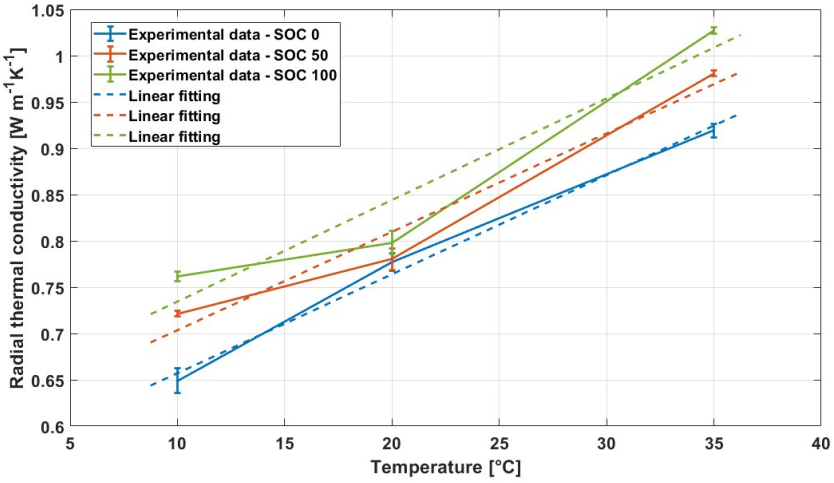

(b) Radial thermal conductivity

Figure 3.53: Thermal parameters estimation as a function of the operating temperature

thermal conductivity curves, leading to the confirmation of the dependency already seen in literature. In particular, the trend is strongly linear for the values estimated at $SoC = 0$ and $SoC = 0.5$; this is not exactly the case for the curve at $SoC = 1$, but an ascending linear trend can expected anyway.

As for the thermal conductivity, a rising trend with the temperature of the test can be noticed also in this case. Moreover, the linear fitting curves are almost parallel with each others, suggesting a dependency of this parameter with the state of charge, but of inferior importance with respect to the one with temperature.

Aged sample

The same procedure was executed for an aged M1B sample. In this regard, the cell which presented the lowest SoH among the ones used in the calendar aging campaign was selected. As described in section 3.3.1, the cell stored at the highest state of charge (which in this case was 100%) suffered the most degradation, mainly due to LLI cause by the formation of passivation layers at the electrodes-electrolyte interfaces. After the period of storage, this battery reached a final SoH equal to around 83%, which approximately corresponds to the substitution indicator for automotive applications of lithium-ion batteries. In this respect, this specific sample could be regarded as a very useful benchmark for the comparison of thermal parameters between cells at beginning of life and end of life conditions.

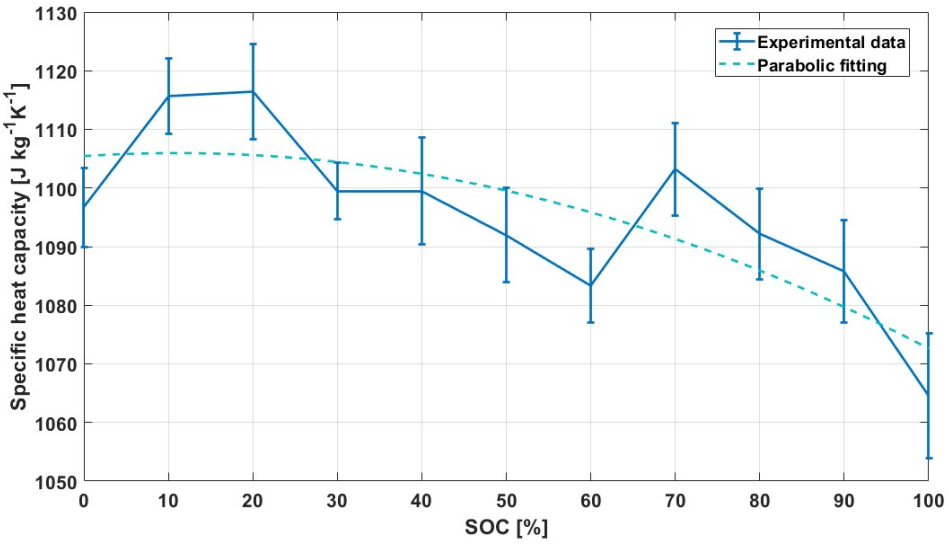

Figure 3.54: Estimated values of specific heat capacity for the aged sample from radial thermal tests, as a function of SOC

In figure 3.54, the estimated specific heat capacity was plotted as a function of the SoC: it can be noticed that a seemingly parabolic trend was obtained in this instance, as it was the case for the BOL cell. However, the value is almost constant with respect to the state of charge, due to the fact that a lower variance was found. Moreover, the estimated values present a general descending trend from $SoC = 0$ to $SoC = 1$, with a peak between 10% and 20% of this parameter.

When compared with the data obtained for the beginning of life case (figure 3.55), it

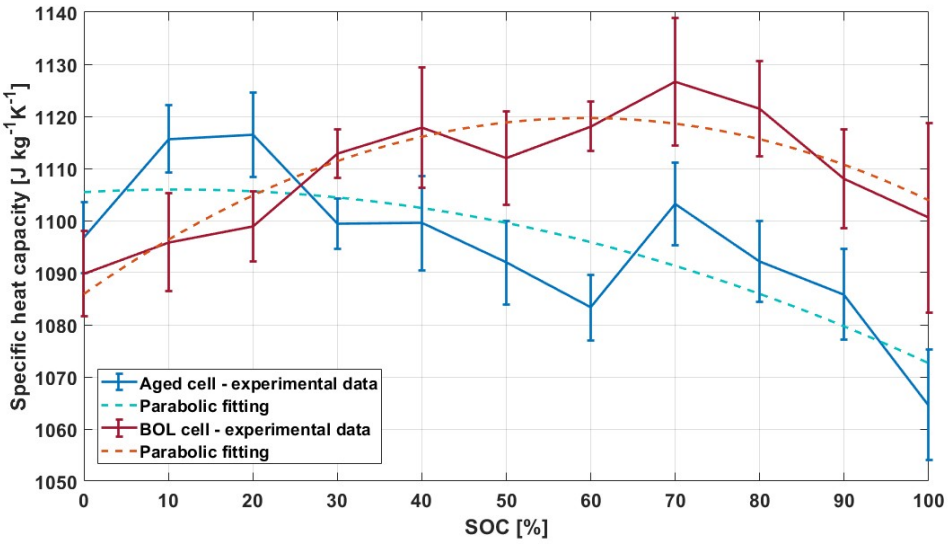

Figure 3.55: Comparison between estimated values of specific heat capacity from radial thermal tests for samples in BOL and aged conditions, as a function of SOC

can be seen that at very low values of SoC the specific heat capacity is very similar between the two curves; at around $SoC = 30\%$, however, the behavior starts to change as a certain divergence is observed, such that a descending trend was found for the aged cell. This difference is kept until the highest state of charge and was estimated outside of the uncertainty range.

In figure 3.56, the estimated radial thermal conductivity of the aged cell can be viewed. No significant variation of this parameter can be observed as a function of the SoC from the graph, as the curve lies around a seemingly constant value of 0.82 $[W\ m^{-1}K^{-1}]$ over the whole range.

The radial thermal conductivity at aged conditions was compared with the estimated values of the BOL cell (figure 3.57). As it can be noticed, their behavior is somewhat similar along the SoC axis, but a visible higher value was estimated for the aged sample. As explained at the beginning of this section, the main degradation phenomena suffered by the aged cell are related with LLI and formation of passivation layers. From an electrical point of view, it is known from literature (section 1.5.1) that the formation of SEI causes an increase of the internal resistance of the cell, as an higher ohmic overpotential is experienced by batteries characterized by this aging mode. From a thermal point of view, however, the dependency was hardly investigated, such that the real effect of passivation layers on thermal parameters is almost unknown. In this regard, the increase

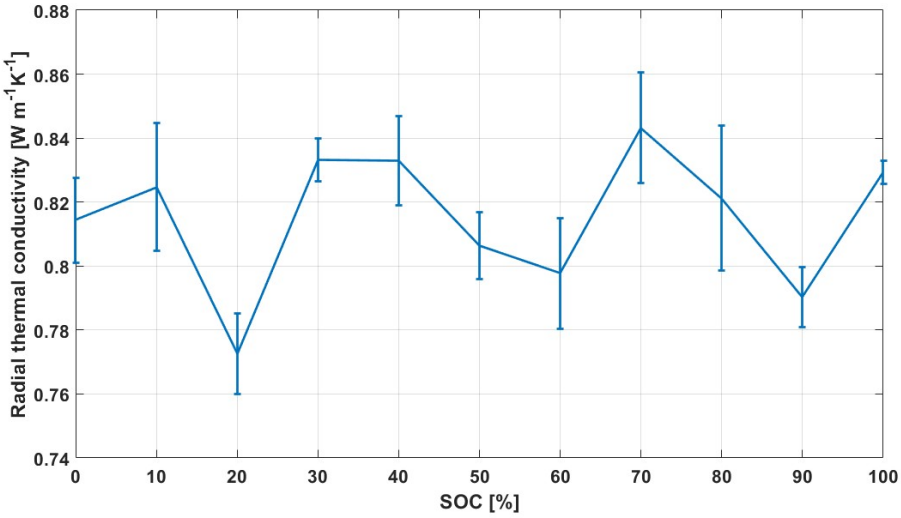

Figure 3.56: Estimated values of thermal conductivity from radial thermal tests for the aged sample, as a function of SOC

of thermal conductivity estimated for the aged cell could be assumed to be attributed to this degradation phenomenon, leading to a lower thermal resistance in aged cells.

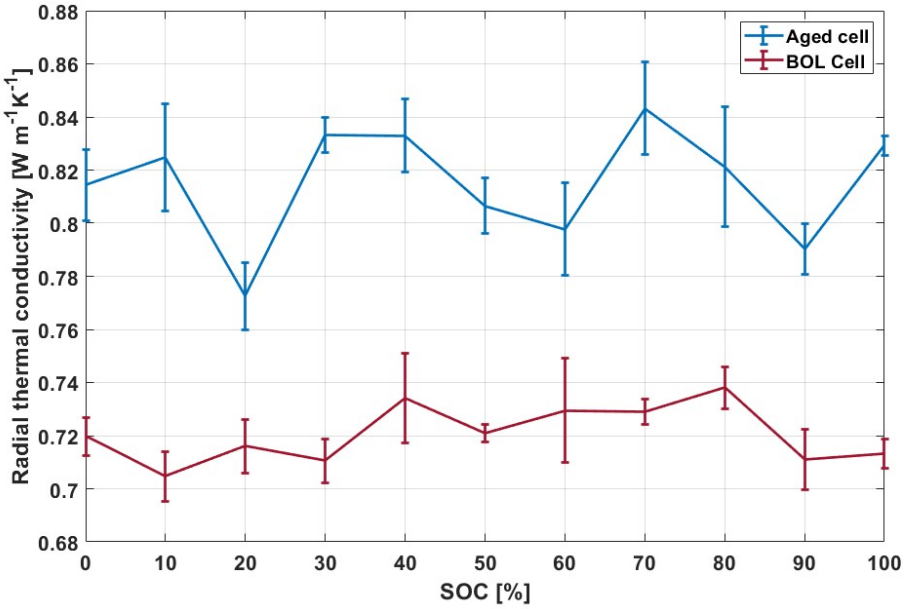

Figure 3.57: Comparison between estimated values of thermal conductivities from radial thermal tests for samples in BOL and aged conditions, as a function of SOC

The same considerations could be done for the thermal diffusivity (figure 3.58): as it was the case for the BOL cell and the previous axial thermal characterization, the shape of

its trend is very similar to the one of the thermal conductivity. In this case, an average value of around 3.3 x 10^{-6} $[m^2/s]$ was found for the aged cell.

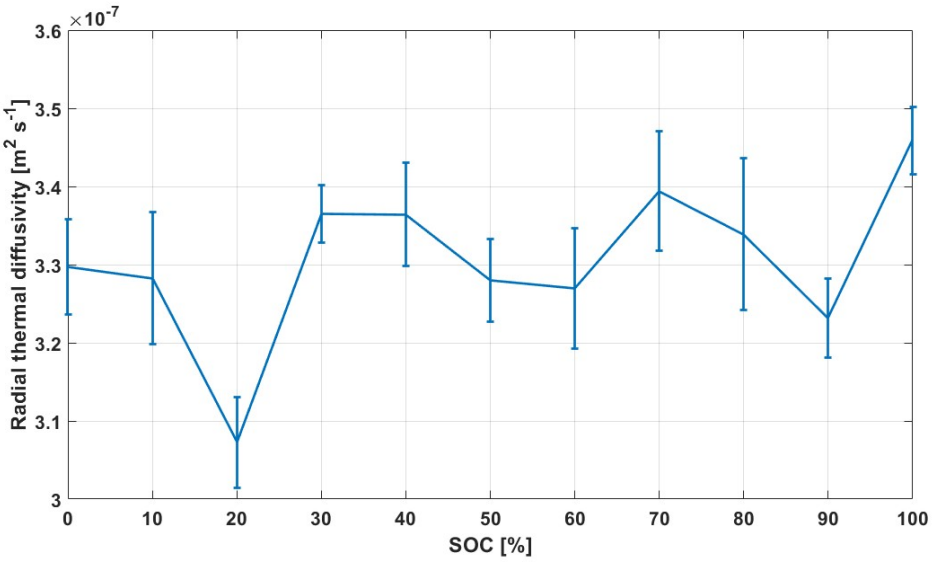

Figure 3.58: Computed values of thermal diffusivity from radial thermal tests for the aged sample, as a function of SOC

In figure 3.59, a comparison between the two radial thermal diffusivity can be seen. Also in this instance, a clear increase of the aged cell thermal parameter can be noticed.

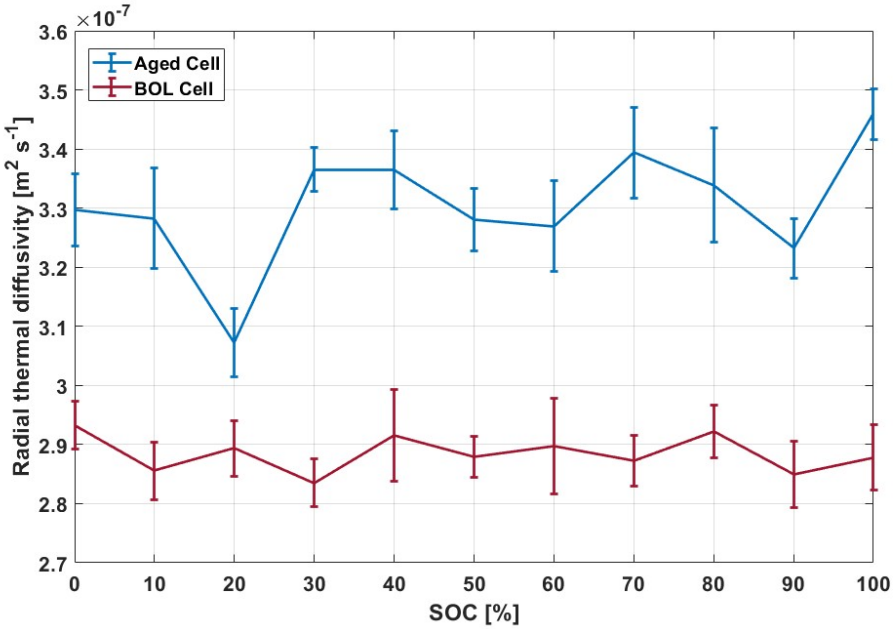

Figure 3.59: Comparison between computed values of thermal diffusivity from radial thermal tests for samples in BOL and aged conditions, as a function of SOC

3.4. Final remarks

In this chapter, the description of the thermal characterization campaign of the samples was provided. To summarize briefly:

- A methodology for the assessment of the anisotropic thermal parameters of cylindrical cells was presented; through the utilization of electrical heaters, a sample is heated in a controlled way with the simultaneous measurement of temperature, so that its thermal conductivity and specific heat capacity can be estimated at once. The methodology was validated through the utilization of an aluminum alloy cylindrical body of known thermal properties.
- For the estimation of radial and axial thermal parameters, four analytical models of the cell were defined, considering several combinations of boundary conditions. In these models, the cell was assumed as an homogeneous volume, characterized by an anisotropic behavior. The models were compared with analogous COMSOL Multiphysics simulations, to verify their accuracy; in this regard a maximum error of 0.17% and 0.24% was found for the radial and axial models, respectively.
- A new methodology was defined for the introduction of optical fiber temperature sensors inside the mandrel of cylindrical cells. This approach must be carried in an inert environment as it employs the use of a small drill for the perforation of the positive pole tab; the sensors are then inserted within the created hole and the cell is subsequently sealed through an epoxy resin, to guarantee no contact with the external environment. An integrity verification of the drilled samples was done afterwards, to assess the effects of this methodology on the cells. In this regard, no appreciable impact was found on the samples after the procedure.
- An experimental campaign was carried for the electrochemical and thermal characterization of the available LFP lithium-ion batteries samples, both at beginning of life and aged conditions. In this regard, four cells were subjected to a calendar aging campaign at different SoC. Consequently, the radial and axial anisotropic behaviors of the cylindrical cells were determined, as a function of the state of charge and operation temperature.
- It was found that the specific heat capacity is characterized by a weak parabolic trend with respect to the SoC, averaging around a value of 1110 $[J\ kg^{-1}K^{-1}]$; similar values were estimated for both the axial and radial tests, verifying the consistency of the methodology. The specific heat capacity of the analyzed aged sample was found to be similar to the BOL case only in the range of SoC between 0 and 40%,

while a lower value was estimated in the remaining range. The biggest difference was found at $SoC = 1$, such that a decrease of 3.3% was assessed.

- More than one order of magnitude difference was found between the values of thermal conductivity, confirming the strong anisotropic behavior found in literature. In particular, the thermal conductivity in the axial direction was estimated to be around 30 $[W\ m^{-1}K^{-1}]$, characterized by certain dependence with the SoC. On the other hand, the radial thermal conductivity in the BOL sample was estimated to have a negligible correlation with the state of charge and to be characterized by a mean value of 0.72 $[W\ m^{-1}K^{-1}]$. Additionally, this parameter was found to be appreciably higher in the aged sample, averaging around 0.82 $[W\ m^{-1}K^{-1}]$. In this regard, an increase of 13.9% was estimated in the degraded sample.

4 | Internal temperature investigation

Following the methodology for the insertion of optical fibers sensors inside the mandrel of cylindrical cells presented in section 3.3.3, an experimental campaign was carried for the characterization of the internal temperature evolution in the samples during operation. In this regard, several tests at different current rates were performed on the M1B samples described in section 3.3.1. Moreover, an additional experimental campaign for the determination of the entropic coefficient of cells was realized, primarily for the computation of the reversible heat generation term.

4.1. Internal temperature measurements

After the thermal characterization presented in the previous chapter, the cells were subjected to charge and discharge tests, with the simultaneous measurement of temperature inside and outside of the volume. In this way, an in-operando description of the internal and external temperature could be obtained. In this regard, a distinction between samples at beginning of life and aged conditions was done, particularly for the assessment on the effects of aging during operation through the comparison between them.

4.1.1. Discharge tests

Beginning of life cell

Discharge tests were performed at different current rates, measuring both the internal and external temperature.
In figure 4.1, the temperature curves during a discharge test at 1C can be seen. As it can be viewed, the trend is ascending throughout the whole test, but some peculiar aspects can be highlighted: in fact, several slope variations are present during the discharge process, which strongly depend on the thermal parameters and the heat generation related with electrochemical reactions within the jelly-roll.

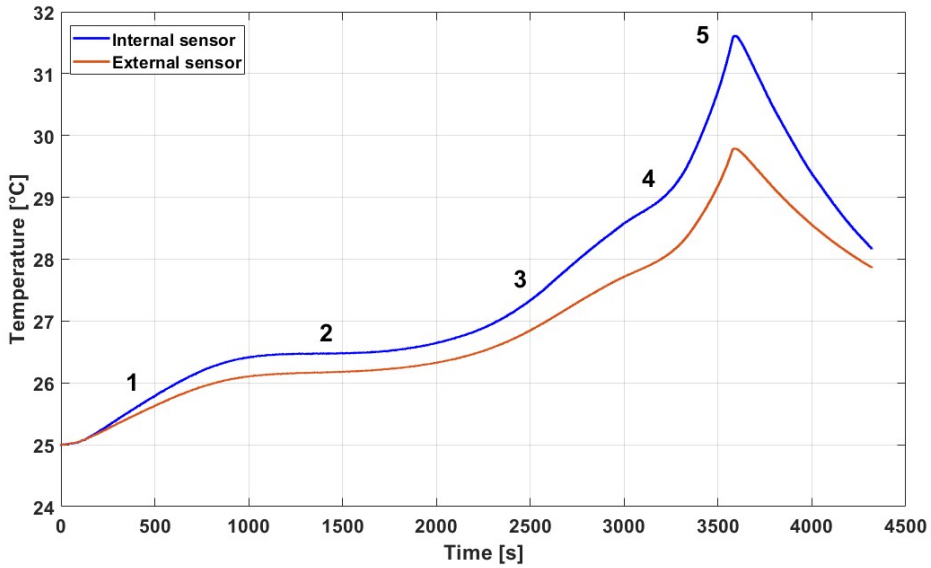

Figure 4.1: Internal and external temperature measurements during a discharge test at 1C on an M1B sample at BOL conditions

On the internal temperature curve (blue line), an initial ramp is present for the first part of the discharge test (1), up to around 1000 $[s]$, after which a plateau can be seen, corresponding to the middle states of charge from 1000 to 2000 $[s]$ (2). Afterwards, the temperature begins again to ramp up, until the end of the discharge process (3 to 5) (a small bending can be seen between 3000 and 3500 $[s]$ (4), suggesting a decrease in the heat generation within the cell).
As it can be noticed, the external temperature sensor (orange line) follows closely the internal one, even if with damped slope changes due to the thermal inertia between the two positions. It must be stressed that, even if the temperature range is very limited, these slope variations can be easily distinguished, thanks to the great accuracy of the FBG sensors. Moreover, a certain divergence can be observed between internal and external temperature measures, mainly related to the (radial) thermal conductivity. Indeed, this parameter is the one that correlates the temperature differences on the radial coordinate. At the end of the discharge test (which corresponds to some seconds before the peak of the temperature curves, as it can be seen in figure 4.2), a difference of around 1.8 $[°C]$ can be noticed between the internal and external sensors.
Afterwards, a very steep temperature decrease is experienced, due to the fact that no generation occurs inside the cell.

Subsequently, the same temperature curve was compared to the DV curve of a discharge test of the same cell at C-rate = 0.04 $[h^{-1}]$ (figure 4.3).

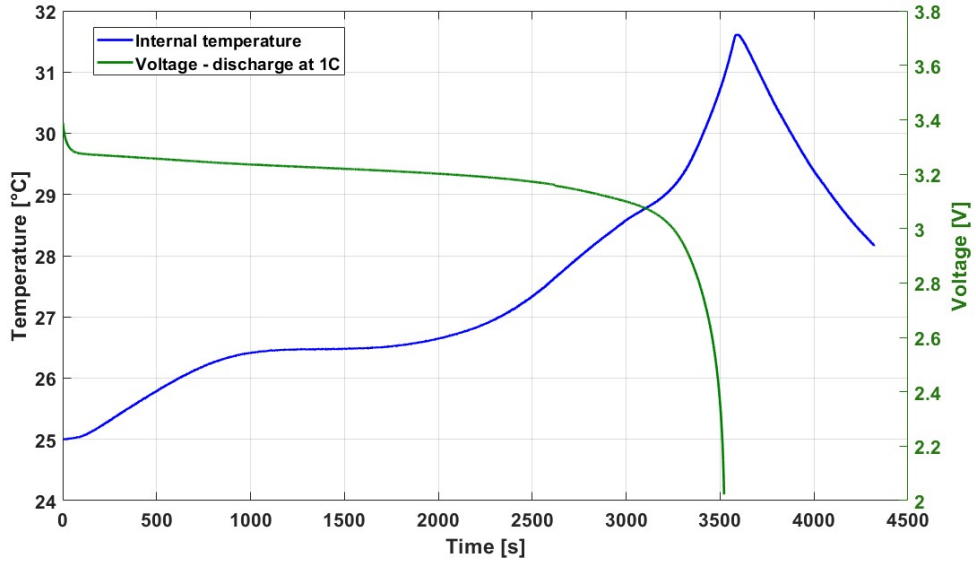

Figure 4.2: Comparison between internal temperature and voltage measurements during a discharge test at 1C on an M1B sample at BOL conditions

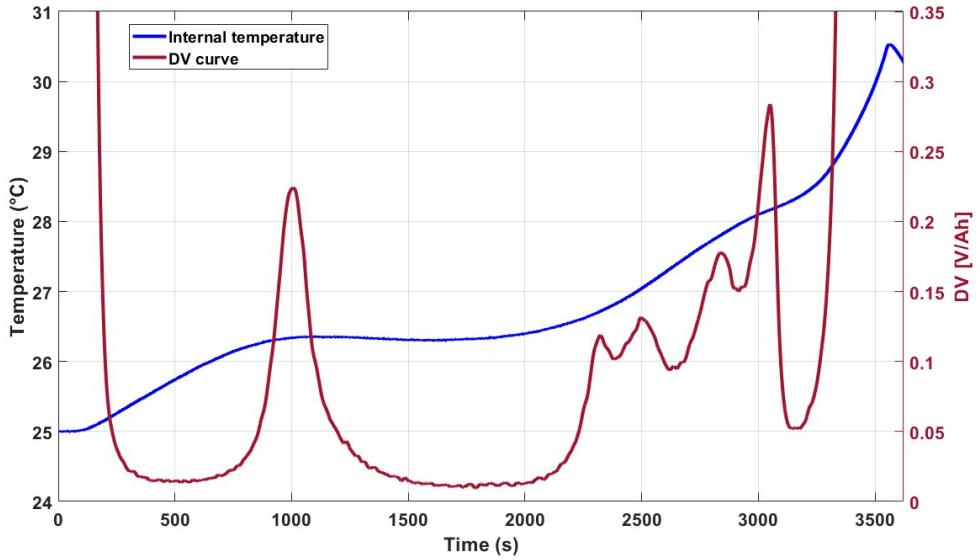

Figure 4.3: Internal temperature during a discharge test at 1C on an M1B sample at BOL conditions, compared to the DV curve of the same cell obtained after a discharge test at 0.04C

This was done to better understand which relationship underwent between the slope changes in the temperature curve and the thermodynamic behavior of the samples, represented by the peaks in the DV curve. The DV curve was translated in the same time domain as the 1C temperature curve, even if the duration of the two tests is not the same:

this was possible due to the fact that a constant current is imposed during the discharge process, so that charge throughput and time axes are interchangeable. In this regard the beginning and the end of the DV curve are not clearly visible in the graph, due to the fact that only the peaks related with the thermodynamic behavior are shown.
As it can be clearly noticed, a correspondence exist between the two curves: in fact, the first peak in the voltage derivative matches almost perfectly with the first "bump" visible in the temperature curve; moreover, also in the subsequent temperature ramp (from around 2000 $[s]$), some similarities can be seen with the peaks in the second part of the discharge curve, leading to the confirmation that a strong correlation exists between temperature and voltage. The link between temperature and voltage is represented by the entropic coefficient, as described in section 1.4.3, which will be addressed further in the following sections.

In addition, discharge tests at a lower temperature were conducted in the climatic chamber, due to the fact that a lower radial thermal conductivity was estimated at this temperature. In particular, several tests were conducted at 10 $[°C]$, measuring both the internal and external temperature of the samples.

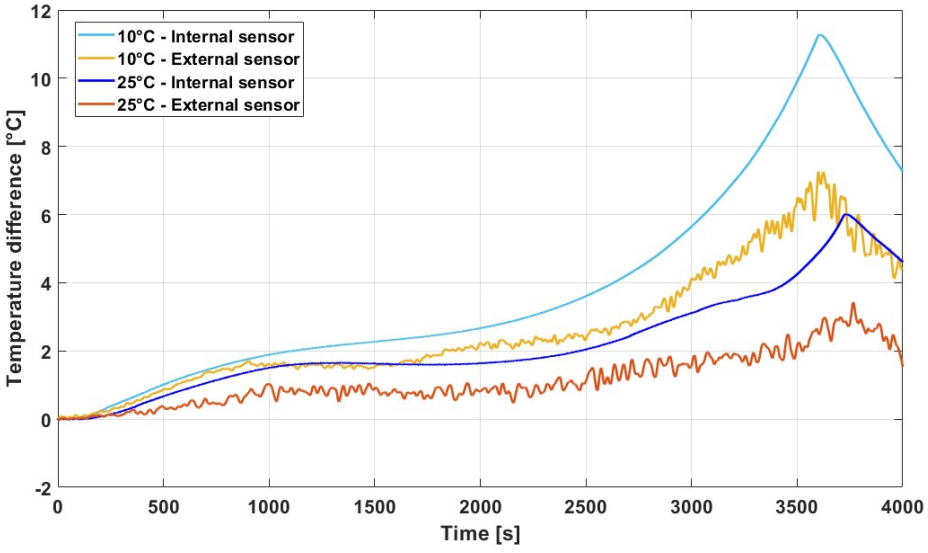

Figure 4.4: Comparison between internal temperature measurements during discharge tests at 1C at different external temperature, on an M1B sample at BOL conditions

As it can be seen in figure 4.4, the internal temperature of the cells during a discharge at low temperature is much higher than the one at 25 $[°C]$, reaching a temperature of more than 5 $[°C]$ higher at the end of the test. Moreover, it can be noticed that the final peak is reached slightly earlier at lower temperatures of the external environment.
Given that an active temperature control was needed for this experiment, a much higher

noise was attained on the external sensor. In fact, as it was explained in section 2.4.1, FBG sensors are capable of measuring simultaneously both temperature and strain variations; for this reason, due to the movement of air volumes inside the climatic chamber, the signal of these optical sensors suffer from a relevant disturbance. In this regard, the external sensors temperature curves were smoothed using a moving average, capable of maintaining the overall behavior but decreasing substantially the measured noise.
The internal temperature curves were then compared with the corresponding voltage curves obtained during the same process (figure 4.5).

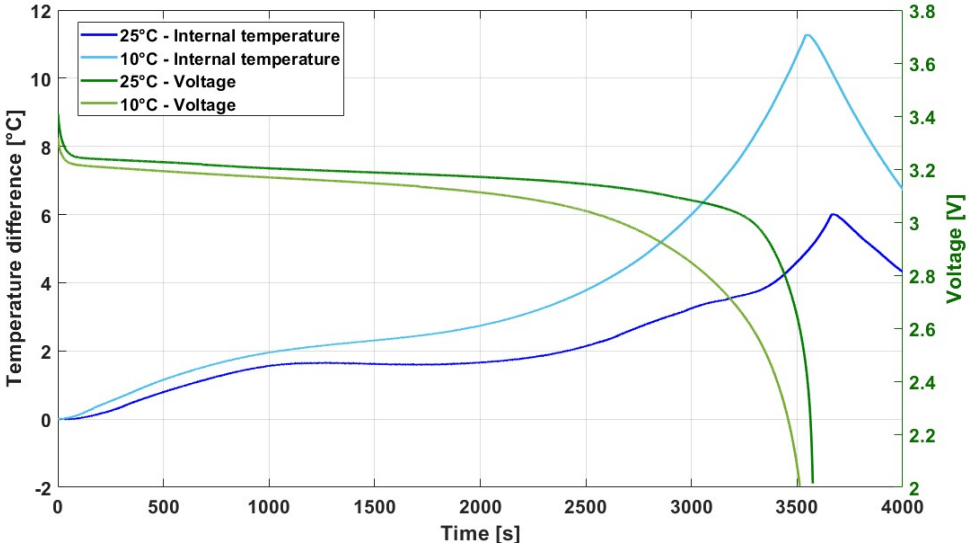

Figure 4.5: Comparison between internal temperature and voltage measurements during discharge tests at 1C on an M1B sample at BOL conditions, at different external temperatures

As it can be observed, a lower voltage curve is obtained for the discharge test at 10 [$°C$]. Moreover, the difference between the two voltage curves increases sharply towards the end of the test, corresponding to the diffusion region. At lower temperature, in fact, lithium-ion batteries are characterized by higher ohmic and diffusion resistances. In turn, this aspect leads to a much higher overpotential during operation, resulting in a greater heat generation. For this reason, a higher temperature is reached at the end of the test. Furthermore, several slope variations during the process become practically invisible because of the increased thermal power, resulting in a much smoother curve.

Additionally, a discharge test at an extreme current rate was performed, to assess the importance of the different contributions to heat generation. In fact, as described in section 1.4.3, equation 1.17, the thermal power generated within the jelly roll can be classified as reversible, related to the electrochemical reaction entropic difference, and

irreversible contributions, linked to overpotentials during operation. The latter term strongly depends on the current rate, as it is proportional to its square value. On the other hand, reversible heat generation is only linearly proportional to current, resulting in a lower contribution as the C-rate is increased. In figure 4.6, the temperature measurement obtained during a discharge test at 10C can be seen.

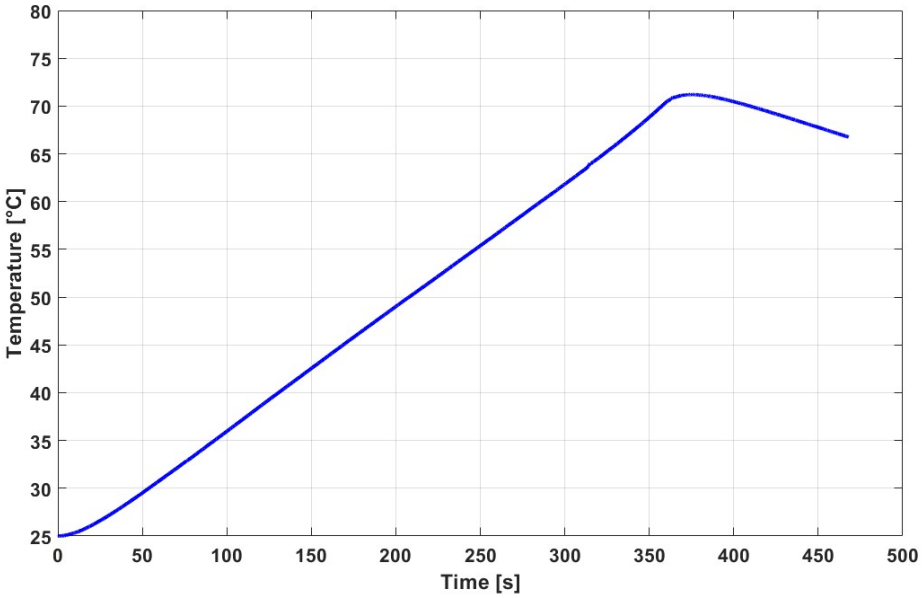

Figure 4.6: Internal temperature measurement during a discharge test at 10C at 25 [$°C$], on a M1B sample at BOL conditions

As it can be noticed, the curve is characterized by a seemingly linear trend, reaching a maximum temperature of around 70 [$°C$] at the end of the process. Moreover, the temperature curve is devoid of the slope variations experienced during the discharge test at 1C, confirming the relative importance between reversible and irreversible contributions.

In addition, very slow discharge tests were performed, using a C-rate = 0.1 [h^{-1}] (figure 4.7). Even if experiments at lower current rates were theoretically possible, in practice it was found that the attainable temperature difference was too low to guarantee a useful assessment. This aspect was worsened by the imperfect temperature control of the climatic chambers. For this reason, a compromise between current rates at quasi-static conditions and temperature variations had to be found.

At such low C-rates, the internal heat generation of the cell can be assumed to be only related to the reversible entropic term, due to the fact that other overpotential contributions can be regarded as negligible.
As it can be seen, the temperature curve presents an almost constant behavior at the

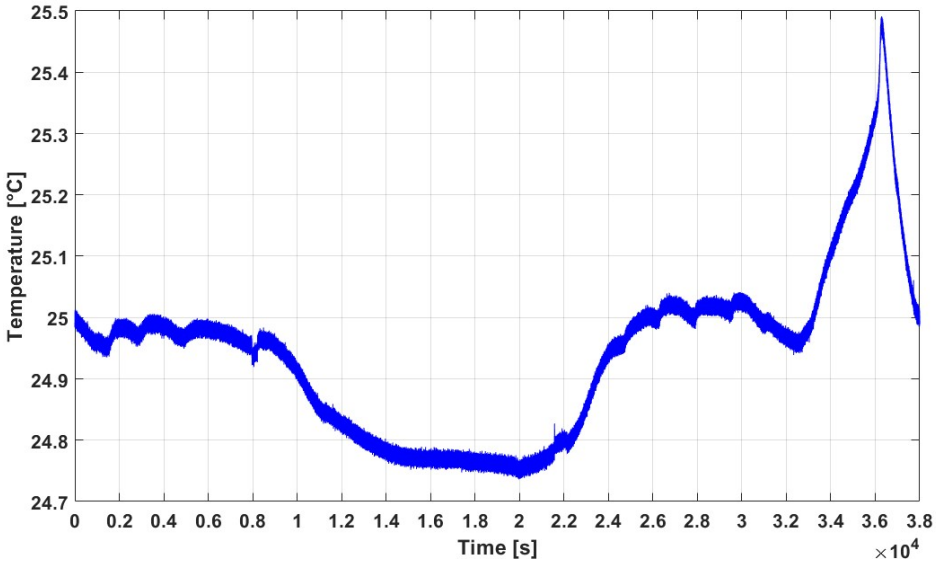

Figure 4.7: Internal temperature measurements during a discharge test at 0.1C on an M1B sample at BOL conditions

beginning of the test, characterized by a plateau that lasts until 8000 $[s]$ of elapsed time are reached. Afterwards, a descending trend is observed, corresponding to a negative contribution of the generated heat, which lasts approximately until 22000 $[s]$ of elapsed time, reaching a maximum temperature difference of 0.25 $[°C]$. Subsequently, a new plateau can be noticed, followed by a steep increase during the final part of the discharge test. At the end of the process, a temperature difference of around 0.5 $[°C]$ is achieved for the internal temperature, which corresponds to the maximum value during the test. In addition, a small but appreciable temperature decrease can be noticed just before the final ramp, approximately at 32000 $[s]$.
Particularly in the plateau regions around the equilibrium temperature, several adjustments can be seen on the curve: in this regard, the most probable cause of these smaller variations was assumed to be related to the active control of the climatic chamber that, for long tests and at such low temperature differences, becomes more relevant. On the other hand, this temperature curve demonstrates the great capability of FBG optical sensors in measuring dynamic variations of temperature.

The same discharge test was repeated at a lower external environment temperature, corresponding to 10 $[°C]$ (figure 4.8).

It can be seen that the curves obtained at 10 and 25 $[°C]$ are almost identical with each others, throughout the whole process. The only differences can be found at around 5000 $[s]$, where a higher temperature is reached for the 10 $[°C]$ test, and at the end of the

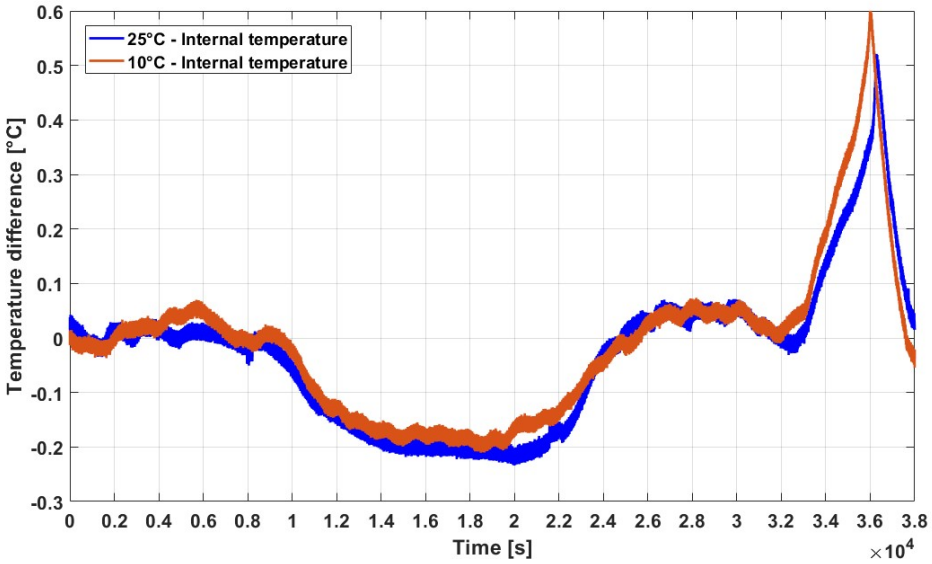

Figure 4.8: Comparison between internal temperature measurements during discharge tests at 0.1C at different external temperature, on an M1B sample at BOL conditions

discharge process, where a greater final temperature is attained; however, both could be regarded as imperfect temperature control of the chamber.

Aged cell

The aged cell was subjected to the same tests as the sample at BOL conditions, measuring both the internal and external temperature. In particular, discharge tests at 1C and 0.1C were performed; consequently, a comparison between cells at BOL and aged conditions was done to assess the main differences.

In figure 4.9, the internal and external temperatures measured on the aged cell during a discharge test at 1C can be seen: the behavior is very similar to the one of the BOL cell, with several slope changes throughout the process. Moreover, the external temperature follows closely the internal one, as it was for the BOL case. The two internal temperature curves were then plotted as comparison (figure 4.10).

Because of the lower available capacity, the duration of the discharge test of the aged cell is significantly lower than the one at beginning of life, leading to a different behavior throughout the process. In addition, the reached temperature is more than 1 $[°C]$ lower than the other curve at the end of the test. On the other hand, at parity of elapsed time (and thus of charge throughput), the aged cell reaches a higher temperature compared to the BOL case. This aspect in particular is very important in real life applications,

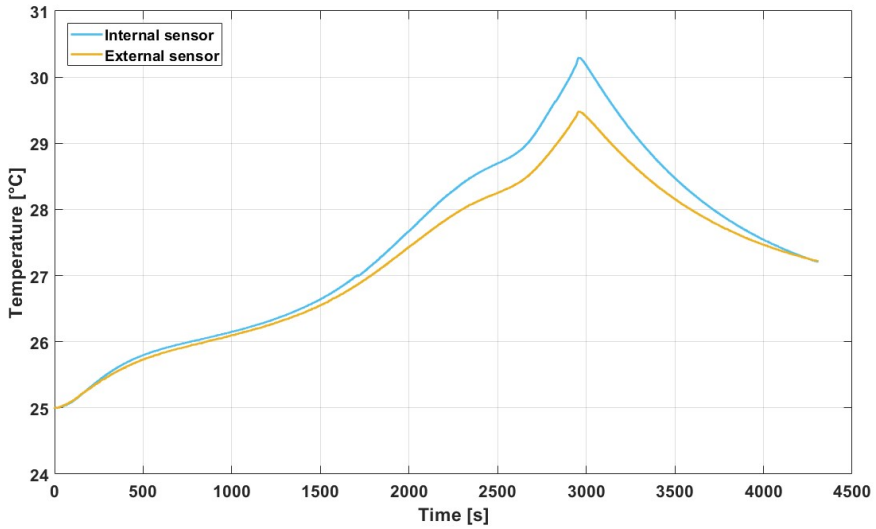

Figure 4.9: Internal and external temperature measurements during a discharge test at 1C on an M1B sample after calendar aging

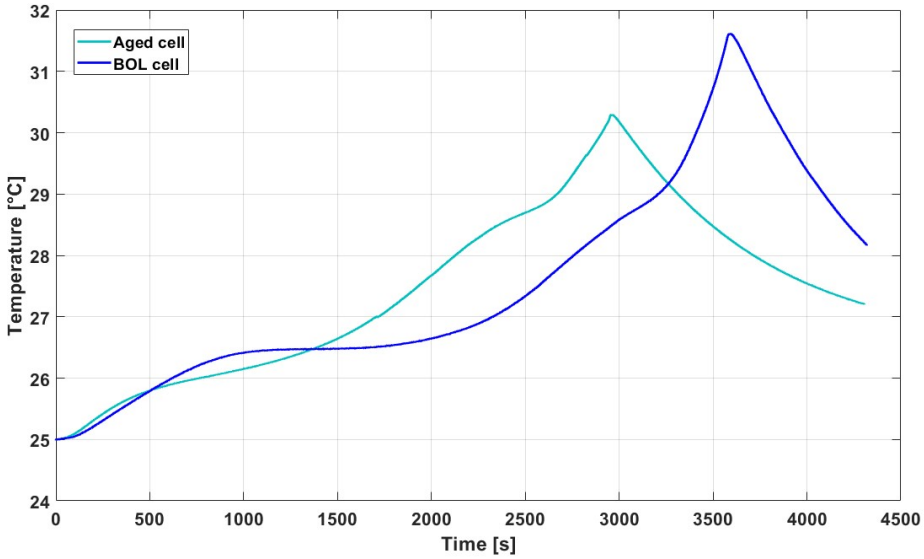

Figure 4.10: Comparison of internal temperature measurements during a discharge test at 1C between M1B samples at BOL and aged conditions

because it demonstrates that aged cells behave differently during operation, especially at the end of the process.

It was known from the electrochemical characterization of the samples (section 3.3.1, figure 3.24) that the main aging mode which acted on the degraded cell was calendar aging, due to the storage period at 60 [$°C$]. This caused a visible shift of the first peak

in the DV curve, related to graphite, towards lower charge throughput: the same aspect can be also seen in the temperature curves. In fact, if the DV curves obtained for the same cells from a discharge at 0.04C were plotted together with the temperature curves (figure 4.11), it can be noticed that the same peak shift can be seen in both curves. In this instance, the DV curves were stretched from the charge domain to the time domain: the DV curves seem to start and finish respectively after and before the corresponding temperature curves. However, it must be considered that only a portion of the curves is visible, due to the fact that in the first and last regions the slope variations in the voltage curve are one order of magnitude higher than in the central part, where a plateau is experienced.

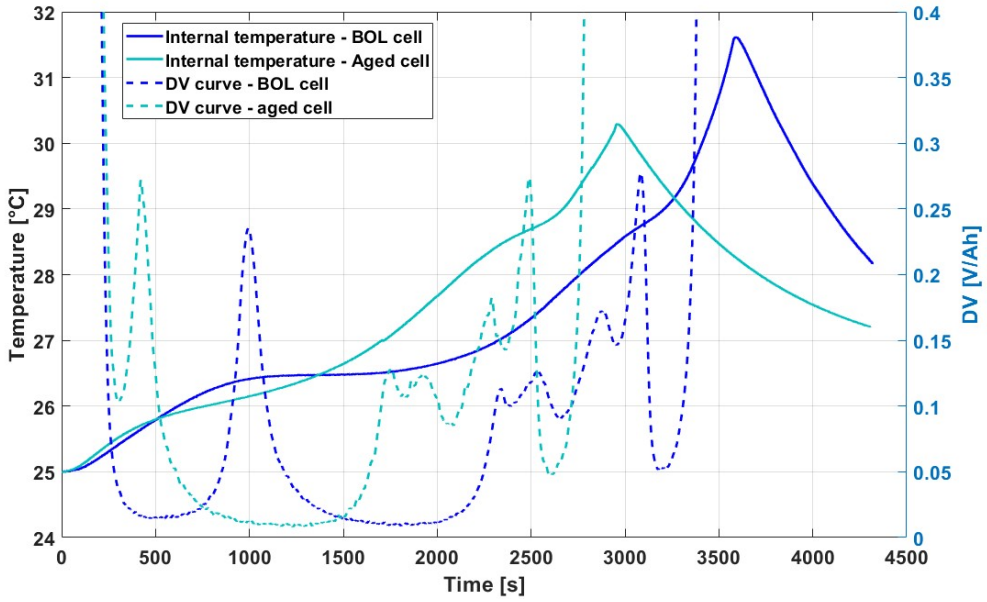

Figure 4.11: Comparison of internal temperature measurements during a discharge test at 1C between M1B samples at BOL and aged conditions, coupled with the DV curves of the respective cells

In the temperature curve of the aged cell, this aspect is reflected in a first "hill" that appears earlier in the curve and that is characterized by a lower temperature ramp; the plateau visible for the BOL cell, instead, is less pronounced for the degraded sample, which lead to a different evolution of temperature in the first part of the discharge test. On the other hand, the second part of the internal temperature measurement is very similar in both curves, as the same slope variations can be noticed. In particular, this attribute could lead to the assumption that very little degradation had happened at the positive electrode during the calendar aging campaign, as the portion regarding its behavior remained almost unchanged. Calendar aging, in fact, is strictly related to the formation of

a passivation layer at the negative electrode, which decreases the cyclable lithium (leading to LLI) and acts as an additional electrical resistance. For this reason, when an aged cell characterized by LLI is charged, it is not capable to reach anymore the same lithiation state at the anode, consequently leading to a shorter discharge process.
This aspect is clearly demonstrated in figure 4.11: the initial part of the temperature curve, corresponding to the highest lithiation states at the anode, is "missing" in the aged sample, while the second half is practically the same between the curves.

In figure 4.12, the comparison between both internal and external temperature curves can be seen.

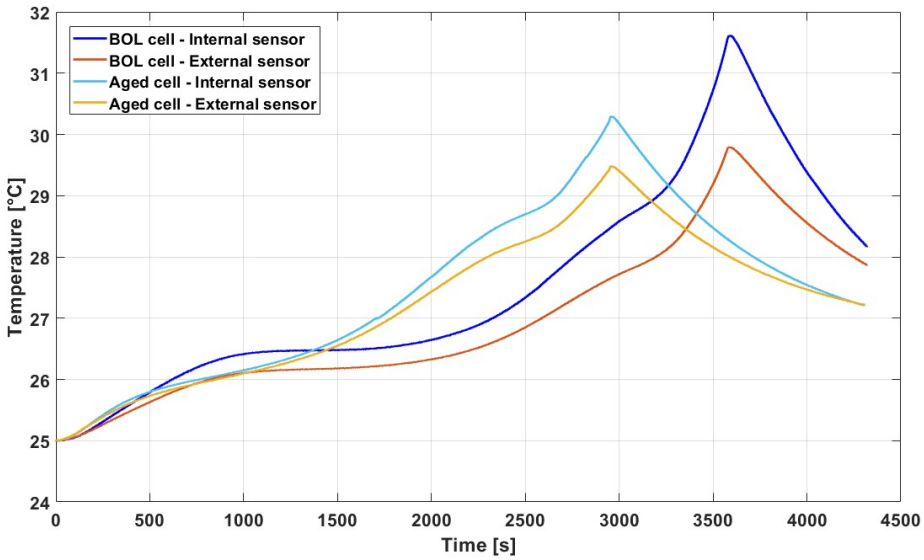

Figure 4.12: Comparison of internal and external temperature measurements during a discharge test at 1C between M1B samples at BOL and aged conditions

Other than the aspects described above, the first difference that can be noticed lies in the final temperature difference between the curve, which in this case is equal to about 0.9 $[°C]$, compared to the 1.8 $[°C]$ witnessed for the BOL sample. In fact, the temperature divergence in the aged cell is significantly lower than the one of the cell at beginning of life throughout the whole discharge process. This can be regarded as a confirmation proof of the increase in the radial thermal conductivity observed in the thermal characterization campaign (section 3.3.4), leading to the conclusion that the worst condition for heat transfer within batteries is achieved at beginning of life.

Figure 4.13 shows the temperature curves obtained from discharge tests of the aged cell at 10 and 25 $[°C]$. Similarly to the beginning of life sample, a higher temperature is

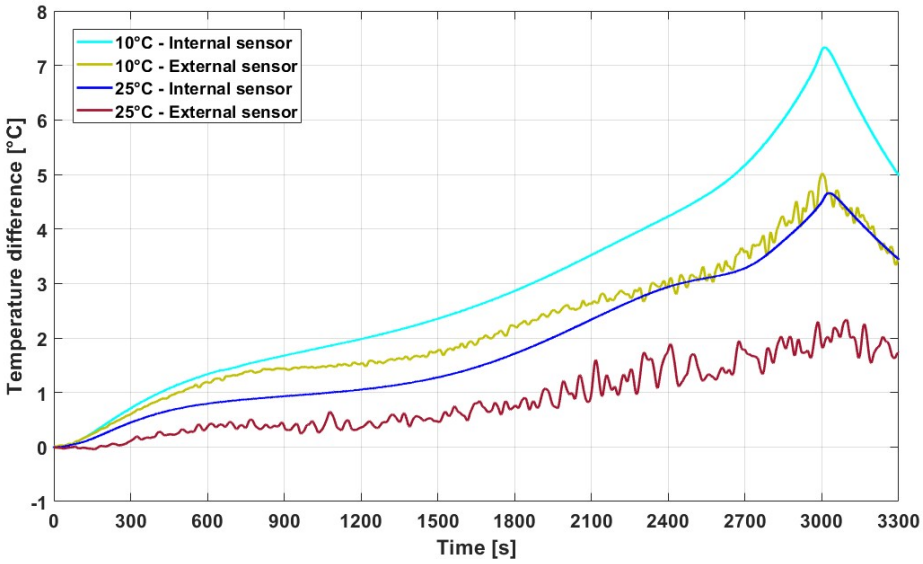

Figure 4.13: Comparison of internal and external temperature measurements during discharge tests at 1C on the aged M1B sample, at different external temperature

achieved at the end of the process for the test at 10 [$°C$], due to the higher overpotentials experienced by the cell. Consequently, a higher irreversible thermal power generation is attained. For this reason, the internal temperature curve is characterized by a smoother evolution, such that slope variations typical of the reversible heat generation term can be hardly seen. Also in this case, the external temperature is characterized by a high grade of noise, resulting in the impossibility to provide a clear description of the thermal resistance between internal and external positions. The maximum temperature difference, which corresponds to the one obtained at the end of the test, lies around 7.5 [$°C$] for the test at 10 [$°C$], compared to less than 5 [$°C$] for the test at 25 [$°C$].

In figure 4.14, the comparison between temperature curves obtained from discharge tests for the BOL and aged cell at 10 [$°C$] can be seen. The same considerations done for the comparison at 25 [$°C$] hold true: in fact, a higher temperature difference is obtained for the BOL cell at the end of the test (equal to around 11 [$°C$]), due to the longer duration; moreover, also in this case, it can be noticed that the first hill-like feature at the beginning of the test is reached earlier for the aged cell, due to the lower available lithium at the negative electrode.
Furthermore, at parity of reached temperature, a similar temperature difference is attained between the internal and external sensors for both samples. This aspect in particular could suggest a lower dependency of the thermal conductivity with aging at lower operating temperatures; however, due to the signal noise it could be difficult to confirm.

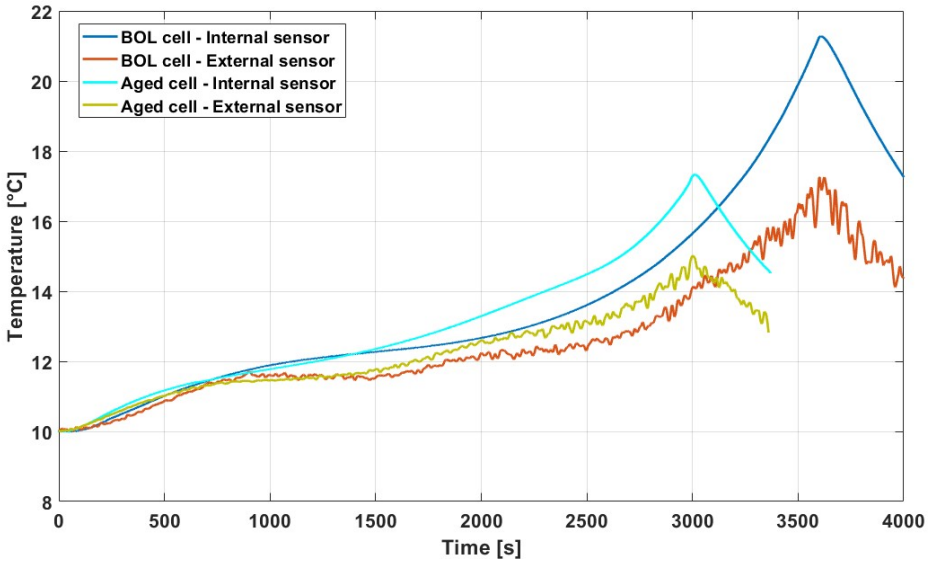

Figure 4.14: Comparison of internal and external temperature measurements during discharge tests at 1C, at 10 [$°C$] between M1B samples at BOL and aged conditions

In figure 4.15, the internal temperature measured during a discharge test at $C-rate = 0.1$ [h^{-1}] can be observed.

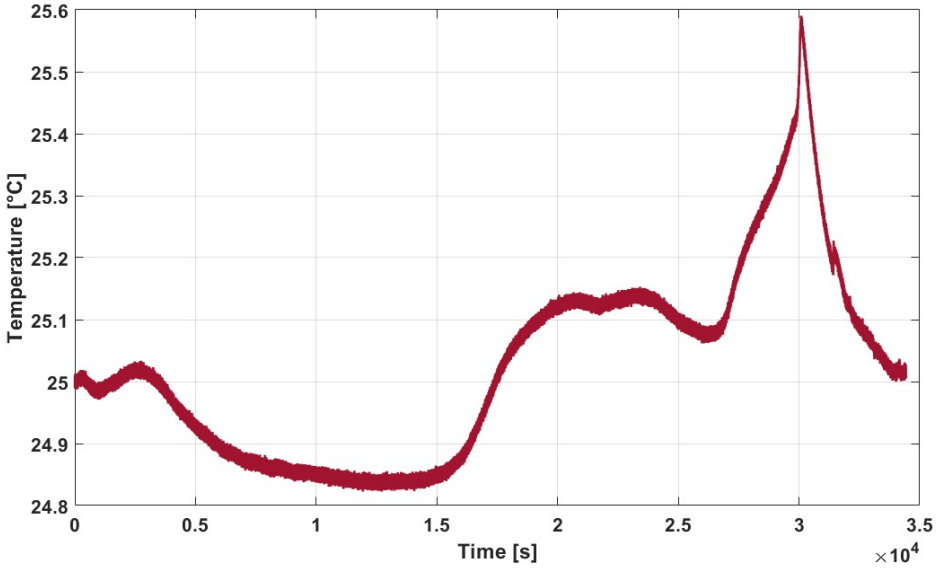

Figure 4.15: Internal temperature measurements during a discharge test at 0.1C on an M1B sample at aged conditions

It can be noted that, in general, the shape is very similar to the one obtained for the beginning of life sample, as the same features can be seen. In fact, a first plateau is present

at the beginning of the test, followed by a "valley" caused by a negative reversible thermal power contribution. Afterwards, another plateau is experienced by the cell, leading to a smaller valley at 26000 $[s]$ and a final temperature ramp characterized by a sharp increase. Finally, the system undergoes a temperature homogenization until thermal equilibrium is reached.

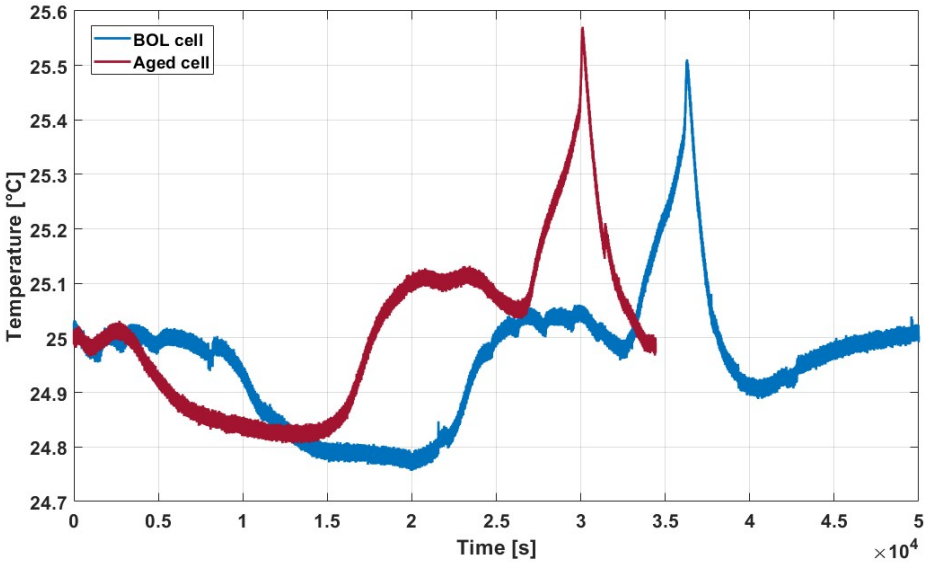

Figure 4.16: Comparison between internal temperature measurements during discharge tests at 0.1C of M1B samples at BOL and aged conditions

When compared to the BOL internal temperature curve (figure 4.16), a clear shift can be noticed between the two curves: in fact, it can be seen that, for the aged sample, the first valley is reached much earlier in time, at 4000 $[s]$, compared to almost 10000 $[s]$ for the BOL cell. Subsequently, a very similar behavior is observed for both tests, leading to a final temperature difference of 0.5 $[°C]$. Then, the two curves were matched at the end of the discharge test, corresponding to the lowest state of charge (figure 4.17).

It can be distinctly recognized that, when the curves are lined up from the final temperature, they are practically identical for most of the experiments: the only appreciable difference lies in the first part of the discharge, corresponding to the higher states of charge.
This experimental evidence can be regarded as a further confirmation of the considerations done for the tests at 1C, related to the lithiation state at the anode prior to the discharge. In this regard, figure 4.16 clearly demonstrates that the shift experienced by the aged cell can be assumed to be dependent only on the reversible heat generation term, linked to the reaction entropy difference. It can be further stated that the reversible ther-

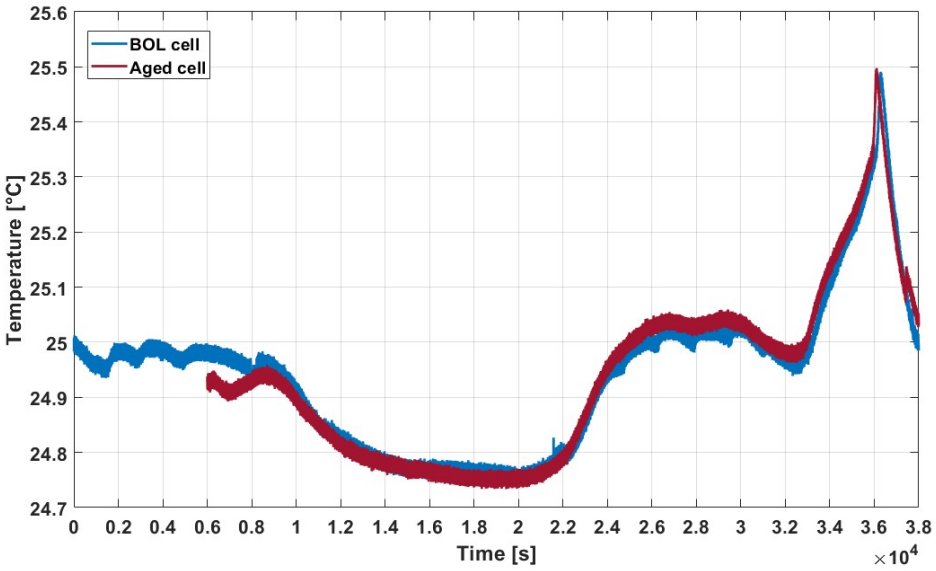

Figure 4.17: Comparison between internal temperature measurements during discharge tests at 0.1C of M1B samples at BOL and aged conditions, paired at the end of the process

mal power term and the resulting internal temperature are directly correlated with the lithiation states at the batteries electrodes and thus on the thermodynamics of the cell.

Finally, a discharge test at the external temperature of 10 $[°C]$ was performed on the aged cell, measuring the internal temperature. The comparison with the same test at 25 $[°C]$ can be seen in figure 4.18.

As it can be observed, the temperature obtained at 10 $[°C]$ is characterized by stronger oscillations than the 25 $[°C]$ case; nonetheless, the FBG sensor is able to seize all of the slope variations. In the same way of the BOL sample, also the temperature curves for the aged cell can be almost perfectly superimposed, confirming the assumption that the reversible heat generation is characterized by a weak dependency with temperature.

4.1.2. Charge tests

Charge tests were performed as well, with the simultaneous measurement of the internal and external temperature through the FBG sensors.

Beginning of life cell

In figure 4.19, the temperature evolution during a charge test at C-rate $= 1$ $[h^{-1}]$ can be seen.

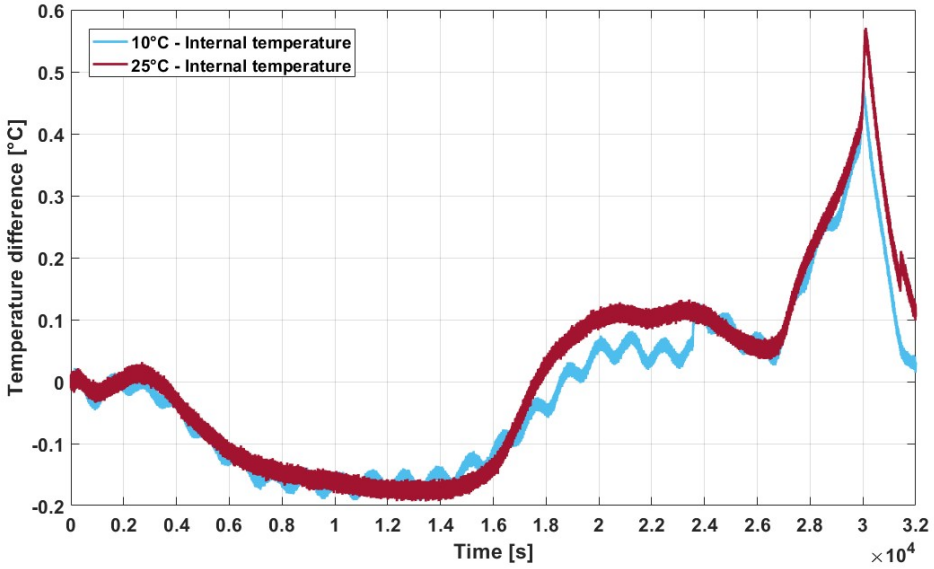

Figure 4.18: Comparison between internal temperature measurements during discharge tests at 0.1C of the aged M1B sample at different external temperature

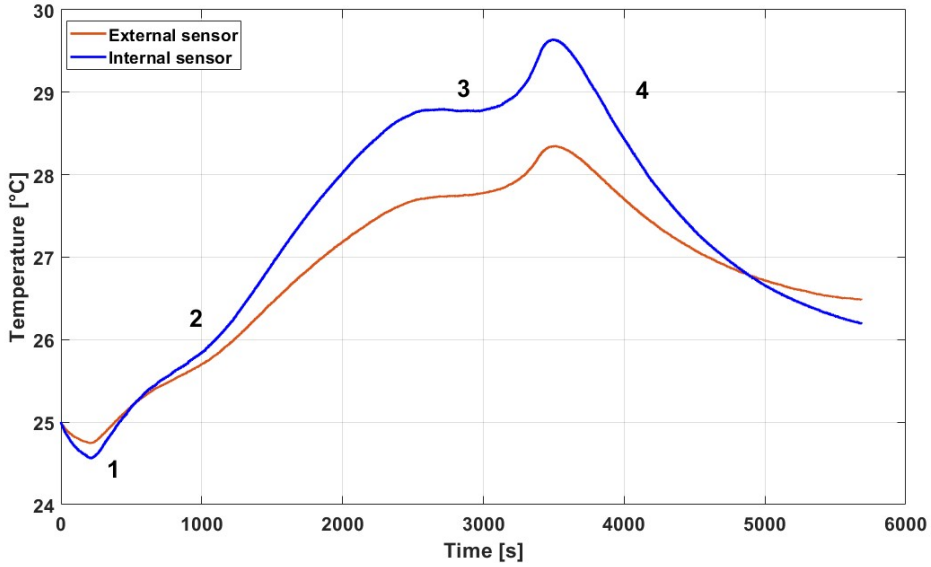

Figure 4.19: Internal and external temperature measurements during a charge test at 1C on an M1B sample at BOL conditions

As it was the case for the discharge tests, it can be observed that several slope changes appear in the curve: in particular, in the first period of the charge process, corresponding to the lowest states of charge, the temperature has a negative trend (1), resulting in a temperature difference of almost 0.5 [$°C$].
Given that the charge process is carried at 1C, several irreversibilities exist, which corre-

spond to the overpotentials arising on the voltage curve during operation, as described in section 1.1.2. These terms always lead to a positive heat generation, that tend to increase the temperature of the system (2). Nonetheless, the fact that a negative slope is obtained experimentally could lead to the assumption that the reversible entropic heat contribution (which is the only other term in the heat production of the cell) has a strong negative trend at the lowest $SoCs$, that outweighs even the overpotentials irreversibilities.
Another notable aspect lies in the plateau observed towards the end of the charge process from 2500 to around 3000 $[s]$ of elapsed time (3), where the temperature slope experiences a strong decrease. Also in this instance, it could be assumed that a negative entropic heat contribution exists. Finally, a temperature decrease is experienced at the end (4).
For what concerns the external temperature, it follows closely the shape of the internal sensor one, also during the first part of the test, after which the two curves cross with each others. Because of the thermal conductivity, a certain divergence can be noticed between the two temperature curves, whose maximum difference lies around 1 $[°C]$ in the final phase of the process.
Similarly to the discharge instance, in figure 4.20, the internal temperature curve was coupled with the corresponding voltage measurement during the charge test.

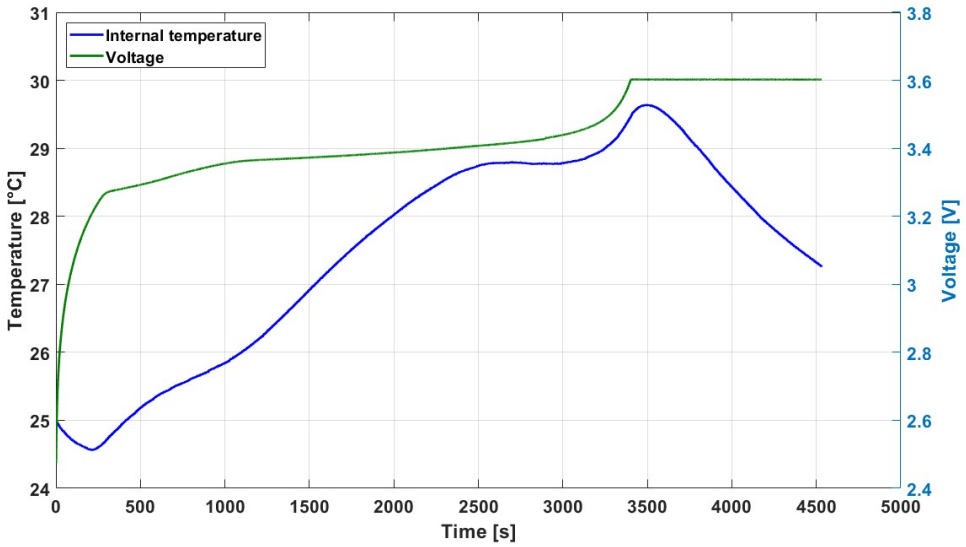

Figure 4.20: Internal temperature and voltage measurements during a charge test at 1C on an M1B sample at BOL conditions

As described in section 2.3.1, the protocol employed for a charge test consists in a first constant current (CC) phase, followed by a constant voltage (CV) one, during which the voltage level is kept at the upper limit. In the figure above, both can be seen, so that a fair comparison can be carried with the the internal temperature. It can be noted that,

contrarily to the discharge test, in this case the final peak visible in the temperature curve is less sharp than its counterpart. In fact, unlike in discharge mode, after the CC phase of the charge process, the current doesn't immediately go to zero, but experiences a slow decrease during the CV phase, until the termination current is reached. In this way, the power given to the cell (and thus the heat generation through the overpotentials) doesn't abruptly drop to zero, but gradually diminishes, causing a smoother temperature curve in the final part of the process; finally, as the current decreases, the cell experiences a cooling process as the temperature goes down.
Additionally, it can be observed that a link exists between the slope changes of the temperature and voltage curves, that can be attributed to thermodynamic variations of the internal states of the cell, as already described for the discharge tests.

After this step, two additional charge tests were performed, starting after different resting periods, to assess the impact that this parameter could have on the resulting temperature curve. The outcomes are presented in figure 4.21. As comparison, the curve related to the "Test 1" was obtained after a very long relaxation time, so that the equilibrium potential could be reached at $SoC = 0$.

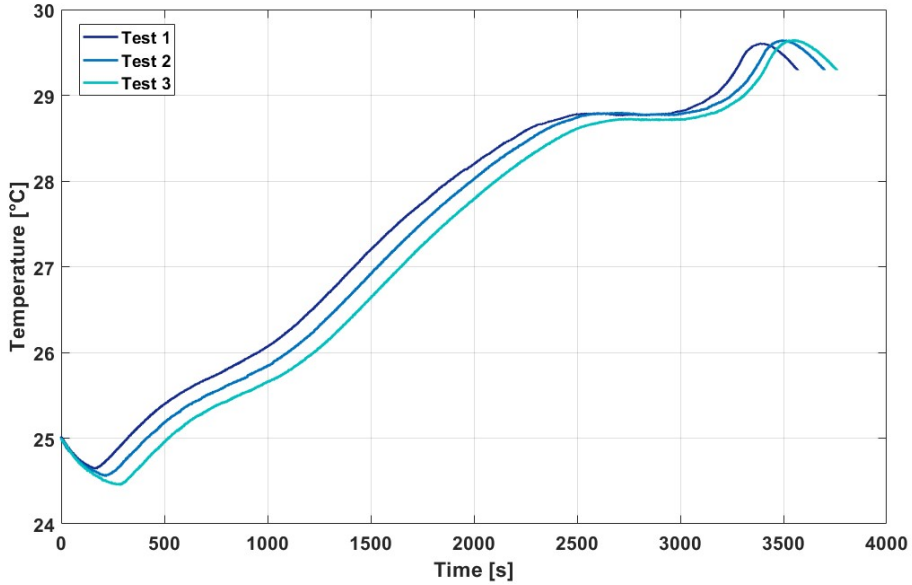

Figure 4.21: Internal temperature measurements during charge tests at 1C, starting after different resting periods on an M1B sample at BOL conditions

As it can be seen, there is great accordance between the curves, throughout almost the whole process: in fact, the measurements have all the same behavior in the central and final part of the test, following seemingly parallel lines and ending at about the same temperature level (around 29.5 $[°C]$). The only apparent difference lies in the first part

of the charge tests, where the temperature curves are characterized by a negative slope. In fact, it can be noticed that the curves at different starting voltage are distinguished by a different first descending trend, which lasts longer as the initial voltage decreases. This difference is then kept for the remainder of the test.
To make things more clear, the same temperature measurements were plotted against their respective voltage curves (figure 4.22): as it can be seen, a decrease of the initial voltage difference causes a shift in the subsequent voltage curve, so that the upper voltage limit is reached later. This deviation is maintained in the temperature curve as well, showing further proof of the strong correlation between them.

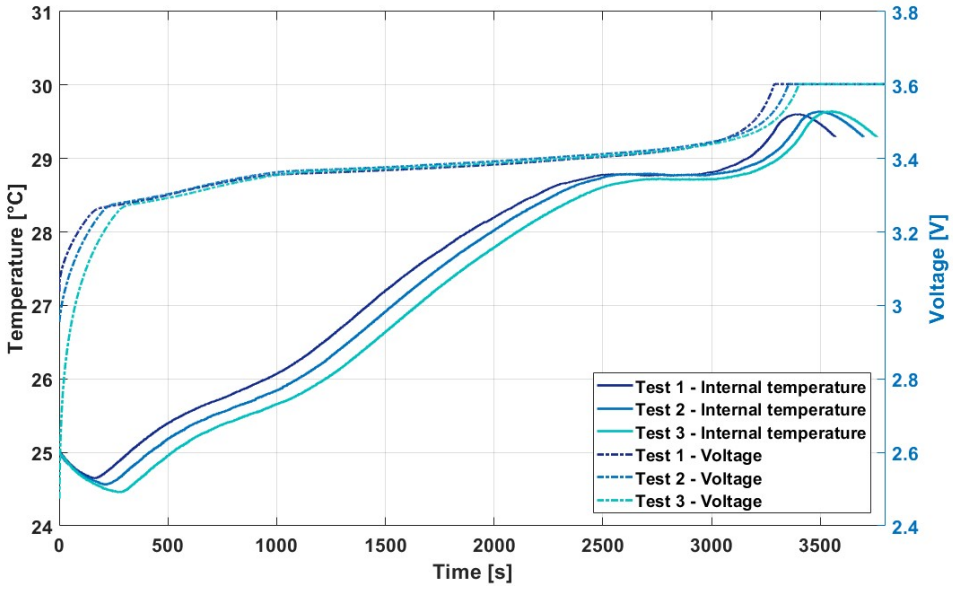

Figure 4.22: Comparison between internal temperature and voltage measurements during charge tests at 1C, starting from different voltage levels on an M1B sample at BOL conditions

Similarly to discharge processes, the internal temperature during the 1C charge test was compared with the DV curve of the same cell obtained after a charge at 0.04C (figure 4.23).
Also in this case, a relatively good accordance can be found between the two curves, such that the peaks in the DV curve correspond to the slope variations on the internal temperature. In addition, it can be noted that the final plateau, situated between 2500 and 3000 $[s]$ of elapsed time, corresponds quite well with the last valley on the DV curve. As observed in the electrochemical characterization of cells in section 3.3.1, this feature corresponds with the highest lithiation states at the negative electrode, and gradually disappears with calendar aging related phenomena.

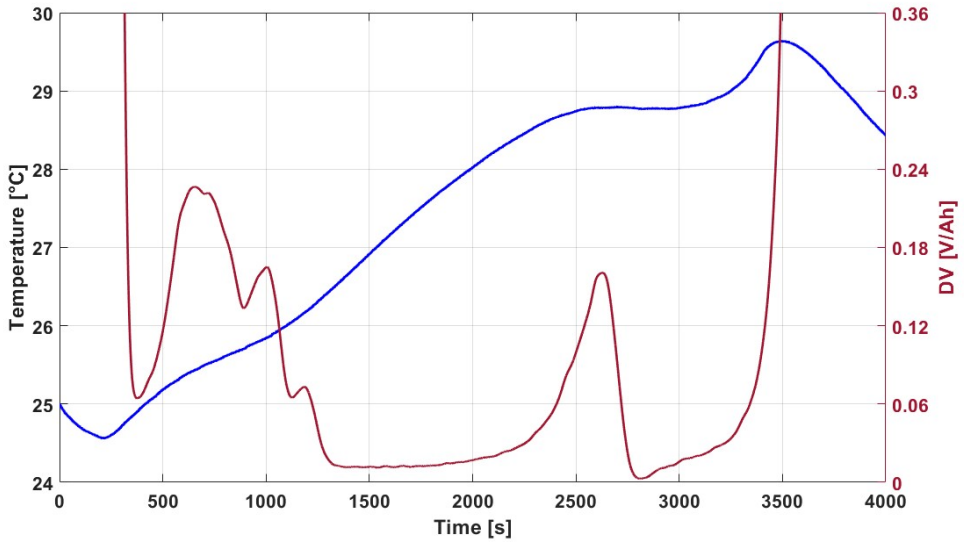

Figure 4.23: Internal temperature during a discharge test at 1C on an M1B sample at BOL conditions, compared to the DV curve of the same cell obtained after a discharge test at 0.04C

In figure 4.24, the comparison between internal temperature curves obtained at different external temperature is presented.

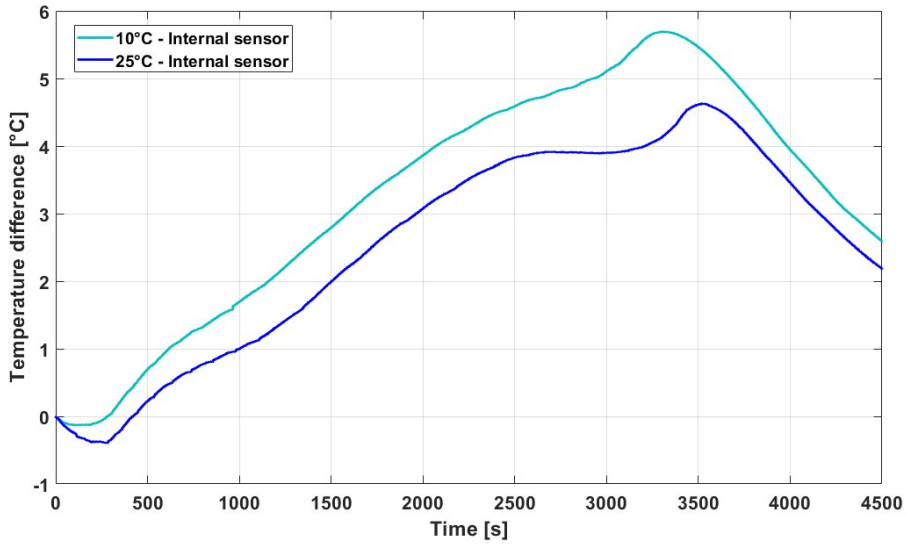

Figure 4.24: Comparison between internal temperature measurements during charge tests at 1C at different external temperature, on an M1B sample at BOL conditions

The same considerations done for the discharge test can be done also in this case: at lower operating temperatures, a slightly higher slope can be noticed, particularly in the initial

and final portion of the temperature curve. In fact, it can be seen that the initial section, characterized by a negative slope at 25 [$°C$], is only partially visible at 10 [$°C$]. Moreover, also the final plateau is hardly noticeable at low temperature, as only a slope variation of low entity can be observed.
For a better understanding of the involved phenomena, the internal temperature measurements were plotted against their respective voltage curves, obtained during the same charge tests. The comparison between them can be seen in figure 4.25.

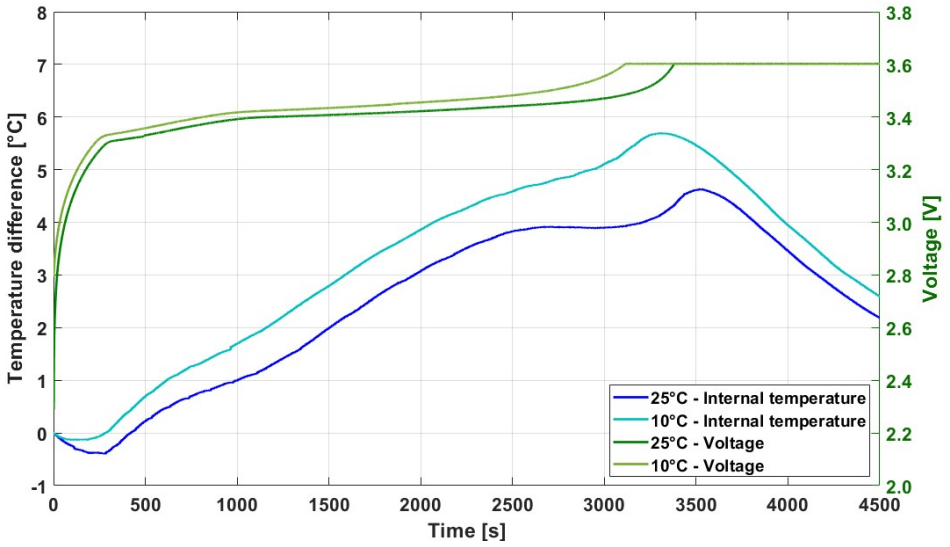

Figure 4.25: Comparison between internal temperature and voltage measurements during charge tests at 1C on an M1B sample at BOL conditions, at different external temperatures

As it was the case for discharge tests, at lower temperature the samples are characterized by a different behavior, because the voltage curve obtained at 10 [$°C$] is slightly higher. Consequently, a higher overpotential is experienced by the cell, resulting in a higher heat generation throughout the whole process: the biggest difference is attained towards the end of the test, explaining in this regard the absence of the final plateau on the internal temperature curve. In general, it can be stated that the higher thermal power generation is the cause of the higher temperature attained during the test at 10 [$°C$].

In addition, charge tests at quasi-equilibrium condition were conducted on the BOL cell. In particular, a charge test at $C-rate = 0.1$ [h^{-1}], already described in section 3.3.3, figure 3.45, was performed. It can be seen that the general shape of the internal temperature measurement strongly resembles the one obtained from the low current rate discharge test, if this was flipped on both axes (figure 4.26). In fact, the central region on the curve is characterized by two plateaus separated by a hill-shaped feature. Moreover,

the small peak at around 5000 $[s]$ is experienced by both processes. However, some differences can be noticed between the two curves, particularly at extreme states of charge, corresponding to the beginning and end of the test: at these conditions, distinct slope variations can be observed on the two curves. In this regard, in the initial part of the charge a smoother valley can be seen, compared to the sharp ditch-shaped feature at the end of discharge. Furthermore, at the end of the charge process, the internal temperature presents a noticeable peak which is not present in the discharge process at the same state of charge. For these reasons, it could be assumed that the reversible entropic heat could depend on the specific process, being different between charge and discharge temperature curves at extreme SoC.

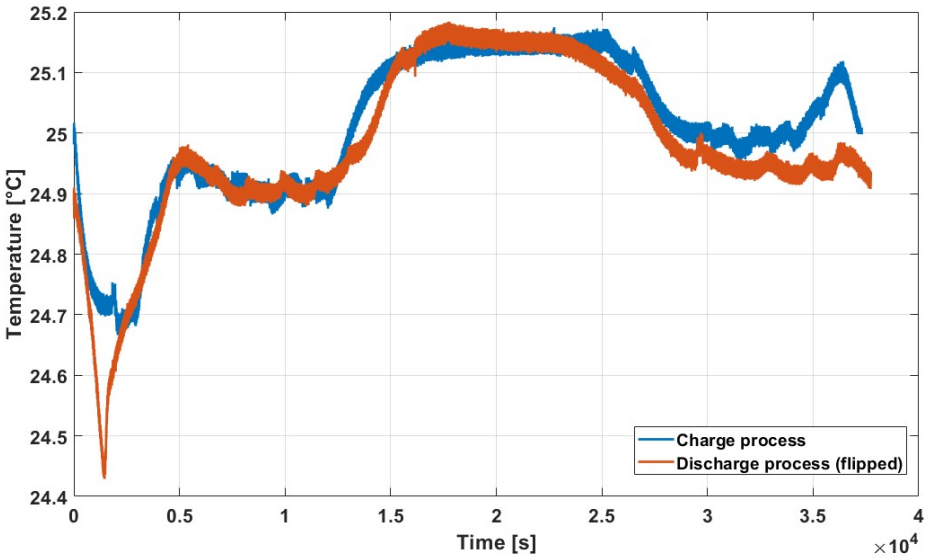

Figure 4.26: Comparison between internal temperature measurements during charge and discharge tests at 0.1C, on an M1B sample at BOL conditions

In addition, the charge test at 0.1C was compared with an analogous test at 10 $[°C]$ (figure 4.27).
The earliest difference encountered between the two curves can be seen at the beginning of the process, where the initial valley in the figure is less pronounced for the test at 10 $[°C]$. This aspect in particular could also explain the "shallower" valley seen in the charge test at 1C, meaning that a lower reversible heat contribution (in absolute terms) is experienced by the batteries at lower operating temperatures. Nonetheless, the two curves are very similar in the central portion, until 22000 seconds. Around this amount of elapsed time, in fact, a small but appreciable bump can be seen in the curve at 10 $[°C]$, resulting in a higher temperature compared to the other. Moreover, the final plateau appears compressed with respect to the curve at 25 $[°C]$, leading to a much higher peak at the end

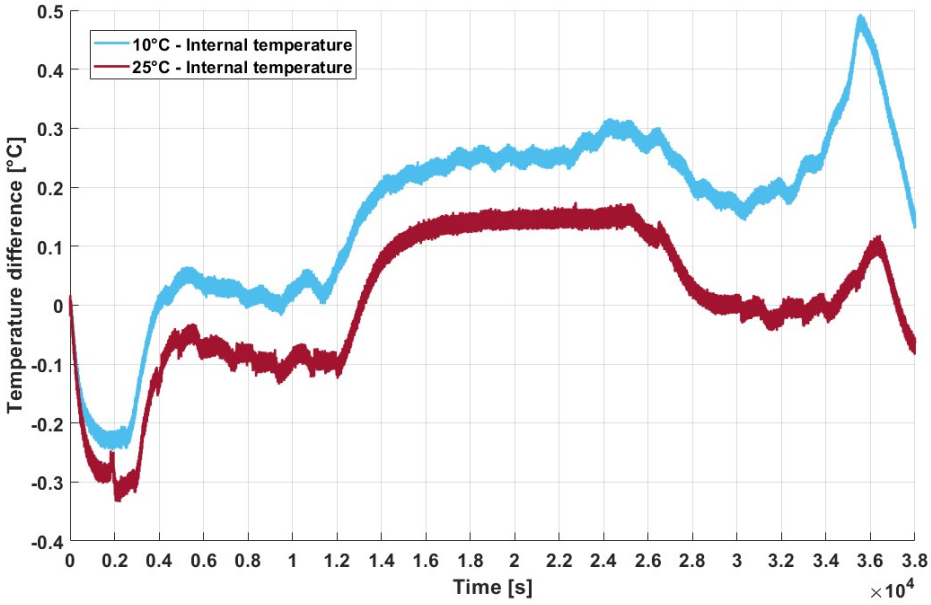

Figure 4.27: Comparison between internal temperature measurements during charge tests at 0.1C at different external temperature, on an M1B sample at BOL conditions

of the process. Apart from this last feature, the light blue temperature curve generally presents less marked slope variations throughout the process, which could explain the same aspect described for the test at 1C.

Aged cell

The aged sample underwent the same discharge tests as the beginning of life cell. In this regard, the internal and external temperatures curves of the aged cell during a 1C charge test can be seen in figure 4.28.
Similar features visible for the BOL could be noticed also in this case: in particular, the first negative trend is repeated at the beginning, as well as the slope variations present in the middle part of the charge process, namely at the central states of charge. Moreover, also the temperature divergence between internal and external sensors can be seen in the graph, which increases at the internal temperature grows.
The greatest difference between beginning of life and aged samples can be noticed in the final part of the temperature ramp, as it can be seen in figure 4.29. In this graph, the two internal temperature curves were compared to assess the main differences between them.

It can be clearly seen that the two temperatures follow the exact same behavior during the first half of the charge process: in this regard, it can be understood that no difference can

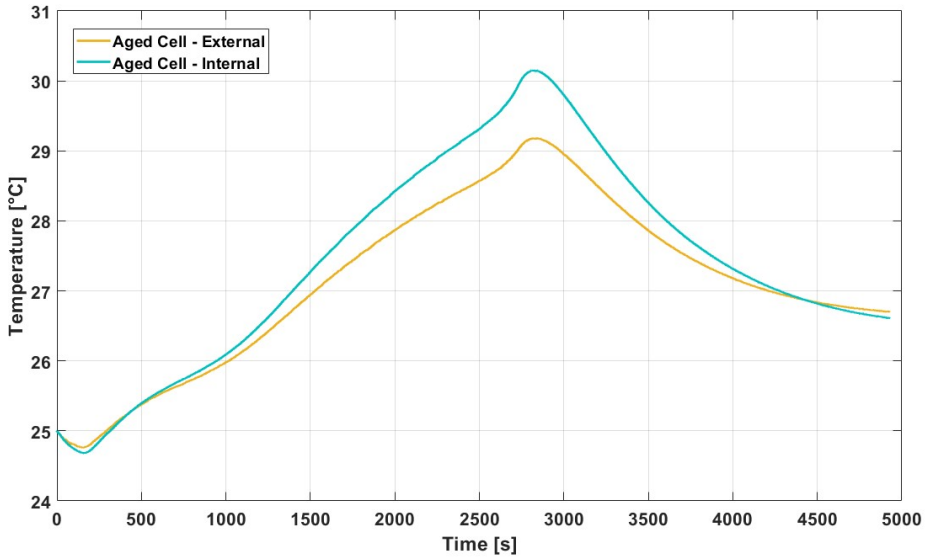

Figure 4.28: Internal and external temperature measurements during a charge test at 1C on an M1B sample after calendar aging

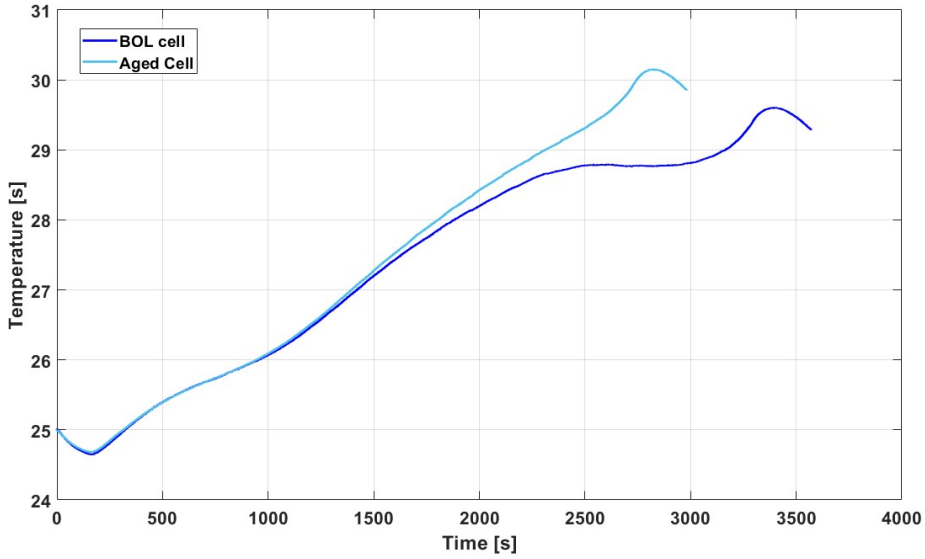

Figure 4.29: Comparison of internal temperature measurements during a charge test at 1C between M1B samples at BOL and aged conditions

be appreciated between the internal states of the two cells at these states of charge. At around 1500 $[s]$ of elapsed time, however, the two curves start to diverge from each others, leading the internal temperature of the degraded cell to reach a higher final temperature at the end of the CC phase of the charge test (that corresponded to about 30.1 $[°C]$). Furthermore, the plateau that was very visible for the BOL cell, was in this case almost

non-existent and only a small slope change in the curve could be seen. This aspect in particular was found to be very interesting: as it was the case in the internal temperature curves during discharge tests, the most significant variation between the BOL and aged cell behaviors was found at very high states of charge, corresponding to the highest lithiation levels for the graphite anode. Moreover, given that the most probable cause of degradation during the calendar aging campaign was SEI formation, these features of the temperature curves could be used as an indication of its advancement.
Finally, both the internal and external temperature measurements obtained from the beginning of life and aged samples were compared in figure 4.30, equivalent to the one obtained from the discharge tests.

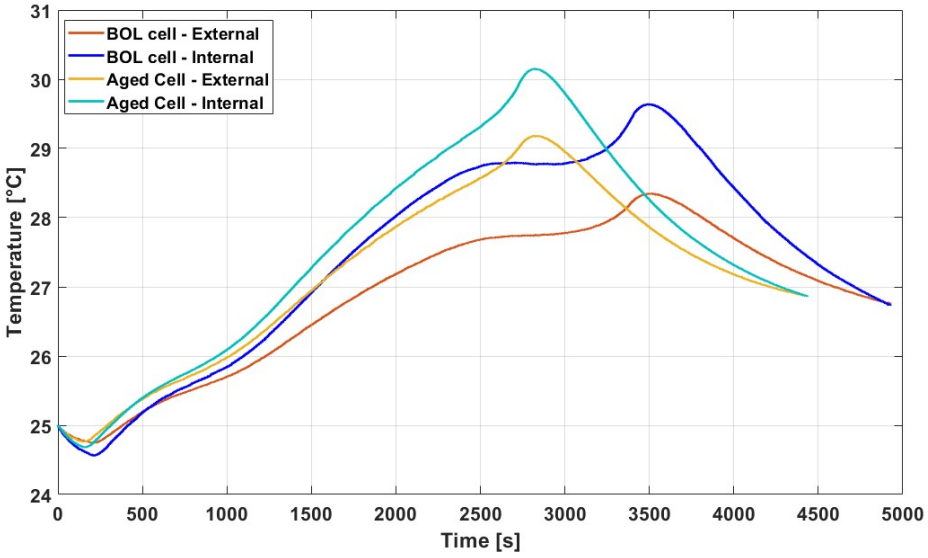

Figure 4.30: Comparison of internal and external temperature measurements during a charge test at 1C between M1B samples at BOL and aged conditions

It can be noticed that, even in the case of charge process, similar conclusions could be drawn. In particular, the external sensors follow the shape of the internal ones, for the duration of the entire test. In the same way, a smaller temperature divergence was experienced by the aged cell, as it was the case for the analogous discharge tests, showing further validation of the increased radial thermal conductivity estimated during the thermal parameters campaign. In fact, at the final peak, a temperature difference of around 1 $[°C]$ was measured.

A similar comparison was done between the aged and BOL cells at 10 $[°C]$, decreasing the operating temperature (figure 4.31).
It can be seen that, also in this case, the general shape is very similar between the two

curves, presenting features. In the initial section, the less steep negative trend found in the beginning of life cell is also encountered in the aged cell. Subsequently, it is observed that the aged cell presents even less pronounced slope variations throughout the process, resulting in an approximately linear trend. This could be caused by the higher overpotentials arising during operation in the aged cell. Furthermore, the external temperature measurements were affected by a great amount on signal noise during the test. For this reason, even if the temperature differences across the cell seems to be comparable, it is difficult to provide a satisfactory assessment.

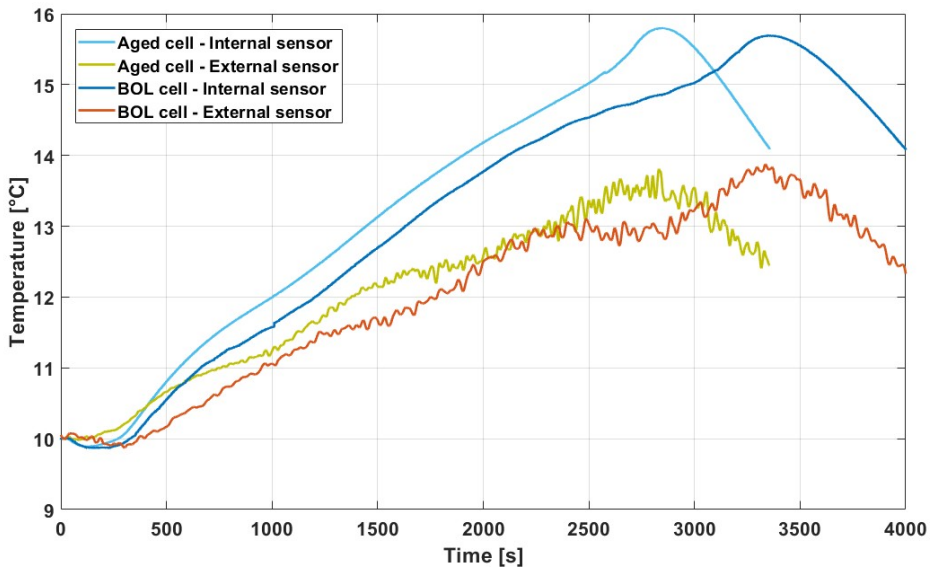

Figure 4.31: Comparison of internal and external temperature measurements during charge tests at 1C and 10 [$°C$] between M1B samples at BOL and aged conditions

Consequently, the comparison between charge tests at 1C at different temperature was done for the aged cell (figure 4.32).

The same considerations made for the BOL cell comparison hold true also in this case. In fact, the curve at 10 [$°C$] is characterized by less evident slope changes compared to the test at 25 [$°C$]. In this regard, it can be noted that working at lower temperature, and thus with higher overpotentials during operation, only emphasize the reduction of slope variations on the internal temperature already caused by aging.

Finally, a comparison was done between charge tests at 0.1C of the cells at BOL and aged conditions (figure 4.33).

It can be observed that the initial part of the curve is very similar between the two cases. However, a higher temperature is reached thereafter for the aged cell, suggesting a higher

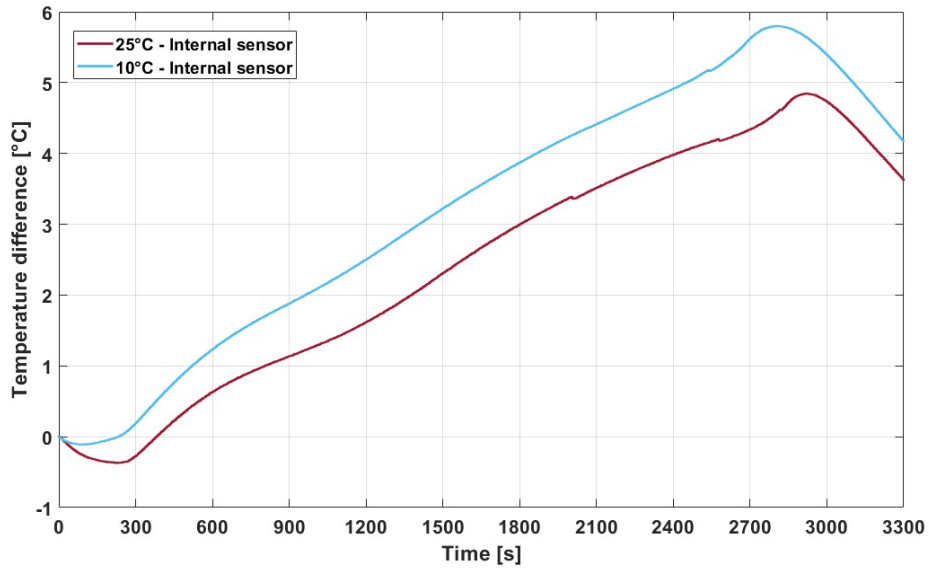

Figure 4.32: Comparison between internal temperature measurements during charge tests at 1C and different external temperature of M1B sample at aged conditions

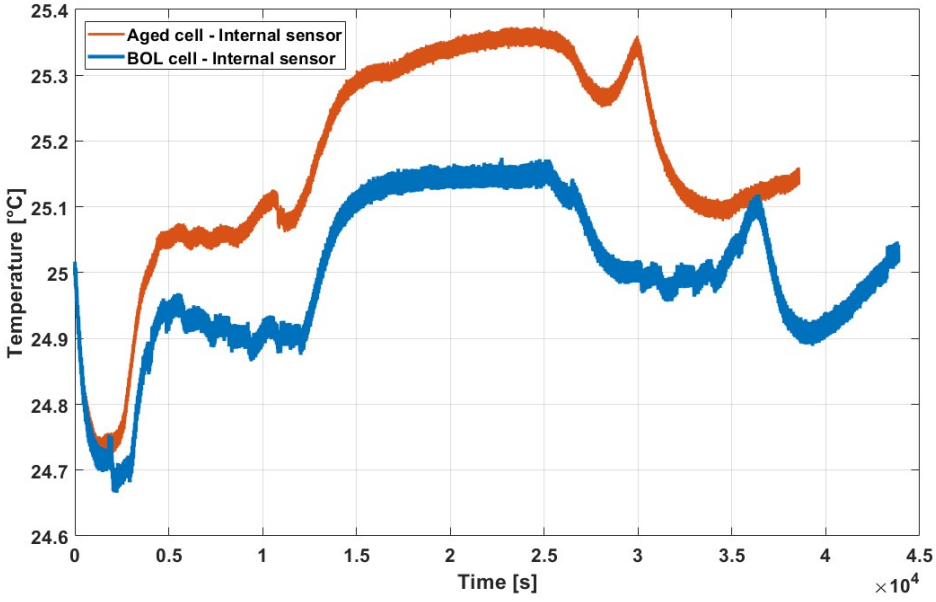

Figure 4.33: Comparison between internal temperature measurements during charge tests at 0.1C of M1B sample at BOL and aged conditions

contribution of the reversible thermal power generation at the corresponding lithiation state (or an imperfect control of the internal temperature by the climatic chamber).
It can be clearly seen that a shorter duration of the test is attained for the aged cell: in this regard, the final plateau visible for the sample at beginning of life, has completely

shrunk in the degraded cell. Even so, the final peak was conserved at the end of the test. This aspect in particular couldn't be seen from analogous discharge tests, further suggesting that a different behavior appeared depending on the process. Moreover, due to the fact that this last feature is maintained, it could be assumed that no apparent relation exists with the degradation mechanisms suffered by the aged cell.
Consequently, to better understand the internal temperature evolution and avoid variations caused by imperfect chamber control, the same curves were matched along the central region in the graph and compared with the corresponding DV curves (figure 4.34).

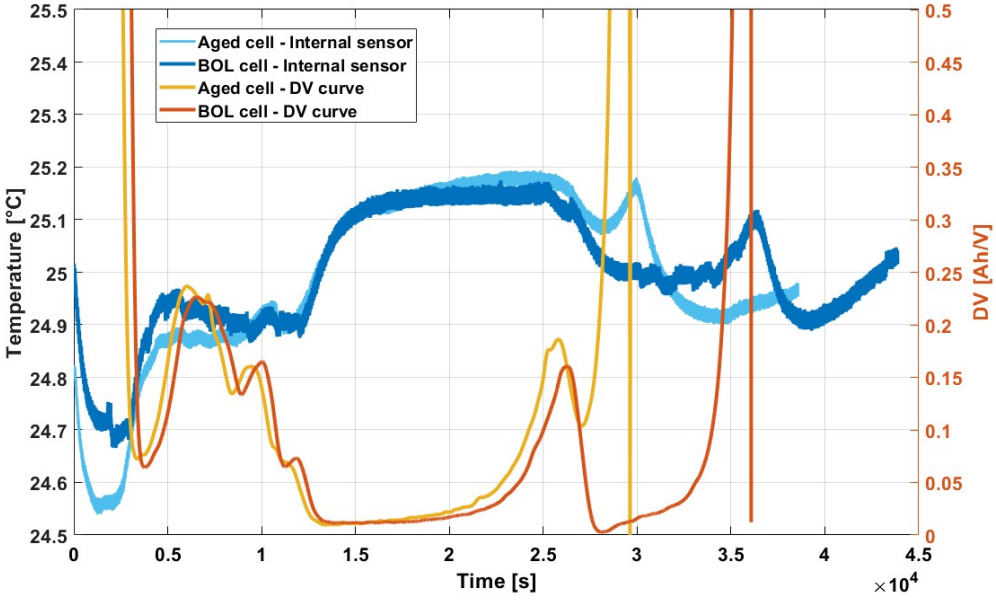

Figure 4.34: Comparison of internal temperature measurements and DV curves obtained from charge tests at 0.1C between M1B sample at BOL and aged conditions

A great conformity can be noticed between the temperature curves, especially within the period between 5000 and 25000 $[s]$. Moreover, a clear correlation is seen with the corresponding DV curves. In particular, the last peak in the internal temperature is perfectly aligned with the steep increase in the DV curve, which corresponds to the final ramp in the voltage curve seen at the end of the charge process. This feature is known to be related with the equilibrium voltage at the positive electrode, as seen from section 1.1.2, figure 1.3. In this regard, the fact that the last peak is conserved between the BOL and aged samples curves strongly suggests that no degradation was experienced by the cathode from the calendar aging campaign, further confirming the assumption of LLI as major degradation mode. On the other hand, the last plateau in the temperature curve of the BOL cell is characterized by a strong similarity with the valley in the DV curves within the same time period, corresponding instead to a phase change in the graphite

anode. As explained in section 3.3.1, the shrinkage of this feature on the DV curve is directly correlated with the loss of lithium inventory caused by calendar aging. In fact, as already observed for discharge processes, during charge the cell is not capable anymore to reach the same lithiation state, corresponding to a lower extent of the final plateau. For this reason, figure 4.34 clearly demonstrates that the same information of the DV curve can be obtained from the internal temperature curve, confirming further the dependency between this parameter and the thermodynamics of batteries.

4.2. Entropic coefficient estimation

The entropic coefficient (EC) represents the equilibrium voltage variation experienced by the cell with respect to a change in the operating temperature. It is thus defined as:

$$EC = \frac{\partial E_{OCV}}{\partial T} \qquad [\mathrm{V\ K^{-1}}] \qquad (4.1)$$

The determination of this term is crucial for the modeling of the behavior of a lithium-ion battery, as it describes the reversible voltage loss as a function of temperature. Consequently, when a current is applied to the cell, this voltage difference is responsible for the generation of a certain amount of heat, called (reversible) entropic heat, related to the entropy difference experienced by the system.
The reversible heating power term becomes less and less important as the current is increased, due to the fact that it depends linearly on the current, whereas ohmic losses increase with the square of it. Nonetheless, the entropic heat cannot be neglected at low current rates, as it constitutes a major part of the overall generated thermal power.
For the reasons stated above, an experimental campaign was carried for the estimation of the entropic coefficient of the analyzed samples, as a function of both the SoC and the operating temperature.
The reference methodology for the estimation of the entropic coefficient relies on quasi-static measurements of a battery's open circuit voltage at different temperatures; the entropic coefficient is then computed as the voltage differences caused by the corresponding temperature variations.
An alternative methodology exists for the estimation of the entropic coefficient [136], which exploits a dynamic temperature profile to induce a voltage variation. This novel approach allows for a great decrease of the time span needed to estimate the entropic coefficient map, at parity of computed points; however, given that many M1B samples were available at beginning of life conditions, the time required for the test didn't represent the limiting factor. For this reason, it was chosen to adopt the quasi-static method, as it

requires a simpler setup than the alternative one.
In this regard, several cells at BOL conditions were selected and prepared: in particular, an assessment of their residual capacity was made, mainly through the employment of discharge tests; following this step, the cells were discharged at the desired states of charge, ranging from 0 to 100% and divided by 5% steps. In this way, a sufficiently extensive representation of the entropic coefficient as a function of the SoC could be made.
A time span of 72 hours was waited for the cells to relax and reach the equilibrium voltage, thus minimizing the effects of voltage drift on the estimation. The cells were positioned on the holders inside the Binder MKF 720 climatic chamber described in section 2.2.1. During this time, the temperature of the chamber was set at a certain value equal to 5 $[°C]$ and a time of 5 hours was waited before changing it again. A temperature range between 5 and 45 $[°C]$ was chosen, with steps of 5 $[°C]$. The voltage of the cell was recorded throughout the test, leading to the estimation of the EC.
An example of the voltage measurement during the test can be seen in figure 4.35.

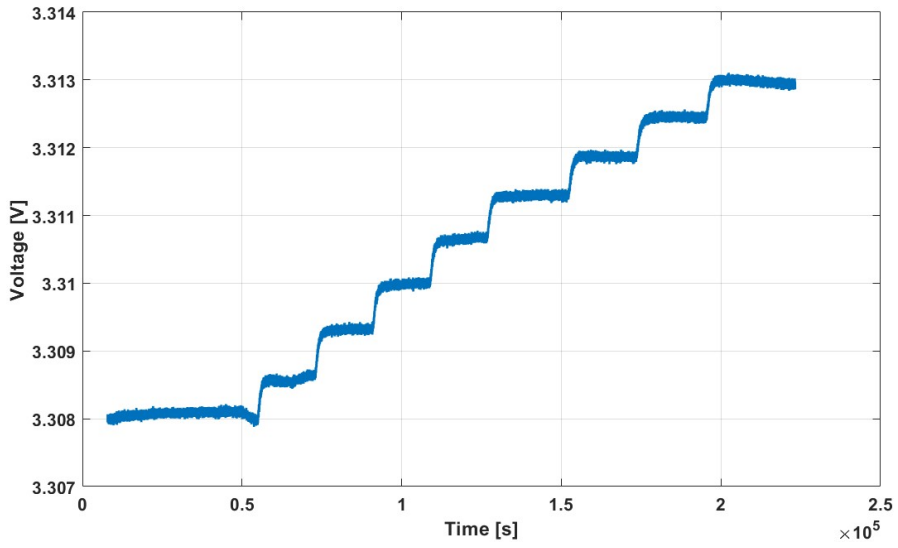

Figure 4.35: Voltage measurement during the test for the entropic coefficient estimation, at a $SoC = 75\%$

As it can be seen, the voltage follows a stair-like trend, characterized by several steps corresponding to the temperature variation of the chamber environment. Moreover, during the rest periods, the voltage remains almost constant, confirming the assumption of reaching the equilibrium value.
Consequently, a map of the entropic coefficient was built from this experimental campaign through the use of its definition, as a function of temperature and state of charge. This can be observed in figure 4.36.

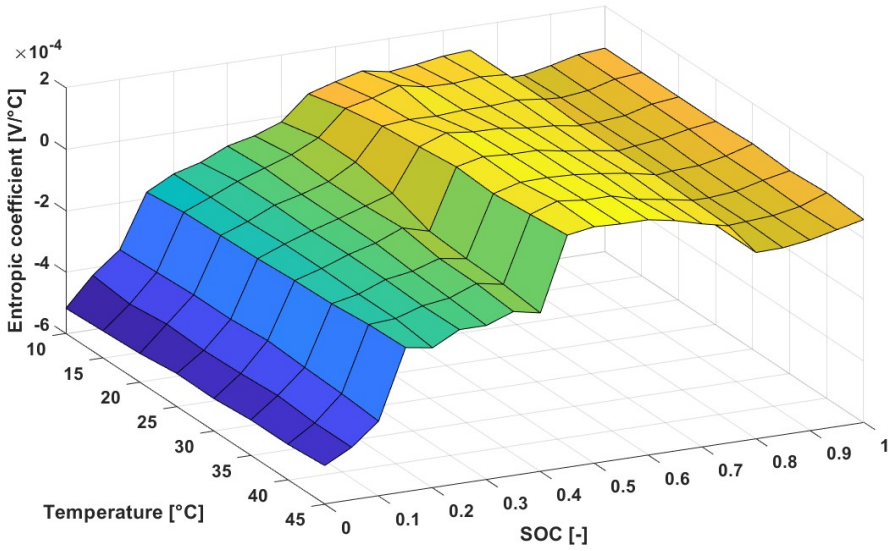

Figure 4.36: Map of the estimated entropic coefficient as a function of temperature and SoC

It can be noted that the map is similar to the one presented in [137] for a LFP pouch battery. In fact, similar slope changes can be noticed. Moreover, it was confirmed that the entropic coefficient is characterized by a very weak dependency with temperature, as the value doesn't experience a high variation.

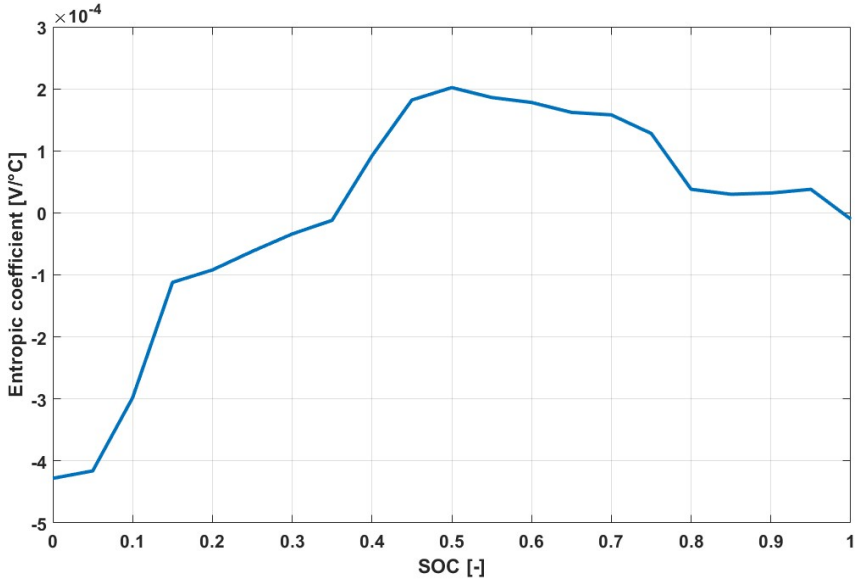

Figure 4.37: Entropic coefficient estimated at 25 [$°C$] as a function of state of charge

In figure 4.38, the comparison between the estimated entropic coefficient curve at 25

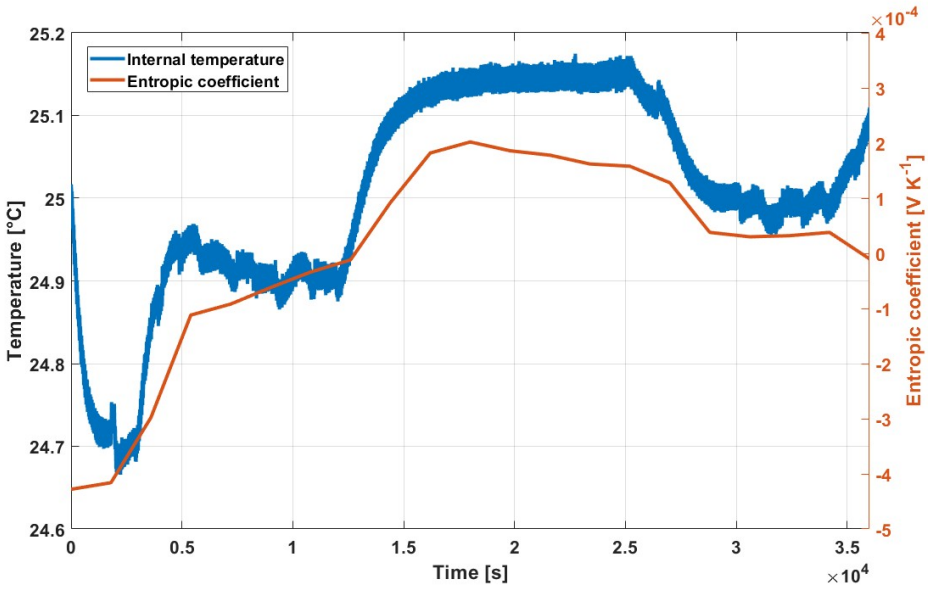

Figure 4.38: Comparison between internal temperature measurement obtained from a charge test at 0.1C and the entropic coefficient curve at 25 [$°C$]

[$°C$] and the internal temperature during a discharge test at 0.1C can be observed. At such low C-rates it is very clear that the dominant term is indeed the one related to the entropic coefficient, as the two curves have almost the same shape. In this regard, a clarification is needed, due to the fact that temperature and reversible heat represent different aspects of the same concept. Indeed, the heat generated within the jelly-roll of a battery is directly correlated with the derivative of the temperature with respect to time and not with temperature itself, through the conservation of energy equation. Consequently, the curves in figure 4.38 are characterized by the same general shape due to the fact that convection thermal power losses arise during very slow charge or discharge processes. These losses acquire greater importance because they have more time to act on the temperature.

In addition, it can be noticed that the entropic coefficient map follows a seemingly parabolic trend with respect to the state of charge: a maximum can be observed in the central part of the curve, while the lowest EC was found at $SoC = 0$ (figure 4.37). In this regard, a correlation of this parameter with the specific heat capacity could be hypothesized, given the fact that both parameters regulate the thermal behavior of a battery. Indeed, it was demonstrated [138] from a thermodynamic stand-point that a strong relationship exists between the entropic coefficient and the heat capacity of an electrochemical cell, reported in equation 4.2.

$$C(Q,T,V) = C(Q_0,T_0,V_0) + p \cdot \left(\frac{\partial V}{\partial T}\right)_p + \int_{T_0}^{T} \frac{\partial C_V^0}{\partial T} dT - \int_{Q_0}^{Q} \frac{\partial E_{OCV}}{\partial T} dQ \quad [\text{J K}^{-1}] \quad (4.2)$$

Where:

- C_0 is the heat capacity of the battery in a reference state, which depends on the state of charge through the charge Q, the temperature T and the volume V;
- p is the pressure, $[N\ m^{-2}]$;
- C_V^0 is the isochoric (ie. at constant volume) heat capacity of the system;
- E_{OCV} is the equilibrium voltage of the cell.

In this equation, it is stated that the heat capacity variation of a battery depends on its thermodynamic conditions. In particular on:

- the isobaric thermal expansion coefficient $\frac{\partial V}{\partial T}$;
- the temperature dependence function of the heat capacity $\frac{\partial C_V^0}{\partial T}$;
- the entropic coefficient $\frac{\partial U}{\partial T}$, as a function of the state of charge through Q.

In general, as described in section 1.2, lithium-ion batteries are characterized by a certain expansion during operation, particularly within the graphite negative electrode. For this reason, if the external shell isn't stiff enough, the total volume of cells can change considerably; this aspect is more important in prismatic or pouch geometries. Given that the battery samples employed during the work of this thesis present a cylindrical geometry, the first term, relative to the thermal expansion of cells, can be neglected. In this regard, a constant volume is assumed implicitly.
In practice, the two estimated curves of entropic coefficient and specific heat capacity as a function of the SoC were compared with each other (figure 4.39)

These trends were estimated at around the same temperature (25 and 20 $[°C]$, respectively), such that also the term relative to the dependency of heat capacity with temperature is negligible.
It can be clearly seen that a great accordance exists between the two curves, due to the fact that similar variations can be noticed. In particular, a much lower value is achieved in both trends at $SoC = 0$, which increases in a similar way as the state of charge increases.

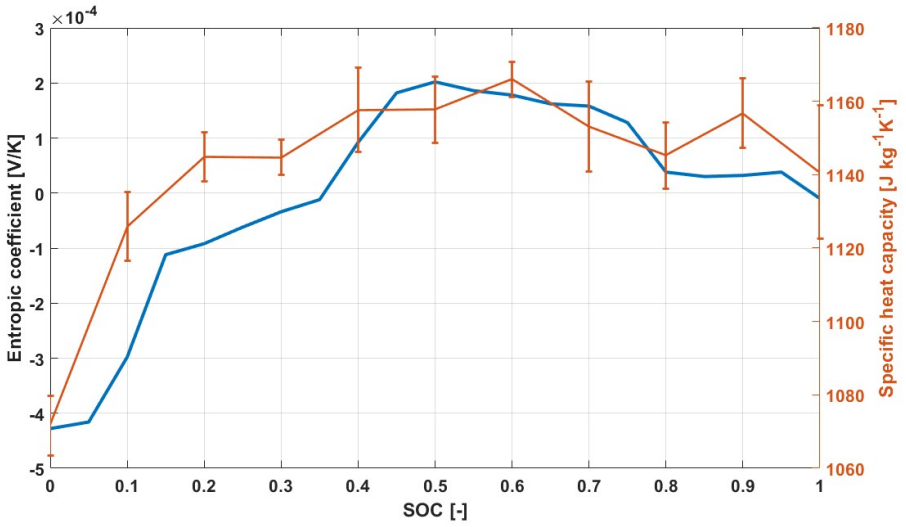

Figure 4.39: Comparison between estimated entropic coefficient curve at 25 [$°C$] and specific heat capacity as a function of the SoC of M1B samples

4.3. Final remarks

In this chapter, the experimental campaign for the characterization of the internal temperature in the analyzed samples was presented and described. In particular:

- An experimental campaign was carried out on the battery samples with internal temperature sensors. In this regard, charge and discharge tests were performed on the cells at BOL and aged conditions, primarily at C-rate equal to 1C and 0.1C, measuring the internal and external temperature throughout the process. Additionally, experiments at different operating temperature were performed, comparing the results.
- The internal temperature curves were analyzed thoroughly, describing their most important features. A clear correlation was found between the slope variations of the internal temperature and the thermodynamic behavior of batteries, through the comparison with DV curves obtained in quasi-static conditions. Moreover, variations in the temperature evolutions were detected between beginning of life and aged samples, demonstrating the visibility of changes of electrodes behavior also in the internal temperature. Furthermore, the increase in the radial thermal conductivity estimated from the previous experimental campaigns was confirmed also from in-operando internal temperature investigations.
- An additional experimental campaign was performed on beginning of life samples for the estimation of the entropic coefficient. In this regard, several cells were tested,

to assess their state of health. The entropic coefficient was computed from the equilibrium voltage differences arising from a variation of the external temperature. Moreover, a dependency between the heat capacity and the entropic coefficient was found in literature. This was later demonstrated experimentally by comparison of the two quantities.

5 | Thermo-electrochemical model of lithium-ion batteries

The definition and implementation of a physics-based thermo-electrochemical model, known as Single Particle Model (SPM), will be presented in this chapter, taking as inputs some of the results from previous experimental campaign. The principal aim of this model is to correctly represent the temperature variations inside lithium-ion batteries and at the same time provide a physical interpretation of the internal operation of the samples, linking thermal and electrochemical related phenomena.

5.1. Introduction to physical models

As described in section 1.4.2, thermal management systems are fundamental for the correct functioning of battery packs, as they control the external cooling system and thus the temperature gradient within the cells. For a fine control of the working conditions, BTMSs generally employ a model of the batteries, able to characterize their thermal behavior through the assumption of thermal parameters. In general, these models can be based on equivalent circuit of the batteries or, more faithfully, on a representation of the real physical phenomena occurring during operation.
Following the results of the experimental campaigns, a physics-based thermo-electrochemical model was defined and implemented, using some of the estimated parameters from the experiments described in the previous chapters.
The primary goal of this model is to correctly represent the temperature evolution inside the analyzed lithium-ion batteries, which can then be validated through the comparison with the already obtained internal temperature description for the samples. Moreover, given that the model is based on conservation equations, a physical interpretation of the underlying phenomena that take place during operation can be made.
The reference model for lithium-ion batteries is known as Doyle-Fuller-Newman (DFN) model, from the names of its most important contributors. The DFN model is often referred to as pseudo-two-dimensional (P2D) model, due to the fact that it employs a

double discretization to characterize the physical behavior of batteries. In this regard, the electrodes are modeled as clusters of solid porous particles, that are approximated as spheres and thus characterized by a certain equivalent radius. Each particle is further described by its position along the thickness of the electrodes, so that a two coordinates system can be identified (figure 5.1).

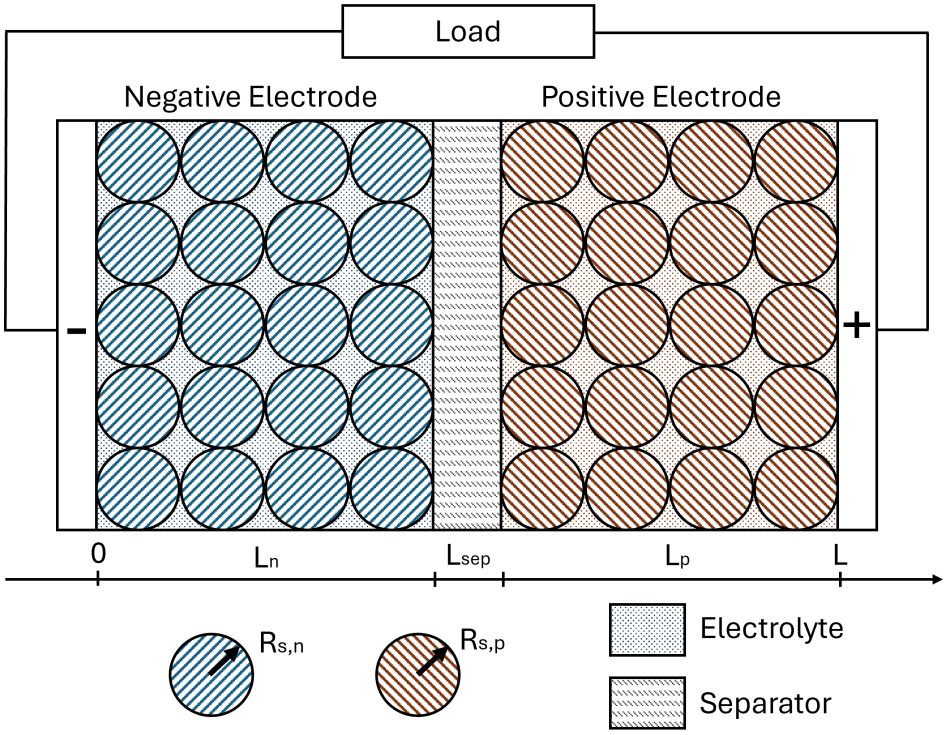

Figure 5.1: Schematization of the DFN lithium-ion battery model [139]

However, the DFN model is most of the times too computationally expensive for some applications, such as BTMS, due to the limited computational resources. In this regard, a corrected Single Particle Model will be presented in the following section, which employs some simplifying assumptions for the P2D, to decrease the computational burden without compromising the accuracy. Afterwards, a bi-dimensional thermal model of the cylindrical cell will be described, for the characterization of temperature gradients along the spacial coordinates.
Both models were implemented in MATLAB® using a state space representation, particularly useful when solving time-variant systems.

5.2. Single Particle Model

A single particle model (SPM) is a physics-based electrochemical model useful for the description of the internal behavior of lithium-ion batteries. This model is able to describe

the batteries performance through a schematic representation of the electrodes, which are defined as porous spherical particles. It can easily couple electrochemical and thermal phenomena, through the definition of the appropriate conservation equations; moreover, it is characterized by a very contained computational time when compared to other models, due to the fact that a greater importance is given to the dominant phenomena. In this regard, the SPM relies on the fact that the lithium transport in the electrolyte phase is characterized by a very small timescale compared to the diffusion phenomena in the electrodes solid particles [139], such that in the simplest form of this representation the electrolyte-related losses are often neglected. In this limit, all of the particles in the electrodes behave in the same way, so that it is needed to only describe one of them, as it is representative for the whole active material domain [89, 140]. Additionally, to increase accuracy at the cost of a small increase in the needed computational time, a correction for the electrolyte behavior was introduced in the presented model, through the implementation of an additional PDE. A schematization of the model, with the main approximation is available in figure 5.2.

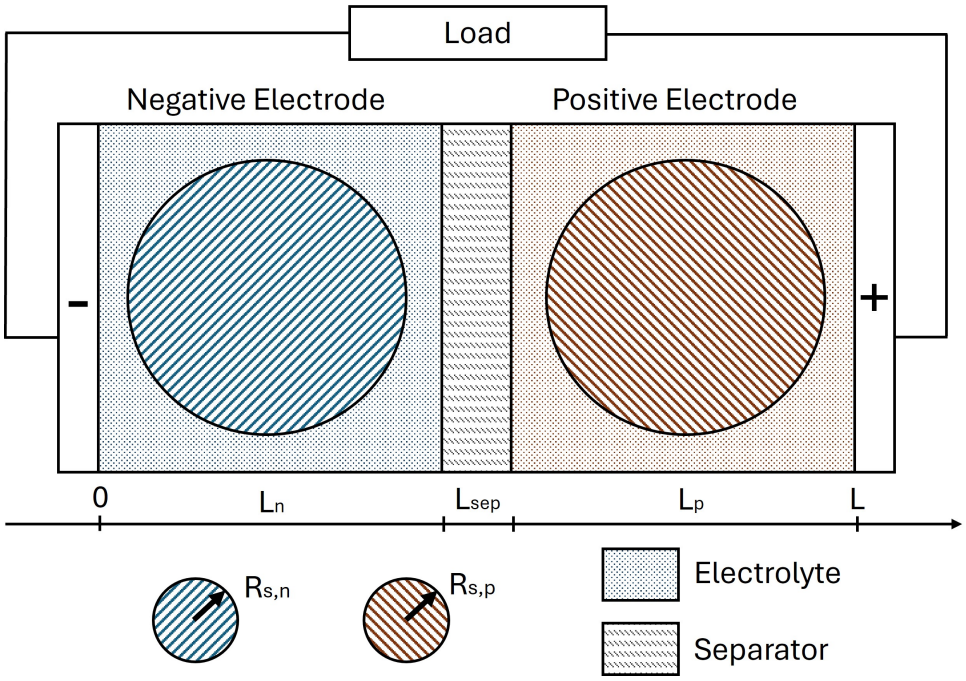

Figure 5.2: Schematization of the SPM lithium-ion battery model [only a single particle is modeled for each electrode]

The fundamental consequence of the assumption of single particles is that the current density gradient can be considered equal to its average value over the electrode's thickness [141]. In this regard, the following relation can be stated:

$$\frac{\partial i}{\partial x} = \frac{i}{L_i} = \frac{I}{A_{el} L_i} \tag{5.1}$$

This assumption is only valid if the operating current rate is low, where the threshold if often considered to be around C-rate = 1 $[h^{-1}]$. At too high values, the gradient of the operating current within the electrodes shouldn't be considered constant and the assumption of a single representative particle is not sufficient anymore.
The proposed model combines both the electrochemical behavior (through the modeling of the redox reactions inside the electrodes) and the thermal behavior, by coupling the heat generated within the jellyroll with the thermal parameters of the cell.

5.2.1. Discretization of domains and change of variable

When solving spatial PDEs, it is always necessary to define a discretization of the analyzed domains, providing in this way a detailed description of the system through the construction of a set of nodes. However, a too dense discretization comes at the cost of higher burden on the computational resources, so a trade off must be found.
In this regard, the best best discretization strategy is the one that, at parity of number of nodes, returns the most faithful description of the system. Following this idea, the coordinates of the single particle model were taken into account:

- the sphere radius is the most important coordinate as the dominant diffusion phenomena inside the solid particles are described along it. Moreover, it is known that the electrochemical reactions occur at the electrode-electrolyte interface, within the external surface of the particles. For these reasons, a discretization in space using the Chebyshev orthogonal collocation method was chosen: Chebyshev nodes (also known as Gauss-Lobatto quadrature points) are constructed using the projection of equi-spaced points on the unit circle onto the real interval (figure 5.3).

  Consequently, by using this method, the solution of the PDE is approximated by a sum of Chebyshev polynomials that interpolate the solution at the N Chebyshev nodes defined on the interval [-1, 1].
  Given a certain positive integer N, the N Chebyshev nodes in the interval $(-1; 1)$ are defined as:

$$x_k = \cos\left(\frac{2k+1}{2N}\pi\right), \qquad \text{with } k = 0, 1, ..., n-1 \tag{5.2}$$

  The most important consequence of this discretization is the fact that the nodes are in general more amassed towards the surface of the sphere, guaranteeing a more

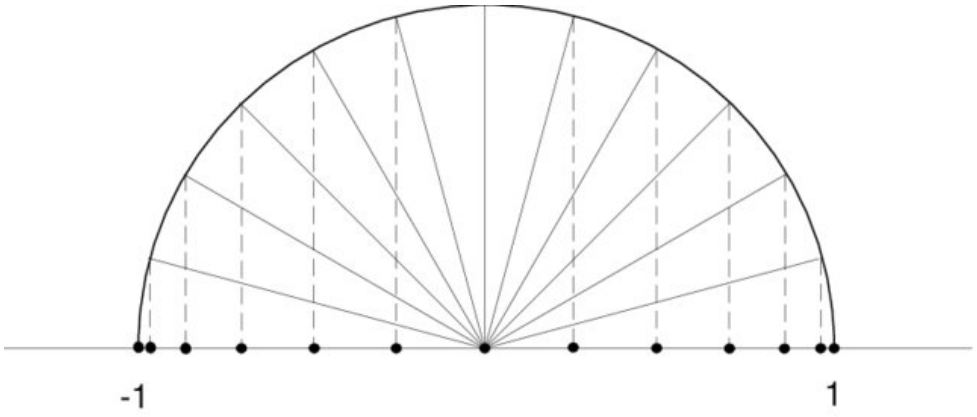

Figure 5.3: Gauss-Lobatto quadrature points for Chebyshev polynomials, constructed from equi-spaced points on the unit circle [142]

precise description within it.
In the model, each particle was characterized by a number of nodes equal to $N_s = 6$. In addition, a change of variable was introduced on the diffusion equations in the solid electrodes particles, with the aim of simplifying the solution. The modified concentration was defined as:

$$u = rc \tag{5.3}$$

Where r is the radius coordinate of the particles and c is the lithium concentration. Moreover, the dimensionless form of the PDE was obtained, through the definition of the radial coordinate:

$$x = \frac{r}{R_{s,i}} \tag{5.4}$$

By introducing the dimensionless radius x and solving the model on the domain $r\,[-R_{s,i}, R_{s,i}]$ mapped onto $x\,[-1, 1]$, the Chebyshev nodes are only clustered at the surface, and by symmetry is possible to solve the equation only on $x\,[0, 1] \rightarrow r\,[0, R_{s,i}]$, halving the number of nodes to solve.

- the linear coordinate x describes the phenomena occurring along the thickness of the cell components. In this regard, a simple equi-spaced discretization was chosen for each component, such that the total number of nodes along this coordinate is given by the sum of nodes within the electrodes and the separator.
  For the electrodes, the number of nodes was chosen as $N_p = N_n = 2$, while for the separator $N_{sep} = 1$.

5.2.2. Governing equations and boundary conditions

The model is based on several conservation equations, which describe different phenomena inside the cell. In this section, these equations and their relative boundary conditions will be stated and explained; moreover, the main assumptions of the model will be applied.

Symbol	Description
Latin	
$a\ [m^{-1}]$	Specific interfacial surface area
$A_{el}\ [m^2]$	Electrode surface area
$b\ [-]$	Bruggeman coefficient
$c\ [mol\ m^{-3}]$	Lithium species concentration
$c_p\ [J\ kg^{-1}K^{-1}]$	Specific heat capacity
$D\ [m^2\ s^{-1}]$	Lithium diffusion coefficient
$EA_K\ [J\ mol^{-1}]$	Rate constant activation energy
$EA_{D_s}\ [J\ mol^{-1}]$	Solid diffusion activation energy
$E_{ocp}\ [V]$	Electrode open circuit potential
$F\ [C\ mol^{-1}]$	Faraday constant
$h\ [Wm^{-2}K^{-1}]$	Heat transfer coefficient
$i\ [A\ m^{-2}]$	Current density
$i_0\ [A\ m^{-2}]$	Exchange current density
$I\ [A]$	Current
$j\ [A\ m^{-2}]$	Reaction current density
$K\ [m\ s^{-1}]$	Reaction rate constant
$k\ [W\ m^{-1}K^{-1}]$	Thermal conductivity
$L\ [m]$	Cell component length
$n\ [-]$	Number of transferred charges
$N\ [mol\ m^{-2}s^{-1}]$	Lithium molar flux
$q\ [W\ m^{-3}]$	Volumetric heat flux
$R\ [J\ mol^{-1}K^{-1}]$	Universal gas constant
$R_{s,i}\ [m]$	Solid particles radius
$t^+\ [-]$	Lithium transference number
$T\ [K]$	Temperature
$\Delta V\ [V]$	Cell Voltage
Greek	
$\alpha\ [-]$	Charge transfer coefficient
$\epsilon\ [-]$	Volume fraction
$\eta\ [V]$	Overpotential
$\kappa_e\ [S\ m^{-1}]$	Electrolyte ionic conductivity
$\kappa_D\ [A\ m^{-1}]$	Electrolyte diffusional conductivity
$\sigma_i\ [S\ m^{-1}]$	Solid particles conductivity
$\phi\ [V]$	Electric potential
$\rho\ [kg\ m^{-3}]$	Density

Symbol	Description
Subscript	
$conv$	Convective
e	Electrolyte
gen	Generated
n	Negative
ohm	Ohmic
ox	Oxidation
p	Positive
red	Reduction
rev	Reversible
s	Solid
sep	Separator
Superscript	
eff	Effective
Coordinate	
r	radial
x	linear
z	axial

Table 5.1: List of symbols, subscript and superscript employed in the SPM model

In table 5.1 is available the list of symbols used in the model's expressions.

Conservation of Li^+ species in the solid phase

The partial differential equation (PDE) 5.5 governs the lithium transport inside the solid particles of the electrodes, which in this context only includes diffusion. In this regard, the particles are modeled as porous spheres, with an average radius R_s, so that the diffusion equation is written in spherical coordinates.

$$\frac{\partial c_{s,i}}{\partial t} = \frac{1}{r^2}\frac{\partial}{\partial r}\left(r^2 D_{s,i}\frac{\partial c_{s,i}}{\partial r}\right) \tag{5.5}$$

Where:

- $c_{s,i}$ is the lithium concentration in the particles solid phase of the i-th electrode, with $i = p, n$;
- $D_{s,i}$ is the lithium diffusion coefficient of the i-th electrode;

The following boundary conditions were applied:

$$\begin{cases} \left.\dfrac{\partial c_{s,i}}{\partial r}\right|_{r=0} = 0 & \text{(5.6a)} \\ \left.\dfrac{\partial c_{s,i}}{\partial r}\right|_{r=R_{s,i}} = -\dfrac{N_i}{D_{s,i}} = -\dfrac{I}{nFA_{el}D_{s,i}} & \text{(5.6b)} \end{cases}$$

They are defined to impose, respectively:

- null flux at the centre of the particles, due to their spherical symmetry;
- the equivalence between the lithium flux at the external particle surface and the lithium flux into the electrolyte, due to the local electrochemical reaction rate; in this context, a uniform reaction rate is assumed over the whole surface of the electrodes' particles and along the electrodes' thickness.

This equation is crucial for the electrochemical model, due to the fact that diffusion inside the electrodes' particles is assumed to be the dominant phenomenon during operation.

Conservation of Li^+ species in the electrolyte phase

This PDE (equation 5.7) describes the conservation of lithium ions in the electrolyte domain within the cell components, along their thickness. It states that the accumulation of lithium in this component (term on left hand side of the equation) coincides with the

sum of the total molar flux across it and a generation term (first and second terms on the right hand side, respectively), caused by the electrochemical reactions occurring at the electrodes (of course this term is null in the separator).

$$\epsilon_{e,i}\frac{\partial c_e}{\partial t} = -\frac{\partial N_e}{\partial x} + \frac{1}{nF}\frac{\partial i_{e,i}}{\partial x} \tag{5.7}$$

Where:

- $\epsilon_{e,i}$ is the volume fraction of electrolyte in the i-th component, with $i = p, s, n$;
- c_e is the lithium concentration in the electrolyte phase;
- N_e is the lithium molar flux in the electrolyte phase, related to transport phenomena;
- $i_{e,i}$ is the current density in the electrolyte within the i-th component;
- n is the charge number of the considered component (which is equal to 1 for Li^+);

The lithium molar flux $N_{e,i}$ can be described by the Nernst-Planck equation, that can be stated as:

$$N_e = -D_e^{eff}\frac{\partial c_e}{\partial x} - n\frac{F}{RT}D_e^{eff}c_e\frac{\partial \phi}{\partial x} + c_e\omega \tag{5.8}$$

Where the three terms represent respectively the diffusion, migration and convection contribution to the molar flux. As stated previously, the convection inside the cell is completely neglected, so that only the first two terms remain. In this equation:

- D_e^{eff} is the effective lithium diffusion coefficient in the electrolyte, that takes into account the structure of the components through the Bruggeman correlation:

  $$D_e^{eff} = D_e\epsilon_e^b \tag{5.9}$$

  Where b is the Bruggeman coefficient, that includes the tortuosity and porosity of the electrodes;

- ϕ is the electric potential inside the cell;

Moreover, the equation can be simplified through the introduction of the transference number t^+, defined as the fraction of the total electric current carried in an electrolyte by a given ionic species [143]. In this way, the Nernst-Planck equation becomes:

$$N_{e,i} = -D_e^{eff}\frac{\partial c_e}{\partial x} + \frac{t^+ i_{e,i}}{nF} \tag{5.10}$$

$$\tag{5.11}$$

Finally, the conservation of Li^+ species in the electrolyte phase can be re-written as:

$$\epsilon_{e,i}\frac{\partial c_e}{\partial t} = \frac{\partial}{\partial x}\left(D_e^{eff}\frac{\partial c_e}{\partial x}\right) - \frac{i_{e,i}}{nF}\frac{\partial t^+}{\partial x} + \frac{(1-t^+)}{nF}\frac{\partial i_{e,i}}{\partial x} \tag{5.12}$$

In equation 5.12, the second term on the right hand side, related to the partial derivative of the transference number with respect to the thickness of the cell is often neglected for simplicity. Furthermore, the last term related to generation, is not null only in the presence of active material, so it can be stated as:

$$\frac{\partial i_{e,i}}{\partial x} = \frac{i}{L_i} = \begin{cases} a_i j_i & \text{if } i = p, n \\ 0 & \text{if } i = s \end{cases} \tag{5.13}$$

Where:

- a_i is the specific interfacial surface area in the i-th electrode;
- j_i is the reaction current density at the i-th electrode;

The following boundary conditions were applied (equation 5.14), stating that no lithium flux is present at the extremes coordinates of the electrochemical cell:

$$\left\{ \frac{\partial c_e}{\partial x}\bigg|_{x=0} = \frac{\partial c_e}{\partial x}\bigg|_{x=L} = 0 \right. \tag{5.14a}$$

Conservation of charge in the electrolyte phase

The charge conservation in the electrolyte is, of course, strongly related with cell potential and the transport of lithium across the components thickness. As it can be noticed in equation 5.15, the derivative in time of the charge per unit surface (ie the current density) corresponds to the sum of two terms, respectively related to:

- the potential gradient in the electrolyte, through the Ohm's law;
- the lithium ions transport inside the electrolyte, caused by the concentration gradient; this term is included due to the fact that lithium ions are charged species.

$$\frac{\partial}{\partial x}\left(\kappa_e^{eff}\frac{\partial \phi_e}{\partial x}\right)+\frac{\partial}{\partial x}\left(\kappa_D^{eff}\frac{\partial}{\partial x}\ln c_e\right)+\frac{\partial i_{e,i}}{\partial x}=0 \tag{5.15}$$

Where:

- $\phi_{e,i}$ is the electric potential within the electrolyte phase;
- κ_e^{eff} is the effective ionic conductivity in the electrolyte, which is defined taking into account the following correction through the Bruggeman correlation:

$$\kappa_e^{eff}=\kappa_e\epsilon_e^b \tag{5.16}$$

- κ_D^{eff} is the effective ionic diffusional conductivity, defined as:

$$\kappa_D^{eff}=\frac{2RT}{F}\kappa_e^{eff}(t^+-1)\left(1+\frac{d\ln f_\pm}{d\ln c_e}\right) \tag{5.17}$$

The boundary conditions were imposed at the extreme coordinates along the linear direction, such that the potential gradient in the electrolyte is null at $x=0$ and $x=L$:

$$\left\{\left.\frac{\partial \phi_e}{\partial x}\right|_{x=0}=\left.\frac{\partial \phi_e}{\partial x}\right|_{x=L}=0 \right. \tag{5.18}$$

Thanks to the assumption in equation 5.1, the charge conservation equations can be solved analytically in the components' domains, as a function of the coordinate x [141]:

$$\begin{aligned}\phi_e(x)=\phi_e(0)+(1-t^+)\frac{2RT}{F}\ln\left(\frac{c_e(x)}{c_e(0)}\right)+\\ -\left(\frac{I}{2A_{el}L_n\kappa_n^{eff}}\right)x^2\end{aligned} \tag{5.19}$$

$$\begin{aligned}\phi_e(x)=\phi_e(0)+(1-t^+)\frac{2RT}{F}\ln\left(\frac{c_e(x)}{c_e(0)}\right)+\\ -\frac{I}{A_{el}}\left(\frac{x-L_n}{\kappa_{sep}^{eff}}+\frac{L_n}{2\kappa_n^{eff}}\right)\end{aligned} \tag{5.20}$$

$$\begin{aligned}\phi_e(x)=\phi_e(0)+(1-t^+)\frac{2RT}{F}\ln\left(\frac{c_e(x)}{c_e(0)}\right)+\\ +\left(\frac{I}{2A_{el}L_p\kappa_p^{eff}}\right)(L-x)^2-\frac{I}{2A_{el}}\left(\frac{L_n}{\kappa_n^{eff}}+\frac{L_{sep}}{2\kappa_{sep}^{eff}}+\frac{L_p}{\kappa_p^{eff}}\right)\end{aligned} \tag{5.21}$$

For the anode, separator and cathode, respectively.

Conservation of charge in the solid phase

Contrarily to the definition in the electrolyte, the conservation of charge in the solid particles is only comprised of the ohmic term, related to the potential gradient within the solid phase along the components' thickness (equation 5.22).

$$\frac{\partial}{\partial x}\left(\sigma_i^{eff}\frac{\partial \phi_s}{\partial x}\right) + \frac{\partial i_{s,i}}{\partial x} = 0 \tag{5.22}$$

In this equation, the ionic conductivity in the solid phase is defined in the same way as its electrolyte phase counterpart, through the Bruggeman correlation:

$$\sigma_i^{eff} = \sigma_i \epsilon_e^b \tag{5.23}$$

In addition, the boundary conditions were imposed as:

$$\begin{cases} \left.\dfrac{\partial \phi_s}{\partial x}\right|_{x=L_n} = \left.\dfrac{\partial \phi_s}{\partial x}\right|_{x=L-L_p} = 0 & \text{(5.24a)} \\ \left.-\sigma_i^{eff}\dfrac{\partial \phi_s}{\partial x}\right|_{x=0} = \left.-\sigma_i^{eff}\dfrac{\partial \phi_s}{\partial x}\right|_{x=L} = \dfrac{I}{A} & \text{(5.24b)} \end{cases}$$

The first set of boundary conditions states that, at the electrode-separator domain interfaces, the current is null: this is physically understandable, as the separator is considered an electronic insulator. The second set of conditions, instead, describes the current density at the extreme points on the x coordinates, in this way creating a link between solid electrodes and electrolyte domains.
In the same way as for the electrolyte phase, the PDE can be solved in closed form, given the equation 5.1 assumption [141]:

$$\phi_s(x) = \phi_s(0) - \frac{I}{A_{el}\sigma_n^{eff}}\left(x - \frac{x^2}{2L_n}\right) \tag{5.25}$$

$$\phi_s(x) = \phi_s(L) - \frac{I}{A_{el}\sigma_p^{eff}}\left((x-L) - \frac{(x-L)^2}{2L_p}\right) \tag{5.26}$$

For the negative and positive electrode, respectively.

Electrochemical kinetics

The electrochemical kinetic behavior of the cell is governed by the Butler-Volmer equation 5.27. This expression describes the relation between the reaction current density in the electrodes of the cell and the overpotentials arising as a consequence of it. In fact, for a reaction to occur, a disequilibrium must be introduced in the system.

$$j_i = \frac{I}{A_{el} L_i a_{s,i}} = i_{0,i} \left[\exp\left(\frac{\alpha_{ox,i} F \eta_i}{RT} \right) - \exp\left(-\frac{\alpha_{red,i} F \eta_i}{RT} \right) \right] \tag{5.27}$$

Where:

- j_i is the reaction current density at the i-th electrode;
- $a_{s,i}$ is the specific interfacial surface area in porous electrodes, which represents the active surface-to-volume ratio in these components; for spherical particles, it can be computed as:

  $$a_{s,i} = 3\frac{\epsilon_{s,i}}{R_{s,i}} \tag{5.28}$$

  Where $\epsilon_{s,i}$ is the active material volume fraction and $R_{s,i}$ is the radius of the particles at the i-th electrode.
- $\alpha_{ox,i}$ and $\alpha_{red,i}$ are the charge transfer coefficients of the forward and backward reactions occurring at the i-th electrode. In lithium-ion batteries these quantities are often taken as equal to 0.5, assuming symmetric reactions.
- $i_{0,i}$ is the exchange current density for the i-th electrode, which is defined as the current density for which both the forward and backward reactions at one electrode are equal, such that the potential is equal to the equilibrium one. In LIBs, it can be evaluated as:

  $$i_{0,i} = F K_i c_{s,i}^{\alpha_{red,i}} \left(c_{s,i,max} - c_{s,i} \right)^{\alpha_{ox,i}} c_{e,avg}^{\alpha_{ox,i}} \tag{5.29}$$

  And, with the assumption of symmetric reactions:

  $$i_{0,i} = F K_i \sqrt{c_{s,i} \left(c_{s,i,max} - c_{s,i} \right) c_{e,avg}} \tag{5.30}$$

Finally, the overpotentials at both electrodes can be computed as:

$$\eta_n = \frac{2RT}{F} \sinh^{-1}\left(\frac{-I}{2 A_{el} a_{s,n} L_n i_{0,n}} \right) \tag{5.31}$$

$$\eta_p = \frac{2RT}{F} \sinh^{-1}\left(\frac{I}{2 A_{el} a_{s,p} L_p i_{0,p}} \right) \tag{5.32}$$

For the negative and positive electrode, respectively.

Operating voltage

The overall battery voltage at any instant can be expressed as the terminal voltage across the modeled cell, ie. the potential difference between the solid particles at the extreme coordinates, corresponding to the current collectors. In other terms:

$$\Delta V = \phi_s(L) - \phi_s(0) \tag{5.33}$$

By considering the current path through the electrochemical cell, equation 5.33 can be expanded to show the potential differences at each section of the modeled cell:

$$\begin{aligned}
\Delta V = {} & \phi_s(L) - \phi_s(L - L_p) + && \text{Negative electrode particles} \\
& + \phi_s(L - L_p) - \phi_e(L - L_p) + && \text{Negative electrode reaction} \\
& + \phi_e(L - L_p) - \phi_e(L_n) + && \text{Electrolyte} \\
& + \phi_e(L_n) - \phi_s(L_n) + && \text{Positive electrode reaction} \\
& + \phi_s(L_n) - \phi_s(0) && \text{Positive electrode particles}
\end{aligned} \tag{5.34}$$

This equation is much more useful for the description of the terminal voltage, as it displays all of the potential drops associated with the physical phenomena occurring inside the cell. In fact, during operation, several losses arise between the two extreme points, which are described by the previously defined equations of the model.
In this regard, equation 5.33 can be rewritten as:

$$\Delta V = E_{OCV} + \eta_p - \eta_n - \eta_e - \eta_{ohm} \tag{5.35}$$

Where:

- E_{OCV} is the open circuit voltage of the cell, corresponding to the equilibrium condition. It is defined as:

  $$E_{OCV} = E_{ocp,p} - E_{ocp,n} + T\frac{\partial(E_{ocp,p} - E_{ocp,n})}{\partial T} \tag{5.36}$$

  Where $E_{ocp,p}$ and $E_{ocp,n}$ are the equilibrium potentials at the positive and negative electrodes, respectively.

- η_e represents the voltage loss related to the lithium concentration gradient in the

electrolyte along the components' thickness. It can be expressed as:

$$\eta_e = (1 - t^+)\frac{2RT}{F}\ln\left(\frac{c_e(L)}{c_e(0)}\right) \tag{5.37}$$

- η_{ohm} is the ohmic loss of the cell, which is related to the resistance to migration of electrons in the electrolyte and solid particles domains of the electrodes. This term mainly depends on the electrical conductivities and the thicknesses of the cell components. It can be expressed as:

$$\begin{aligned}\eta_{ohm} &= \eta_{ohm,e} + \eta_{ohm,s} = \\ &= \frac{I}{2A_{el}}\left(\frac{L_n}{\kappa_n^{eff}} + \frac{L_{sep}}{2\kappa_{sep}^{eff}} + \frac{L_p}{\kappa_p^{eff}}\right) + \frac{I}{2A_{el}}\left(\frac{L_n}{\sigma_n^{eff}} + \frac{L_p}{\sigma_p^{eff}}\right)\end{aligned} \tag{5.38}$$

Conservation of energy

The conservation of energy equation describes the evolution of temperature inside the battery, as a consequence of the generated heat within the jelly-roll.
Its structure is the same as equation 1.20, described in section 1.4.4; here it will be reported again taking into account the parameters of the model:

$$\rho c_p \frac{\partial T}{\partial t} = \nabla \cdot [k(T, \boldsymbol{x})\nabla T] + q \tag{5.39}$$

In this single particle model, the battery is modeled with a lumped description of the temperature, such that the first term on the right hand side of the equation, relative to heat transfer inside the cell, is neglected; this assumption will be relaxed in the bi-dimensional thermal model in section 5.3. The equation can then be re-written as:

$$\rho c_p \frac{dT}{dt} = q_{gen} + q_{conv} \tag{5.40}$$

Where:

- q_{gen} is the heat generation per unit volume inside the electrochemical cell. Following Bernardi's model [54], it can be expressed as:

$$\begin{aligned} q_{gen} &= q_{rev} + q_{\eta} + q_{ohm} + q_e \\ &= -\frac{I}{A_{el}L_{tot}} T \frac{\partial (E_{ocp,p} - E_{ocp,n})}{\partial T} + \\ &+ \frac{I}{A_{el}L_p}\eta_p - \frac{I}{A_{el}L_n}\eta_n + \frac{I}{A_{el}L_{tot}}\eta_{ohm} + \frac{I}{A_{el}L_{tot}}\eta_e \end{aligned} \tag{5.41}$$

- q_{conv} is the heat transferred to the external environment through convection. It can be written as:

$$q_{conv} = -\frac{hA_{ext}}{V_{cyl}}(T - T_{amb}) \tag{5.42}$$

5.2.3. Model parameters

In this section are reported the values and expressions used for the model parameters. In particular, in table 5.2 are available the constant values, characterized by the domain inside the SPM cell and source.

The specific heat capacity was modeled through the estimated values obtained from the thermal characterization experimental campaign in chapter 3.

Equilibrium curves

Equilibrium potential curves are very important for the model operation, as they define the base shape of the voltage curve of the battery. In this regard, the equilibrium potential of both electrodes was available from the laboratory database, only from a discharge test at 0.02C, as from charge tests it was not measured

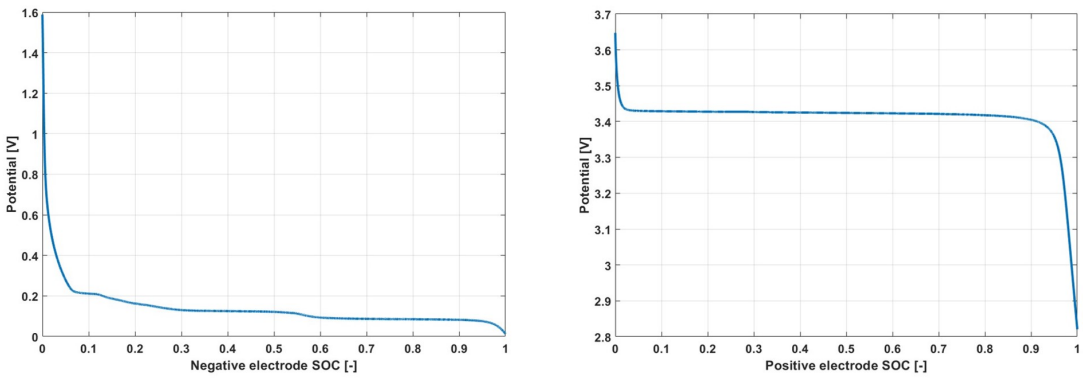

(a) Negative electrode (b) Positive electrode

Figure 5.4: Open circuit potential curves of the electrodes, employed for the single particle model

Parameter	Description	N	S	P	Source
A_{el} $[m^2]$	Electrode surface area	0.1886		0.1886	PT
$c_{s,max}$ $[mol\ m^{-3}]$	Maximum Li concentration in solid particles	$3.10{\cdot}10^{4}$		$2.28{\cdot}10^{4}$	PT
$D_{s,i,0}$ $[m^2 s^{-1}]$	Lithium diffusivity in solid particles	$1.48{\cdot}10^{-15}$		$1.22{\cdot}10^{-16}$	PT
EA_K $[J\ mol^{-1}]$	Rate constant activation energy	$2.00{\cdot}10^{4}$		$3.00{\cdot}10^{4}$	PT
EA_{D_s} $[J\ mol^{-1}]$	Solid diffusion activation energy	$3.50{\cdot}10^{4}$		$4.38{\cdot}10^{4}$	PT
L_i $[m]$	Component thickness	$4.51{\cdot}10^{-7}$	$2.50{\cdot}10^{-7}$	$7.00{\cdot}10^{-7}$	PT
$R_{s,i}$ $[m]$	Solid particles radius (0.04C)	$4.20{\cdot}10^{-6}$		$0.09{\cdot}10^{-6}$	Cal
$x_{i,1}$ $[-]$	Stoichiometry limits at $SoC = 1$	0.7446		0.00147	PT
$x_{i,0}$ $[-]$	Stoichiometry limits at $SoC = 0$	0.005		0.7246	PT
α $[-]$	Charge transfer coefficient	0.5		0.5	Lit
$\epsilon_{s,i}$ $[-]$	Active material volume fraction	0.4775		0.378	PT
$\epsilon_{e,i}$ $[-]$	Electrolyte volume fraction	0.33	0.54	0.332	PT
σ_i $[S\ m^{-1}]$	Solid particles conductivity	100		10	Lit
b $[-]$	Bruggeman coefficient	1.5			PT
$c_{e,avg}$ $[mol\ m^{-3}]$	Average Li electrolyte concentration	$1.20{\cdot}10^{3}$			Lit
D_e $[m^2 s^{-1}]$	Lithium diffusivity in electrolyte	$2.00{\cdot}10^{-10}$			Lit
t^+ $[-]$	Transference number	0.3753			PT
$\kappa_{e,i}$ $[S\ m^{-1}]$	Electrolyte ionic conductivity	0.5			Lit
ρ $[kg\ m^{-3}]$	Density	2252			Exp
F $[C\ mol^{-1}]$	Faraday constant	96485			
R $[J\ mol^{-1}K^{-1}]$	Universal gas constant	8.314			
T_0 $[K]$	Reference temperature	298.15			
$\Delta V_{min/max}$ $[V]$	Voltage limits	2.0 / 3.6			

Table 5.2: Parameters employed in the single particle model
N: anode; **S**: separator; **P**: cathode; **PT**: Previous thesis [22]; **Lit**: Literature [139, 141]; **Exp**: Experimental; **Cal**:Calibration

Particles radii

During real operation, the behavior of the electrodes is rather complex throughout intercalation and de-intercalation reactions of lithium ions. Moreover, the LFP cathode technology employed in the analyzed samples is characterized by solid particles of different dimensions. For these reasons, the radii of the active material particles in the electrodes were used as calibration parameters of the model, following the idea described in [141].

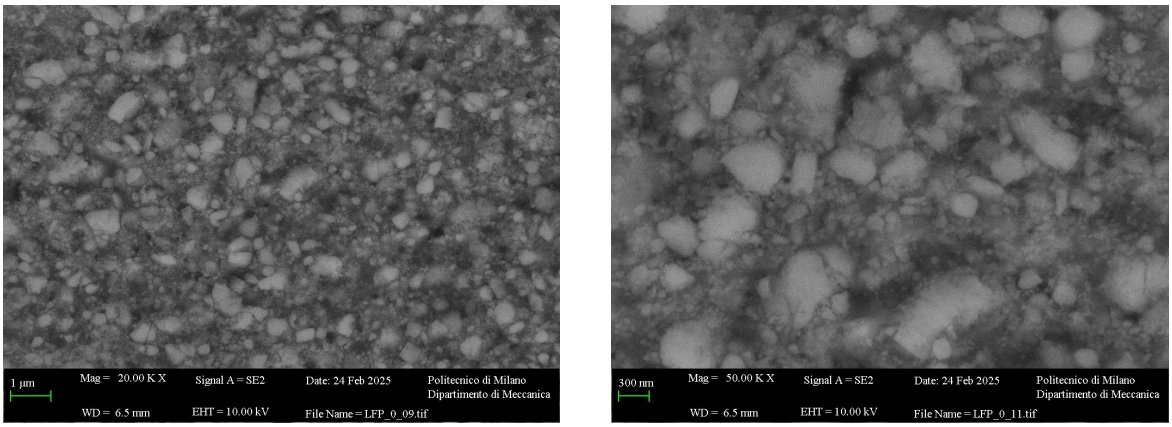

(a) 20.00 KX Magnification (b) 50.00 KX Magnification

Figure 5.5: Front sections of the LFP positive electrode of the M1B samples, obtained from a SEM analysis with different magnification levels

In figure 5.5, a Scanning Electron Microscope (SEM) analysis of the LFP cathode used in the M1B samples can be seen. The images represent the front section of the negative electrode and were obtained at different magnification levels, using respectively 20.00 KX and 50.00 KX multipliers. In the figure, the white regions correspond to the electrode's solid particles: as it can be clearly noticed, these particles are distributed uniformly within the volume, but are present in very different shapes and sizes, in a range of three orders of magnitude from few $[nm]$ to 1 $[\mu m]$. Because of this reason, their electrochemical behavior during intercalation and de-intercalation reactions is characterized by a great variation depending on the particles size.
In this regard, given the model parameters, the radii were adjusted as a function of the current rate: as a general rule, the higher the current and the smaller the particles, due to the fact that, at high C-rates, smaller particles dominate the reaction overpotentials [141].
In figure 5.6 the particles radii considered for the single particle model are presented.

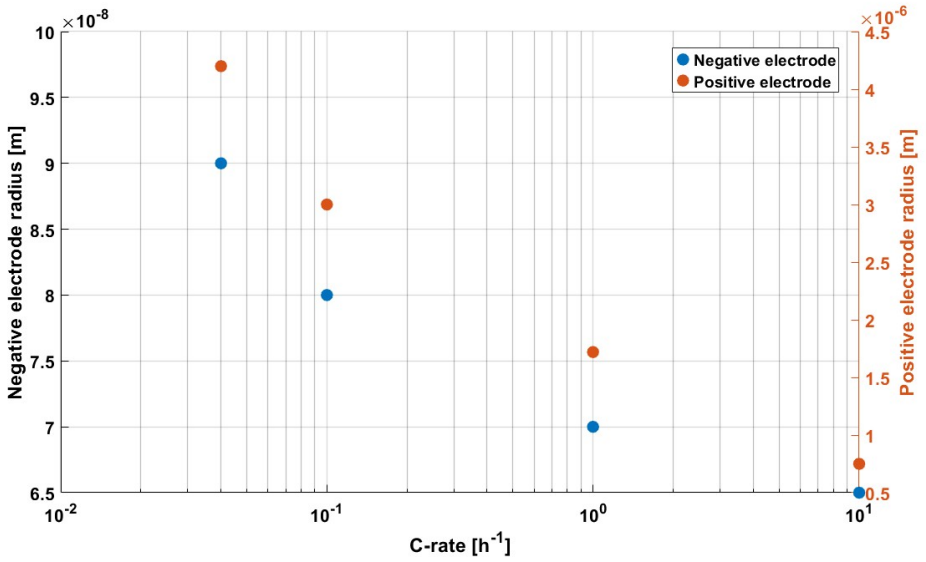

Figure 5.6: Calibrated solid particles radii for the single particle model

Lithium diffusion coefficient in the solid phase

Lithium diffusivity in the solid phase of the electrodes particles was modeled through an Arrhenius-type relation with temperature:

$$D_{s,i} = D_{s,i,0} \cdot \exp\left[\frac{EA_{D_{s,i}}}{R}\left(\frac{1}{T_0} - \frac{1}{T}\right)\right] \tag{5.43}$$

Where $EA_{D_{s,i,0}}$ is the reference activation energy related to the diffusion coefficient in the i-th electrode, computed at the reference temperature T_0.

Reaction rate constant

In the same way, also the electrochemical reactions rate constants were described by an Arrhenius-type dependence, to take into account their variation with temperature. This can be stated as:

$$K_i = K_{i,0} \cdot \exp\left[\frac{EA_{K_i}}{R}\left(\frac{1}{T_0} - \frac{1}{T}\right)\right] \tag{5.44}$$

5.2.4. Aging modeling

As described in section 3.3.1, four M1B samples were subjected to a calendar aging campaign at different storage conditions, reaching the final SoH stated in table 3.5. In the same section, it was determined that the main degradation mechanisms were related with loss of lithium inventory, due to the formation of passivation layers at the electrodes-

electrolyte interfaces. This particular aging mode is not accompanied by appreciable damage on the anode and cathode structures, but it is related with loss of cyclable lithium species between electrodes. For this reason, in the SPM, the calendar aging experienced by the cells was modeled with the introduction of a LLI parameter. This quantity applies a correction on the available lithium during discharge by decreasing the maximum stoichiometry limit at the negative electrode [70]:

$$x_{n,1,aged} = x_{n,1,BOL} \cdot (1 - LLI) \tag{5.45}$$

5.3. 2D Thermal model

Consequently to the definition of the single particle electrochemical model, a spatial thermal model was created to account for the temperature differences within the battery volume. In this regard, a two dimensional model will be presented in this section, starting from the assumption of radial symmetry of the samples. The main idea behind this additional discretization lies in the possibility to adequately represent the thermal inertia of the analyzed batteries, through the introduction of the estimated thermal conductivities. In this way, a comparison between internal and external temperature curves can be made.
This thermal model takes inspiration from the one described in [144] for the prismatic geometry. Nonetheless, it was completely re-visited and re-written for the cylindrical geometry and adapted to the single particle model previously described.

5.3.1. Governing equations and assumptions

The 2D thermal model is based on the relaxation of the assumption of a bulk temperature in the SPM: in this regard, a double discretization along the radial and axial coordinates of the cylindrical cell is applied, assuming radial symmetry.

In addition, the internal components of the battery are modeled through the definition of their most important parameters, namely the specific heat capacity, the thermal conductivities and the density, other than their relative position within the cell itself. To increase accuracy, the components taken into account were: the jelly-roll, the positive and negative tabs, the external shell and the current collectors foils. A schematization of the cell internal geometry can be seen in figure 5.7.

The main assumption is that the jelly-roll is treated as an homogeneous solid domain, such that the internal heat generation is equally distributed within this component. Moreover,

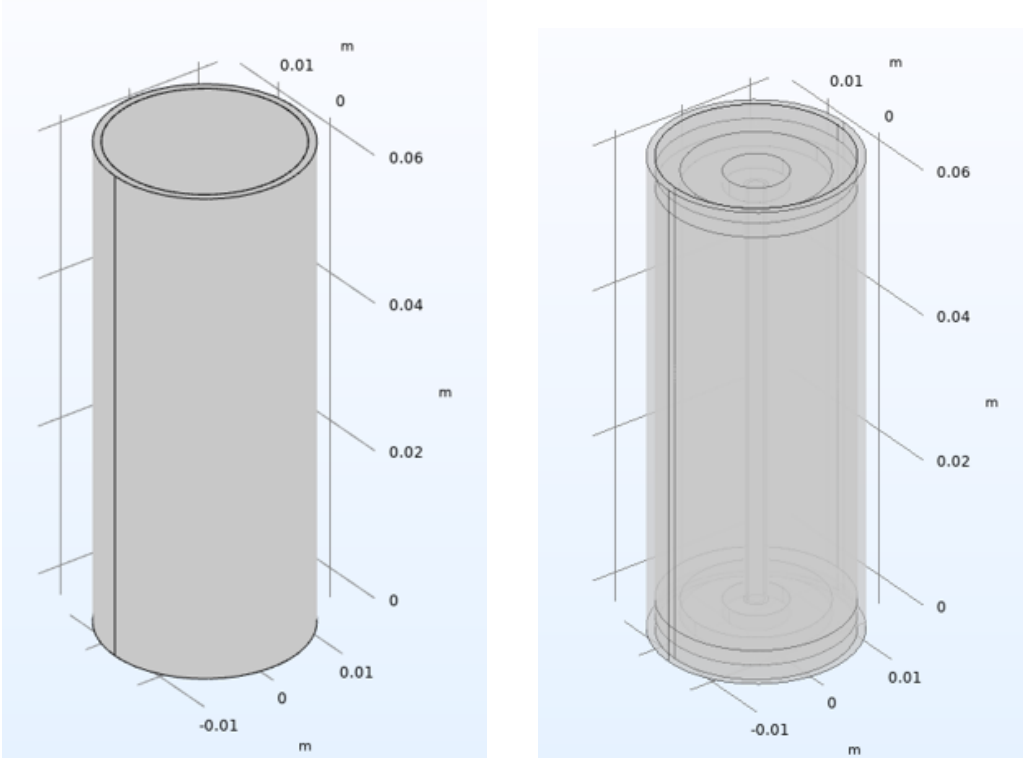

(a) External view (b) Translucent view

Figure 5.7: Schematization of the 2D thermal model internal components; in (a), the external shell and tab; in (b) a translucent view of the internal components.

convection is neglected within the cell as well as all heat transfer through radiation. Following these assumptions, a mesh of nodes within the internal components of the battery is generated, where adjacent nodes are related with each others through a lumped thermal resistance.

In this way, each node can be connected to at most four neighbouring nodes through as many heat transfer functions.

The relation for a generic node at point (r, z) is given by:

$$m_{r,z} c_{p_{r,z}} \frac{dT_{r,z}}{dt} = \dot{Q}_{r,z} + \frac{T_{r+1,z} - T_{r,z}}{R_{r_{r,z}}} + \frac{T_{r-1,z} - T_{r,z}}{R_{r_{r,z}}} + \\ + \frac{T_{r,z+1} - T_{r,z}}{R_{z_{r,z}}} + \frac{T_{r,z-1} - T_{r,z}}{R_{z_{r,z}}} \tag{5.46}$$

Where:

- $m_{r,z}$ is the mass of the node;
- $c_{p_{r,z}}$ is the specific heat capacity of the node;

- $\dot{Q}_{r,z}$ is the thermal power generated within the node; this term is considered only in the jelly-roll nodes and is defined as for equation 5.41;
- $R_{r_{r,z}}$ and $R_{z_{r,z}}$ are, respectively, the thermal resistances in the radial and axial directions, that are defined as:

$$R_{r_{r,z}} = \frac{\ln(r_2/r_1)}{2\pi k_r(z_2 - z_1)} \tag{5.47}$$

$$R_{z_{r,z}} = \frac{2(z_2 - z_1)}{k_z(r_2^2 - r_1^2)} \tag{5.48}$$

  Where r_1 and r_2 are, respectively, the internal and external radial coordinates of the node; in the same way, z_1 and z_2 are, respectively, the lower and upper axial coordinates; k_r and k_z are the radial and axial thermal conductivity, respectively.

Additional particular cases of the generic equation can be defined; in particular, equation 5.46 becomes:

$$m_{r,z}c_{p_{r,z}}\frac{dT_{r,z}}{dt} = \dot{Q}_{r,z} + \frac{T_{r+1,z} - T_{r,z}}{R_{r_{r,z}}} + \frac{T_{r,z+1} - T_{r,z}}{R_{z_{r,z}}} + \frac{T_{r,z-1} - T_{r,z}}{R_{z_{r,z}}} \tag{5.49}$$

if the node is adjacent to the core of the cell, at $r = 0$, or

$$m_{r,z}c_{p_{r,z}}\frac{dT_{r,z}}{dt} = \dot{Q}_{ht} + hA(T_{amb} - T_{r,z}) \tag{5.50}$$

if the node is adjacent to the external environment.
$\dot{Q}_{ht}$ represents the heat transfer towards internal nodes, as for equation 5.46; h is the heat transfer coefficient; A is the overall external surface area subjected to convection losses. In this instance, the external environment is modeled as an additional node with constant temperature equal to T_{amb}.

Reorganizing the previous relations in a state-space representation, the following equation can be defined:

$$\dot{\boldsymbol{T}} = \boldsymbol{D}\dot{Q} + \boldsymbol{H}\boldsymbol{T} \tag{5.51}$$

Where:

- $\boldsymbol{D}$ is the heat generation distribution array, representing the volume fraction of jelly-roll in the node over its total volume;
- $\boldsymbol{H}$ is the heat transfer matrix, including all of the heat transfer functions between adjacent nodes.

5.4. Model validation and interpretation of results on experimental data

After the parameters calibration, the SPM model was validated through the comparison with previously obtained experimental data. In this regard, given that the model is more representative for charge and discharge tests at very low C-rates, the voltage curve obtained during a discharge process at 0.04C was used. The comparison can be seen in figure 5.8.

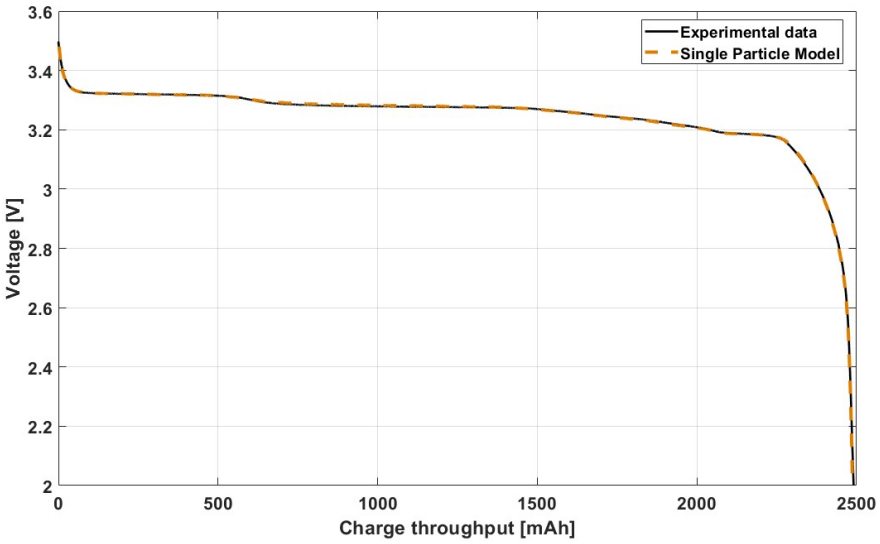

Figure 5.8: Comparison between single particle model and experimental data curves for a discharge test at 0.04C

As it can be noticed, the model is capable of matching almost perfectly the discharge test experimental data, leading to an excellent representation. The maximum detected error was found to be equal to 5 $[mV]$, in the central part of the curve.
An additional comparison between the DV curves of model and experimental data was made (figure 5.9).

It can be observed that a great accordance can be found with the experimental curve also in this case. In this regard, the model is able to correctly represent the voltage curve slope variations, such that the peaks related with the thermodynamic behavior of the cell are visible. A certain noise is present in the SPM curve due to the numerical solution. In this regard, a moving average filter was applied on the results to obtain a smoother curve.

Subsequently, the same input parameters were used for the comparison between the model and discharge tests at a C-rate equal to 0.1C and 1C. According to the previous assump-

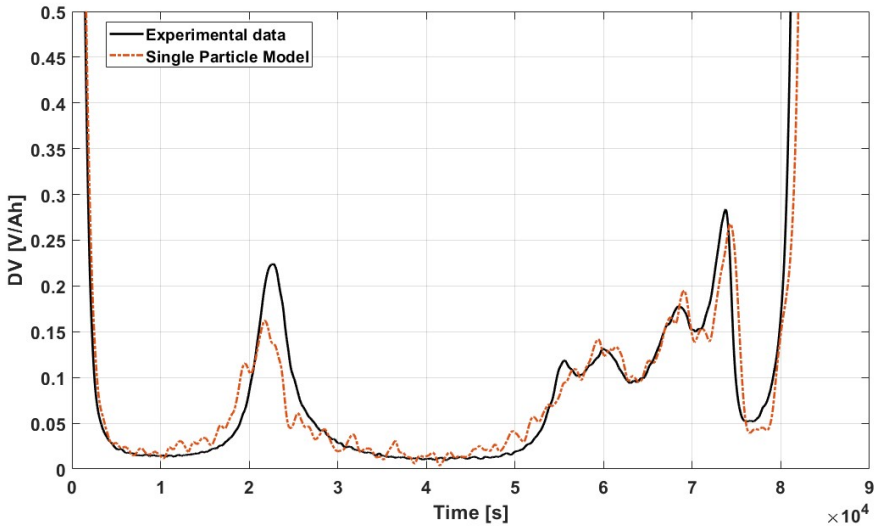

Figure 5.9: Comparison between single particle model and experimental data DV curves for a discharge test at 0.04C

tions, the radii of the solid particles of both electrodes were used as the only calibration parameters.

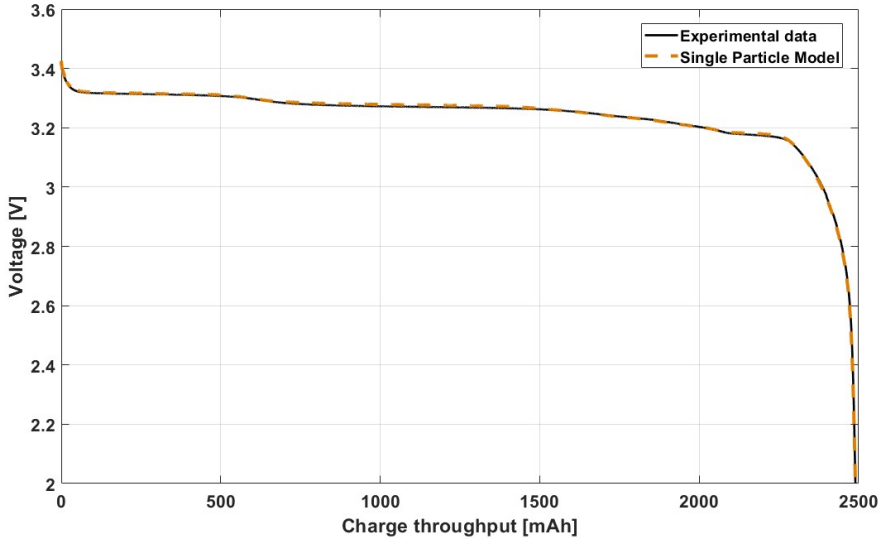

Figure 5.10: Comparison between single particle model and experimental data curves for a discharge test at 0.1C

The shape of the curves in figure 5.10 is very similar to the one obtained from the test at 0.04C. Indeed, both current rates could be assumed to reach the quasi-equilibrium condition, as defined in section 2.3.2. For what concerns the model, it is able to almost perfectly represent the voltage curve, even taking into account the different overpotential

losses, with a maximum error of 8.9 $[mV]$. In particular, at the initial points of the simulations, the SPM is capable to represent the first ohmic voltage loss experienced by real cells, decreasing accordingly its value.

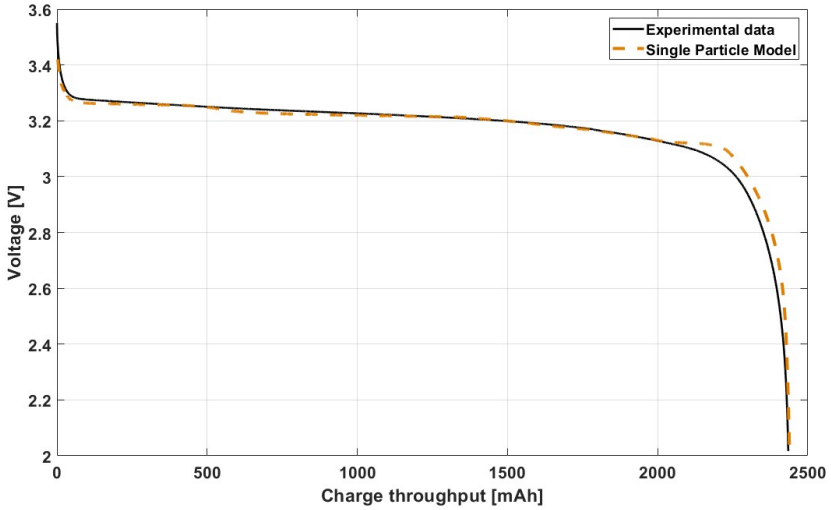

Figure 5.11: Comparison between single particle model and experimental data curves for a discharge test at 1C

In figure 5.11, it can be seen that the model and experimental data curves are in very good agreement also for a discharge test at 1C: the initial ohmic loss, directly correlated with the current rate, is correctly represented; moreover, also the behavior of the real cell during the central part of the discharge test is very well predicted, thanks to the electrolyte correction introduced in the model. In fact, even if the SPM is designed for very low current rates (because of its fundamental assumptions), the curve follows closely the experimental one. On the other hand, it can be noticed that a small divergence between the curves occurs towards the end of the discharge test, at around 2200 $[mAh]$. This is related to the equilibrium curve of the graphite negative electrode, which shows a "bump" at this lithiation state. Indeed, several slope variations can be noticed on the model curve, even at C-rate = 1 $[h^{-1}]$. These deviations indirectly derive from the assumptions employed in the model, as some secondary phenomena effects are neglected. A good match between experimental and model data is nonetheless achieved, such that the final charge throughput is the same.

The maximum error between the curves was found to be equal to 134.6 $[mV]$, corresponding to the described bump at the end of the curve; in the remaining part of the curve, instead, the maximum error was estimated to be equal to 19.5 $[mV]$. A comparison between the discharge tests obtained at 0.04C and 1C can be seen in figure 5.12.

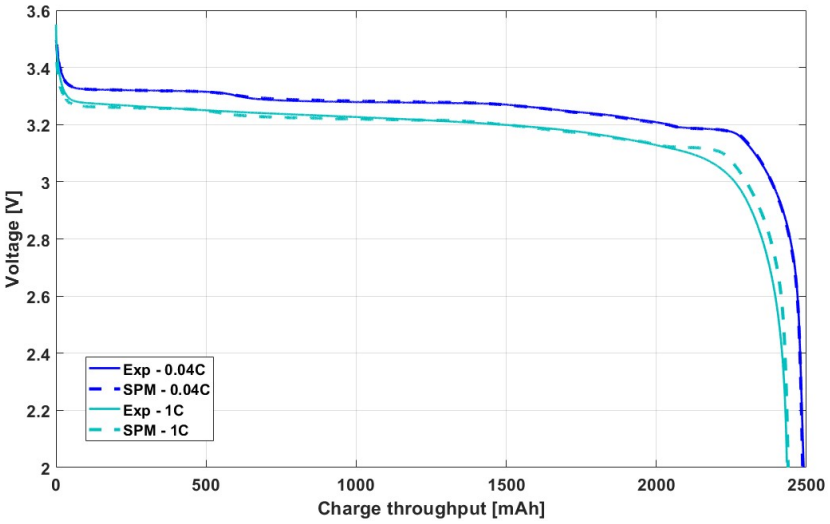

Figure 5.12: Comparison between single particle model and experimental data curves for discharge tests at 0.04C and 1C

Due to the model implementation, it was possible to represent the concentration evolution inside the solid particles and electrolyte, leading to a better understanding of the lithium transport within the cell's components. In figure 5.13, the concentration evolution during a 1C discharge process can be seen. It can be noted that a concentration gradient is established during operation, both in the positive and negative electrodes. This phenomenon is much more important within the anode particles, due to the fact that their radius was defined as almost two order of magnitude higher than the cathode. Within the latter, only a slight variation along the radial coordinate is experienced.

After a first differentiation from the initial equilibrium stoichiometry, the concentration gradients reach a seemingly steady-state, corresponding to the average behavior of the cell during operation. At a certain point, around 1800 $[s]$ of elapsed simulation time, a switch between the stoichiometric levels of the electrodes occurs, as the cathode approaches a higher lithiation state.

In figure 5.14, instead, the concentration evolution of lithium ions inside the electrolyte domain can be seen. In the graph, only the extreme coordinates along the linear discretization are represented, due to the fact that their divergence produces the voltage loss related with transport in the electrolyte. Also in this case, it can be noticed that a gradient is established within the electrolyte. This difference between extreme coordinates is kept almost constant during the whole process, with a clear descending trend for both curves. Indeed given that, according to the model, the dominant transport phenomena in the electrolyte is diffusion, a first time transient is experienced by the system, until

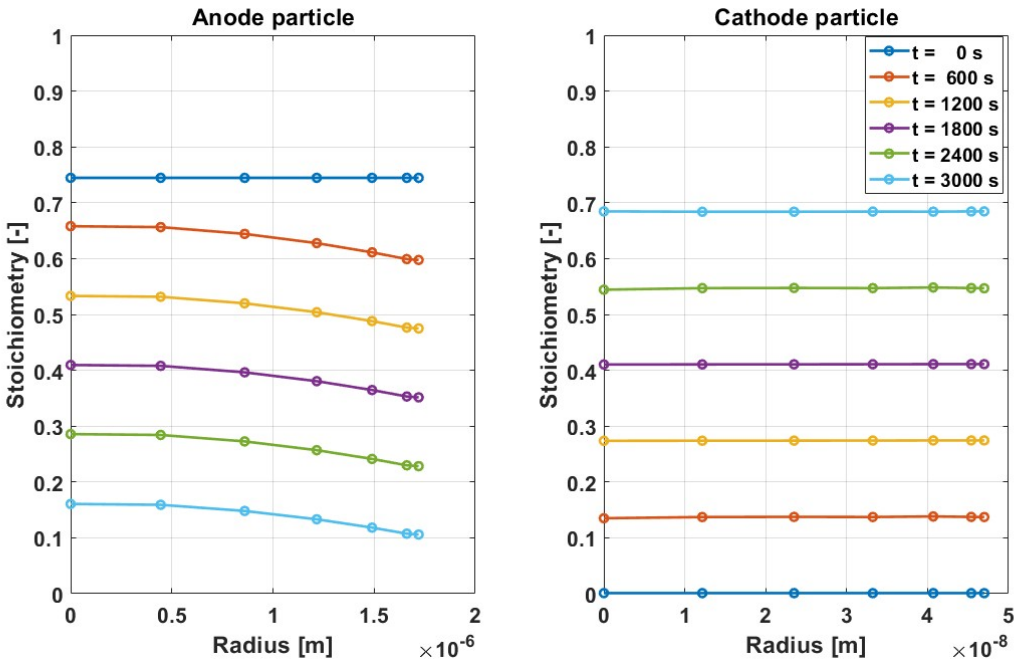

Figure 5.13: Evolution of the concentration of lithium species inside the positive and negative electrode solid particles, during a 1C discharge simulation

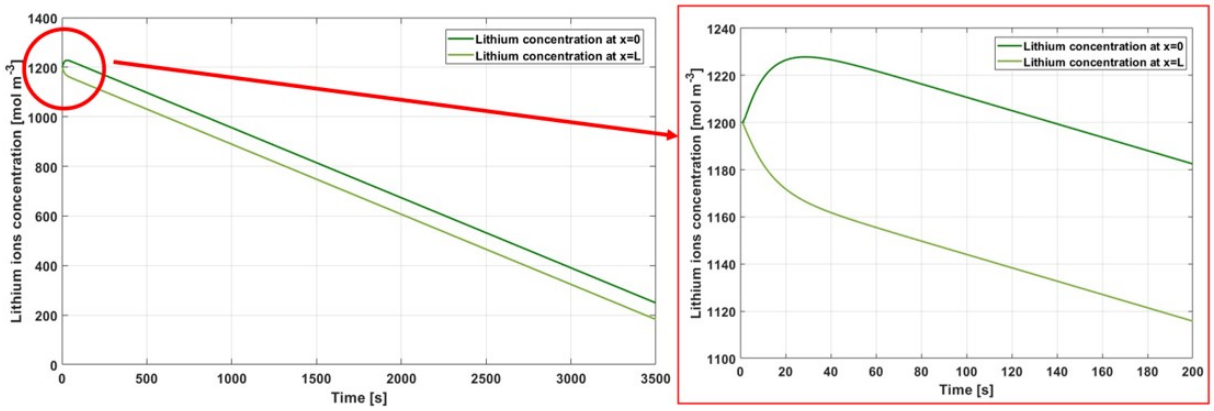

Figure 5.14: Evolution of lithium ions concentration in electrolyte, during a discharge simulation at 1C

a steady state asymptotic behavior is reached. The model correctly represents the phenomenon because a higher concentration is expected at $x = 0$, which lies in the negative electrode domain: during discharge processes, in fact, lithium ions flow from the anode towards the cathode; for this reason, a negative gradient is established to allow for the transport.

Subsequently to the assessment of the voltage curves and concentration gradients, the modeled internal temperature was taken into account. The value of this state variable

strongly depends on the conservation of energy equation, and thus on the internal heat generation within the jelly-roll. As described in the previous section, several contributions take part in the heat generation within the cell, that can be divided as irreversible and reversible terms. In this regard, the irreversible term is given by all of the overpotentials arising during operation, comprising of ohmic, electrochemical reaction and transport phenomena related losses. By the model definition, solid particles and electrolyte ohmic drops (η_{ohm}) only depend on the current rate applied to the cell and, as such, are characterized by a constant behavior during CC discharge tests. Moreover, electrolyte transport related losses (η_e) strongly depend on the operating temperature and concentration gradient inside the electrolyte domain. Apart from the first time transient, the latter is approximately constant during the whole process, so this loss can be assumed to be only temperature dependent (which is characterized by very limited variations anyway). Finally, electrochemical reactions overpotentials feature very marked changes throughout the process, especially at the beginning and at the end. By definition through the Butler-Volmer equation (section 5.2.2), these voltage drops strongly depend on the available lithium at the electrode-electrolyte interfaces and thus on the lithium species concentration within the electrodes solid particles. Consequently, a higher overpotential is attained at the start and at the end of the simulation, due to the fact that one of the two electrodes is almost completely emptied of lithium.

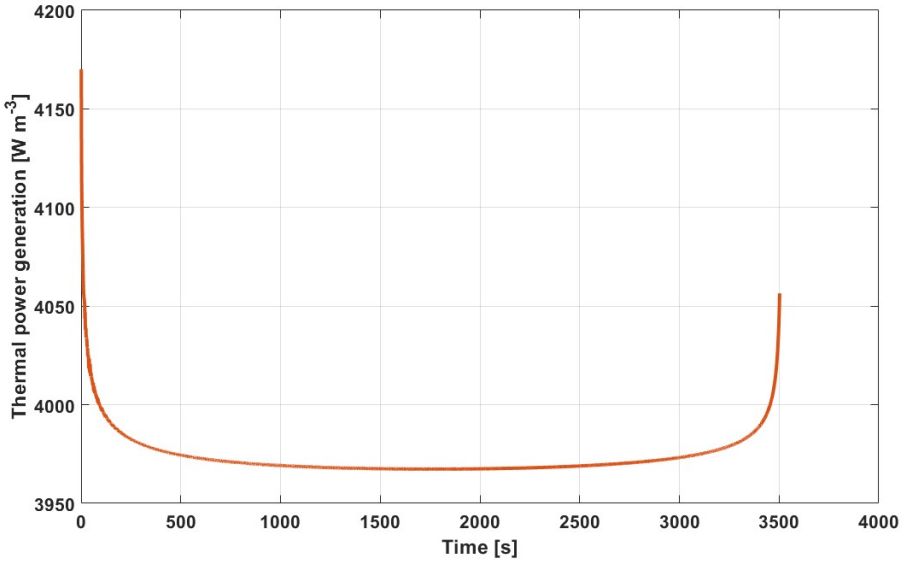

Figure 5.15: Irreversible thermal power generation during a discharge test at 1C

In figure 5.15 the sum of all contribution can be seen, where the shape is mostly determined by electrochemical reaction overpotentials. In this regard, a higher loss in observed at the beginning and at the end of the discharge simulation, confirming the previous statement.

On the other hand, a plateau can be seen in the central part of the process, where the main contribution is given by the ohmic losses.

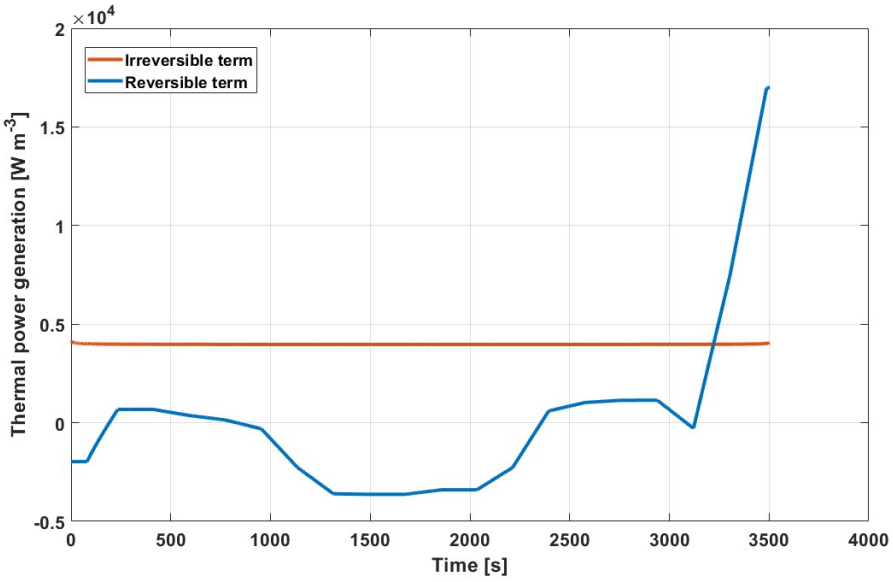

Figure 5.16: Comparison between reversible and irreversible thermal power generation terms during a discharge process simulation at 1C

In figure 5.16, instead, the comparison between irreversible and reversible heat generation terms for a discharge process at 1C is presented. It can be seen that, at such current rates, the order of magnitude of both contribution is the same. The reversible term is characterized by some variations, as it floats around a certain average value. It can be noticed that the latter, however, is close to zero, such that an almost null contribution is achieved at the end of the process.
The temperature curve obtained from the same simulation can be seen in figure 5.17.

The entropic coefficient employed for this model was slightly tweaked with respect to the one obtained experimentally, as the latter didn't represent correctly the internal behavior of the analyzed cell. In this regard, the internal temperature curve obtained from the experimental test at 1C was used for the fitting of the coefficient (figure 5.18). As described in section 4.1, the internal temperature evolution was measured inside the mandrel of the cylindrical samples. Given that, instead, thermal power is generated within the jelly-roll, this procedure implicitly assumes the equivalence between the two positions in the radial direction. In general, this is not necessarily true, but can be regarded as a safe assumption due to the mandrel material, which is characterized by a high thermal conductivity.

The same entropic coefficient map was applied to a discharge process carried at a C-rate equal to 0.1 $[h^{-1}]$, plotting the internal temperature as output (figure 5.19). A different

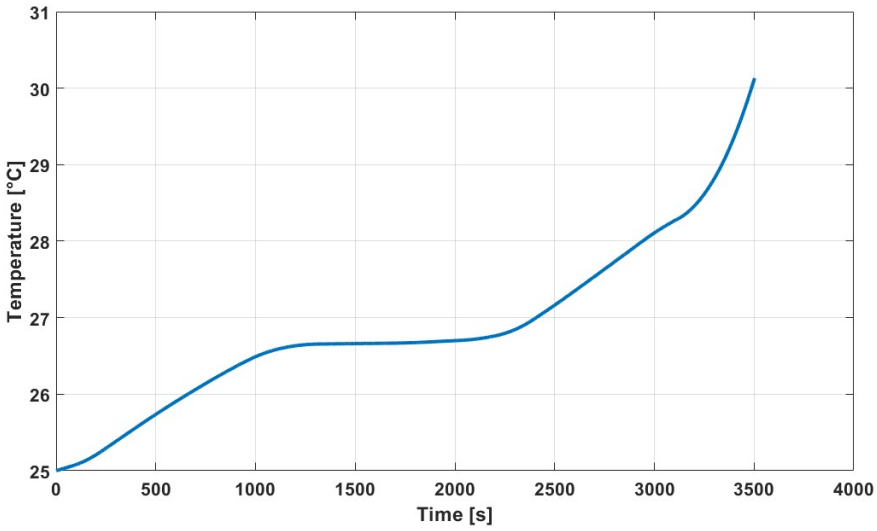

Figure 5.17: Internal temperature evolution during a discharge process simulation at 1C

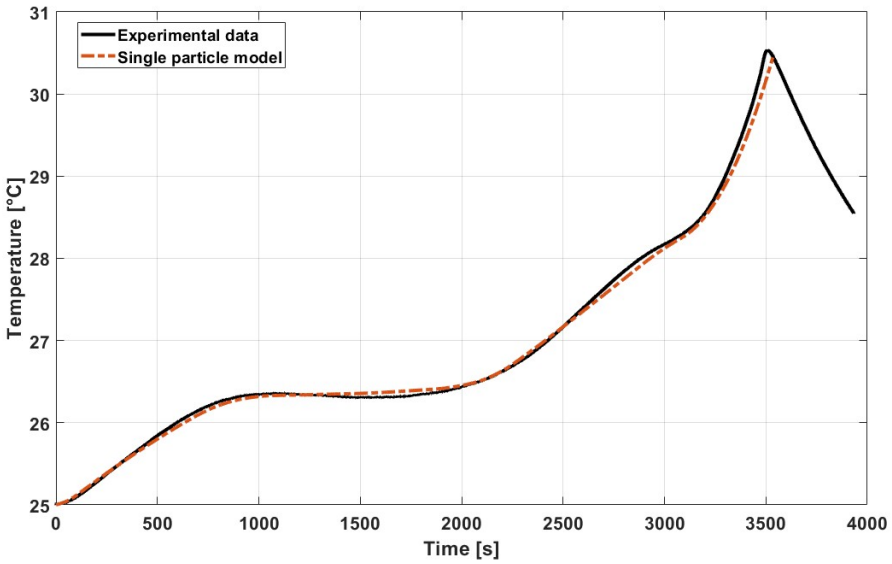

Figure 5.18: Comparison of internal temperature evolution between single particle model and experimental data, during a discharge process at 1C

heat transfer coefficient was used, as convection becomes more and more important as the duration of the test increases.

It can be clearly seen that a very good agreement was found between the model and previous experimental data, verifying once again the goodness of the model in predicting the internal behavior of the modeled lithium-ion batteries. In this regard, the maximum error between the curves was found to be equal to 0.3 $[°C]$, at the end of the process (corresponding to 1.21% on the curve).

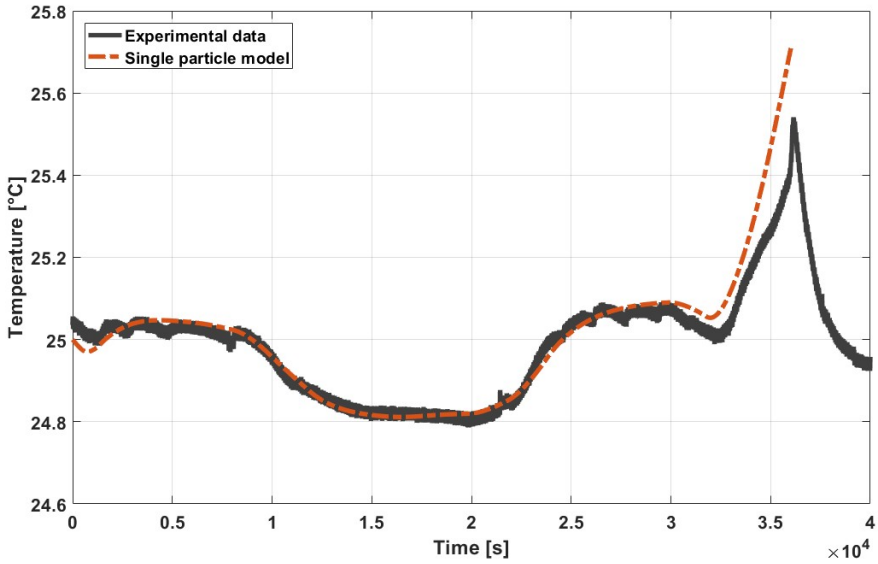

Figure 5.19: Comparison of internal temperature evolution between single particle model and experimental data, during a discharge process at 0.1C

Furthermore, this simulation demonstrates that the entropic heat contribution is much more important than irreversible terms at very low C-rates, leading to the confirmation of the assumptions described in the internal temperature experimental campaign 4.1. If this contribution was to be neglected, a much greater error would be attained.

Finally, the differentiation between internal and external temperature evolutions was represented through the introduction of the estimated values of radial and axial thermal conductivity. These were implemented as an input for the 2D thermal model previously defined, together with other material properties and operating parameters. For this validation step, the bulk temperature obtained from the SPM using a null heat transfer coefficient was employed. This curve was imposed on the internal nodes of the bi-dimensional mesh, constituting the inner volume of the mandrel. The cylindrical cell was then simulated, taking as output the temperature at the same axial coordinate but on the external surface (figure 5.20).

It can be seen that a discrete agreement was found between the model and the experimental curves for the external temperature sensor. On the other hand, the main difference between the two can be noticed at the beginning of the process, where a different slope is experienced by the simulated temperature evolution. In particular, this divergence is caused by the assumption of imposing the internal temperature and not the heat generation within the jelly roll: from the methodology described in section 3.3.3, in fact, only the temperature inside the mandrel could be measured, which in turn doesn't correspond

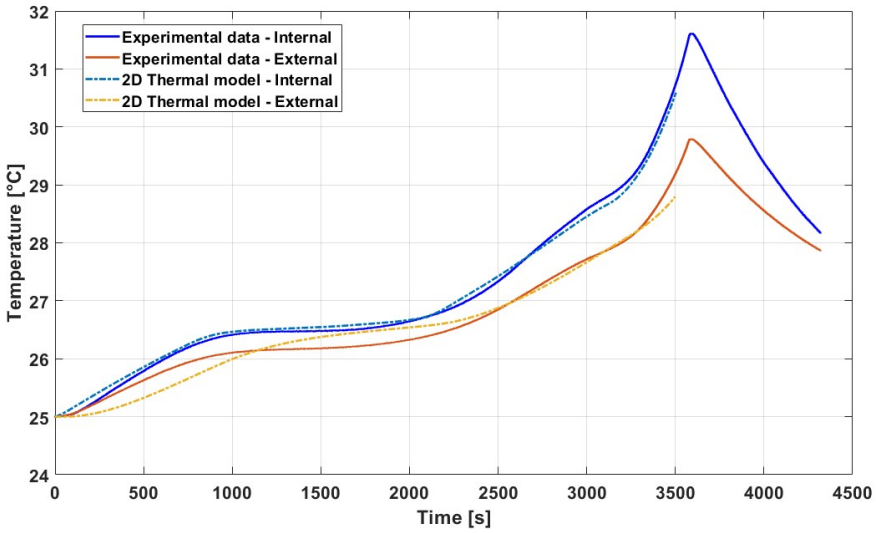

Figure 5.20: Comparison of internal and external temperature evolution between 2D thermal model and experimental data, during a discharge process at 1C

to the volume where thermal power is produced. Accepting the error caused by this difference, the internal temperature was taken as input, given that it was the only available experimental data curve. At the end of the simulation, a similar temperature difference between the curves is nonetheless obtained.

5.4.1. Aging modeling validation

The LLI correction was applied to the single particle model, as described in section 5.2.4 and compared with the discharge tests at 0.04C obtained from the calendar aging campaign samples (section 3.3.1, figure 3.23). The results can be viewed in figure 5.21.

As it can be seen, the model is able to correctly predict the effects of aging on the voltage curves of the degraded cells. In fact, analogous curves are characterized by a very close match and a similar final charge throughput is achieved for all four tested samples. The maximum error between the experimental curves and their corresponding model simulation was found to be equal to 44.3 $[mV]$, obtained for "Cell 1". For "Cell 4", instead, which was the sample employed for the thermal and internal temperature experimental campaigns, a maximum error of 11.2 $[mV]$ was estimated. It can be noted that the biggest difference between experimental data and model is experienced for all samples in the first bump of the curve: as described in section 3.3.1, this feature is related with the equilibrium potential of the negative electrode and,for this reason, could suggest an imperfect description of aging in the model. A very good result is nonetheless achieved,

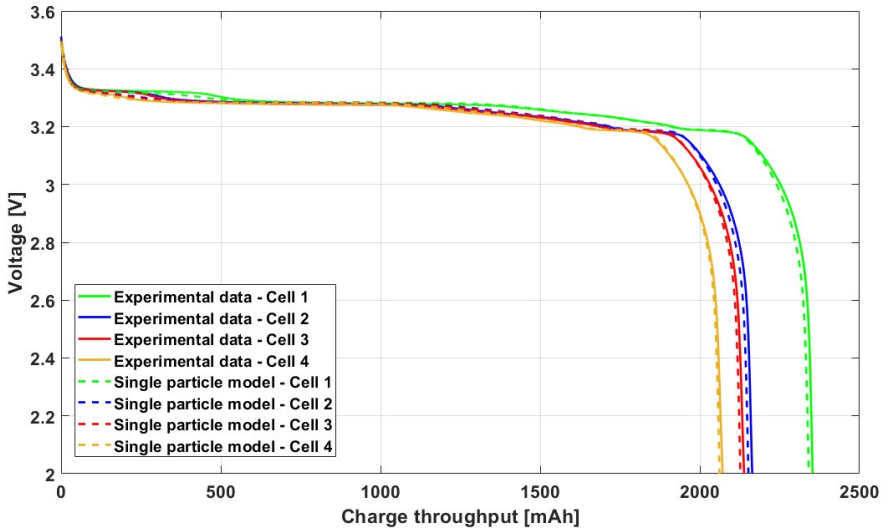

Figure 5.21: Comparison between experimental data and model simulation for discharge processes at 0.04C, for the M1B samples after calendar aging

as shown from the obtained errors between experiments and simulations.

In addition, the internal temperature curves of BOL and aged samples obtained from discharge tests at 0.1C were compared with the single particle model (figure 5.22).

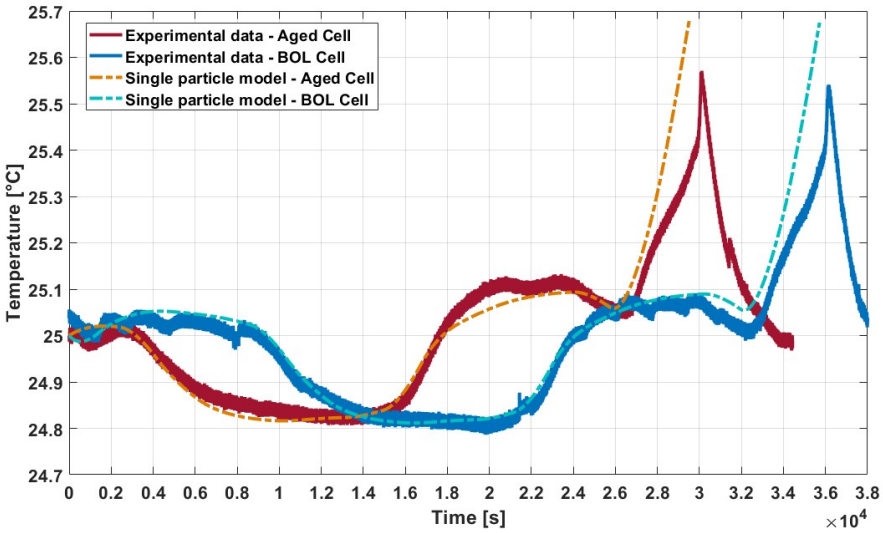

Figure 5.22: Comparison between experimental data and model simulations for internal temperature curves during discharge processes at 0.1C, for BOL and aged samples

For this step, the same entropic coefficient map was employed. In this regard, it is important to note that in practice this parameter depends on the actual lithiation state of

electrodes and not on the state of charge, which can only be regarded as a proxy of this physical quantity. When a sample is in BOL conditions, both descriptions are equivalent, as they represent the same aspect. In aged conditions, however, a different lithiation state is reached at $SoC = 100\%$, leading to a compression of the state of charge range. Following this idea, the entropic coefficient was modeled as a function of the actual lithiation state and not on the SoC, leading to a more accurate description of the physical behavior of batteries.

As it can be observed from the graph, a great accordance was found between the curves also in this case, as the simulation correctly represents the main slope variations. A shift was experienced on the entropic coefficient in the first period, thanks to the correction applied to the initial stoichiometry as for equation 5.45. Apart from the initial differentiation, the two curves are characterized by the same behavior, leading to almost parallel lines at the end of the process.

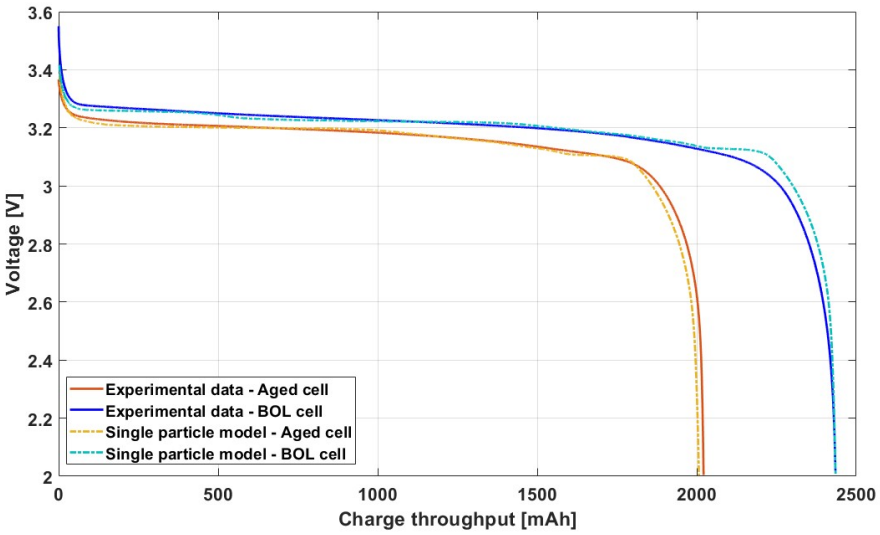

Figure 5.23: Comparison between experimental data and model simulations for voltage curves during discharge processes at 1C, for BOL and aged samples

Furthermore, discharge simulations at C-rate equal to 1 $[h^{-1}]$ were taken into account. In this regard, both voltage and internal temperature curves were analyzed, as they provide a somewhat complete description of the process.

As it can be seen from figure 5.23, even at higher current rates, the model is able to correctly predict the internal temperature of aged cells, due to the applied correction on the lithiation state. As described in section 1.5.1, it is known that the formation of passivation layers at the electrodes-electrolyte interfaces increases the internal resistance of the cell, leading to a higher ohmic loss during charge and discharge processes. It can

be noticed that this aspect is well represented on the simulated voltage curve of the aged cell, due to the fact that a lower voltage is found at parity of charge throughput.

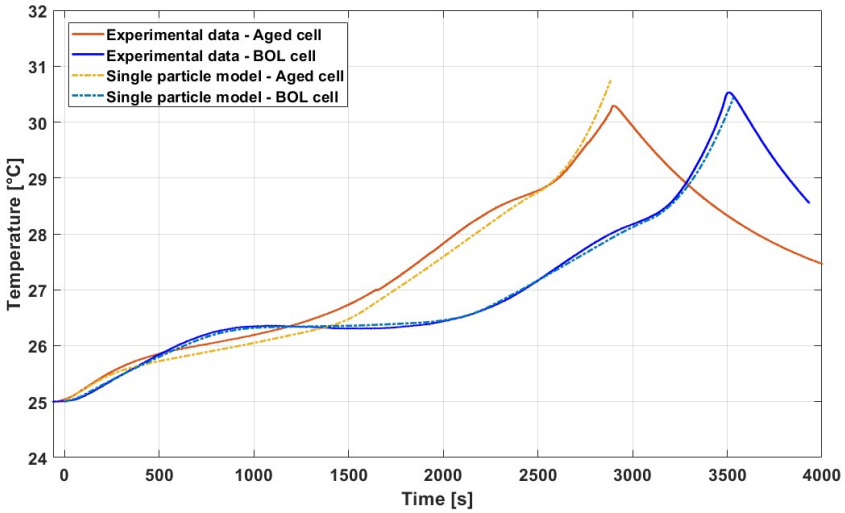

Figure 5.24: Comparison between experimental data and model simulations for voltage curves during discharge processes at 1C, for BOL and aged samples

In the same way, the internal temperature obtained from the simulation of the aged sample (figure 5.24) follows closely the experimental data. In particular, the decrease of the initial lithiation state at the negative electrode, represented by an earlier "bump" in the experimental data (see section 4.1), was predicted by the model, leading to a further confirmation of the previous assumptions.

5.4.2. Sensitivity analysis on thermal parameters

Following the validation of the model, a sensitivity analysis was done on the thermal parameters, to assess the impact of their value on the temperature curves. In this regard, the estimated values obtained during the thermal characterization experimental campaign were employed, considering their variation as a function of the state of charge and temperature. For this step, the nodal representation of the 2D thermal model allowed for the comparison between the temperature curves obtained from internal temperature measurements (presented in section 4.1) with the corresponding nodes in the mesh. Following this idea, the nodes related to the mandrel core were employed for this further validation step.

The specific heat capacity was considered as a constant value, computing the average value with respect to the SoC by using the correlation found from the thermal characterization campaign (section 3.3.4); $\pm 5\%$ and $\pm 10\%$ variations were then applied to better understand the impact of this parameter on the internal temperature evolution.

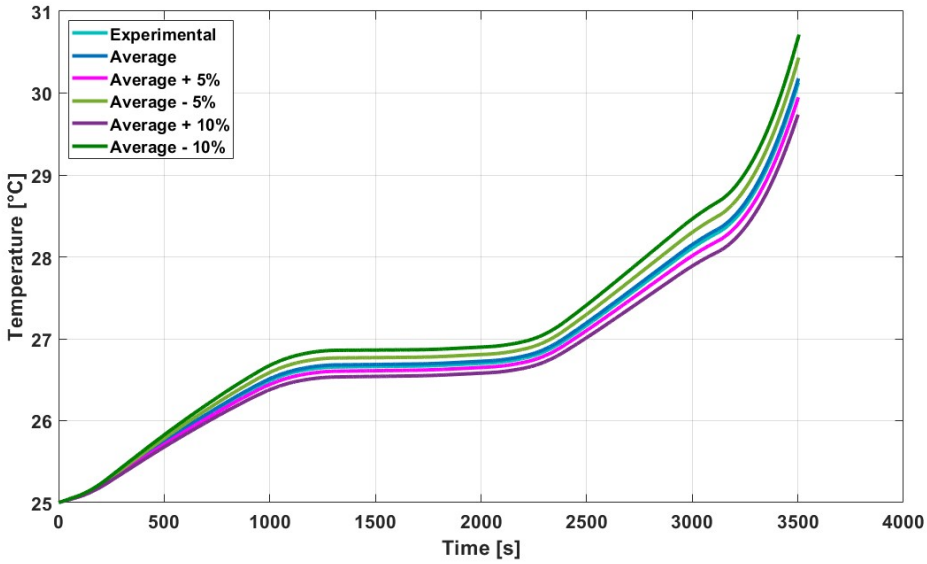

Figure 5.25: Results of the sensitivity analysis on the specific heat capacity

In figure 5.25 the results of the sensitivity analysis on the specific heat capacity are presented. It can be noticed that a very low difference is found between the internal temperature curves employing variable or constant values. In particular, the temperature curve employing the average value is almost completely overlaid on the one using the estimated specific heat capacity from the experimental campaign, due to the very weak dependency of this parameter with the state of charge. On the other hand, a difference of around 0.5 $[°C]$ is achieved on the temperature at the end of the process with an increase or decrease of the average value of $\pm 10\%$. When compared with the global temperature change, this divergence appears to be significant for the thermal behavior of batteries, leading to the risk of an imperfect design of the cooling system for battery packs even at 1C. Moreover, given that the samples employed in this thesis are characterized by high power capabilities, this aspect could result in increased and cumulated errors for processes at higher C-rates as the temperature variations grow considerably. Nevertheless, several estimated values of specific heat capacity exist in literature, depending on internal materials, geometry and assembly. For this reason, a characterization of this parameter should be always considered for specific samples.

Subsequently, the radial thermal conductivity was analyzed, performing a sensitivity assessment on this parameter by employing the 2D thermal model (figure 5.26).

It can be observed that a negligible change is achieved through the model on the external temperature, even with an increase or decrease of $\pm 10\%$ on the radial thermal conductivity. This result suggests that a very low error can be achieved also for far off assumption

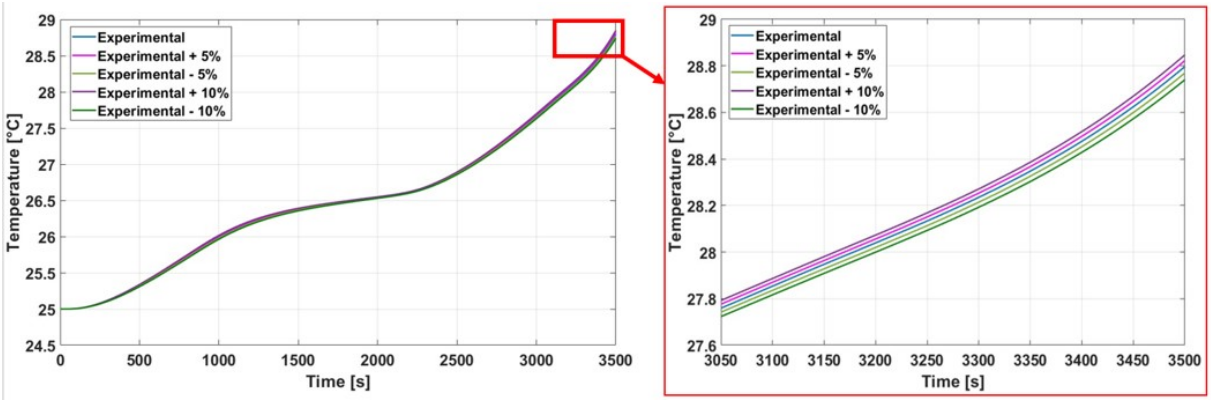

Figure 5.26: Results of the sensitivity analysis on the radial thermal conductivity

of the analyzed parameter.

5.5. Final remarks

In this chapter, the description of the thermo-electrochemical model employed for the characterization of the LIB samples was presented. To summarize briefly:

- A single particle model was conceptualized and implemented in MATLAB®, through the definition of conservation equations for the internal components of a battery. In this regard, the conservation equations of charge and lithium species in the electrolyte and solid particles were considered, other than the conservation of energy employing all heat generation terms. The electrochemical reaction kinetics, instead, were described by the Butler-Volmer equation. A discretization employing Chebyshev nodes was used for the spherical electrodes particles.

- A two-dimensional thermal model was defined and implemented in MATLAB®, for the characterization of the temperature differences within the cylindrical samples. The model is based on a nodal description of the battery volume, such that the temperature evolution is described by a network of thermal resistances. The internal components domains were defined in the model, through the definition of their thermal parameters and relative position within the cell.

- The single particle model was validated on the previously obtained experimental data, through the calibration of the physical quantities governing the internal operation. A very good match was found between measured and simulated processes, both for voltage and internal temperature curves. In particular, an error of 5 $[mV]$ was estimated for a discharge at 0.04C, while a maximum error of 134.6 $[mV]$ was found for a discharge process at 1C, which was caused by the model assumptions. LLI and related aging phenomena were modeled through a correction on the stoichiometry of the anode: the maximum error was found to be equal to 44.3 $[mV]$, on the voltage curve of a discharge at 0.04C.

- The internal temperature evolution was described by the conservation of energy equation, linking overpotentials from the electrochemical behavior with the corresponding heat generation. The entropic coefficient map was calibrated on the internal temperature curve of a discharge test at 1C, and validated using the same map on a discharge test at 0.1C. The maximum error was found to be equal to 0.3 $[°C]$.

- A sensitivity analysis was done on the model for the thermal parameters. A very little variation of the internal temperature evolution was found by using an average value with respect to the experimental data, concluding that the choice of a constant

value can be regarded as a safe assumption. On the other hand, by changing the specific heat capacity in the range of ±10%, an appreciable temperature divergence was found at the end of the process, suggesting the need of a characterization on the specific sample. In contrast, the same variation on the radial thermal conductivity produced a negligible change in the final temperature, concluding that little variations can be achieved even assuming different values.

6 | Conclusion and future aspects

This master thesis continues the research on the definition of innovative and easy-to-implement approaches for the characterization of lithium-ion batteries, fitting into the European framework of circular economy for these devices. Following a comprehensive literature review on the main operating aspects of LIBs it is found that very limited investigation was done on the effects of aging phenomena on their thermal behavior. For these reasons, the principal aim of this work lies in the definition of innovative methodologies for the thermal characterization of batteries, providing in turn a better physical understanding on the effects of degradation on the most important parameters governing the thermal behavior.
In particular, the main objectives that were achieved during this thesis work are:

- An innovative methodology for the assessment of the anisotropic thermal parameters of cylindrical cells is presented, capable of estimating both thermal conductivity and specific heat capacity simultaneously. The methodology is validated through the utilization of an aluminum alloy cylindrical body of known thermal properties.
- Four analytical models of the cell are defined for the estimation of thermal parameters, considering different boundary conditions for the characterization of the anisotropic behavior of LIBs. These models were compared with analogous COMSOL Multiphysics simulations, to verify their accuracy; in this regard a maximum error of 0.17% and 0.24% was found for the radial and axial models, respectively.
- A new methodology is defined for the introduction of FBG optical fiber temperature sensors inside the mandrel of cylindrical cells, employing the drilling of their positive pole in an inert environment. An integrity verification of the drilled samples is done afterwards, to assess the effects of this methodology on the cells. In this regard, no appreciable impact is found on the samples after the procedure.
- An experimental campaign is carried for the electrochemical and thermal characterization of the available LFP lithium-ion batteries samples, both at beginning of life and aged conditions. For this purpose, four cells are subjected to a calendar aging campaign at different SoC. Consequently, the radial and axial anisotropic

behaviors of the cylindrical cells are determined, as a function of the state of charge and operation temperature.

- From the experimental campaign, it is evaluated that the specific heat capacity is characterized by a weak parabolic trend with respect to the SoC, averaging around a value of 1110 $[J\ kg^{-1}K^{-1}]$; similar values are estimated for both the axial and radial tests, verifying the consistency of the methodology. The specific heat capacity of the analyzed aged sample is found to be similar to the BOL case only in the range of SoC between 0 and 40%, while a lower value is estimated in the remaining range. The biggest difference is found at $SoC = 1$, such that a decrease of 3.3% is assessed.

- More than one order of magnitude difference is found between the values of thermal conductivity, confirming the strong anisotropic behavior found in literature. In particular, the thermal conductivity in the axial direction is estimated to be around 30 $[W\ m^{-1}K^{-1}]$, characterized by certain dependence with the SoC. On the other hand, the radial thermal conductivity in the BOL sample is estimated to have a negligible correlation with the state of charge and to be characterized by a mean value of 0.72 $[W\ m^{-1}K^{-1}]$. Additionally, this parameter is found to be appreciably higher in the aged sample, averaging around 0.82 $[W\ m^{-1}K^{-1}]$, resulting in an increase of 13.9%.

- An experimental campaign is carried out on the battery samples with internal temperature sensors. Charge and discharge tests are performed on the cells at BOL and aged conditions, and at different operating temperature, primarily at C-rate equal to 1C and 0.1C, measuring the internal and external temperature throughout the process. A clear correlation is found between the slope variations of the internal temperature and the thermodynamic behavior of batteries, through the comparison with DV curves obtained in quasi-static conditions. Moreover, variations in the temperature evolutions are detected between beginning of life and aged samples, demonstrating the visibility of changes of electrodes behavior also in the internal temperature. Furthermore, the increase in the radial thermal conductivity estimated from the previous experimental campaigns is confirmed also from in-operando internal temperature investigations.

- An additional experimental campaign is performed on BOL samples for the estimation of the entropic coefficient. In this regard, the entropic coefficient was computed from the equilibrium voltage differences arising from a variation of the external temperature. Moreover, a dependency between the heat capacity and the entropic coefficient is found in literature and is later demonstrated experimentally by com-

parison of the two quantities.

- A single particle model is conceptualized and implemented in MATLAB®, through the definition of physically grounded conservation equations for the internal components of a battery. A discretization employing Chebyshev nodes is used for the spherical electrodes particles.
- A two-dimensional thermal model is defined and implemented in MATLAB®, for the characterization of the temperature differences within the cylindrical samples. The model is based on a nodal description of the battery volume, such that the temperature evolution is described by a network of thermal resistances. The internal components domains are defined in the model, through the description of their thermal parameters and relative position within the cell.
- The models are validated on the previously obtained experimental data, through the calibration of the physical quantities governing the internal operation. A very good match is found between measured and simulated processes, both for voltage and internal temperature curves. In particular, an error of 5 $[mV]$ is estimated for a discharge at 0.04C, while a maximum error of 134.6 $[mV]$ is found for a discharge process at 1C, caused by the model assumptions. LLI and related aging phenomena are modeled through a correction on the stoichiometry of the anode: the maximum error is found to be equal to 44.3 $[mV]$, on the voltage curve of a discharge at 0.04C.
- The internal temperature evolution is described by the conservation of energy equation, linking overpotentials from the electrochemical behavior with the corresponding heat generation. The entropic coefficient map is calibrated on the internal temperature curve of a discharge test at 1C, and validated using the same map on a discharge test at 0.1C. The maximum error is found to be equal to 0.3 $[°C]$. In addition, the validation of the internal temperature evolution on aged samples is done on a 0.1C discharge process.
- A sensitivity analysis was done on the model for the thermal parameters. A variation of the specific heat capacity in the range of $\pm 10\%$, resulted in an appreciable temperature divergence at the end of the process, suggesting the need of a characterization on the specific sample. In contrast, the same variation on the radial thermal conductivity produced a negligible change in the final temperature, concluding that little variations can be achieved even assuming different values.

6.1. Final considerations

The thermal behavior of lithium-ion batteries must be always taken into account in the design of safe and efficient battery management systems. In this regard, it is fundamental to provide a reliable estimation of the main parameters governing heat transfer within batteries: these were identified to be the specific heat capacity and the thermal conductivity.

From a practical point of view, a very weak dependency was found between these parameters and the lithiation state of electrodes. This aspect could lead to the conclusion that an averaged form of them can be taken for generic applications, as very limited errors are obtained even for far off assumptions. Moreover, when aging is taken into account, an increase in thermal conductivity is experienced in the analyzed cells, suggesting the possibility of sizing battery thermal management systems only considering the BOL condition, as the latter represents the worst situation in terms of heat transfer.

Nevertheless, from a research standpoint, the investigation of these operational aspects is crucial for a better understanding of the thermodynamic and kinetic phenomena occurring within LIBs as it provides innovative ways for their characterization. For instance, the correlation found between the entropic coefficient and the heat capacity of batteries, demonstrated theoretically and experimentally, links inextricably the electrochemistry domain with the thermal behavior, through the thermodynamics of the system. A further confirmation of this aspect was provided by the internal temperature evolution of batteries during operation, measured through very accurate FBG optical sensors.

Furthermore, even if heat transfer is estimated to be worse at beginning of life, due to the lower thermal conductivity value, only a thorough and complete evaluation of the internal temperature at different conditions is able to describe the real performance.

In the end, it is demonstrated that the changes undergone by the internal components caused by degradation phenomena have an effect on the thermal parameters of lithium-ion batteries, due to the fact that the materials are effectively changing internally. In particular, it can be stated that passivation layers at the electrode-electrolyte interfaces, which were known to have an appreciable impact on the electrical behavior, influence the thermal behavior as well.

For these reasons, an extensive analysis of the latter is necessary for the correct representation of the internal and external states of batteries, as it ensures a deeper comprehension of their operating principles.

6.2. Future aspects

This thesis provides a comprehensive assessment on the effects of aging on the thermal behavior of the analyzed lithium-ion batteries, leading to a deeper understanding of the main related phenomena through the combination of experimental investigation and physics-based modeling. For future works, several activities can be suggested to further improve the comprehension of these aspects:

- Carry additional experimental campaigns for the analysis of the effects of different types of aging on thermal parameters of lithium-ion batteries, both individually or in combination with each others.
- Perform deeper analyses on the expansion of electrodes during operation, particularly for the assessment of pressure variations within the jellyroll and their effect on degradation phenomena and consequent changes in thermal behavior. In this regard, one of the main advantages of FBG sensors lies in the capability of measuring simultaneously temperature and strain variations, creating a possible pathway for this analysis also on individual electrodes.
- Improvements of the Single Particle Model, providing an advanced description of the internal phenomena and corresponding physical parameters. In particular:
  - Measurement of the equilibrium potential for both electrodes during charge processes, providing a better understanding on the related hysteresis phenomenon.
  - Computation of the entropic coefficient for individual electrodes, for the analysis of the different effects of aging on the single components.
  - introduction of diffusion coefficients as a function of the actual lithiation state of the electrodes, leading to a more precise description of these phenomena during operation.

Bibliography

[1] Vaclav Smil. *World History and Energy*. Elsevier, 2004.

[2] World Energy Council. World energy trilemma framework. https://www.worldenergy.org/transition-toolkit/world-energy-trilemma-framework, 2010. Accessed: 2024-12-18.

[3] Agnieszka Widuto. Energy transition in the eu, 2023.

[4] United Nations Framework Convention on Climate Change (UNFCCC). Kyoto protocol to the united nations framework convention on climate change. https://unfccc.int/documents/2409, 1997. Accessed: 2024-12-18.

[5] European Commission. Eu emissions trading system (eu ets). https://climate.ec.europa.eu/eu-action/eu-emissions-trading-system-eu-ets_en, 2005. Accessed: 2024-12-18.

[6] United Nations Framework Convention on Climate Change (UNFCCC). The paris agreement. https://unfccc.int/process-and-meetings/the-paris-agreement, 2015. Accessed: 2024-12-18.

[7] European Commission. The european green deal: Striving to be the first climate-neutral continent. https://commission.europa.eu/strategy-and-policy/priorities-2019-2024/european-green-deal_en, 2019. Accessed: 2024-12-18.

[8] Enas Taha Sayed, Abdul Ghani Olabi, Abdul Hai Alami, Ali Radwan, Ayman Mdallal, Ahmed Rezk, and Mohammad Ali Abdelkareem. Renewable energy and energy storage systems. *Energies*, 16(3), 2023.

[9] Enas Taha Sayed, Abdul Ghani Olabi, Abdul Hai Alami, Ali Radwan, Ayman Mdallal, Ahmed Rezk, and Mohammad Ali Abdelkareem. Renewable energy and energy storage systems, 2023.

[10] Dirk Uwe Sauer, Georg Fuchs, Benedikt Lunz, and Matthias Leuthold. Technology overview on electricity storage - overview on the potential and on the deployment

perspectives of electricity storage technologies. Technical report, Smart Energy for Europe Platform GmbH (SEFEP), 06 2012.

[11] Matteo Muratori, Marcus Alexander, Doug Arent, Morgan Bazilian, Ercan M. Dede, John Farrell, Chis Gearhart, David Greene, Alan Jenn, Matthew Keyser, Timothy Lipman, Sreekant Narumanchi, Ahmad Pesaran, Ramteen Sioshansi, Emilia Suomalainen, Gil Tal, Kevin Walkowicz, and Jacob Ward. The rise of electric vehicles-2020 status and future expectations, 2021.

[12] Nele Rietmann, Beatrice Hügler, and Theo Lieven. Forecasting the trajectory of electric vehicle sales and the consequences for worldwide co2 emissions. *Journal of Cleaner Production*, 261, 2020.

[13] IRENA. Electricity storage and renewables: Costs and markets to 2030. Technical report, International Renewable Energy Agency, Abu Dhabi, 2017.

[14] Zhonghao Rao and Shuangfeng Wang. A review of power battery thermal energy management, 2011.

[15] John Warner. *The handbook of lithium-ion battery pack design: Chemistry, components, types and terminology.* Elsevier, 2015.

[16] European Commission. Critical raw materials. `https://single-market-economy.ec.europa.eu/sectors/raw-materials/areas-specific-interest/critical-raw-materials_en`, 2023. Accessed: 2025-02-26.

[17] Ghassan Zubi, Rodolfo Dufo-López, Monica Carvalho, and Guzay Pasaoglu. The lithium-ion battery: State of the art and future perspectives. *Renewable and Sustainable Energy Reviews*, 89:292–308, 2018.

[18] Mogalahalli V. Reddy, Alain Mauger, Christian M. Julien, Andrea Paolella, and Karim Zaghib. Brief history of early lithium-battery development. *Materials*, 13, 2020.

[19] Krishneel Prakash, Muhammad Ali, Md Nazrul Islam Siddique, Aneesh A. Chand, Nallapaneni Manoj Kumar, Daoyi Dong, and Hemanshu R. Pota. A review of battery energy storage systems for ancillary services in distribution grids: Current status, challenges and future directions, 2022.

[20] IEA. Batteries and secure energy transitions. Technical report, IEA, Paris https://www.iea.org/reports/batteries-and-secure-energy-transitions, Licence: CC BY 4.0, 2024.

[21] Jianwu Wen, Yan Yu, and Chunhua Chen. A review on lithium-ion batteries safety issues: Existing problems and possible solutions, 2012.

[22] Roberto Evangelista. Experimental investigation and widespread application of physical model for the understanding of lithium-ion battery degradation. Master's thesis, Politecnico di Milano, 2022.

[23] Karrick Mergo Mbeya, Nicolas Damay, Guy Friedrich, Christophe Forgez, and Maxime Juston. Off-line method of the separation of the electrodes equilibrium state of the li-ion batteries. In *ELECTRIMACS 2019*, 05 2019.

[24] Xing Zhou, Zhengqiang Pan, Xuebing Han, Languang Lu, and Minggao Ouyang. An easy-to-implement multi-point impedance technique for monitoring aging of lithium ion batteries. *Journal of Power Sources*, 417, 2019.

[25] Bruno Scrosati. History of lithium batteries, 2011.

[26] Jakob Asenbauer, Tobias Eisenmann, Matthias Kuenzel, Arefeh Kazzazi, Zhen Chen, and Dominic Bresser. The success story of graphite as a lithium-ion anode material-fundamentals, remaining challenges, and recent developments including silicon (oxide) composites, 2020.

[27] Hee Je Kim, T. N.V. Krishna, Kamran Zeb, Vinodh Rajangam, Chandu V.V. Muralee Gopi, Sangaraju Sambasivam, Kummara Venkata Guru Raghavendra, and Ihab M. Obaidat. A comprehensive review of li-ion battery materials and their recycling techniques, 2020.

[28] Hui Cheng, Joseph G. Shapter, Yongying Li, and Guo Gao. Recent progress of advanced anode materials of lithium-ion batteries, 2021.

[29] Hao He, Jingjing Huang, Jiarui Wang, and Xin Xu. Research status and prospect of electrode materials for lithium-ion battery. *Applied and Computational Engineering*, 23, 2023.

[30] Michael Hess. Kinetics and stage transitions of graphite for lithium-ion batteries. *Ph.D. thesis, ETH Zurich*, 2013.

[31] Sujong Chae, Seong Hyeon Choi, Namhyung Kim, Jaekyung Sung, and Jaephil Cho. Integration of graphite and silicon anodes for the commercialization of high-energy lithium-ion batteries, 2020.

[32] Naoki Nitta, Feixiang Wu, Jung Tae Lee, and Gleb Yushin. Li-ion battery materials: Present and future, 2015.

[33] C. H. Chen, J. Liu, M. E. Stoll, G. Henriksen, D. R. Vissers, and K. Amine. Aluminum-doped lithium nickel cobalt oxide electrodes for high-power lithium-ion batteries. *Journal of Power Sources*, 128, 2004.

[34] Yu Kun Liu, Chen Zi Zhao, Juan Du, Xue Qiang Zhang, Ai Bing Chen, and Qiang Zhang. Research progresses of liquid electrolytes in lithium-ion batteries, 2023.

[35] Sheng Shui Zhang. A review on electrolyte additives for lithium-ion batteries, 2006.

[36] Ao Li, Anthony Chun Yin Yuen, Wei Wang, Ivan Miguel De Cachinho Cordeiro, Cheng Wang, Timothy Bo Yuan Chen, Jin Zhang, Qing Nian Chan, and Guan Heng Yeoh. A review on lithium-ion battery separators towards enhanced safety performances and modelling approaches, 2021.

[37] Hun Lee, Meltem Yanilmaz, Ozan Toprakci, Kun Fu, and Xiangwu Zhang. A review of recent developments in membrane separators for rechargeable lithium-ion batteries, 2014.

[38] Pengcheng Zhu, Dominika Gastol, Jean Marshall, Roberto Sommerville, Vannessa Goodship, and Emma Kendrick. A review of current collectors for lithium-ion batteries, 2021.

[39] Mitsuru Yamada, Tatsuya Watanabe, Takao Gunji, Jianfei Wu, and Futoshi Matsumoto. Review of the design of current collectors for improving the battery performance in lithium-ion and post-lithium-ion batteries, 2020.

[40] Yeonguk Son, Hyungyeon Cha, Taeyong Lee, Yujin Kim, Adam Boies, Jaephil Cho, and Michael De Volder. Analysis of differences in electrochemical performance between coin and pouch cells for lithium-ion battery applications. *Energy and Environmental Materials*, 7, 2024.

[41] EPEC engineered technologies. Prismatic and pouch battery packs. `https://www.epectec.com/batteries/prismatic-pouch-packs.html`, 2025. Accessed: 2025-01-06.

[42] Grepow. Prismatic vs pouch vs cylindrical lithium ion battery cell. `https://www.grepow.com/blog/prismatic-vs-pouch-vs-cylindrical-lithium-ion-battery-cell.html`, 2024. Accessed: 2025-01-06.

[43] Justin Holloway and Maria Balart Murria. Safety componentry for mitigating catastrophic failure in lithium-ion cylindrical cells. *ECS Meeting Abstracts*, MA2023-01, 2023.

[44] Sahithi Maddipatla, Lingxi Kong, and Michael Pecht. Safety analysis of lithium-ion cylindrical batteries using design and process failure mode and effect analysis, 2024.

[45] Bin Xu, Lingxi Kong, Guangrui Wen, and Michael G. Pecht. Protection devices in commercial 18650 lithium-ion batteries. *IEEE Access*, 9:66687–66695, 2021.

[46] Qian Wang, Bin Jiang, Bo Li, and Yuying Yan. A critical review of thermal management models and solutions of lithium-ion batteries for the development of pure electric vehicles, 2016.

[47] Hafiz Muhammad Ali. Thermal management systems for batteries in electric vehicles: A recent review, 2023.

[48] Xuning Feng, Dongsheng Ren, Xiangming He, and Minggao Ouyang. Mitigating thermal runaway of lithium-ion batteries, 2020.

[49] Xuning Feng, Minggao Ouyang, Xiang Liu, Languang Lu, Yong Xia, and Xiangming He. Thermal runaway mechanism of lithium ion battery for electric vehicles: A review, 2018.

[50] Daniela Galatro, Maan Al-Zareer, Carlos Da Silva, David A. Romero, and Cristina H. Amon. Thermal behavior of lithium-ion batteries: Aging, heat generation, thermal management and failure. *Frontiers in Heat and Mass Transfer*, 14, 2020.

[51] Divyesh Ubale and Prafulla Ubale. A critical review on recent developments in battery thermal management system of electric vehicles. In *Materials Today: Proceedings*, volume 68, 2022.

[52] Taehoon Kim, Wentao Song, Dae Yong Son, Luis K. Ono, and Yabing Qi. Lithium-ion batteries: outlook on present, future, and hybridized technologies, 2019.

[53] Ahmad Pesaran. Battery thermal management in evs and hevs : Issues and solutions. *Advanced Automotive Battery Conference*, 2001.

[54] Dawn Bernardi, Ellen Pawlikowski, and John Newman. General energy balance for battery systems. In *Electrochemical Society Extended Abstracts*, volume 84-2, 1984.

[55] Davide Ottolina. Characterization of real-life heterogeneous aging within lithium-ion battery modules through electro-thermal measurements and a lumped 0-d model. Master's thesis, Politecnico di Milano, 2024.

[56] Hans Dieter Baehr Karl Stephan. *Heat and Mass Transfer*. Springer, 2006.

[57] John H. Lienhard. A heat transfer textbook, fourth edition. *Phlogiston Press*, 2017.

[58] Lichuan Wei, Zhao Lu, Feng Cao, Liyu Zhang, Xi Yang, Xiaoling Yu, and Liwen Jin. A comprehensive study on thermal conductivity of the lithium-ion battery. *International Journal of Energy Research*, 44, 2020.

[59] S. J. Drake, D. A. Wetz, J. K. Ostanek, S. P. Miller, J. M. Heinzel, and A. Jain. Measurement of anisotropic thermophysical properties of cylindrical li-ion cells. *Journal of Power Sources*, 252, 2014.

[60] Luca Tendera, Dominik Wycisk, Carlos Gonzalez, Gerrit Karl Mertin, Hendrik Pegel, and Kai Peter Birke. Effects of geometric, structural and operational parameters on the thermal conductivity of lithium-ion cells. *Journal of Power Sources*, 549, 2022.

[61] K. A. Murashko, J. Pyrhönen, and J. Jokiniemi. Determination of the through-plane thermal conductivity and specific heat capacity of a li-ion cylindrical cell. *International Journal of Heat and Mass Transfer*, 162, 2020.

[62] Sylvain Cailliez, David Chalet, and Philippe Mannessiez. Simultaneous identification of the heat capacity and the anisotropic thermal conductivities of a li-ion pouch cell by a non-destructive analytical approach. *Journal of Power Sources*, 542, 2022.

[63] Georgi Kovachev, Andrea Astner, Gregor Gstrein, Luigi Aiello, Johann Hemmer, Wolfgang Sinz, and Christian Ellersdorfer. Thermal conductivity in aged li-ion cells under various compression conditions and state-of-charge. *Batteries*, 7, 2021.

[64] Luca Tendera, Dominik Wycisk, Alexander Fill, and Kai Peter Birke. The in-plane thermal conductivity of lithium-ion cells: Parametric influences and simulative prediction. In *IEEE International Symposium on Industrial Electronics*, volume 2023-June, 2023.

[65] Gavin White, Alastair Hales, Yatish Patel, and Gregory Offer. Novel methods for measuring the thermal diffusivity and the thermal conductivity of a lithium-ion battery. *Applied Thermal Engineering*, 212, 2022.

[66] Lei Sheng, Lin Su, Hengyun Zhang, Yidong Fang, Haifeng Xu, and Wen Ye. An improved calorimetric method for characterizations of the specific heat and the heat generation rate in a prismatic lithium ion battery cell. *Energy Conversion and Management*, 180, 2019.

[67] Matthias Faber, Oliver Buitkamp, Simon Ritz, Martin Börner, Jonathan Berger, Julian Friedrich, Arno Arzberger, and Dirk Uwe Sauer. A method to determine the

specific heat capacity of lithium-ion battery cells using thermal insulation. *Journal of Power Sources*, 583, 2023.

[68] Thomas S. Bryden, Borislav Dimitrov, George Hilton, Carlos Ponce de León, Peter Bugryniec, Solomon Brown, Denis Cumming, and Andrew Cruden. Methodology to determine the heat capacity of lithium-ion cells. *Journal of Power Sources*, 395, 2018.

[69] Stephen J. Bazinski and Xia Wang. Experimental study on the influence of temperature and state-of-charge on the thermophysical properties of an lfp pouch cell. *Journal of Power Sources*, 293, 2015.

[70] Christoph R. Birkl, Matthew R. Roberts, Euan McTurk, Peter G. Bruce, and David A. Howey. Degradation diagnostics for lithium ion cells. *Journal of Power Sources*, 341, 2017.

[71] Anthony Barré, Benjamin Deguilhem, Sébastien Grolleau, Mathias Gérard, Frédéric Suard, and Delphine Riu. A review on lithium-ion battery ageing mechanisms and estimations for automotive applications, 2013.

[72] Xianke Lin, Kavian Khosravinia, Xiaosong Hu, Ju Li, and Wei Lu. Lithium plating mechanism, detection, and mitigation in lithium-ion batteries, 2021.

[73] Pallavi Verma, Pascal Maire, and Petr Novák. A review of the features and analyses of the solid electrolyte interphase in li-ion batteries, 2010.

[74] E. Peled and S. Menkin. Review—sei: Past, present and future. *Journal of The Electrochemical Society*, 164, 2017.

[75] Seong Jin An, Jianlin Li, Claus Daniel, Debasish Mohanty, Shrikant Nagpure, and David L. Wood. The state of understanding of the lithium-ion-battery graphite solid electrolyte interphase (sei) and its relationship to formation cycling, 2016.

[76] Henry Adenusi, Gregory A. Chass, Stefano Passerini, Kun V. Tian, and Guanhua Chen. Lithium batteries and the solid electrolyte interphase (sei)—progress and outlook, 2023.

[77] J. Vetter, P. Novák, M. R. Wagner, C. Veit, K. C. Möller, J. O. Besenhard, M. Winter, M. Wohlfahrt-Mehrens, C. Vogler, and A. Hammouche. Ageing mechanisms in lithium-ion batteries. *Journal of Power Sources*, 147, 2005.

[78] M. Broussely, Ph Biensan, F. Bonhomme, Ph Blanchard, S. Herreyre, K. Nechev,

and R. J. Staniewicz. Main aging mechanisms in li ion batteries. In *Journal of Power Sources*, volume 146, 2005.

[79] Najmus Saqib, Chase M. Ganim, Austin E. Shelton, and Jason M. Porter. On the decomposition of carbonate-based lithium-ion battery electrolytes studied using operando infrared spectroscopy. *Journal of The Electrochemical Society*, 165, 2018.

[80] H. H. Lee, C. C. Wan, and Y. Y. Wang. Thermal stability of the solid electrolyte interface on carbon electrodes of lithium batteries. *Journal of The Electrochemical Society*, 151, 2004.

[81] K. Edström, T. Gustafsson, and J. O. Thomas. The cathode-electrolyte interface in the li-ion battery. In *Electrochimica Acta*, volume 50, 2004.

[82] Jangwhan Seok, Wontae Lee, Hyunbeom Lee, Sangbin Park, Chanyou Chung, Sunhyun Hwang, and Won Sub Yoon. Aging mechanisms of lithium-ion batteries, 2024.

[83] Thomas Waldmann, Björn Ingo Hogg, and Margret Wohlfahrt-Mehrens. Li plating as unwanted side reaction in commercial li-ion cells – a review, 2018.

[84] Qianqian Liu, Chunyu Du, Bin Shen, Pengjian Zuo, Xinqun Cheng, Yulin Ma, Geping Yin, and Yunzhi Gao. Understanding undesirable anode lithium plating issues in lithium-ion batteries. *RSC Advances*, 6, 2016.

[85] Zhe Li, Jun Huang, Bor Yann Liaw, Viktor Metzler, and Jianbo Zhang. A review of lithium deposition in lithium-ion and lithium metal secondary batteries. *Journal of Power Sources*, 254, 2014.

[86] Kenji Takahashi and Venkat Srinivasan. Examination of graphite particle cracking as a failure mode in lithium-ion batteries: A model-experimental study. *Journal of The Electrochemical Society*, 162, 2015.

[87] Geun-Chang Chung, Hyung-Jin Kim, Seung-Il Yu, Song-Hui Jun, Jong wook Choi, and Myung-Hwan Kim. Origin of graphite exfoliation an investigation of the important role of solvent cointercalation. *Journal of The Electrochemical Society*, 147, 2000.

[88] Chun Zhan, Tianpin Wu, Jun Lu, and Khalil Amine. Dissolution, migration, and deposition of transition metal ions in li-ion batteries exemplified by mn-based cathodes-a critical review, 2018.

[89] Liya Guo, Daisy B. Thornton, Mohamed A. Koronfel, Ifan E.L. Stephens, and Mary P. Ryan. Degradation in lithium ion battery current collectors, 2021.

[90] Simon Müller, Patrick Pietsch, Ben Elias Brandt, Paul Baade, Vincent De Andrade, Francesco De Carlo, and Vanessa Wood. Quantification and modeling of mechanical degradation in lithium-ion batteries based on nanoscale imaging. *Nature Communications*, 9, 2018.

[91] Peter Keil, Simon F. Schuster, Jörn Wilhelm, Julian Travi, Andreas Hauser, Ralph C. Karl, and Andreas Jossen. Calendar aging of lithium-ion batteries. *Journal of The Electrochemical Society*, 163, 2016.

[92] Julius Schmitt, Arpit Maheshwari, Michael Heck, Stephan Lux, and Matthias Vetter. Impedance change and capacity fade of lithium nickel manganese cobalt oxide-based batteries during calendar aging. *Journal of Power Sources*, 353, 2017.

[93] John Wang, Justin Purewal, Ping Liu, Jocelyn Hicks-Garner, Souren Soukazian, Elena Sherman, Adam Sorenson, Luan Vu, Harshad Tataria, and Mark W. Verbrugge. Degradation of lithium ion batteries employing graphite negatives and nickel-cobalt-manganese oxide + spinel manganese oxide positives: Part 1, aging mechanisms and life estimation. *Journal of Power Sources*, 269, 2014.

[94] Arpit Maheshwari, Michael Heck, and Massimo Santarelli. Cycle aging studies of lithium nickel manganese cobalt oxide-based batteries using electrochemical impedance spectroscopy. *Electrochimica Acta*, 273, 2018.

[95] Luca Tendera, Dominik Wycisk, Carlos Gonzalez, Jochen Stadler, and Kai Peter Birke. Influence of state of health and individual aging mechanisms on the thermal conductivity of lithium-ion cells. *Journal of Energy Storage*, 62, 2023.

[96] A123 Systems. Nanophosphate high power lithium ion cell anr26650m1-a. `https://www.buya123products.com/uploads/vipcase/844c1bd8bdd1190ebb364d572bc1e6e7.pdf`. Accessed: 2025-01-27.

[97] A123 Systems. Anr26650m1b lithium ion cylindrical cell. `https://www.buya123products.com/uploads/vipcase/21b3e568fb44ba9ca2c0d4c1aa534ed3.pdf`. Accessed: 2025-01-27.

[98] Alessandro Innocenti. An innovative methodology to estimate the parameters of a lithium ion battery physical model. Master's thesis, Politecnico di Milano, 2020.

[99] Andrea Rondi Davide Conti. Experimental investigation of lithium-ion battery automotive related aging and model-based interpretation. Master's thesis, Politecnico di Milano, 2022.

[100] Gian Marco Trippetta. Analysis of degradation of lithium-ion batteries coming from real automotive application. Master's thesis, Politecnico di Milano, 2022.

[101] Chroma ATE Inc. Dc electronic load model 63600 series. https://www.chromaate.com/it/product/dc_electronic_load_63600_series_65. Accessed: 2025-01-27.

[102] National Instruments. Ni rmx-4124. https://www.ni.com/it-it/shop/model/rmx-4124.html. Accessed: 2025-01-27.

[103] National Instruments. Ni usb-6218. https://www.ni.com/docs/en-US/bundle/usb-6218-specs/page/specs.html. Accessed: 2025-01-27.

[104] National Instruments. Ni 9211. https://www.ni.com/it-it/shop/model/ni-9211.html. Accessed: 2025-01-27.

[105] Binder. Model mkf 720 | dynamic climate chambers for rapid temperature changes with humidity control. https://www.binder-world.com/int-en/products/climate-chambers/dynamic-climate-chambers/product/mkf-720. Accessed: 2025-01-27.

[106] Binder. Model kt 53 | cooling incubators with peltier technology. https://www.binder-world.com/int-en/products/incubators/cooling-incubators/product/kt-53. Accessed: 2025-01-27.

[107] Chroma ATE Inc. Dc power supply model 62000p. https://www.chromaate.com/en/product/dc_power_supply_62000p_series_210. Accessed: 2025-01-27.

[108] National Instruments. What is ni labview? https://www.ni.com/en/shop/labview.html. Accessed: 2025-01-27.

[109] Arduino S.r.l. Arduino uno rev3. https://store.arduino.cc/products/arduino-uno-rev3. Accessed: 2025-01-27.

[110] Cambridge Dictionary. https://dictionary.cambridge.org/dictionary/english/glove-box. Accessed: 2025-01-21.

[111] Jacomex. Puremod glovebox - modular design for a wide range of applications. https://www.jacomex.com/glove-box/puremod/. Accessed: 2025-01-27.

[112] Pfeiffer Vacuum+Fab Solutions. Pascal 2021, c2 version, 1-phase motor, 180 – 254 v, 50/60 hz, ce/ul/csa. https://www.pfeiffer-vacuum.com/global/en/shop/products/221C2MHEN. Accessed: 2025-01-27.

[113] Naixing Yang, Xiongwen Zhang, Guojun Li, and Dong Hua. Study on the charg-

ing behaviors of lithium-ion batteries by analysis of li distribution in the electrode particles. *ECS Transactions*, 66, 2015.

[114] Alexandros Ch Lazanas and Mamas I. Prodromidis. Electrochemical impedance spectroscopy - a tutorial, 2023.

[115] Haifeng Dai, Bo Jiang, and Xuezhe Wei. Impedance characterization and modeling of lithium-ion batteries considering the internal temperature gradient. *Energies*, 11, 2018.

[116] Isabel Jiménez Gordon, Sylvie Grugeon, Aurélie Débart, Gwennaëlle Pascaly, and Stéphane Laruelle. Electrode contributions to the impedance of a high-energy density li-ion cell designed for ev applications. *Solid State Ionics*, 237, 2013.

[117] Woosung Choi, Heon Cheol Shin, Ji Man Kim, Jae Young Choi, and Won Sub Yoon. Modeling and applications of electrochemical impedance spectroscopy (eis) for lithium-ion batteries, 2020.

[118] Salim Erol and Mark E. Orazem. The influence of anomalous diffusion on the impedance response of licoo2|c batteries. *Journal of Power Sources*, 293, 2015.

[119] A. S. Keefe, Samuel Buteau, I. G. Hill, and J. R. Dahn. Temperature dependent eis studies separating charge transfer impedance from contact impedance in lithium-ion symmetric cells. *Journal of The Electrochemical Society*, 166, 2019.

[120] Emile Webster. A critical review of the common thermocouple reference functions, 2021.

[121] Massimo Morante. Fiber bragg gratings sensors for harsh environments. Master's thesis, Università di Pisa, 2018.

[122] Stephen J. Mihailov. Fiber bragg grating sensors for harsh environments, 2012.

[123] Susana Novais, Micael Nascimento, Lorenzo Grande, Maria Fátima Domingues, Paulo Antunes, Nélia Alberto, Cátia Leitão, Ricardo Oliveira, Stephan Koch, Guk Tae Kim, Stefano Passerini, and João Pinto. Internal and external temperature monitoring of a li-ion battery with fiber bragg grating sensors. *Sensors (Switzerland)*, 16, 2016.

[124] Micael Nascimento, Marta S. Ferreira, and João L. Pinto. Real time thermal monitoring of lithium batteries with fiber sensors and thermocouples: A comparative study. *Measurement: Journal of the International Measurement Confederation*, 111, 2017.

[125] Markus S. Wahl, Lena Spitthoff, Harald I. Muri, Asanthi Jinasena, Odne S. Burheim, and Jacob J. Lamb. The importance of optical fibres for internal temperature sensing in lithium-ion batteries during operation. *Energies*, 14, 2021.

[126] Joe Fleming, Tazdin Amietszajew, Euan McTurk, Dave Greenwood, and Rohit Bhagat. Development and evaluation of in-situ instrumentation for cylindrical li-ion cells using fibre optic sensors. *HardwareX*, 3, 2018.

[127] Euan McTurk, Tazdin Amietszajew, Joe Fleming, and Rohit Bhagat. Thermo-electrochemical instrumentation of cylindrical li-ion cells. *Journal of Power Sources*, 379, 2018.

[128] C. P. Aiken, J. Xia, David Yaohui Wang, D. A. Stevens, S. Trussler, and J. R. Dahn. An apparatus for the study of in situ gas evolution in li-ion pouch cells. *Journal of The Electrochemical Society*, 161, 2014.

[129] L. D. Ellis, J. P. Allen, L. M. Thompson, J. E. Harlow, W. J. Stone, I. G. Hill, and J. R. Dahn. Quantifying, understanding and evaluating the effects of gas consumption in lithium-ion cells. *Journal of The Electrochemical Society*, 164, 2017.

[130] Tessa Krause, Daniel Nusko, Luciana Pitta Bauermann, Matthias Vetter, Marcel Schäfer, and Carlo Holly. Methods for quantifying expansion in lithium-ion battery cells resulting from cycling: A review. *Energies*, 17(7), 2024.

[131] Julian Self. In situ volume studies of li-ion pouch cells. Master's thesis, Dalhousie University, 2015.

[132] Arexons. Acqua distillata demineralizzata. `https://arexons.it/media/uploads/products/pdf/ST3510-acqua-distillata-demineralizzata_arlzXgP.pdf`. Accessed: 2025-01-27.

[133] J. C. Jaeger H. S. Carlslaw. *Conduction of heat in solids*. Clarendon Press, Oxford, 1959.

[134] Yujie Zhu and Chunsheng Wang. Strain accommodation and potential hysteresis of lifepo4 cathodes during lithium ion insertion/extraction. *Journal of Power Sources*, 196, 2011.

[135] Lucca Matuck, João P. Santos, Fábio Freitas, Luís B. Fontes, Jörg Bierlich, Sylvie Geniès, João L. Pinto, Marta S. Ferreira, Olivier Raccurt, and Micael Nascimento. Towards smart and secure batteries: Linking pressure and temperature profiles with electrochemical behavior through hybrid optical fiber sensors. *Chemical Engineering Journal*, 500:156806, 2024.

[136] Gerrit Karl Mertin, Dominik Wycisk, Marc Oldenburger, Gerry Stoye, Alexander Fill, Kai Peter Birke, and Andreas Dirk Wieck. Dynamic measurement of the entropy coefficient for battery cells. *Journal of Energy Storage*, 51, 2022.

[137] Stephen Bazinski and Xia Wang. Determining entropic coefficient of the lfp prismatic cell at various temperatures and charge/discharge states. *ECS Transactions*, 45, 2013.

[138] Gerrit Karl Mertin, Marc Oldenburger, Ernst Richter, Markus Hans Hofmann, and Kai Peter Birke. Revised theory of entropy and reversible energy flow in galvanic cells. *Journal of Power Sources*, 482, 2021.

[139] Scott G. Marquis, Valentin Sulzer, Robert Timms, Colin P. Please, and S. Jon Chapman. An asymptotic derivation of a single particle model with electrolyte. *Journal of The Electrochemical Society*, 166, 2019.

[140] Iulian Munteanu, Antoneta Iuliana Bratcu, Pierre-Xavier Thivel, Yann Bultel, Didier Georges, and Céline Decaux. Single-particle model of li-ion battery – model calibration and validation against real data in an electric vehicular application∗∗this work has been funded by irga ("initiatives de recherche à grenoble alpes") project padesoh ("partial-differential-equation-model-based estimation of battery state of health"), within the framework of "investissement d'avenir" anr-15-idex-02 french national research and innovation funding programme. *IFAC-PapersOnLine*, 58(13):23–30, 2024. 12th IFAC Symposium on Control of Power and Energy Systems - CPES 2024.

[141] E. Prada, D. Di Domenico, Y. Creff, J. Bernard, V. Sauvant-Moynot, and F. Huet. Simplified electrochemical and thermal model of lifepo 4 -graphite li-ion batteries for fast charge applications. *Journal of The Electrochemical Society*, 159, 2012.

[142] Jeffrey Orrey. A generalized fourier pseudospectral method for elastodynamics. Master's thesis, University of Colorado, 1995.

[143] Dafaalla M.D. Babiker, Zubaida Rukhsana Usha, Caixia Wan, Mohmmed Mun ELseed Hassaan, Xin Chen, and Liangbin Li. Recent progress of composite polyethylene separators for lithium/sodium batteries, 2023.

[144] Yu wei Pan, Yang Hua, Sida Zhou, Rong He, Yulong Zhang, Shichun Yang, Xinhua Liu, Yubo Lian, Xiaoyu Yan, and Billy Wu. A computational multi-node electrothermal model for large prismatic lithium-ion batteries. *Journal of Power Sources*, 459, 2020.

A | Appendix A

During the thermal characterization experimental campaign, two additional M1A samples were tested, estimating specific heat capacity and radial and axial thermal conductivity values.

This type of sample was only characterized at aged conditions, due to the unavailability of the same kind of cells at beginning of life. It is known from their datasheet (section 2.1) that they are characterized by a lower capacity and a lower mass (thus a lower density at parity of volume) compared to the subsequent M1B samples, leading to a substantial difference in the estimated thermal parameters with respect to the latter.

Given that one of the objectives of the thesis is to characterize the effects of aging on batteries, similar samples are needed. For this reason, the study of these cells was later abandoned, as they didn't offer a useful comparison with M1B samples.

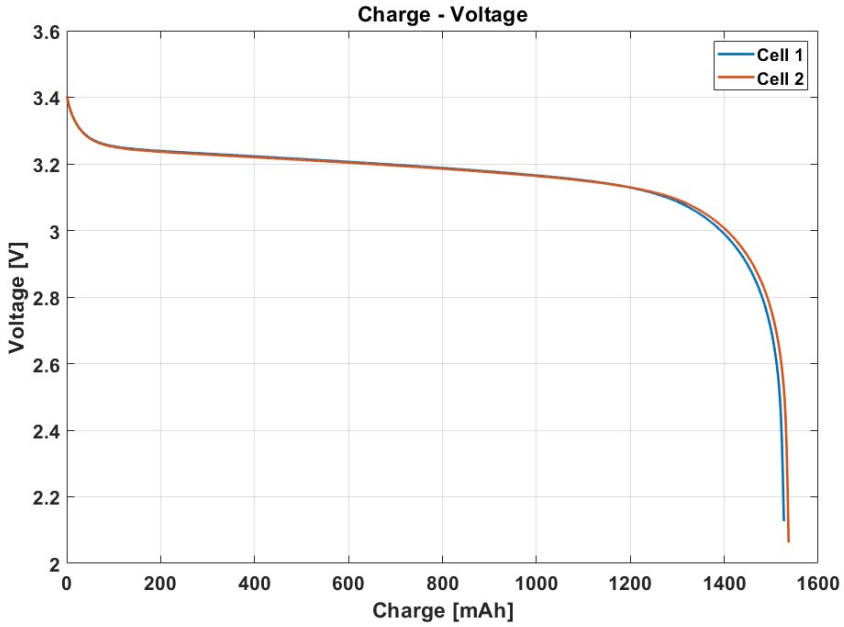

Figure A.1: Voltage curves obtained from discharge tests at 1C for M1A samples in aged conditions

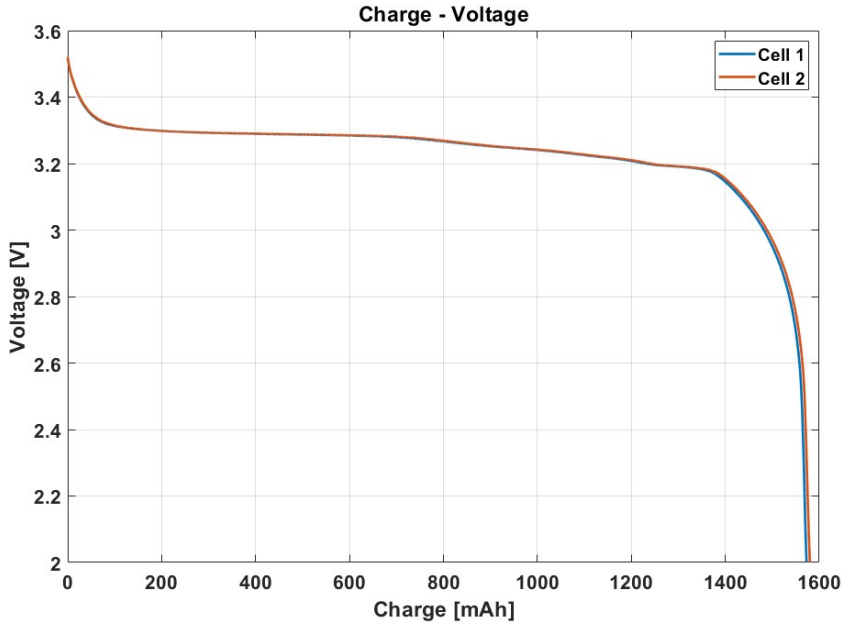

Figure A.2: Voltage curves obtained from discharge tests at 0.04C for M1A samples in aged conditions

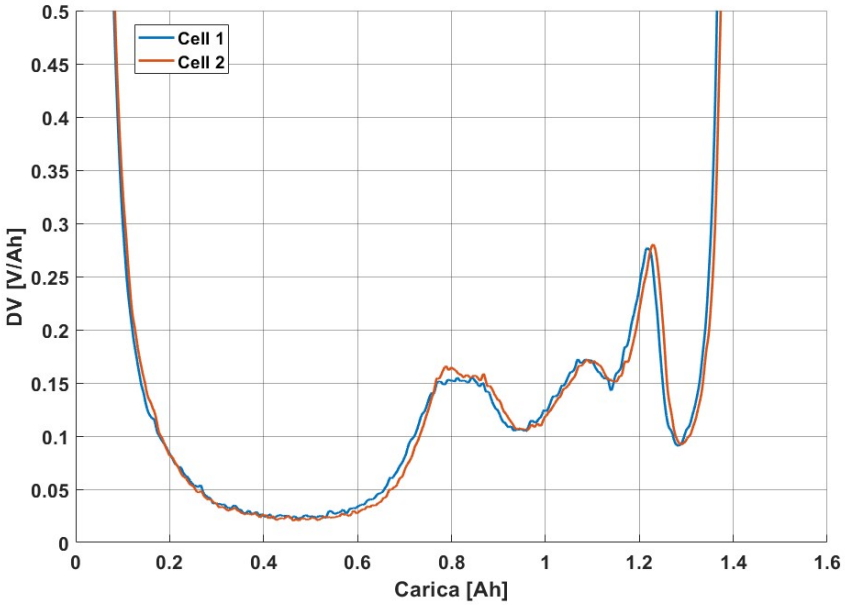

Figure A.3: DV curves obtained from discharge tests at 0.04C for M1A samples in aged conditions

In figure A.1 and figure A.2 the discharge tests of the samples can be seen. It can be noticed that they are characterized by a very low residual capacity, such that the first slope variation is absent in both curves even if the cathode and anode chemistry is the same.

This was later confirmed by the DV curve obtained from the same discharge processes at 0.04C (figure A.3).

In figures A.4 and A.5 are presented the EIS results at $SoC = 1$ and $SoC = 0$, respectively, for both of the analyzed M1A samples.

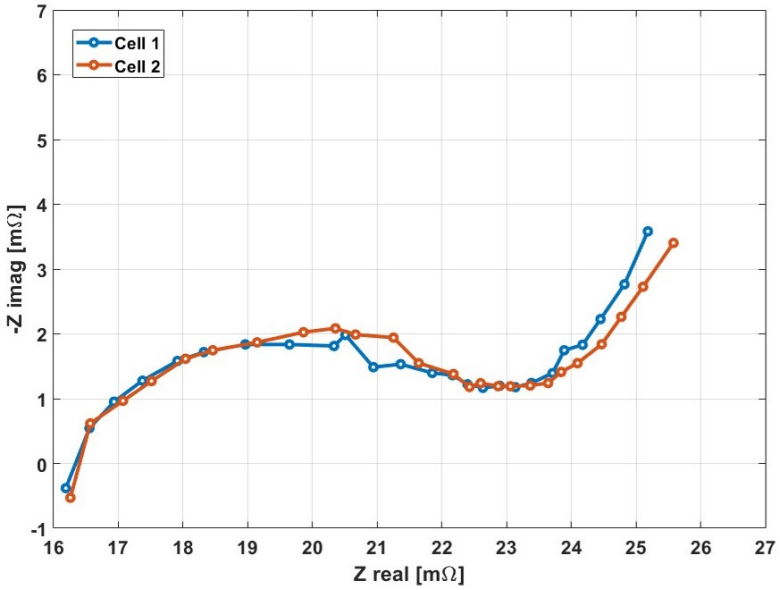

Figure A.4: Nyquist plot obtained from EIS analyses at SOC = 100% for M1A samples in aged conditions

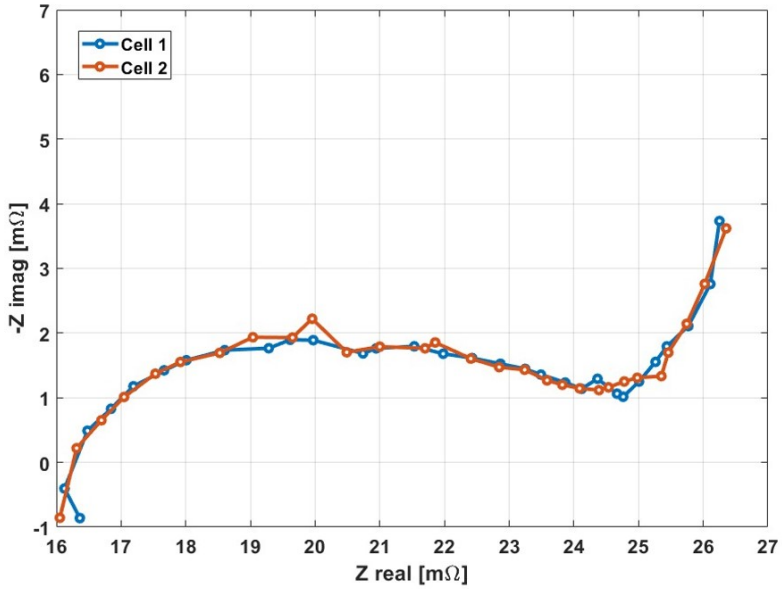

Figure A.5: Nyquist plot obtained from EIS analyses at SOC = 0 for M1A samples in aged conditions

It can be seen that both samples are characterized by a very high HFR, much higher than the one experienced in M1B samples. Moreover, the extensively developed semicircle leads to a very high charge transfer resistance.

The results of the thermal characterization are presented below. In this regard "Cell 2" was employed for the axial characterization, while the drilling methodology was applied on "Cell 1", before the radial thermal characterization was done.
In particular, figure A.6 represents the results of the specific heat capacity estimation from axial thermal tests.

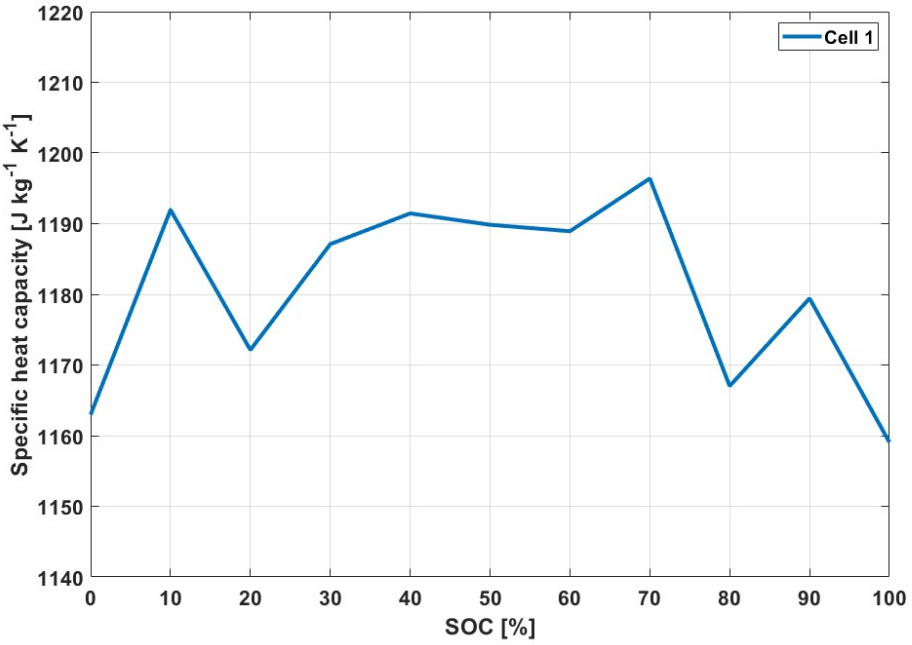

Figure A.6: Estimated values of specific heat capacity from axial thermal tests for M1A samples

It can be seen that the parabolic trend seen for M1B samples is observed also in this case, even if the values are somewhat different due to the lower density of M1A samples.

In addition, in figure A.7 the estimated values of axial thermal conductivity can be seen. It can be noted that the shape is similar to the results of the analogous tests for M1B samples, especially at high states of charge. In this case, the absolute values are slightly higher than the previously described experimental campaign, providing a proof of the increase of thermal conductivity (in this case axial) even for this sample type.

In figure A.8 the axial thermal diffusivity is presented. For this step, a density of 2086 $[kg\ m^{-3}]$ was used, computed from the mass and volume of M1A samples.

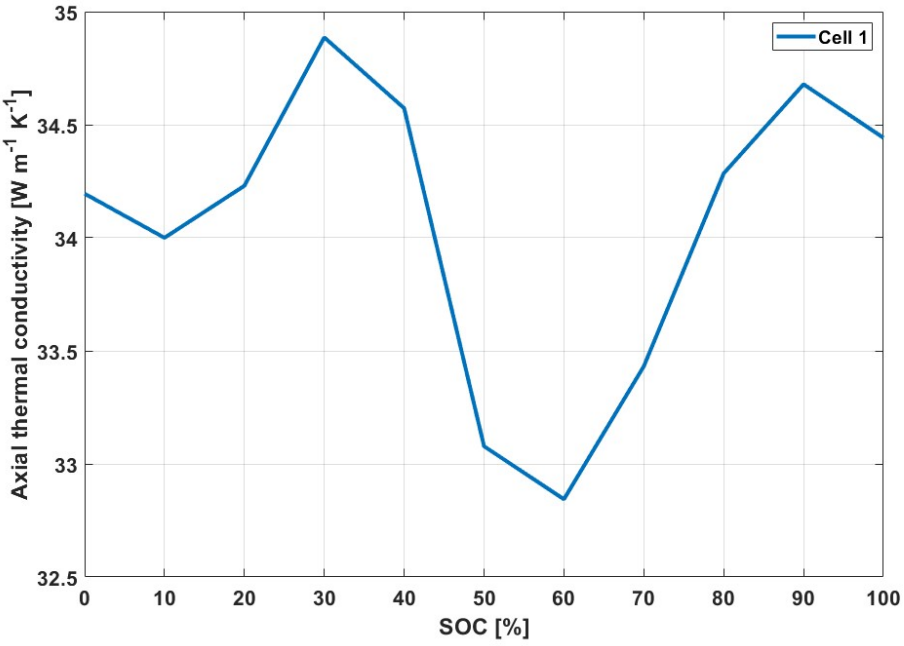

Figure A.7: Estimated values of axial thermal conductivity from axial thermal tests for M1A samples

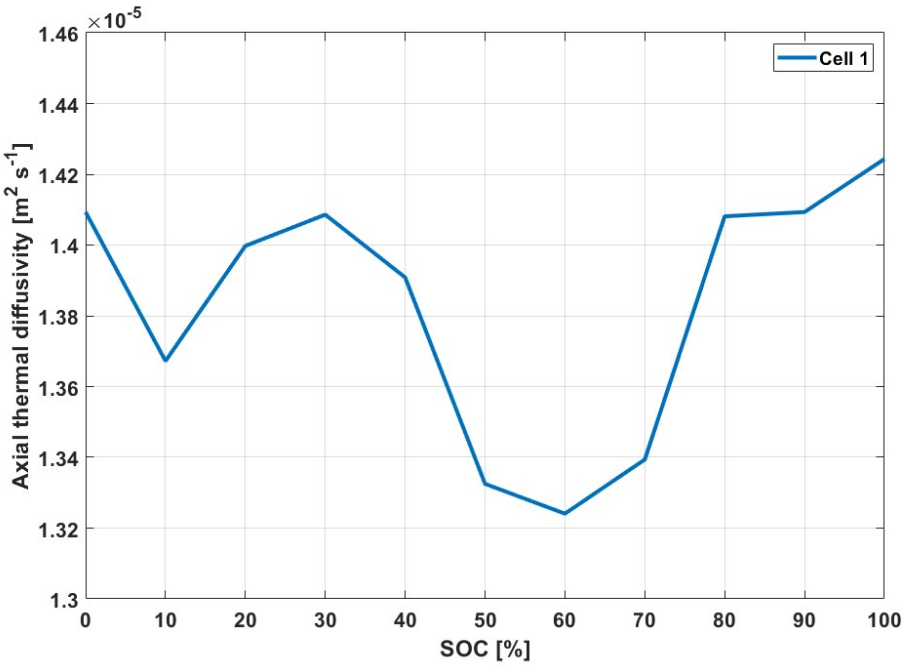

Figure A.8: Estimated values of axial thermal diffusivity from axial thermal tests for M1A samples

Finally, the results of the radial thermal characterization for M1A samples are showed.

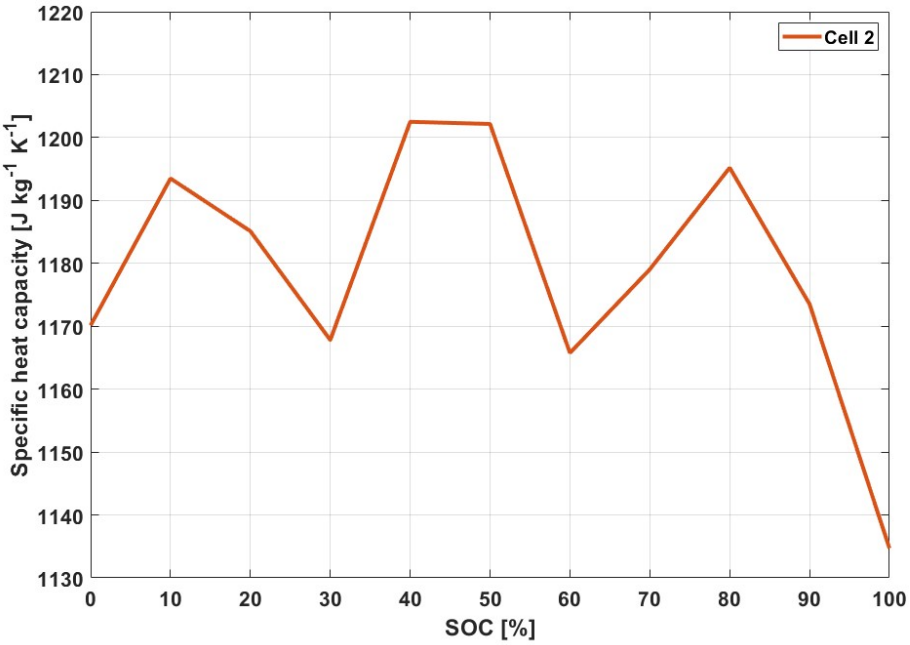

Figure A.9: Estimated values of specific heat capacity from radial thermal tests for M1A samples

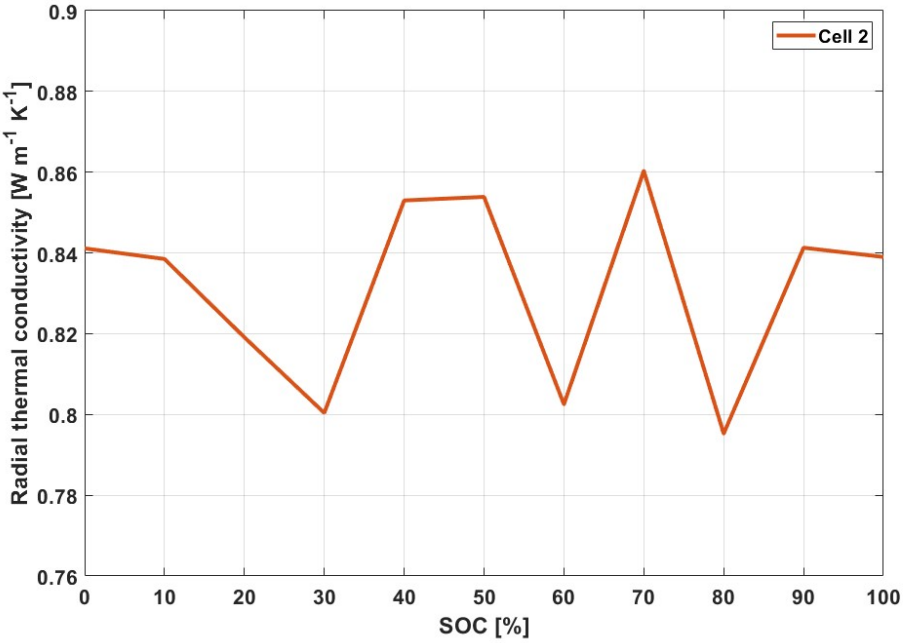

Figure A.10: Estimated values of radial thermal conductivity from radial thermal tests for M1A samples

In figure A.9 it can be seen that the estimated specific heat capacity is very similar to the one obtained for the same samples with axial thermal tests, leading to the verification of the consistency of both methods (in this regard, the same thermal efficiency used for radial tests on M1B samples was employed).
In figure A.10, instead, the radial thermal conductivity results can be viewed: this parameter presents a negligible dependency with the SoC, averaging around a value of 0.84 $[W\ m^{-1}K^{-1}]$. In this regard, this quantity is very similar to the one obtained from the aged M1B sample, leading to the verification of a similar thermal behavior between the two; however, given the different internal structure (M1A samples are characterized by a less dense jelly-roll), a fair comparison couldn't be done.
Finally, in figure A.11, the radial thermal diffusivity is reported, computed in the same way as the axial tests.

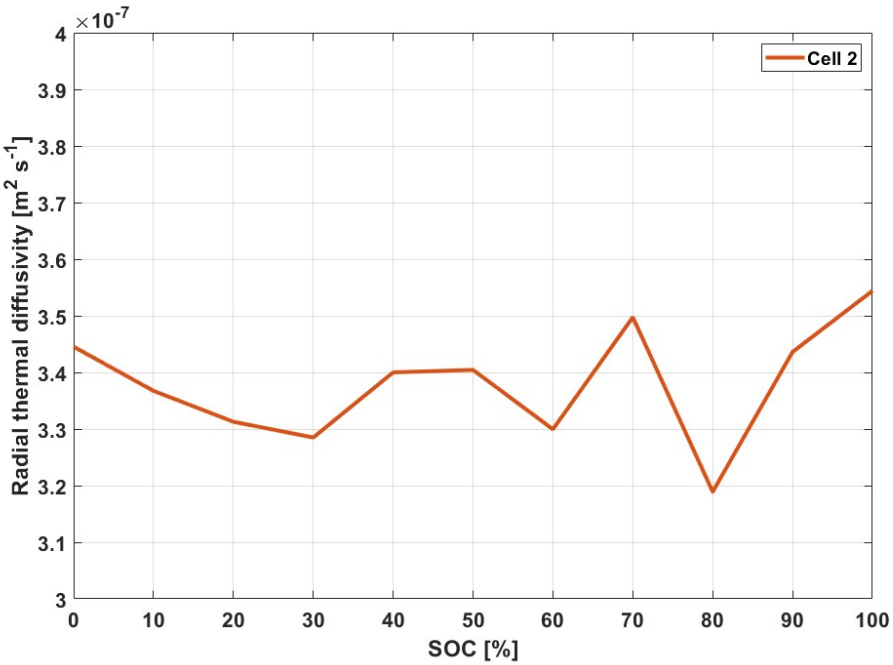

Figure A.11: Estimated values of radial thermal diffusivity from radial thermal tests for M1A samples

List of Figures

List of Tables

List of Symbols

Variable	Description	SI unit
Latin		
$\boldsymbol{a_s}$	Specific interfacial surface area	$[m^{-1}]$
$\boldsymbol{a_i}$	Chemical activity of i-th species ($i = Li^+, C, LiC, MO, LiMO$)	$[-]$
$\boldsymbol{A_{el}}$	Electrode surface area	$[m^2]$
$\boldsymbol{b}$	Bruggeman coefficient	$[-]$
$\boldsymbol{c_e}$	Lithium species concentration in electrolyte	$[mol\ m^{-3}]$
$\boldsymbol{c_{e,avg}}$	Average lithium species concentration in electrolyte	$[mol\ m^{-3}]$
$\boldsymbol{c_s}$	Lithium species concentration in solid particles	$[mol\ m^{-3}]$
$\boldsymbol{c_{s,max}}$	Maximum lithium concentration in solid particles	$[mol\ m^{-3}]$
$\boldsymbol{c_p}$	Specific heat capacity	$[J\ kg^{-1}K^{-1}]$
$\boldsymbol{C}$	Heat capacity	$[J\ K^{-1}]$
$\boldsymbol{D_s}$	Lithium diffusion coefficient in solid particles	$[m^2\ s^{-1}]$
$\boldsymbol{D_e}$	Lithium diffusion coefficient in electrolyte	$[m^2\ s^{-1}]$
$\boldsymbol{e}$	Emissive power	$[W\ m^{-2}]$
$\boldsymbol{EA_K}$	Rate constant activation energy	$[J\ mol^{-1}]$
$\boldsymbol{EA_{D_s}}$	Solid diffusion activation energy	$[J\ mol^{-1}]$
$\boldsymbol{EC}$	Entropic coefficient	$[V\ K^{-1}]$
$\boldsymbol{E_{ocp}}$	Electrode open circuit potential	$[V]$
$\boldsymbol{E_{OCV}}$	Battery open circuit voltage	$[V]$
$\boldsymbol{f_{max}}$	Maximum frequency	$[s^{-1}]$
$\boldsymbol{f_{min}}$	Minimum frequency	$[s^{-1}]$
$\boldsymbol{F}$	Faraday constant	$[C\ mol^{-1}]$
$\boldsymbol{F_b}$	Buoyancy force	$[N]$
$\boldsymbol{F_T}$	Tension force	$[N]$

Variable	Description	SI unit
$\boldsymbol{F_w}$	Weight force	$[N]$
$\boldsymbol{g}$	Acceleration of gravity	$[m\ s^{-2}]$
$\boldsymbol{h}$	Heat transfer coefficient	$[W\ m^{-2}K^{-1}]$
$\boldsymbol{i}$	Current density	$[A\ m^{-2}]$
$\boldsymbol{i_0}$	Exchange current density	$[A\ m^{-2}]$
$\boldsymbol{I}$	Current	$[A]$
$\boldsymbol{j}$	Reaction current density	$[A\ m^{-2}]$
$\boldsymbol{J}$	Exchanged energy	$[J]$
$\boldsymbol{k}$	Thermal conductivity (generic)	$[W\ m^{-1}K^{-1}]$
$\boldsymbol{k_{iso}}$	Thermal conductivity (isotropic)	$[W\ m^{-1}K^{-1}]$
$\boldsymbol{k_r}$	Radial thermal conductivity	$[W\ m^{-1}K^{-1}]$
$\boldsymbol{k_z}$	Axial thermal conductivity	$[W\ m^{-1}K^{-1}]$
$\boldsymbol{K}$	Reaction rate constant	$[m\ s^{-1}]$
$\boldsymbol{L}$	Cylindrical battery length	$[m]$
$\boldsymbol{L_i}$	Cell components thickness ($i = n, p, sep, tot$)	$[m]$
$\boldsymbol{m}$	Mass of the battery	$[kg]$
$\boldsymbol{n}$	Number of transferred charges	$[-]$
$\boldsymbol{n_i}$	Refractive index	$[-]$
$\boldsymbol{N}$	Lithium molar flux	$[mol\ m^{-2}s^{-1}]$
$\boldsymbol{N_f}$	Number of frequencies	$[-]$
$\boldsymbol{N_c}$	Number of cycles	$[-]$
$\boldsymbol{p}$	Pressure	$[N\ m^{-2}]$
$\boldsymbol{p_\epsilon}$	Strain-optic coefficient	$[-]$
$\boldsymbol{q}$	Volumetric heat flux	$[W\ m^{-3}]$
$\boldsymbol{\dot{q}}$	Heat flux	$[W\ m^{-2}]$
$\boldsymbol{\dot{q}_{conv}}$	Convective heat flux	$[W\ m^{-2}]$
$\boldsymbol{\dot{q}_r}$	Radial heat flux	$[W\ m^{-2}]$
$\boldsymbol{\dot{q}_z}$	Axial heat flux	$[W\ m^{-2}]$
$\boldsymbol{Q}$	Exchanged capacity	$[C]$
$\boldsymbol{Q_{nom}}$	Nominal capacity	$[C]$
$\boldsymbol{Q_{res}}$	Residual capacity	$[C]$

Variable	Description	SI unit
$\dot{Q}$	Thermal power generation	$[W]$
r	Radial coordinate	$[m]$
R	Universal gas constant	$[J\ mol^{-1}K^{-1}]$
R	Battery external radius	$[m]$
R_s	Solid particles radius	$[m]$
R_r	Radial thermal resistance	$[K\ W^{-1}]$
R_z	Axial thermal resistance	$[K\ W^{-1}]$
t	Time coordinate	$[s]$
t^+	Lithium transference number	$[-]$
T	Temperature	$[K]$
T_0	Reference or initial temperature	$[K]$
u	Modified concentration	$[mol\ m^{-2}]$
u_i	Uncertainty of i-th term	$[-]$
V	Volume	$[m^3]$
V_{cyl}	Cylinder volume	$[m^3]$
ΔV	Cell Voltage	$[V]$
W	Electrical power	$[W]$
x	Linear coordinate	$[m]$
x_1	Stoichiometry limit at $SoC = 1$	$[m]$
x_0	Stoichiometry limit at $SoC = 0$	$[m]$
z	Axial coordinate	$[m]$
Z	Impedance	$[\Omega]$
Greek		
α	Thermal diffusivity (generic)	$[m^2\ s^{-1}]$
α_r	Radial thermal diffusivity	$[m^2\ s^{-1}]$
α_z	Axial thermal diffusivity	$[m^2\ s^{-1}]$
α_{ox}	Charge transfer coefficient (oxidation)	$[-]$
α_{red}	Charge transfer coefficient (reduction)	$[-]$
β	Relative thermal expansion coefficient (FBG)	$[K^{-1}]$
γ	Relative thermal index refraction coefficient (FBG)	$[K^{-1}]$
ϵ	Body emissivity	$[-]$

Variable	Description	SI unit
$\boldsymbol{\epsilon}$	Strain variation	$[-]$
$\boldsymbol{\epsilon_e}$	Volume fraction of electrolyte	$[-]$
$\boldsymbol{\epsilon_s}$	Volume fraction of solid particles	$[-]$
$\boldsymbol{\eta}$	Overpotential (generic)	$[V]$
$\boldsymbol{\eta_n}$	Negative electrode reaction overpotential	$[V]$
$\boldsymbol{\eta_p}$	Positive electrode reaction overpotential	$[V]$
$\boldsymbol{\eta_e}$	Electrolyte transport overpotential	$[V]$
$\boldsymbol{\eta_{ohm}}$	Ohmic overpotential	$[V]$
$\boldsymbol{\eta_c}$	Columbic efficiency	$[-]$
$\boldsymbol{\eta_{en}}$	Energy efficiency	$[-]$
$\boldsymbol{\kappa}$	Electrolyte ionic conductivity	$[S\ m^{-1}]$
$\boldsymbol{\kappa_D}$	Electrolyte diffusional ionic conductivity	$[A\ m^{-1}]$
$\boldsymbol{\lambda_B}$	Bragg wavelength	$[m]$
$\boldsymbol{\Lambda}$	Grating period	$[m]$
$\boldsymbol{\xi}$	Effectiveness of radial heater	$[-]$
$\boldsymbol{\pi}$	Greek pi	$[-]$
$\boldsymbol{\rho}$	Battery Mass density	$[kg\ m^{-3}]$
$\boldsymbol{\sigma}$	Solid particles conductivity	$[S\ m^{-1}]$
$\boldsymbol{\phi}$	Electric potential	$[V]$
$\boldsymbol{\varphi}$	Phase shift	$[-]$
$\boldsymbol{\omega}$	Angular frequency	$[s^{-1}]$
Other		
$\boldsymbol{\nabla}$	Nabla operator	$[-]$
$\boldsymbol{\nabla^2}$	Laplace operator	$[-]$
Superscript		
eff	Effective	$[-]$